Large Deflection Inextensible Beams and Plates and their Responses to Nonconservative Forces: Theory and Computations

by

Kevin A. McHugh

Department of Mechanical Engineering and Materials Science
Duke University

Date: _____

Approved:

_____
Earl H. Dowell, Advisor

_____
Donald Bliss

_____
Laurens Howle

_____
Lawrence Virgin

_____
Thomas Witelski

Dissertation submitted in partial fulfillment of the requirements for the degree of Doctor of Philosophy in the Department of Mechanical Engineering and Materials Science in the Graduate School of Duke University
2020

Abstract

Large Deflection Inextensible Beams and Plates and their Responses to Nonconservative Forces: Theory and Computations

by

Kevin A. McHugh

Department of Mechanical Engineering and Materials Science
Duke University

Date: _____

Approved:

_____
Earl H. Dowell, Advisor

_____
Donald Bliss

_____
Laurens Howle

_____
Lawrence Virgin

_____
Thomas Witelski

An abstract of a dissertation submitted in partial fulfillment of the requirements for the degree of Doctor of Philosophy in the Department of Mechanical Engineering and Materials Science in the Graduate School of Duke University
2020

Abstract

There is a growing interest among aeroelasticity researchers for insight into large deflection oscillations of aerospace structures. Here, a new beam and plate model is derived using Hamilton's Principle to lay the structural framework for a nonlinear, large deflection aeroelastic model. Two boundary conditions of the beam are explored: cantilevered and free-free. For a plate, the cantilevered boundary condition is considered. In these conditions, the nonlinearity stems from the structure's large curvature rather than from stretching. Therefore, this model makes use of the simplifying assumption that the the structure has no strain along the midplane; thus the model is "inextensible." Insight into the nonlinearity of this system is gained by applying harmonic loads to the structure, and stability conditions are also investigated by applying nonconservative follower loads.

Upon validating the structural model, the model is then coupled with aerodynamic models to form new, nonlinear aeroelastic models. Using classical aeroelasticity tools such as Piston Theory to model aerodynamic forces on the largely deflected cantilever, new insights are gained into the stability behavior of the system, the post-flutter behavior of the system, and the utility of these classic techniques with these novel configurations. With the large deflection cases, several novel nonlinearities are introduced, and it is shown that the systems are highly sensitive to the inclusion of these nonlinearities. Of course these classical aerodynamic theories are derived assuming small deflections, so attention is given to ensure that the Classical Piston

Thoery is applicable in the current configurations. Also a new aerodynamic theory is proposed for pressures on structures undergoing large deflections. In total, this document proposes and explores new methodologies for modeling aeroelastic structures which tend to undergo large elastic deformations.

Contents

List of Tables

List of Figures

List of Abbreviations and Symbols

Symbols

λ	Lagrange multiplier
EI	Flexural Rigidity
f	Constraint function
F	Force applied
g_u, g_v	Special functions
h	Thickness of beam or plate
$\mathcal{L}$	Lagrangian
L	Beam length
m	Mass per unit length of beam
T	Kinetic energy
u	Longitudinal deflection
V	Potential energy
w	Transverse deflection
x	Spatial coordinate
x_F	Location of applied force
$\dot{}$	Denotes time derivative

Abbreviations

FEM	Finite Element Method

FNL	Fully Nonlinear
INL	Inertia Nonlinearity
LCO	Limit Cycle Oscillation
RMS	Root Mean Square
SNL	Stiffness Nonlinearity

Acknowledgements

Many thanks are due to:

- My Advisor: Dr. Earl Dowell, for all of the traits that make him an exceptional advisor: his personality, patience, and pedagogy
- My Committee: Drs. Philip Beran, Donald Bliss, Laurens Howle, Lawrence Virgin, Thomas Witelski, for their years of friendly teaching, collaboration, and support
- The team at Wright-Patterson Air Force Base, especially Drs. Philip Beran, Charles Tyler, and Raymond Kolonay, for welcoming and teaching me during my internships and into the future
- Department of Defense SMART Scholarship, made possible by ASEE and LMI, for making this financially possible

Much personal appreciation is reserved for:

- Charlotte, for making Duke and Durham my home
- My family, for supporting me always
- The Dunn family, for keeping me fed and watered

1

Introduction

1.1 Motivation

The introduction of novel materials and designs of aerospace structures adds complexity and uncertainty to the study of structural dynamics and aeroelasticity of aircraft. Coupled with manufacturing costs associated with prototyping a system, these advancements drive the need for robust mathematical models of previously unfamiliar dynamical behaviors. This includes but is certainly not limited to large amplitude structural deformations.

This study is motivated by large aspect ratio wings such as those common to high altitude, long endurance (HALE) aircraft, whose wings deform greatly under typical loads. These aircraft include the Helios aircraft, a very high aspect ratio flying wing design doomed to a pitching oscillation failure due to gust response [1]; the X-56 "Mutt" Aeroelastic Demonstrator test-bed [2]; and its spin-off, the "Mini-Mutt" [3]. Research on the X-56 and the Mini-Mutt is ongoing, and a comprehensive survey of other aeroelastic case studies is given by Livne [4]. These cases point to a need for improved modeling capabilities and physical insight into the complex systems. In fact, the mishap report for the Helios aircraft states that the root

cause of the crash was due to a "lack of adequate analysis methods [which] led to an inaccurate risk assessment" and the report recommends developing "more advanced, multidisciplinary (structures, aeroelastic, aerodynamics, ..., etc) '***time-domain***' analysis methods appropriate to highly flexible, 'morphing' vehicles."

In addition to these examples of aircraft in subsonic flight, we are also motivated by the recent attention to supersonic and hypersonic flight as a research interest. Specifically, there is interest in the structural dynamics of the cantilevered plate in axial flow as it serves as the control surfaces on the trailing edge of the aircraft [5, 6].

The large deflections common among these examples are highly nonlinear and the equations of motion are difficult to solve analytically, so we seek computationally inexpensive methods to model these systems. A natural beginning for this study is to simplify these complex geometries to beams and then expand to plates. These fundamental geometries allow a basic understanding of mathematical intricacies of such nonlinearities and the forces that govern them.

For a component such as a beam which is fixed at opposing boundaries, a nonlinear tension is induced due to longitudinal stretching in the beam when deflection amplitude is on the order of the beam's thickness. However, for a cantilevered or free-free component, such as a simple wing or fuselage, the beam essentially does not stretch in this manner and a nonlinearity due to curvature arises at deflections on the order of the component length. Utilizing this knowledge, the model may be constrained to be inextensible along its plane which greatly simplifies the equations of motion. This document explores the role of this inextensibility constraint on the nonlinear structural dynamics of the cantilevered and free-free beam and plate models.

In addition to exploring the properties of the structural nonlinearities, this work also investigates the interesting dynamical properties brought forth by nonconservative loads, including point follower loads and piston theoretic aerodynamic loads.

With a linear structural model excited by nonconservative loads, once the system loses stability, the structural response grows to infinity either by static divergence or by dynamic flutter. However, with a nonlinear model, the nonlinear stiffness restricts the responses to harmonic (or sometimes chaotic) oscillations of finite amplitude, called limit cycle oscillations (LCO). The methodologies presented here may be used to investigate LCO behavior to determine if, for example, an instability is a catastrophic flutter event or a restricted limit cycle oscillation.

The further aim of this work is to explore a new supersonic aeroelastic model to gain theoretical insight while enforcing mathematical robustness and demonstrating computational efficiency. A new application of a classic aeroelastic method—piston theory—is demonstrated on the nonlinear beam model to simulate the response of a trailing edge control surface in supersonic flow.

In short, this dissertation develops a new methodology for studying large deflection aeroelastic systems. Through novel derivations of the equations of motion for beams and plates, the reader is provided with a thorough grasp of the structural nonlinearities which are significant for these configurations. The analysis of the aerodynamic theories and modeling approaches offers similar appreciation for the new challenges that large deflections bring for aerodynamic nonlinearities. The numerical model created for this work is compact, robust, and transparent, which allows for a clear understanding of how each mathematical term affects the predictions of how the physical system behaves, unlike opaque and expensive commercial finite element or computational fluid dynamics models. Thus, the work presented herein offers new tools for predicting responses of beam- and plate-like structures to a wide range of loading types for the structural engineer and aeroelastician alike.

1.2 Literature and Contributions

The inextensible beam model has attracted the attention of several researchers for its fundamental role in nonlinear structural dynamics [7–18]. Recently Tang et al. [8] developed an appealing form of the equations of motion that accounts for both nonlinear stiffness and nonlinear inertia. Their work develops the intextensibility constraint based upon the work of Novozhilov [15], which enforces zero strain along the beam's longitudinal neutral axis. It also reports a static experiment that validates the theoretical model for the nonlinear stiffness [8]. A recent experiment considered the dynamic response of such beams subjected to base excitation and provided a further assessment of the theoretical model, hinting that while the model adequately captures the nonlinear stiffess and inertia, there may be a need for future work with a nonlinear fluid damping model [19]. The current study fits nicely with the collection of work done by Raviv, Tang, and Dowell [7, 8, 19], using the original inextensibility formulation as inspiration. However, this work adds to this literature through the use of the Lagrange multiplier to enforce inextensibility. This proves to be a more computationally efficient method for coupling longitudinal to transverse displacements.

The effects of both cantilever and free-free boundary conditions on the inextensible beam are studied herein. An interesting characteristic of the (uniform) cantilevered beam is that the first bending mode acts nearly linearly [8,17,20], while the cantilever's second bending mode exhibits a softening nonlinearity [17, 20]. Here we investigate these characteristics of the cantilever beam and also develop an analysis of the free-free beam in the same manner, which appears to be the first of this kind of characterization for the free-free beam.

A cantilevered beam loaded with a compressive, nonconservative follower force is known as Beck's beam problem [21]. This structure has been studied both ex-

perimentally and computationally in the literature for its interesting Hopf bifurcation behavior [22–29], and a comprehensive survey of research studies was published by Langthjem and Sugiyama [30]. Most studies of this classical system are linear [21, 22, 26, 29] with the exception of Luongo and D'Annibale's [28] pioneering paper on a nonlinear study. The nonlinear model proposed here allows the Hopf bifurcation and the limit cycle oscillation (LCO) to be investigated in greater detail than previous studies.

This same type of force is interesting when applied to a free-free beam. Beal [31] investigated the stability of missiles and rockets subjected to a thrust force at one end. Using a linear eigenvalue approach, he determined the critical thrust force at which a missile becomes structurally unstable. Using our nonlinear time-dependent method, we show agreement with this critical force and illuminate for the first time the missile's behavior due to a force *beyond* the critical force.

Using lessons learned from the nonconservative point force, we can study aerodynamic forces. In this document we study supersonic flow moving axially over a cantilevered plate. Currao et al. [5] performed an experiment in this configuration well *below* the flutter boundary, and here we use Piston Theory to explore the limit cycles *after* the flutter point. Piston Theory, introduced by Lighthill [32] and developed into an aeroelastic tool by Ashley and Zartarian [33], is utilized throughout the literature for high speed potential flow [34–36] and is relevant to contemporary studies in supersonic configurations [5]. Supersonic flow theories such as Simple Wave Theory and Shock Expansion Theory are thoroughly described in classic gas dynamics books by Hayes and Probstein [37] and Liepmann and Roshko [38]. The current work proposes a method to increase the utility of these classic theories for large deflection structural motion.

Finally, the cantilevered plate model, an extension of the beam model to three dimensions, is explored. While the literature on plate theory is ample [39–42], there

is relatively little on inextensible plate theory [8]. The potential energy derived from Tang et al. [8] is used in this work and the inextensible constraint is implemented through a novel Lagrange multiplier technique, as it was for the beam. However, it is proposed that the potential energy as derived by previous authors is insufficient as there is an inconsistency in the assumptions regarding inextensibility of plates.

For further discussion of the current literature, each chapter contains its own introduction and literature review.

1.3 Organization

Most chapters herein are reproduced from the body of work completed and published thus far[1]. Chapter 2, published originally in the Journal of Applied Mechanics in 2016 [43], is an introduction into two methods of deriving the equations of motion of the inextensible beam, and it is shown that the two are equivalent. It also introduces the path forward for the inextensible plate model. In Chapter 3, also published in the Journal of Applied Mechanics [44], the equations of motion derived in Chapter 2 are modally expanded using the Raleigh-Ritz method, and the beam responses are computed. Here, the nonlinear softening versus stiffening terms are evaluated and yield an interesting balancing effect. Chapter 4, presented at ASME's August 2018 IDETC/CIE conference [45] and also published in AMSE's Journal of Computational and Nonlinear Dynamics [46], foreshadows our interest in aeroelastic phenomena such as flutter and LCO by applying a nonconservative follower force to a cantilevered beam to induce an instability. This classic problem, known as Beck's Beam, offers an interesting perspective on the constraint force itself. Chapter 5, presented at American Mathematical Society's Joint Mathematics Meetings January 2019 conference and also published in AMSE's Journal of Computational

[1] Relevant copyrights are noted at the beginning of each chapter and the rights to reproduce in the dissertation format are expressly granted in each journal's copyright agreement.

and Nonlinear Dynamics [47], extends this same approach to a free-free beam. This configuration was originally studied for linear stability of missiles by Beal [31], and to the authors' knowledge, our study is the first to describe the limit cycle oscillations of a missile subject to a post-critical thrust load. The free-free boundary conditions allow the investigation of rigid body rotation and translation modes, and it is shown that while the rotation mode is coupled to the bending mode, the translation modes are fully uncoupled. Chapter 6, published in the proceedings of and presented at The International Forum on Aeroelasticity and Structural Dynamics 2019 conference [48] couples the structural model to a piston theoretic fluid model. The beam is cantilevered in axial, supersonic flow and post-critical limit cycle oscillation behavior is observed with two structural and two fluid nonlinearities. Following this work, the work described in Chapter 7 was undertaken to explore the utility of piston theoretic fluid models on highly deflected structures. Here we characterize the envelopes in which several theories are useful. Finally, the inextensible beam is extended to the inextensible plate in Chapter 8. It is found that the bending response of the plate is accurate to finite element comparison cases, but the torsion response is quantitatively inaccurate. A new formulation for potential energy is derived in order to consider shearing along the plate's midplane. Finally, the work is summarized with concluding remarks and future work is suggested in Chapter 9.

2

Equations of Motion for an Inextensible Beam Undergoing Large Deflections

2.1 Introduction

To study largely deflected aircraft structures, the inextensible beam model is a natural choice. By assuming that there can be no elastic strain along the principle axis of the beam, the complexity of the model is greatly reduced. This assumption holds for cantilevered or free-free boundary conditions, which makes it ideal for modeling wings, control surfaces, or full aircraft dynamics. This chapter details the theory to be used throughout the rest of the document, and includes material originally published by ASME's Journal of Applied Mechanics [43].

The inextensible beam model has been studied by a number of investigators [7–18, 49]. Several studies have used Hamilton's Principle and Lagrange's Equation to derive the equations of motion for a beam [16,18,49]. While rigorous and laudable, these derivations and the resulting equations of motion may be seen as less intuitive than the methods proposed in the current work for two reasons. First, they utilize of a change of coordinates to a Lagrangian coordinate system such that the axes are fixed

to the beam throughout its deflection. Second, these models include two out-of-plane coordinates rather than only one, i.e. they are three-dimensional rather than two-dimensional. Because the work in this dissertation views the beam as a simplification of the plate—which only has one out-of-plane coordinate—the second out-of-plane coordinate to describe the beam motion is not relevant and therefore may be ignored. This greatly simplifies the eqauations of motion to more familiar Euler-Bernoulli-type expressions with the inclusion of significant geometric nonlinearities.

In contrast to these studies, recently an attractive form of the equations has been developed using two-dimensional Eulerian coordinates that accounts for and easily highlights both nonlinear stiffness and nonlinear inertia, and a static experiment has been reported that validates the theoretical model for the nonlinear stiffness [8]. A recent experiment also considered the dynamic response of such beams and provided a further assessment of the theoretical model, hinting at future work with a nonlinear fluid damping model [19]. In the computations done to date and reported in the literature with this model, a modal expansion has been employed directly to enable a Raleigh-Ritz analysis starting from the appropriate expressions for kinetic and potential energy as well as virtual work due to external forces [7, 8].

In the present work, Hamilton's principal is used to formally derive the equations of motion and also the associated boundary conditions with the Eulerian coordinates. In the Rayleigh-Ritz approach the individual basis functions in the modal series only need to satisfy the geometric boundary conditions, while the natural boundary conditions are satisfied implicitly through the use of Lagrange's equations. However it is of some interest to determine the natural boundary conditions from Hamilton's Principle and that is done here for a cantilevered beam and for a free-free beam. Of course a beam that is fixed at both ends (pinned or clamped) will not be inextensible and indeed the nonlinearity for that case is well known to be an induced tension due to extensibility. For such fixed-fixed beams the tension induced nonlinearity

becomes significant when the beam deflections are on the order of its thickness. For a cantilevered or a free-free beam, the beam is essentially inextensible and the geometric nonlinearities associated with nonlinear curvature prove to be dominant. These nonlinearities becomes significant only when the deflections are much larger, i.e. on the order of the beam length. Moreover it has been shown [8] that the nonlinear inertia and stiffness effects tend to offset each other and thus the effects of the nonlinearity are more subtle.

Here two alternative (and as we will show equivalent) approaches will be considered using Hamilton's Principle. In the first approach the inextensibility condition that relates axial (u) to transverse deflection (w) will be considered as a constraint equation which is included in the Lagrangian via a Lagrange Muliplier (λ). The Lagrange Multiplier may be physically interpreted as the total force that enforces the constraint and the axial gradient of the constraint force is the distributed axial force that appears in both the axial and transverse equations of motion in the usual form for such a force. In the second approach the constraint equation is used to express u in terms of w and the Lagrangian is written only in terms of w. As will be seen, both approaches give an equivalent result. However the first approach gives some added insight into the nature of the natural boundary conditions, and therefore serves as the basis for the subsequent chapters of this document.

In both cases the ultimate equation of motion that can be expressed entirely in terms of w is a nonlinear partial integral-differential equation. Moreover it is shown that this integral-differential equation is dependent on the boundary conditions and in particular is different for a cantilevered beam and a free-free beam. This is because the (natural) boundary conditions on u and λ are different for a cantilevered beam than for a free-free beam.

Note that the following derivations are for a non-uniform beam or plate.

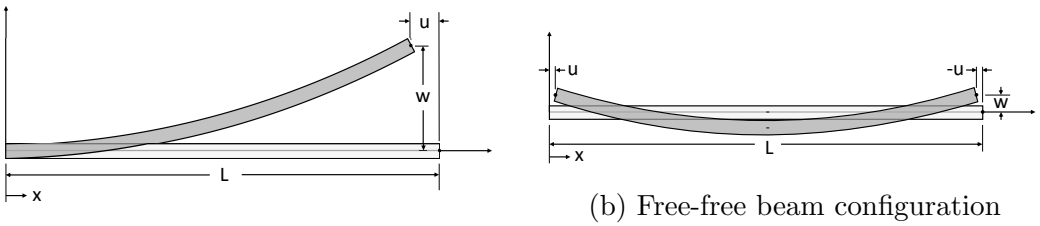

(a) Cantilevered beam configuration

(b) Free-free beam configuration

FIGURE 2.1: (a) Cantilevered and (b) Free-free beam configuration schematics

2.2 A Derivation of the Equations of Motion Using u, w, and λ

2.2.1 Kinetic and Potential Energy and Virtual Work

Figure 2.1 illustrates the cantilevered and free-free beam configurations which are studied herein. The expressions for kinetic energy, potential energy and virtual work are given by Eqns. 2.1, 2.2, and 2.3 respectively. See the list of nomenclature for the various symbols. u and w are the axial and transverse beam deflection, as illustrated in Figs. 2.1a and 2.1b, and λ is the Lagrange mulitiplier. The overdot notation is used to express a time derivative. The constraint equation expressing the inextensibility condition is Eqn. 2.4. It is noted that in constructing the expression for potential energy, the constraint equation has been used as in the literature [7, 8] so that the potential energy can be written entirely in terms of the transverse deflection, w.

$$T = \frac{1}{2}\int_0^L m[\dot{u}^2 + \dot{w}^2]\, dx \tag{2.1}$$

$$V = \frac{1}{2}\int_0^L EI\Big(\frac{\partial^2 w}{\partial x^2}\Big)^2\Big[1 + \Big(\frac{\partial w}{\partial x}\Big)^2\Big]\, dx \tag{2.2}$$

$$\delta W = \int_0^L F\delta(x - x_F)\, dx \tag{2.3}$$

$$f \equiv \frac{\partial u}{\partial x} + \frac{1}{2}\Big(\frac{\partial w}{\partial x}\Big)^2 = 0 \tag{2.4}$$

The Lagrangian will be expressed with the constraint equation added via the Lagrange multiplier. See Eqn. 2.5.

$$\mathcal{L} = T - V + \int_0^L \lambda f \; dx \tag{2.5}$$

Taking the variation of Eqn. 2.5 in the usual way and preforming the necessary integration by parts with respect to time and space, Hamilton's Principle provides the Euler-Lagrange equations of motion and the associate boundary conditions. Note virtual changes or variations in both u and w are considered. Indeed a virtual change in λ simply reproduces the equation of constraint, Eqn. 2.4. Equation 2.6 shows the virtual changes in the Hamiltonian integral and Eqns. 2.7 and 2.8 provide the equations of motion associated with u and w respectively. In the next section, the boundary conditions are considered. Note that full derivations of Eqn. 2.6 are provided in Appendix A.

$$\delta T = \int_0^L m[\dot{u}\delta\dot{u} + \dot{w}\delta\dot{w}]\ dx \tag{2.6a}$$

$$\delta V = \int_0^L \left\{ -\frac{\partial}{\partial x}\left[EI\Big(\frac{\partial^2 w}{\partial x^2}\Big)^2\frac{\partial w}{\partial x}\right] + \frac{\partial^2}{\partial x^2}\left[EI\frac{\partial^2 w}{\partial x^2}\left[1+\Big(\frac{\partial w}{\partial x}\Big)^2\right]\right]\right\}\delta w\ dx$$

$$-\frac{\partial}{\partial x}\left[\Big(EI\frac{\partial^2 w}{\partial x^2}\Big)\left[1+\Big(\frac{\partial w}{\partial x}\Big)^2\right]\right]\delta w\Big|_0^L + EI\frac{\partial^2 w}{\partial x^2}\left[1+\Big(\frac{\partial w}{\partial x}\Big)^2\right]\frac{\partial}{\partial x}\delta w\Big|_0^L \tag{2.6b}$$

$$+EI\Big(\frac{\partial^2 w}{\partial x^2}\Big)^2\frac{\partial w}{\partial x}\delta w\Big|_0^L$$

$$\delta\Big(\int_0^L \lambda f\ dx\Big) = \int_0^L \Big[f\delta\lambda - \frac{\partial\lambda}{\partial x}\delta u - \frac{\partial}{\partial x}\Big(\lambda\frac{\partial w}{\partial x}\Big)\delta w\Big]\ dx + \lambda\delta u\Big|_0^L + \lambda\frac{\partial w}{\partial x}\delta w\Big|_0^L \tag{2.6c}$$

The two equations of motion are determined by returning to Hamilton's Principle [50]. By minimizing the Lagrangian and assuming the virtual changes are arbitrary, we may gather the terms from each virtual change and set their totals to zero as follows.

$$\delta u: \quad m\ddot{u} + \frac{\partial\lambda}{\partial x} = 0 \tag{2.7}$$

$$\delta w: \quad m\ddot{w} - \frac{\partial}{\partial x}\left[EI\Big(\frac{\partial^2 w}{\partial x^2}\Big)^2\frac{\partial w}{\partial x}\right] + \frac{\partial^2}{\partial x^2}\left[EI\frac{\partial^2 w}{\partial x^2}\left[1+\Big(\frac{\partial w}{\partial x}\Big)^2\right]\right]$$

$$+\frac{\partial}{\partial x}\Big(\lambda\frac{\partial w}{\partial x}\Big) = F\delta(x-x_F) \tag{2.8}$$

Note that from Eqns. 2.7 and 2.8 one may identify λ as the in-plane force (positive in compression) experienced by the bending beam and $\dfrac{\partial\lambda}{\partial x}$ as the distributed in-plane force (positive in the direction opposite to u) that creates the in-plane inertia.

2.2.2 Boundary Conditions

Here three sets of boundary conditions are considered, i.e a clamped boundary, a pinned boundary and a free boundary.

Clamped Boundary

For a clamped boundary, u, w and $\dfrac{\partial w}{\partial x}$ are all zero and thus the virtual changes of these quantities are all zero and the corresponding tail terms in Eqn. 2.6 are zero.

Pinned Boundary

For a pinned boundary u and w are zero, but $\dfrac{\partial w}{\partial x}$ is not zero. Hence by examination of the tails terms in Eqn. 2.6, it is seen that

$$EI\frac{\partial^2 w}{\partial x^2} = 0.$$

This is the same natural boundary condition as for classical linear beam theory.

Free Boundary

For a free boundary none of u, w or $\dfrac{\partial w}{\partial x}$ are zero. Hence by an examination of the tails terms in Eqn. 2.6 we see that the natural boundary conditions are as follows:

$$\lambda = 0 \tag{2.9}$$

$$EI\frac{\partial^2 w}{\partial x^2} = 0 \tag{2.10}$$

and thus

$$\frac{\partial}{\partial x}\left(EI\frac{\partial^2 w}{\partial x^2}\right) = 0. \tag{2.11}$$

It is interesting to note that the explicit boundary conditions on w and its spatial derivatives are the same as for the classical linear beam theory. However, as will be

seen subsequently the boundary conditions on u and λ are important to determining the solution for w.

2.2.3 Solving for u and λ in Terms of w

The Cantilevered Beam

For a cantilevered beam, the boundary conditions are clamped at $x = 0$. Thus the determination of u and λ in terms of w proceeds as follows.

From Eqn. 2.4 and noting that $u = 0$ at $x = 0$, define the special function g_u:

$$u(x) = g_u(x) \quad \text{where} \quad g_u(x) \equiv -\frac{1}{2}\int_0^x \left(\frac{\partial w}{\partial \xi}\right)^2 d\xi \tag{2.12}$$

Then from Eqns. 2.12 and 2.7,

$$\frac{\partial \lambda}{\partial x} = -m\ddot{u} = -m\ddot{g}_u \tag{2.13}$$

and thus

$$\lambda(x) = -\int_0^x m\ddot{g}_u(\xi)\ d\xi + \lambda(x = 0). \tag{2.14}$$

But $\lambda = 0$ at $x = L$ and thus

$$\lambda(x = L) = 0 = -\int_0^L m\ddot{g}_u(\xi)\ d\xi + \lambda(x = 0) \tag{2.15}$$

and using Eqns. 2.14 and 2.15

$$\lambda(x) = \int_x^L m\ddot{g}_u(\xi)\ d\xi. \tag{2.16}$$

Equations 2.16, 2.8 and noting the definition of g_u (Eqn. 2.12) determine a single nonlinear integral-partial differential equation for w:

$$m\ddot{w} - \frac{\partial}{\partial x}\left[EI\left(\frac{\partial^2 w}{\partial x^2}\right)^2 \frac{\partial w}{\partial x}\right] + \frac{\partial^2}{\partial x^2}\left[EI\frac{\partial^2 w}{\partial x^2}\left[1 + \left(\frac{\partial w}{\partial x}\right)^2\right]\right] + \frac{\partial}{\partial x}\left[\int_x^L m\ddot{g}_u(\xi)d\xi \frac{\partial w}{\partial x}\right] = F\delta(x - x_F). \tag{2.17}$$

The Free-Free Beam

For a free-free beam both ends are free of course. Thus the determination of u and λ in terms of w proceeds as follows. From Eqn. 2.4 and noting that u is NOT zero at $x = 0$,

$$u(x) = g_u(x) + u(x = 0). \tag{2.18}$$

From Eqns. 2.13 and 2.18 and noting that $\lambda = 0$ at $x = 0$,

$$\lambda(x) = -\int_0^x m\ddot{g}_u(\xi)\ d\xi - mx\ddot{u}(x = 0). \tag{2.19}$$

But noting that $\lambda = 0$ also at $x = L$,

$$\ddot{u}(x = 0) = -\frac{1}{L}\int_0^L \ddot{g}_u(\xi)\ d\xi. \tag{2.20}$$

Also u can be obtained from Eqn. 2.20 by a double integration with respect to time. Note however that only $\ddot{u}$, λ and $\dfrac{\partial\lambda}{\partial x}$ are needed for solving the equations of motion for w. Even so, formally one has

$$u(x = 0, t) = \int_0^t \left[\int_0^{t_2} \ddot{u}(x = 0, t_1)\ dt_1\right] dt_2. \tag{2.21}$$

From Eqns. 2.19 and 2.20,

$$\lambda = -\int_0^x m\ddot{g}_u\ d\xi + \frac{x}{L}\int_0^L m\ddot{g}_u\ d\xi. \tag{2.22}$$

From Eqns. 2.22 and 2.8 and noting the definition of g_u (see Eqn. 2.12 et seq), one may determine a single nonlinear integral-partial differential equation for w:

$$m\ddot{w} - \frac{\partial}{\partial x}\left[EI\Big(\frac{\partial^2 w}{\partial x^2}\Big)^2\frac{\partial w}{\partial x}\right] + \frac{\partial^2}{\partial x^2}\left[EI\frac{\partial^2 w}{\partial x^2}\left[1 + \Big(\frac{\partial w}{\partial x}\Big)^2\right]\right]$$
$$+ \frac{\partial}{\partial x}\left[\Big(-\int_0^x m\ddot{g}_u\ d\xi + \frac{x}{L}\int_0^L m\ddot{g}_u\ d\xi\Big)\frac{\partial w}{\partial x}\right] = F\delta(x - x_F). \tag{2.23}$$

Note this equation differs from that for a cantilevered beam because of the different expressions for λ, i.e. Eqn. 2.22 versus Eqn. 2.16, which in turn reflects the different boundary conditions in the nonlinear model.

2.3 A Direct Derivation of the Equation of Motion in Terms of w Only

The second approach does not use the Lagrange Multiplier. Instead, the constraint between transverse deflection and axial deflection is considered by writing the variation in u in terms of the variation in w. Here, the Lagrangian is simply expressed as the following:

$$\mathcal{L} = T - V \tag{2.24}$$

The variation in kinetic and potential energies are equal to Eqns. 2.6a and 2.6b. Consider the kinetic energy term, which after integrating by parts with respect to time and deleting the tail terms as customary [50], results in

$$\delta\left[\frac{1}{2}\int_{t_1}^{t_2}\int_{0}^{L} m\dot{u}^2 \; dx \; dt\right] = -\int_{t_1}^{t_2}\int_{0}^{L} m\ddot{u}\delta u \; dx \; dt \tag{2.25}$$

To solve for one equation of motion without the Lagrange multiplier, the δu term must be expressed in terms of δw. Because of the difference in boundary conditions, the derivation for the cantilevered beam and the free-free beam differ from this point onward.

2.3.1 The Cantilevered Beam

From Eqn. 2.4 and noting the boundary condition implied in Eqn. 2.12, one may determine the variation or virtual change in u.

$$\delta u = -\int_0^x \frac{\partial w}{\partial \xi}\delta\left(\frac{\partial w}{\partial \xi}\right) \; d\xi. \tag{2.26}$$

Further, Eqn. 2.26 may be integrated by parts with respect to x to obtain the following:

$$\delta u = -\frac{\partial w}{\partial \xi}\delta w\Big|_0^x + \int_0^x \frac{\partial^2 w}{\partial \xi^2}\delta w(\xi)\ d\xi. \tag{2.27}$$

Now the entire relevant kinetic energy term from Eqn. 2.25 may be rewritten as follows:

$$\delta\left[\frac{1}{2}\int_{t_1}^{t_2}\int_0^L m\dot{u}^2\ dx\ dt\right] = -\int_{t_1}^{t_2}\int_0^L m\ddot{u}\delta u\ dx\ dt$$

$$= \int_{t_1}^{t_2}\int_0^L m\ddot{u}\frac{\partial w(x)}{\partial x}\delta w(x)\ dx\ dt - \int_{t_1}^{t_2}\int_0^L m\ddot{u}(x)\left[\int_0^x \frac{\partial^2 w(\xi)}{\partial \xi^2}\delta w(\xi)\ d\xi\right] dx\ dt \tag{2.28}$$

Note that in Eqn. 2.28 there is a double spatial integral over the variables x and ξ. The order of this double integral may be interchanged and the result taking into account the proper limits on the integrals is as follows:

$$\int_0^L m\ddot{u}(x)\left[\int_0^x \frac{\partial^2 w(\xi)}{\partial \xi^2}\delta w(\xi)\ d\xi\right] dx = \int_0^L \left[\int_\xi^L m\ddot{u}(x)\ dx\right]\frac{\partial^2 w}{\partial \xi^2}\delta w(\xi)\ d\xi \tag{2.29}$$

In Eqn. 2.29, both x and ξ are dummy integration variables and so they may be interchanged. Combining Eqns. 2.28 and 2.29, including the interchange of variables, we can write the following:

$$\delta\left[\frac{1}{2}\int_{t_1}^{t_2}\int_0^L m\dot{u}^2\ dx\ dt\right] = \int_{t_1}^{t_2}\int_0^L m\ddot{u}\frac{\partial w}{\partial x}\delta w(x)\ dx\ dt - \int_{t_1}^{t_2}\int_0^L \left[\int_x^L m\ddot{u}(\xi)\ d\xi\right]\frac{\partial^2 w}{\partial x^2}\delta w(x)\ dx\ dt \tag{2.30}$$

To write this equation in terms of w only, consider the $\ddot{u}$ terms. From Eqn. 2.12 it may be determined that

$$\ddot{u} = -\int_0^x \left[\frac{\partial^2 w}{\partial \xi \partial t}\frac{\partial^2 w}{\partial \xi \partial t} + \frac{\partial^3 w}{\partial \xi \partial t^2}\frac{\partial w}{\partial \xi}\right] d\xi \tag{2.31}$$

By substituting Eqn. 2.31 into Eqn. 2.30, we now see that all terms in Lagrangian (Eqn. 2.24) are written in terms of w and δw, so the equation of motion for the cantilevered beam may be written as

$$m\ddot{w} - \frac{\partial}{\partial x}\left[EI\Big(\frac{\partial^2 w}{\partial x^2}\Big)^2\frac{\partial w}{\partial x}\right] + \frac{\partial^2}{\partial x^2}\left[EI\frac{\partial^2 w}{\partial x^2}\left[1+\Big(\frac{\partial w}{\partial x}\Big)^2\right]\right]$$
$$+ m\frac{\partial w}{\partial x}\left[-\int_0^x\left(\Big(\frac{\partial^2 w}{\partial\xi\partial t}\Big)^2 + \frac{\partial^3 w}{\partial\xi\partial t^2}\frac{\partial w}{\partial\xi}\right)d\xi\right]$$
$$+ m\frac{\partial^2 w}{\partial x^2}\int_x^L\left[\int_0^x\left(\Big(\frac{\partial^2 w}{\partial\xi\partial t}\Big)^2 + \frac{\partial^3 w}{\partial\xi\partial t^2}\frac{\partial w}{\partial\xi}\right)d\xi_1\right]d\xi_2 = F\delta(x-x_F) \quad (2.32)$$

2.4 Demonstrating the Equivalence of the Two Approaches for Deriving the Equations of Motion

2.4.1 The Cantilevered Beam

For a cantilevered beam, the equivalence between the two approaches is relatively simple. Consider Eqn. 2.30. Recall that from Eqns. 2.12, 2.14, and 2.16, one has

$$\lambda(x) = \int_x^L m\ddot{u}(\xi)\,d\xi$$
$$\frac{\partial\lambda(x)}{\partial x} = -m\ddot{u}$$

So finally we have

$$\delta\left[\frac{1}{2}\int_{t_1}^{t_2}\int_0^L m\dot{u}^2\,dx\,dt\right] = -\int_{t_1}^{t_2}\int_0^L\frac{\partial\lambda}{\partial x}\frac{\partial w}{\partial x}\delta w\,dx\,dt - \int_{t_1}^{t_2}\int_0^L\lambda\frac{\partial^2 w}{\partial x^2}\delta w\,dx\,dt$$
$$= -\int_{t_1}^{t_2}\int_0^L\frac{\partial}{\partial x}\left(\lambda\frac{\partial w}{\partial x}\right)\delta w\,dx\,dt \quad (2.33)$$

Which can be seen as the final term in Eqn. 2.8. This demonstrates the equivalence of the two approaches. In the next section, a more general proof is demonstrated.

2.4.2 General Proof

To prove the equality of the two methods, it must be shown that for a cantilevered beam or a free-free beam, Eqn. 2.33 holds, without specifically defining the cantilever or free-free boundary conditions.

We begin in the conventional manner [50] by taking the variation of the relevant term, integrating by parts with respect to time, and setting the initial conditions to zero ($IC = 0$):

$$\delta\left[\frac{1}{2}\int_{t_1}^{t_2}\int_{0}^{L} m\dot{u}^2 \, dx \, dt\right] = \int_{t_1}^{t_2}\int_{0}^{L} m\dot{u}\frac{\partial}{\partial t}\delta u \, dx \, dt \tag{2.34}$$

$$= \int_{0}^{L} m\dot{u}\delta u \, dx\Big|_{t_1}^{t_2} - \int_{t_1}^{t_2}\int_{0}^{L} m\ddot{u}\delta u \, dx \, dt \tag{2.35}$$

$IC = 0$

Substitution from Eqn. 2.7, i.e.

$$-m\ddot{u} = \frac{\partial \lambda}{\partial x}$$

gives

$$\delta\left[\frac{1}{2}\int_{t_1}^{t_2}\int_{0}^{L} m\dot{u}^2 \, dx \, dt\right] = \int_{t_1}^{t_2}\int_{0}^{L} \frac{\partial \lambda}{\partial x}\delta u \, dx \, dt \tag{2.36}$$

From the constraint equation we know how δu is expressed in terms of δw.

$$\frac{\partial u}{\partial x} + \frac{1}{2}\Big(\frac{\partial w}{\partial x}\Big)^2 = 0 \tag{2.37}$$

Which can be rewritten by taking a variation and integrating with respect to the spatial variable:

$$\int_{0}^{x}\Big[\frac{\partial}{\partial \xi}\delta u + \frac{\partial w}{\partial \xi}\frac{\partial}{\partial \xi}\delta w\Big] \, d\xi = 0 \tag{2.38}$$

Evaluating the integral,

$$\delta u(x) - \delta u(0) + \int_0^x \frac{\partial w}{\partial \xi}\frac{\partial}{\partial \xi}\delta w \; d\xi = 0 \tag{2.39}$$

Integrating by parts and rearranging to solve for δu,

$$\delta u(x) = \int_0^x \frac{\partial^2 w}{\partial \xi^2}\delta w \; d\xi - \frac{\partial w}{\partial \xi}\delta w\Big|_0^x + \delta u(0) \tag{2.40}$$

Substitute this expression for δu into the right hand side of Eqn. 2.36,

$$\delta\left[\frac{1}{2}\int_{t_1}^{t_2}\int_0^L m\dot{u}^2 \; dx \; dt\right] = \int_{t_1}^{t_2}\int_0^L \frac{\partial \lambda}{\partial x}\left[\int_0^x \frac{\partial^2 w}{\partial \xi^2}\delta w \; d\xi - \frac{\partial w}{\partial \xi}\delta w\Big|_0^x + \delta u(0)\right] dx \; dt \tag{2.41}$$

$$= \int_{t_1}^{t_2}\int_0^L \frac{\partial \lambda}{\partial x}\left[\delta u(0) - \frac{\partial w}{\partial \xi}\delta w\Big|_0^x\right] dx \; dt + \int_{t_1}^{t_2}\int_0^L \frac{\partial \lambda}{\partial x}\left[\int_0^x \frac{\partial^2 w}{\partial \xi^2}\delta w \; d\xi\right] dx \; dt \tag{2.42}$$

$$= \int_{t_1}^{t_2}\int_0^L \frac{\partial \lambda}{\partial x}\left[\delta u(0) - \frac{\partial w}{\partial \xi}\delta w\Big|_0^x\right] dx \; dt + \cancelto{0}{\int_{t_1}^{t_2}\left[\lambda \int_0^x \frac{\partial^2 w}{\partial \xi^2}\delta w \; d\xi\right]\Big|_0^L dt} - \int_{t_1}^{t_2}\int_0^L \lambda \frac{\partial^2 w}{\partial x^2}\delta w \; dx \; dt \tag{2.43}$$

Note that the final term in Eqn. 2.42 was integrated by parts with respect to x. For a free end, $\lambda = 0$. For a clamped end, $\delta w = 0$. Therefore, for both the free-free beam and the cantilevered beam, the second term in Eqn. 2.43 vansishes.

Evaluating at x and 0 where necessary, Eqn. 2.43 may be written as follows:

$$\delta\left[\frac{1}{2}\int_{t_1}^{t_2}\int_{0}^{L} m\dot{u}^2\ dx\ dt\right] = \int_{t_1}^{t_2}\int_{0}^{L}\frac{\partial\lambda}{\partial x}\delta u(0)\ dx\ dt - \int_{t_1}^{t_2}\int_{0}^{L}\frac{\partial\lambda}{\partial x}\frac{\partial w}{\partial x}\delta w(x)\ dx\ dt$$

$$+\int_{t_1}^{t_2}\int_{0}^{L}\frac{\partial\lambda}{\partial x}\frac{\partial w}{\partial x}\delta w(x)\Big|_{x=0}\ dx\ dt - \int_{t_1}^{t_2}\int_{0}^{L}\lambda\frac{\delta^2 w}{\delta x^2}\delta w\ dx\ dt$$

$$= -\int_{t_1}^{t_2}\int_{0}^{L}\frac{\partial\lambda}{\partial x}\frac{\partial w}{\partial x}\delta w(x)\ dx\ dt - \int_{t_1}^{t_2}\int_{0}^{L}\lambda\frac{\delta^2 w}{\delta\xi^2}\delta w\ dx\ dt$$

$$+\int_{t_1}^{t_2}\int_{0}^{L}\frac{\partial\lambda}{\partial x}\Big(\delta u(x) + \frac{\partial w}{\partial x}\delta w(x)\Big)\Big|_{x=0}\ dx\ dt \quad (2.44)$$

The final term in Eqn. 2.44 may be integrated, noting that $\dfrac{\partial\lambda}{\partial x}$ is not evaluated at $x = 0$ but rather is still a function of x. This term becomes:

$$\int_{0}^{L}\frac{\partial\lambda}{\partial x}\Big(\delta u(x) + \frac{\partial w}{\partial x}\delta w(x)\Big)\Big|_{x=0}\ dx = \big(\lambda(x=L) - \lambda(x=0)\big)\Big[\delta u(0) + \frac{\partial w}{\partial x}\delta w(0)\Big] \quad (2.45)$$

Again for a free end at $x = 0$ or $x = L$, $\lambda = 0$. For a clamped end at $x = 0$, $\delta u = 0$ and $\delta w = 0$. Therefore, for both the free-free beam and the cantilevered beam, this term vanishes and we are left with the two terms which prove the method equivalent to the Lagrange multiplier method, i.e. Eqn. 2.44 reduces to Eqn. 2.33.

Again it is noted that the equation of motion, Eqn. 2.8, when written in terms of λ, is the same for a cantilevered beam and a free-free beam. However, the expressions for λ in terms of w differ for the two sets of boundary conditions.

2.5 The Modal Formulations

The modal formulations are discussed in [7, 8] when using the constraint equation directly without a Lagrange multiplier. The corresponding modal formulation using the Lagrange multiplier is used in the remainder of this dissertation.

2.6 The Cantilevered Plate

One of the principal motivations for this work is to consider a cantilevered plate which has one clamped edge and three free edges. With the foregoing results in hand the extension of the beam analysis to a plate is relatively straightforward as described below. For simplicity a rectangular plate is considered.

The previous numbering system will be retained with the addition of subscripts so that the correspondence with the beam results will be clear.

The kinetic energy, potential energy and virtual work are given by Eqns. 2.46, 2.47 and 2.48 where x and y are the spatial coordinates and u,v are the inplane displacements. See [8] for a derivation of the potential energy expression.

$$T = \frac{1}{2}\int_0^{L_y}\int_0^{L_x} m[\dot{u}^2 + \dot{v}^2 + \dot{w}^2]\; dx\; dy \tag{2.46}$$

$$V = \frac{1}{2}\int_0^{L_y}\int_0^{L_x} \frac{Eh^3}{12(1-\nu^2)}\left[1 + \left(\frac{\partial w}{\partial x}\right)^2 + \left(\frac{\partial w}{\partial y}\right)^2\right]$$
$$\left[\left(\frac{\partial^2 w}{\partial x^2}\right)^2 + \left(\frac{\partial^2 w}{\partial y^2}\right)^2 + 2\nu\frac{\partial^2 w}{\partial x^2}\frac{\partial^2 w}{\partial y^2} + 2(1-\nu)\left(\frac{\partial^2 w}{\partial x \partial y}\right)^2\right]\; dx\; dy \tag{2.47}$$

$$\delta W = \int_0^{L_y}\int_0^{L_x} F\delta(x - x_F)\delta(y - y_F)\; dx\; dy \tag{2.48}$$

The two constraint equations are now given by Eqns. 2.49 and 2.50.

$$f_u \equiv \frac{\partial u}{\partial x} + \frac{1}{2}\Big(\frac{\partial w}{\partial x}\Big)^2 = 0 \tag{2.49}$$

$$f_v \equiv \frac{\partial v}{\partial y} + \frac{1}{2}\Big(\frac{\partial w}{\partial y}\Big)^2 = 0 \tag{2.50}$$

$$\mathcal{L} = T - V + \int_0^{L_x} \lambda_u f_u \, dx + \int_0^{L_y} \lambda_v f_v \, dy \tag{2.51}$$

The Lagranian is given by Eqn. 2.51 where λ_u and λ_v are the two Lagrange multipliers that enforce the two constraint equations. As before, taking the variation of the Lagranian and invoking Hamilton's Principle provides the equations of motion. The variation in the Lagrange multipliers simply gives back the constraint equations. Also as before, the variations in u and v give the inplane equations of motion and allow us to determine the Lagrange multipliers in terms of the out of plane displacement and derivatives thereof.

As the computation for the plate is entirely analogous to that for a beam, the results are simply given.

$$\lambda_u(x,y) = \int_x^{L_x} m\ddot{g}_u(\xi) \, d\xi \tag{2.52}$$

$$\lambda_v(x,y) = -\int_0^{y} m\ddot{g}_v(\zeta) \, d\zeta + \frac{y}{L_y}\int_0^{L_y} m\ddot{g}_v(\zeta) \, d\zeta \tag{2.53}$$

The two different forms for the two different Lagrange multipliers reflect that clamped-free boundary conditions in the x direction and the free-free boundary conditions in the y direction. Note that if we considered a plate with all four edges free then Eqn. 2.52 would be replaced by Eqn. 2.53, with u replacing v and x replacing y. Also note that these are the only two boundary conditions that may be applicable here. A plate with two opposing edges clamped will not satisfy the inextensibility

criterion. A plate with two or three adjacent edges clamped may exhibit a stretching-induced nonlinearity rather than the nonlinearity due to high curvature, i.e. it is not fully inextensible, and is therefore outside of the scope of this study.

Now with the two Lagrange multipliers known, a variation of the Lagrangian with respect to w and invoking Hamilton's Principle will give the Euler-Largange equation that governs w. Note that this equation is solely in terms of w and the two Lagrange multipliers as well as the associated boundary conditions.

Note for practical computations once the two Lagrange mulipliers are known in terms of w, then one may use the Lagrangian and a modal expansion for w to derive the governing equations for the modal coefficients directly using Lagrange's equations and the above Lagrangian with the u and v terms suppressed. Note that a considerable advantage of the present formulation is the ability to decouple the determination of u and v from that of w through the use of the constraint equations and the Lagrange multipliers.

2.7 Concluding Remarks

The Euler-Lagrange equations and associated boundary conditions have been derived from Hamilton's Principle for an inextensible beam undergoing large deflections. Two alternative approaches have been used and they are shown to give equivalent results. In one approach the inextensibility constraint between the axial and transverse deflections has been appended to the system Lagrangian via a Lagrange multiplier. In the other approach the inextensibility constraint has been used to express the axial deflection in terms of the transverse deflection and the equation of motion for the transverse deflection has been determined directly.

The first approach allows a more insightful determination of the boundary conditions.

Explicit results are given for a cantilevered beam and a free-free beam. It is

seen that when the governing system equation is expressed solely in terms of the transverse deflection, w, that (1) it is a nonlinear integral/partial differential equation and (2) it differs for a cantilevered versus a free-free beam. The latter result reflects the difference in the boundary conditions for the axial deflection and the Lagrange multiplier for the cantilevered beam versus free-free beam.

It is also interesting to note that the boundary conditions on the transverse deflection are the same as those of the classical linear beam theory.

The Lagrange multiplier approach has also been extended to a cantilevered or free-free plate and provides a more rigorous foundation for a plate theory based upon the inextensibility assumption. In particular as is true for the beam, the governing Euler-Lagrange equation for the plate bending deflection depends on the in-plane boundary conditions.

Finally it is noted that that having determined the Lagrange multipliers in terms of w, the results may be substituted back into the Lagrangian and by then taking only a variation with respect to w, and one may construct the Euler-Lagrange equation for w. Alternatively by expressing w in a modal expansion, one may determine the equations for the modal coefficients from the Lagrangian which is now expressed entirely in terms of w from Lagrange's equations.

Appendix A: Derivation of Eqn. 2.6

Full derivations of the three parts of Eqn. 2.6 from Section 2.2.1 are given below. Equations 2.6a, 2.6b, and 2.6c are the resulting components of the Hamiltonian integral after a virtual change has taken place. In Eqn. 2.6a, the virtual change operator has simply been distributed into the equation, but no major simplification has taken place, as the simplification requires integration in time. To arrive at the equation which contribute terms to the equations of motion, Eqn. 2.6a is rewritten

here and simplified as follows.

$$\delta T = \int_0^L m[\dot{u}\delta\dot{u} + \dot{w}\delta\dot{w}]\ dx \tag{2.54}$$

$$\int_{t_1}^{t_2} \delta T\ dt = \int_{t_1}^{t_2}\int_0^L m[\dot{u}\frac{\partial}{\partial t}\delta u + \dot{w}\frac{\partial}{\partial t}\delta w]\ dx\ dt \tag{2.55}$$

Integration by parts in time yields

$$\int_{t_1}^{t_2} \delta T\ dt = \int_0^L \Big[-\int_{t_1}^{t_2} m\ddot{u}\delta u\ dt - \int_{t_1}^{t_2} m\ddot{w}\delta w\ dt + m\dot{u}\delta u\Big|_{t_1}^{t_2} + m\dot{w}\delta w\Big|_{t_1}^{t_2}\Big]\ dx \tag{2.56}$$

The first two terms on the right hand side are used in Eqns. 2.7 and 2.8.

Equation 2.6b is derived from the virtual change of Equation 2.2 as follows.

$$\begin{aligned}
\delta V &= \frac{1}{2}\int_0^L EI\delta\Big[\big(\frac{\partial^2 w}{\partial x^2}\big)^2\big[1+\big(\frac{\partial w}{\partial x}\big)^2\big]\Big]\ dx \\
&= \frac{1}{2}\int_0^L EI\Big[2\big(\frac{\partial^2 w}{\partial x^2}\big)\big[1+\big(\frac{\partial w}{\partial x}\big)^2\big]\frac{\partial^2}{\partial x^2}\delta w + 2\big(\frac{\partial^2 w}{\partial x^2}\big)^2\frac{\partial w}{\partial x}\frac{\partial}{\partial x}\delta w\Big]\ dx \\
&= \int_0^L EI\big(\frac{\partial^2 w}{\partial x^2}\big)\big[1+\big(\frac{\partial w}{\partial x}\big)^2\big]\frac{\partial^2}{\partial x^2}\delta w\ dx + \int_0^L EI\big(\frac{\partial^2 w}{\partial x^2}\big)^2\frac{\partial w}{\partial x}\frac{\partial}{\partial x}\delta w dx
\end{aligned} \tag{2.57}$$

Integrating the first term in Eqn. 2.57 by parts yields

$$\begin{aligned}
&\int_0^L EI\big(\frac{\partial^2 w}{\partial x^2}\big)\big[1+\big(\frac{\partial w}{\partial x}\big)^2\big]\frac{\partial^2}{\partial x^2}\delta w\ dx \\
&= \underbrace{EI\frac{\partial^2 w}{\partial x^2}\Big[1+\Big(\frac{\partial w}{\partial x}\Big)^2\Big]\frac{\partial}{\partial x}\delta w\Big|_0^L}_{A} - \int_0^L \frac{\partial}{\partial x}\Big[EI\frac{\partial^2 w}{\partial x^2}\Big[1+\Big(\frac{\partial w}{\partial x}\Big)^2\Big]\Big]\frac{\partial}{\partial x}\delta w\ dx
\end{aligned} \tag{2.58}$$

Integration by parts of the second term in this equation yields

$$
\begin{aligned}
&-\int_0^L \frac{\partial}{\partial x}\left[EI\frac{\partial^2 w}{\partial x^2}\left[1+\Big(\frac{\partial w}{\partial x}\Big)^2\right]\right]\frac{\partial}{\partial x}\delta w\ dx \\
&= \underbrace{-\frac{\partial}{\partial x}\left[\Big(EI\frac{\partial^2 w}{\partial x^2}\Big)\left[1+\Big(\frac{\partial w}{\partial x}\Big)^2\right]\right]\delta w\Big|_0^L}_{B} + \underbrace{\int_0^L \frac{\partial^2}{\partial x^2}\left[EI\frac{\partial^2 w}{\partial x^2}\left[1+\Big(\frac{\partial w}{\partial x}\Big)^2\right]\right]\delta w\ dx}_{C}
\end{aligned}
\tag{2.59}
$$

Integrating the second term in Eqn. 2.57 by parts yields

$$
\int_0^L EI\Big(\frac{\partial^2 w}{\partial x^2}\Big)^2\frac{\partial w}{\partial x}\frac{\partial}{\partial x}\delta w dx = \underbrace{EI\Big(\frac{\partial^2 w}{\partial x^2}\Big)^2\frac{\partial w}{\partial x}\delta w\Big|_0^L}_{D} - \underbrace{\int_0^L \frac{\partial}{\partial x}\left[EI\Big(\frac{\partial^2 w}{\partial x^2}\Big)^2\frac{\partial w}{\partial x}\right]\delta w\ dx}_{E}
\tag{2.60}
$$

The terms remaining are labeled A-E. The summation of these terms results in Eqn. 2.6b.

Equation 2.6c is derived from the virtual change the last term in Eqn. 2.5, where f is defined by Eqn. 2.4. The details of the derivation are as follows.

$$
\delta\Big(\int_0^L \lambda f\ dx\Big) = \int_0^L \delta\left[\lambda\frac{\partial u}{\partial x}+\frac{\lambda}{2}\Big(\frac{\partial w}{\partial x}\Big)^2\right] dx \tag{2.61}
$$

$$
= \int_0^L \left[\delta\lambda\frac{\partial u}{\partial x}+\lambda\delta\frac{\partial u}{\partial x}+\frac{1}{2}\delta\lambda\Big(\frac{\partial w}{\partial x}\Big)^2+\lambda\Big(\frac{\partial w}{\partial x}\Big)\delta\frac{\partial w}{\partial x}\right] dx \tag{2.62}
$$

$$
= \int_0^L \left[\delta\lambda\left(\frac{\partial u}{\partial x}+\frac{1}{2}\Big(\frac{\partial w}{\partial x}\Big)^2\right)+\lambda\delta\frac{\partial u}{\partial x}+\lambda\Big(\frac{\partial w}{\partial x}\Big)\delta\frac{\partial w}{\partial x}\right] dx \tag{2.63}
$$

Integrating the last two terms by parts in space yields Eqn. 2.6c.

3

Nonlinear Responses of Inextensible Cantilever and Free-Free Beams Undergoing Large Deflections

3.1 Introduction

To gain understanding of the beam at large deflection, this chapter details the effects of the structural nonlinearities of the cantilever and free-free beam. The modal form of the equations from Chapter 2 are derived using the Rayleigh-Ritz approach and employed in a Runge-Kutta time marching solver to illustrate beam response to static and dynamic loads. The work in this chapter was originally published in ASME's Journal of Applied Mechanics [44].

Nonlinear responses of the inextensible beam have been studied in various contexts and configurations in the literature. Lacarbonara [42] provides a contemporary overview of and includes several methods for enforcing inextensibility for several boundary conditions. While the cantilevered beam configuration has been more widely studied [8, 16, 17, 19, 20, 27, 43, 49, 51], there is relatively little in the literature on the free-free configuration. The theoretical solution to the free-free case is of great interest since it is difficult to model experimentally. With the advent of lighter com-

posite materials used for wings and rotors, both the cantilever and free-free beam configurations are fundamental to understanding these system dynamics. This work compares the results of the current model to that of other published cantilever models and extends the model to the free-free configuration.

Several studies have used Hamilton's Principle and Lagrange's Equation to derive the equations of motion for a beam. Three such studies utilize a change of coordinates to a Lagrangian coordinate system such that the axes are fixed to the beam throughout its deflection [16, 18, 49]. They also use analytical approaches to solve the equations of motion; Crespo da Silva and Glynn [20] as well as Lacarbonara and Yabuno [18] use perturbation methods, while Hamdan and Dado [16] use the two-term harmonic balance method.

The present work instead uses an Eulerian coordinate system to describe the beam deflection, a formulation developed by Novozhilov [15] which has been used previously in the literature [8, 19, 43]. This coordinate system is intuitive for understanding the beam deflection in both the longitudinal and transverse directions. In addition, the present work does not seek an analytical solution to these equations of motion, but rather employs a 4th order Runge-Kutta numerical solution method to solve for the beam's motion in time.

Following the work of Tang and Dowell [8], this work uses the Rayleigh-Ritz method and the Lagrange equations to derive the equations of motion. As demonstrated in Chapter 2, a Lagrange multiplier λ is added to the Lagrange equations to enforce the inextensibility condition, defined as zero axial strain along the beam [15]. This differs from the method previously used [8, 19] in which the constraint equation was directly incorporated into both the potential and kinetic energy terms. This allows for an alternative and perhaps clearer understanding of how the inextensibility affects the system.

The results presented here for the cantilevered beam reiterate results published

[8,17,20] which observed that the first bending mode acts nearly linearly. Previously published results also indicate that the cantilever's second bending mode exhibits a softening nonlinearity due to nonlinear inertia [17, 20]. Here we show agreement with this assessment and also extend it to free-free beams. The free-free beam shows some softening at the first bending resonant peak, and shows a substantial softening at the third bending resonance.

3.2 Methods

3.2.1 A Derivation of the Equations of Motion

The same system from Chapter 2 is evaluated here, so Figure 2.1 illustrates the cantilevered and free-free geometries and the coordinate system used herein.

The equations of motion were derived from the Euler-Lagrange equations,

$$\frac{\partial}{\partial t}\Big(\frac{\partial \mathcal{L}}{\partial \dot{q}_i}\Big) - \frac{\partial \mathcal{L}}{\partial q_i} = Q_i \tag{3.1}$$

where the generalized coordinates q_i are for the spatial coordinates u and w and also for the Lagrange Multiplier λ, and Q_i represents the generalized forces. The Lagrangian, including the work done by the constraint force is as follows.

$$\mathcal{L} = T - V + \int_0^L \lambda f \; dx \tag{3.2}$$

The kinetic and potential energy as well as the constraint f, respectively, are as follows [8, 43]. Note that the potential energy expression is from Tang et al. [8], in which the strain term from Novozhilov's formulation [15] is expanded in a Taylor series in $\partial w/\partial x$.

$$T = \frac{1}{2}\int_0^L m[\dot{u}^2 + \dot{w}^2] \; dx \tag{3.3}$$

$$V = \frac{1}{2}\int_0^L EI\Big(\frac{\partial^2 w}{\partial x^2}\Big)^2\Big[1+\Big(\frac{\partial w}{\partial x}\Big)^2\Big]\,dx \tag{3.4}$$

$$f = \frac{\partial u}{\partial x} + \frac{1}{2}\Big(\frac{\partial w}{\partial x}\Big)^2 = 0 \tag{3.5}$$

The constraint f is derived from Novozhilov's [15] strain relations for an inextensible beam. This relation between the longitudinal and transverse slope ensures that the strain along the beam is always zero, so $f = 0$. This constraint has also already been applied to the potential energy term, V, to express it only as a function of the transverse deflection w [8,19,43]. Unlike previous derivations [8,19], however, the effect of the constraint on the kinetic energy term will naturally be incorporated later in the derivation through the use of the Lagrange multiplier. It may be noted that the constraint f is dimensionless.

To solve the system of equations, each coordinate was expanded into modal form, following the Raleigh-Ritz approach. Note that the subscripts will remain consistent in such a way that i correlates with the number of u modes retained, j with the number of w modes, and k with the number of λ modes.

$$u = \sum_i \Psi_i^u(x)u_i(t) \tag{3.6}$$

$$w = \sum_j \Psi_j^w(x)w_j(t) \tag{3.7}$$

$$\lambda = \sum_k \Psi_k^\lambda(x)\lambda_k(t) \tag{3.8}$$

The modal functions Ψ are chosen to satisfy the geometric constraints, i.e. $u = w = \dfrac{\partial w}{\partial x} = 0$ for a clamped end and $\lambda = 0$ for a free end. These modal functions are all

normalized such that the length variable ξ runs from 0 to 1 and the endpoints are at 1,0, or -1 depending on the geometric constraints.

Here, the mode shapes for the cantilevered beam are:

$$\Psi_i^u = \sin\Big(\frac{2i-1}{2}\pi\xi\Big) \tag{3.9}$$

$$\Psi_j^w = \frac{1}{2}\big(\cosh(\beta_j L\xi) - \cos(\beta_j L\xi) + R_j \sin(\beta_j L\xi) - R_j \sinh(\beta_j L\xi)\big) \tag{3.10}$$

$$\Psi_k^\lambda = \sin\Big(\frac{2k-1}{2}\pi(1-\xi)\Big) \tag{3.11}$$

where β_j and R_j are solved from the cantilevered classical linear eigenmode equation and the boundary condition equation. Respectively,

$$0 = \cos(\beta_j L)\cosh(\beta_j L) + 1 \tag{3.12}$$

$$R_j = (\cosh(\beta_j L) + \cos(\beta_j L))/(\sinh(\beta_j L) + \sin(\beta_j L)) \tag{3.13}$$

The mode shapes for the free-free beam are:

$$\Psi_i^u = \cos\big(i\pi\xi\big) \tag{3.14}$$

$$\Psi_j^w = \frac{1}{2}\big(\cosh(\beta_j L\xi) + \cos(\beta_j L\xi) - R_j \sin(\beta_j L\xi) - R_j \sinh(\beta_j L\xi)\big) \tag{3.15}$$

$$\Psi_k^\lambda = \sin\big(k\pi\xi\big) \tag{3.16}$$

where β_j and R_j are solved from the free-free classical linear eigenmode equation and the boundary condition equation. Respectively,

$$0 = \cos(\beta_j L)\cosh(\beta_j L) - 1 \tag{3.17}$$

$$R_j = (\cosh(\beta_j L) - \cos(\beta_j L))/(\sinh(\beta_j L) - \sin(\beta_j L)) \tag{3.18}$$

In the examples in this work, rigid body translation for w is included for the free-free beam, whereas rigid body rotation is excluded.

Kinetic Energy

The modal terms to be entered into the Euler-Lagrange equations are derived as follows. Considering first the kinetic energy terms, and noting again that the $\dot{u}$ terms become nonlinear in w through the constraint equation:

$$T = \frac{1}{2}\int_0^L m\Big[\sum_{i1}\sum_{i2}\Psi^u_{i1}\Psi^u_{i2}\dot{u}_{i1}\dot{u}_{i2} + \sum_{j1}\sum_{j2}\Psi^w_{j1}\Psi^w_{j2}\dot{w}_{j1}\dot{w}_{j2}\Big]\,dx \tag{3.19}$$

$$\frac{\partial T}{\partial \dot{u}_i} = \frac{1}{2}\int_0^L m\Big[\sum_{i1}\Psi^u_{i1}\Psi^u_i\dot{u}_{i1} + \sum_{i2}\Psi^u_{i2}\Psi^u_i\dot{u}_{i2}\Big]\,dx = \int_0^L m\Psi^u_i\sum_{i1}\Psi^u_{i1}\dot{u}_{i1}\,dx \tag{3.20}$$

$$\frac{\partial}{\partial t}\frac{\partial T}{\partial \dot{u}_i} = \int_0^L m\Psi^u_i\sum_{i1}\Psi^u_{i1}\ddot{u}_{i1}\,dx = m\int_0^L \Psi^u_i\Psi^u_i\,dx\ddot{u}_i = mM^u_{i,i}\ddot{u}_i \tag{3.21}$$

where orthogonality of mode shapes is utilized in the last step, and where

$$M^u_{i,i} = \int_0^L \Psi^u_i\Psi^u_i\,dx \tag{3.22}$$

Similarly,

$$\frac{\partial}{\partial t}\frac{\partial T}{\partial \dot{w}_j} = mM^w_{j,j}\ddot{w}_j \tag{3.23}$$

where

$$M^w_{j,j} = \int_0^L \Psi^w_j\Psi^w_j\,dx \tag{3.24}$$

The rest of the derivatives of kinetic energy are zero, and therefore only one kinetic energy term is entered into the Lagrange Equation for each of the spatial coordinates.

Potential Energy

Writing the potential energy from Eqn. 3.4 in its modal form,

$$V = \frac{1}{2}\int_0^L EI\Big(\sum_{j1}\sum_{j2}\Psi_{j1}^{w\prime\prime}\Psi_{j2}^{w\prime\prime}w_{j1}w_{j2} + \sum_{j1}\sum_{j2}\sum_{j3}\sum_{j4}\Psi_{j1}^{w\prime\prime}\Psi_{j2}^{w\prime\prime}\Psi_{j3}^{w\prime}\Psi_{j4}^{w\prime}w_{j1}w_{j2}w_{j3}w_{j4}\Big)\,dx \quad (3.25)$$

Then for use in the Euler-Lagrange Equation,

$$\begin{aligned}\frac{\partial V}{\partial w_j} = \frac{1}{2}\int_0^L EI\Big(&\Psi_j^{w\prime\prime}\sum_{j2}\Psi_{j2}^{w\prime\prime}w_{j2} + \Psi_j^{w\prime\prime}\sum_{j1}\Psi_{j1}^{w\prime\prime}w_{j1} \\ &+ \Psi_j^{w\prime\prime}\sum_{j2}\sum_{j3}\sum_{j4}\Psi_{j2}^{w\prime\prime}\Psi_{j3}^{w\prime}\Psi_{j4}^{w\prime}w_{j2}w_{j3}w_{j4} \\ &+ \Psi_j^{w\prime\prime}\sum_{j1}\sum_{j3}\sum_{j4}\Psi_{j1}^{w\prime\prime}\Psi_{j3}^{w\prime}\Psi_{j4}^{w\prime}w_{j1}w_{j3}w_{j4} \\ &+ \Psi_j^{w\prime}\sum_{j1}\sum_{j2}\sum_{j4}\Psi_{j1}^{w\prime\prime}\Psi_{j2}^{w\prime\prime}\Psi_{j4}^{w\prime}w_{j1}w_{j2}w_{j4} \\ &+ \Psi_j^{w\prime}\sum_{j1}\sum_{j2}\sum_{j3}\Psi_{j1}^{w\prime\prime}\Psi_{j2}^{w\prime\prime}\Psi_{j3}^{w\prime}w_{j1}w_{j2}w_{j3}\Big)\,dx \end{aligned} \quad (3.26)$$

Because all of the j indices have the same range, this may be condensed and simplified as

$$\frac{\partial V}{\partial w_j} = \sum_{j1}\int_0^L EI\Psi_{j1}^{w\prime\prime}\Psi_j^{w\prime\prime}\,dx\; w_{j1} + \sum_{j1}\sum_{j2}\sum_{j3}EIP_{j1,j2,j3,j}w_{j1}w_{j2}w_{j3} \quad (3.27)$$

where the nonlinear stiffness term $P_{j1,j2,j3,j}$ is defined as

$$P_{j1,j2,j3,j} \equiv \int_0^L (\Psi_{j1}^{w\prime\prime}\Psi_{j2}^{w\prime\prime}\Psi_{j3}^{w\prime}\Psi_j^{w\prime} + \Psi_{j1}^{w\prime\prime}\Psi_{j2}^{w\prime}\Psi_{j3}^{w\prime}\Psi_j^{w\prime\prime})\,dx \quad (3.28)$$

Now it is possible to manipulate the first term of Eqn. 3.27 to yield a simpler term. It is known that

$$EI\Psi_j^{w(4)} - m\omega_j^2\Psi_j^w = 0 \tag{3.29}$$

By projecting Ψ_{j1}^w onto this,

$$\int_0^L EI\Psi_j^{w(4)}\Psi_{j1}^w \, dx - m\omega_i^2 \int_0^L \Psi_j^w\Psi_{j1}^w \, dx = 0 \tag{3.30}$$

Integrating the first term by parts and then eliminating tail terms from the boundary conditions leads to

$$\int_0^L EI\Psi_j^{w\prime\prime}\Psi_{j1}^{w\prime\prime} \, dx - m\omega_i^2 \int_0^L \Psi_j^w\Psi_{j1}^w \, dx = 0 \tag{3.31}$$

By orthogonality, it may be concluded that

$$\int_0^L EI\Psi_j''\Psi_j'' \, dx = m\omega_j^2 M_{j,j} \tag{3.32}$$

Therefore, the change in potential energy is

$$\frac{\partial V}{\partial w_j} = m\omega_j^2 M_{j,j}^w w_j + \sum_{j1}\sum_{j2}\sum_{j3} EIP_{j1,j2,j3,j}w_{j1}w_{j2}w_{j3} \tag{3.33}$$

The other derivatives of the potential energy are zero.

Lagrange Multiplier

Next consider the Lagrange multiplier term. The modal expansion of the constraint f in Eqn. 3.5 is

$$f = \sum_i \Psi_i^{w\prime}u_i + \frac{1}{2}\sum_{j1}\sum_{j2}\Psi_{j1}^{w\prime}\Psi_{j2}^{w\prime}w_{j1}w_{j2} \tag{3.34}$$

Then,

$$\int_0^L \lambda f \; dx = \int_0^L \sum_k \Psi_k^\lambda \lambda_k \Big(\sum_i \Psi_i^{u\prime} u_i + \frac{1}{2} \sum_{j1} \sum_{j2} \Psi_{j1}^{w\prime} \Psi_{j2}^{w\prime} w_{j1} w_{j2} \Big) \; dx \tag{3.35}$$

$$= \int_0^L \Big(\sum_k \sum_i \Psi_k^\lambda \Psi_i^{u\prime} \lambda_k u_i + \frac{1}{2} \sum_k \sum_{j1} \sum_{j2} \Psi_k^\lambda \Psi_{j1}^{w\prime} \Psi_{j2}^{w\prime} \lambda_k w_{j1} w_{j2} \Big) \; dx \tag{3.36}$$

Therefore, the relevant derivatives are:

$$\frac{\partial}{\partial u_i} \Big(\int_0^L \lambda f \; dx \Big) = \sum_k \int_0^L \Psi_i^{u\prime} \Psi_k^\lambda \; dx \; \lambda_k \tag{3.37}$$

$$\frac{\partial}{\partial w_j} \Big(\int_0^L \lambda f \; dx \Big) = \sum_k \sum_{j1} \int_0^L \Psi_k^\lambda \Psi_{j1}^{w\prime} \Psi_j^{w\prime} \; dx \; \lambda_k w_{j1} \tag{3.38}$$

$$\frac{\partial}{\partial \lambda_k} \Big(\int_0^L \lambda f \; dx \Big) = \sum_i \int_0^L \Psi_k^\lambda \Psi_i^{u\prime} \; dx \; u_i + \frac{1}{2} \sum_{j1} \sum_{j2} \int_0^L \Psi_k^\lambda \Psi_{j1}^{w\prime} \Psi_{j2}^{w\prime} \; dx \; w_{j1} w_{j2} \tag{3.39}$$

Generalized Forces

The generalized forces Q_i are found from the expression for virtual work done on the system. (See references [35, 52] for further detail.)

$$\delta W = \sum_i Q_i \delta q_i \tag{3.40}$$

For this chapter, only vertical forces are considered, which are in the w direction. Therefore, the virtual work done by vertical forces is as follows.

$$\delta W = \sum_j Q_j \delta w_j \tag{3.41}$$

Defining virtual work as the applied force per unit length $\tilde{F}$ times the virtual displacement, we integrate over the length of the beam.

$$\delta W = \int_0^L \tilde{F} \delta w \; dx \tag{3.42}$$

Now, substitute the expression for w (Eqn. 3.7) and simplify.

$$\delta W = \int_0^L \tilde{F} \delta \left(\sum_j \Psi_j^w w_j \right) \; dx$$

$$\delta W = \sum_n \int_0^L \tilde{F} \Psi_j^w \; dx \; \delta w_j$$

By Eqn. 3.41, the generalized forces are found.

$$Q_j = \int_0^L \tilde{F} \Psi_j^w \; dx \tag{3.43}$$

For a point force as in this chapter, this becomes

$$Q_j = F \Psi_n |_{(x = x_F)} \tag{3.44}$$

Where F is total force rather than force per unit length.

System Of Equations

By combining terms in the three Lagrange Equations, a system of equations is obtained.

$$0 = mM^u_{ii}\ddot{u}_i - \sum_k \int_0^L \Psi^{w\prime}_i \Psi^\lambda_k \; dx \; \lambda_k \tag{3.45}$$

$$\begin{aligned} Q_j =& mM^w_{jj}\ddot{w}_j + 2m\zeta_j\omega_j M^w_{jj}\dot{w}_j + m\omega_j^2 M^w_{jj} w_j \\ &+ \sum_{j1}\sum_{j2}\sum_{j3} EI \; P_{j1,j2,j3,j} w_{j1} w_{j2} w_{j3} \\ &- \sum_k \sum_{j1} \int_0^L \Psi^\lambda_k \Psi^{w\prime}_{j1} \Psi^{w\prime}_j \; dx \; \lambda_k w_{j1} \end{aligned} \tag{3.46}$$

$$0 = \sum_i \int_0^L \Psi^\lambda_k \Psi^{w\prime}_i \; dx \; u_i + \frac{1}{2}\sum_{j1}\sum_{j2} \int_0^L \Psi^\lambda_k \Psi^{w\prime}_{j1} \Psi^{w\prime}_{j2} \; dx \; w_{j1} w_{j2} \tag{3.47}$$

Normalizing the modal coefficients u_i and w_j and normalizing the integral terms such that the integration is from 0 to 1 with respect to $x/L \equiv \xi$ produces several useful definitions. The 1-dimensional vectors and the 2-dimensional matrices can be rewritten from italicized index notation to boldface matrix notation as indicated with the right arrows. However, the 3 and 4-dimensional tensors will be left in index form to avoid the introduction of tensor notation.

$$u_i \equiv \frac{u_i}{L} \;\Rightarrow\; \mathbf{u}, \quad w_j \equiv \frac{w_j}{L} \;\Rightarrow\; \mathbf{w}, \quad \lambda_k \;\Rightarrow\; \boldsymbol{\lambda}$$

$$M^u_{ii} \equiv \int_0^1 \Psi^u_i \Psi^u_i \; d\xi \;\Rightarrow\; \mathbf{M_u}, \quad M^w_{jj} \equiv \int_0^1 \Psi^w_j \Psi^w_j \; d\xi \;\Rightarrow\; \mathbf{M_w}$$

$$A_{ik} \equiv \int_0^1 \Psi^{w\prime}_i \Psi^\lambda_k \; d\xi \;\Rightarrow\; \mathbf{A}, \quad B_{kj_1j} \equiv \int_0^1 \Psi^\lambda_k \Psi^{w\prime}_{j_1} \Psi^{w\prime}_j \; d\xi$$

$$P_{j_1j_2j_3j} \equiv \int_0^1 (\Psi^{w\prime\prime}_{j_1}\Psi^{w\prime\prime}_{j_2}\Psi^{w\prime}_{j_3}\Psi^{w\prime}_j + \Psi^{w\prime\prime}_{j_1}\Psi^{w\prime}_{j_2}\Psi^{w\prime}_{j_3}\Psi^{w\prime\prime}_j) \; d\xi$$

$$\zeta_j \;\Rightarrow\; \boldsymbol{\zeta}, \qquad \omega_j \;\Rightarrow\; \boldsymbol{\omega}, \qquad \omega_j^2 \;\Rightarrow\; \boldsymbol{\omega^2}, \qquad Q_j \;\Rightarrow\; \mathbf{Q}$$

A discussion on vector/matrix size and characteristics may be appropriate at this point. Vectors $\mathbf{u}$, $\mathbf{w}$, and $\boldsymbol{\lambda}$ are length I, J, and K, respectively. Matrices $\mathbf{M_u}$ and $\mathbf{M_w}$ are diagonal matrices of size I^2 and J^2, respectively. Matrix $\mathbf{A}$ is of size I x K. Tensor B is three-dimensional of size K x J x J, and P is four-dimensional of size J^4. Matrices $\boldsymbol{\zeta}$, $\boldsymbol{\omega}$, and $\boldsymbol{\omega^2}$ are diagonal matrices of length J with each nonzero entry as the corresponding damping coefficient, modal natural frequency, or modal natural frequency squared, respectively.

The final two terms in Eqn. 3.46 are tensor summations which simplify to vectors of length J, and the final term in Eqn. 3.47 is a tensor summation which simplifies to a vector of length K. These may be represented in their final vector form as follows.

$$\left\{\mathbf{Pw^3}\right\} = \sum_{j_1}\sum_{j_2}\sum_{j_3} L^{-2}EI\ P_{j_1 j_2 j_3 j} w_{j_1} w_{j_2} w_{j_3}$$

$$\left\{\mathbf{Bw\lambda}\right\} = \sum_{k}\sum_{j_1} B_{k j_1 j} w_{j_1} \lambda_k$$

$$\left\{\mathbf{Bww}\right\} = \sum_{j_1}\sum_{j_2} B_{k j_1 j_2} w_{j_1} w_{j_2}$$

The system of equations is then

$$0 = L^2 m \mathbf{M_u}\ddot{\mathbf{u}} - \mathbf{A}\boldsymbol{\lambda} \tag{3.48}$$

$$\begin{aligned}\mathbf{Q} =& L^2 m \mathbf{M_w}\ddot{\mathbf{w}} + 2L^2 m \boldsymbol{\zeta}\boldsymbol{\omega}\mathbf{M_w}\dot{\mathbf{w}} + L^2 m \boldsymbol{\omega^2}\mathbf{M_w}\mathbf{w} \\ &+ L^{-2}EI\ \left\{\mathbf{Pw^3}\right\} - \left\{\mathbf{Bw\lambda}\right\}\end{aligned} \tag{3.49}$$

$$0 = \mathbf{A^T u} + \frac{1}{2}\left\{\mathbf{Bww}\right\} \tag{3.50}$$

3.2.2 Solution

To solve this system of equations, differentiate Eqn. 3.50 in time twice and solve for $\ddot{\mathbf{u}}$. Then substitute $\ddot{\mathbf{u}}$ from Eqn. 3.48 into this new equation to get an expression for

$\boldsymbol{\lambda}$. Finally, this expression for $\boldsymbol{\lambda}$ is substituted into Eqn. 3.49 to get one equation of motion for $\mathbf{w}$. From this, both $\mathbf{u}$ and $\boldsymbol{\lambda}$ may then be solved once $\mathbf{w}$ is known.

The second time derivative of Eqn. 3.50 is

$$0 = \mathbf{A^T}\ddot{\mathbf{u}} + \left\{\mathbf{B}\dot{\mathbf{w}}\dot{\mathbf{w}}\right\} + \left\{\mathbf{B}\mathbf{w}\ddot{\mathbf{w}}\right\} \tag{3.51}$$

where the vectors $\left\{\mathbf{B}\dot{\mathbf{w}}\dot{\mathbf{w}}\right\}$ and $\left\{\mathbf{B}\mathbf{w}\ddot{\mathbf{w}}\right\}$ are defined as

$$\left\{\mathbf{B}\dot{\mathbf{w}}\dot{\mathbf{w}}\right\} \equiv \sum_{j_1}\sum_{j_2} B_{kj_1j_2}\dot{w}_{j_1}\dot{w}_{j_2}$$

$$\left\{\mathbf{B}\mathbf{w}\ddot{\mathbf{w}}\right\} \equiv \sum_{j_1}\sum_{j_2} B_{kj_1j_2}w_{j_1}\ddot{w}_{j_2}$$

Then from Eqn. 3.48, $\ddot{\mathbf{u}}$ can be written as

$$\ddot{\mathbf{u}} = \frac{1}{L^2 m}\mathbf{M_u^{-1}}\mathbf{A}\boldsymbol{\lambda} \tag{3.52}$$

Inserting this into Eqn. 3.51, we find λ in terms of w.

$$\boldsymbol{\lambda} = -L^2 m\Big([\mathbf{A}\mathbf{M_u^{-1}}\mathbf{A}]^{-1}\left\{\mathbf{B}\dot{\mathbf{w}}\dot{\mathbf{w}}\right\}\Big) - L^2 m\Big([\mathbf{A}\mathbf{M_u^{-1}}\mathbf{A}]^{-1}\left\{\mathbf{B}\mathbf{w}\ddot{\mathbf{w}}\right\}\Big) \tag{3.53}$$

As expected, each term in Eqn. 3.53 is a vector of length K and has units of force. Finally, we substitute this expression for $\boldsymbol{\lambda}$ into Eqn. 3.49 to solve for $\ddot{\mathbf{w}}$, which provides the equation of motion for the transverse deflection.

$$\begin{aligned}\ddot{\mathbf{w}} = &\Big(mL^2[\mathbf{B}\mathbf{A}\mathbf{M_u}\mathbf{A}\mathbf{B}\mathbf{w}\mathbf{w}] + mL^2\mathbf{M_w}\Big)^{-1} \\ &\Big(\mathbf{Q} - mL^2\boldsymbol{\omega}^{\mathbf{2}}\mathbf{M_w}\mathbf{w} - 2L^2 m\boldsymbol{\zeta}\boldsymbol{\omega}\mathbf{M_w}\dot{\mathbf{w}} \\ &- L^{-2}EI\left\{\mathbf{P}\mathbf{w}^{\mathbf{3}}\right\} - mL^2\left\{\mathbf{B}\mathbf{A}\mathbf{M_u}\mathbf{A}\mathbf{B}\dot{\mathbf{w}}\dot{\mathbf{w}}\mathbf{w}\right\}\Big)\end{aligned} \tag{3.54}$$

Here, several new matrices and vectors have been introduced as calculated from the tensor summations and are defined as follows.

$$[\mathbf{BAM_uABww}] =$$

$$\sum_{k_1} B_{k_1 j 3 j} \sum_{k} \left(\left(\sum_{i_1} \sum_{i_2} A_{k 1 i_1} (M^u_{i_1 i_2})^{-1} A_{i_2 k} \right)^{-1} \sum_{j_1} \sum_{j_2} B_{k j_1 j_2} w_{j_1} w_{j_2} \right)$$

$$\left\{\mathbf{BAM_uAB\dot{w}\dot{w}w}\right\} =$$

$$\sum_{j3} \sum_{k_1} B_{k_1 j 3 j} \sum_{k} \left(\left(\sum_{i_1} \sum_{i_2} A_{k 1 i_1} (M^u_{i_1 i_2})^{-1} A_{i_2 k} \right)^{-1} \right.$$

$$\left. \sum_{j_1} \sum_{j_2} B_{k j_1 j_2} \dot{w}_{j_1} \dot{w}_{j_2} \right) w_{j3}$$

This single equation of motion (3.54) is marched through time using a 4th order Runge-Kutta solver, Matlab's ODE45. The physical transverse deflection is then transformed from the modal coefficients using Eqn. 3.7, which allows the longitudinal deflection to be solved from the constraint equation 3.5.

This method easily allows investigations of different boundary conditions. By altering the dimensionless mode shapes outside of the ODE solver, one may compute coefficient matrices for different boundary conditions one time only. This "bank" of dimensionless modal coefficients for different boundary conditions decreases computational time and up-front effort.

To understand the influence of the stiffness nonlinearity versus the inertia nonlinearity, each of these terms is isolated and explored. Figures 3.2, 3.3, 3.6 and 3.7 show 4 cases for each loading condition: Stiffness only, Inertia only, FNL (Fully Nonlinear), and Linear. The linear case considers only the first three terms of Eqn. 3.49: linear inertia, linear damping, and linear stiffness. The stiffness only case considers the linear terms plus the 4th term which represents nonlinear stiffness; the inertia

only case considers the linear terms plus the final term as nonlinear inertia; and the FNL case considers all terms.

3.2.3 Physical Model Properties

To validate our model, static and dynamic comparisons are drawn to Tang et al. [8], and therefore we use their model parameters. Material properties used are shown in Table 3.1. Width, thickness, and length are identical to reported values whereas the modulus E and density ρ were chosen such that natural frequencies reported by Tang et al. were matched. For each case, the modal damping is $\zeta = 0.01$ for all modes. This quantity, again, was chosen to match published methods and results [8].

Table 3.1: Material Properties of Beam

Width	Thickness	Length	E	ρ
0.0285 m	0.0018 m	0.5080 m	69.3 GPa	2840 kg/m

3.3 Results

3.3.1 Cantilevered Beam Results

For cantilevered static tests, varying mass loads acting under gravity are placed at the tip of the beam, and transverse and longitudinal deflection data are calculated. The u deflection is calculated via the constraint equation. Modal convergence occurs after 4 modes for the static cases, but here 5 modes are used in each coordinate, as reported by Tang et al [8]. Figure 3.1 demonstrates agreement between published results—including experimental results—and the current results for the deflection normalized by L in the w and u directions, respectively. The agreement shown here between the current model and previously published results is encouraging and validating. It is thought that any disagreement between computational and experimental data is due to a difference of the manufacturer's reported versus actual material properties. It

may be noted that the stiffness of the beam is inversely related to the slope of these plots, indicating that the beam stiffens under higher loads.

Comparing the present *dynamic* results to those published [8] is useful in identifying new insights into the cantilevered beam problem. Forward and backward frequency sweeps are conducted to demonstrate nonlinear effects of the model. The forcing amplitude is set at $F = 0.147N$ and acts at $x_F = 0.7 * L$ in the w direction to match the published configuration [8]. The frequency is swept from 4.5 to 6.5 Hz, capturing the behavior around the linear natural frequency at 5.5 Hz. A convergence study was performed and it was determined that 3 modes in w and 6 modes in u and λ are necessary to ensure modal convergence at all time steps. The beam vibration reaches a steady state after about 35 seconds, and the final second at each frequency is used to calculate the RMS response of each frequency step.

In Figure 3.2, these frequency sweeps are shown normalized to the linear natural frequency, Ω. Each case isolates the stiffness and inertia nonlinearities and compares to the full nonlinear case which includes both nonlinearities. For the isolated stiffness or inertia nonlinearity cases, hysteresis occurs. By plotting forward and backward frequency sweeps, both stable branches of the nonlinear response curves are shown. However, the unstable branch which connects the two is not illustrated because the numerical solution always tends to one of these stable branches.

It is interesting to note that by solving these cases at higher frequency resolutions, the fully nonlinear behavior is somewhat different than previously reported by Tang [8]. The present results agree that the stiffness nonlinearity increases the resonant frequency while the inertia nonlinearity decreases it, as well that the fully nonlinear case shows a balance between the two nonlinear effects. However, the maximum RMS amplitude of the fully nonlinear case is not significantly less than those of either the isolated stiffness or inertia nonlinearity cases, as previously reported. Its steep peak has important implications for experimental verification of such a case,

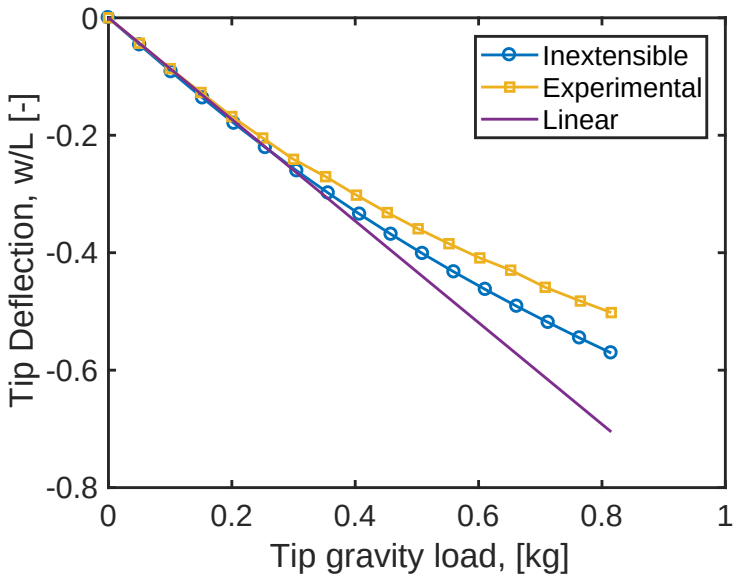

(a)

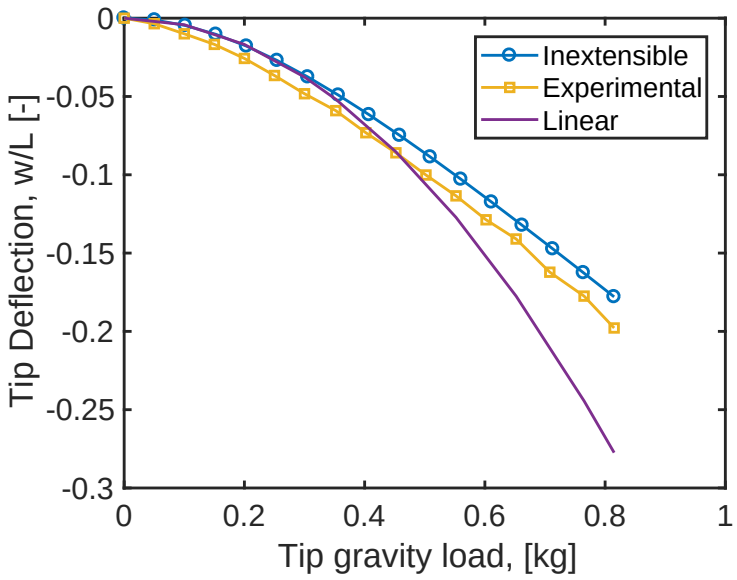

(b)

FIGURE 3.1: Deflection of beam tip in (a) w and (b) u directions due to varying mass loads on tip

as the frequency sweep must have very high resolution to avoid the risk of passing over the maximum resonant amplitude. Also note that the full nonlinear case shows essentially no hysteresis, and as such the forward and backward frequency sweeps are essentially identical.

The offsetting contribution of the inertia and stiffness nonlinearities is in agreement with results previously published [8, 17, 20] which show that the first resonant mode acts nearly linearly.

Figure 3.3 shows the 2nd resonant response of the cantilever beam. Here, 3 w modes and 6 u and λ modes were used again. Note that the fully nonlinear beam result is significantly softened, even though the stiffness only case shows a strong stiffening effect. Hysteresis is strong and the resonant frequency is shifted by about 6.5% from the linear resonant frequency.

To illustrate the relationship between forcing amplitude and the nonlinear effects, Figure 3.4 plots the linear and nonlinear responses for different loads with a backward frequency sweep across the second natural frequency. Even at low loads and small deflections (under 5 percent of the beam length), the inertia nonlinearity is still seen to shift the resonance frequency downwards. At higher loads, as expected, the beam exhibits stronger hysteresis as the resonance frequency continues to decrease.

3.3.2 Free-Free Results

The free-free beam model was subjected to similar tests as the cantilevered beam model, but the free-free beam exhibits additional subtleties.

To assess the free-free model, static computations were again performed, using 10 modes, and compared to a FEM solution. The beam was held in static rigid body equilibrium by applying an upward force load F at $x = L/2$ and downward forces $F/2$ at $x = 0$ and $x = L$. Total deflection in the w direction is computed as the difference in w between $x = L/2$ and $x = L$. As a comparison, the same

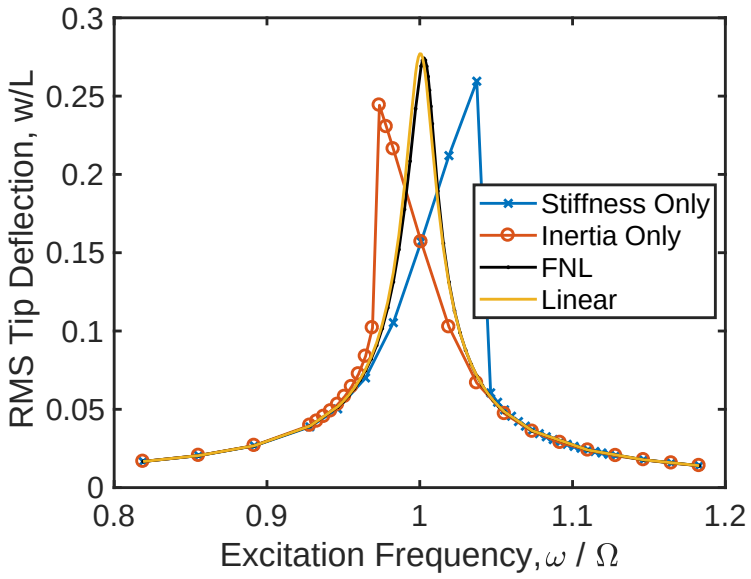

(a)

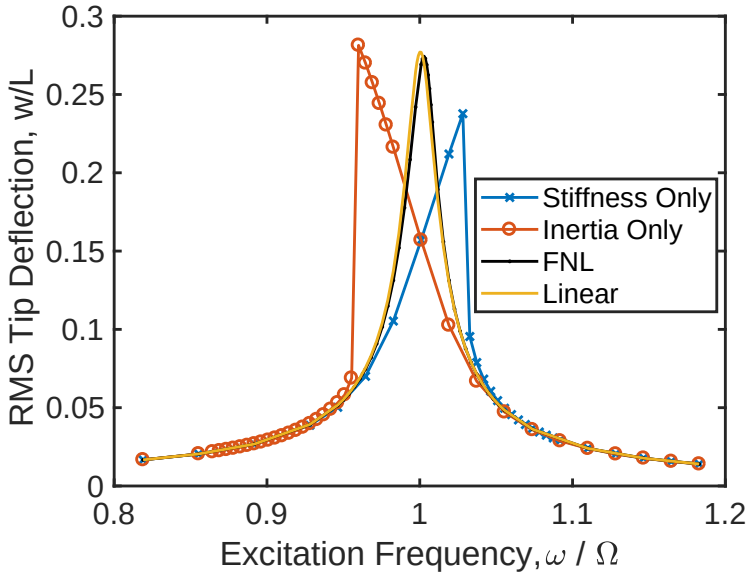

(b)

FIGURE 3.2: 1st mode RMS response diagrams of cantilevered beam to sinusoidal excitation force of $F = 0.147N$ at $X_F = 0.7 * L$ for (a) forward and (b) backward frequency sweep

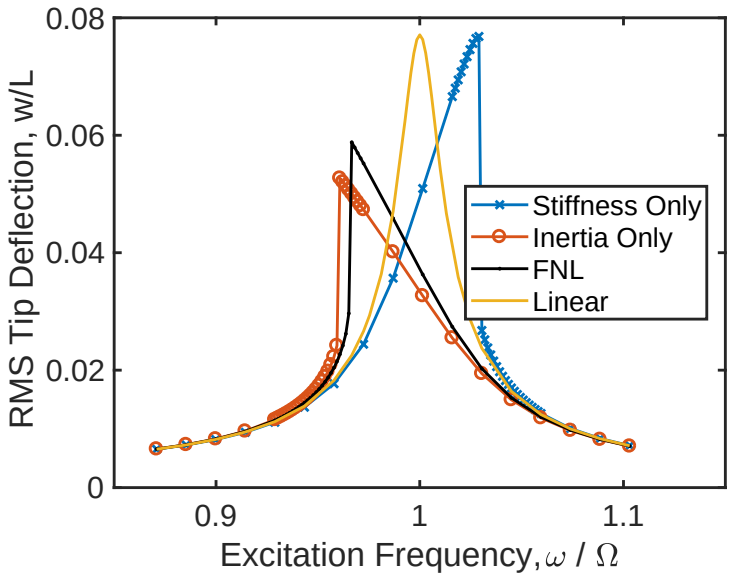

(a)

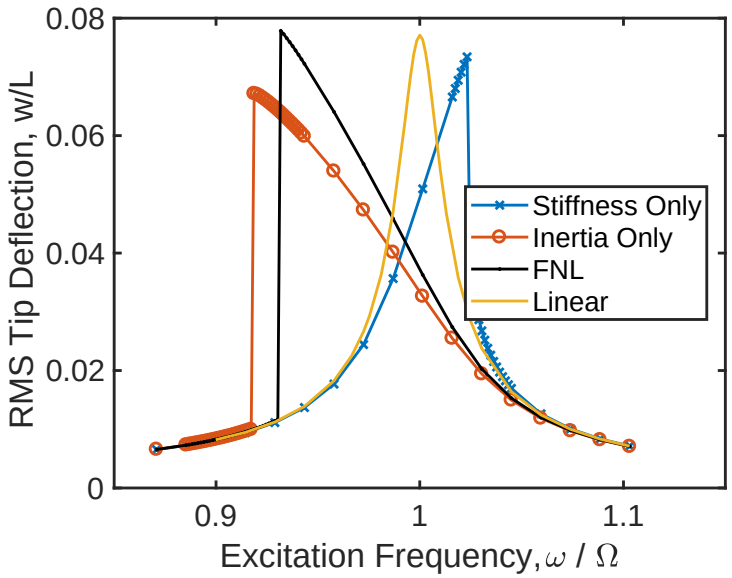

(b)

FIGURE 3.3: 2nd mode RMS response diagrams of cantilevered beam to sinusoidal excitation force of $F = 1.96N$ at $X_F = 0.3 * L$ for (a) forward and (b) backward frequency sweep

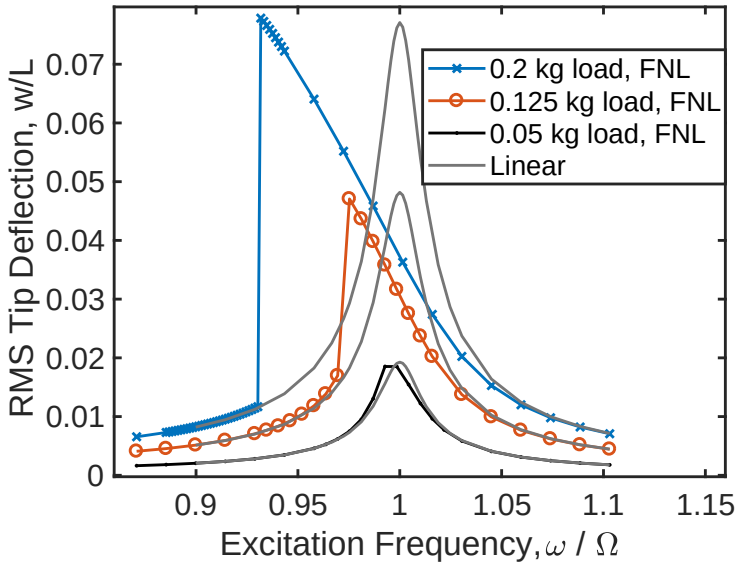

FIGURE 3.4: 2nd mode linear vs nonlinear cantilever RMS responses to varying loads acting at $X_F = 0.3 * L$, backward frequency sweep

configuration was generated and computed in the commercial FEM software ANSYS. Figure 3.5 compares the results of different forces with the different solving methods. It illustrates the difference between the nonlinear and linear cases and shows that our model reasonably agrees with the FEM code.

For the dynamic computations, frequency sweeps showed the nature of the nonlinear effects on resonance and hysteresis. A sinusoidal force with amplitude $F = 1.47N$ was applied in the w direction at $x_F = L/2$. 4 w modes and 9 u and λ modes were computed as determined by a convergence study. Notably, since the rigid body translational mode was included, the beam could react to the forces exerted on it by accelerating in the w direction. To inhibit this motion, if the beam's rigid body translation was greater or less than L, a weak uniformly distributed force of $\pm 0.02N$ was applied to contain the beam. Deflection is measured as the difference in maximum w from the resting position of the beam after this rigid-body motion has been removed. The beam motion reaches steady state after about 7 seconds, and the final 0.1 second is used to calculate the RMS response to each frequency.

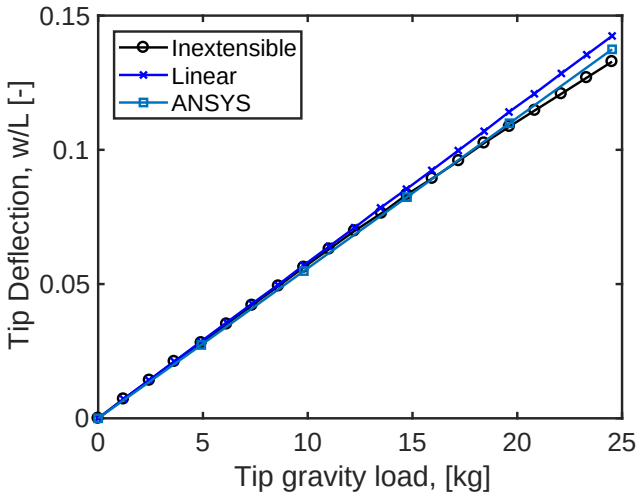

FIGURE 3.5: w deflection vs static load of free-free beam in 1st bending mode for current formulation and ANSYS solution

Figures 3.6a and 3.6b plot the RMS deflection data for the forward and backward frequency sweeps, respectively, around the first linear natural frequency. Unlike the cantilevered beam, the full nonlinear case for the free-free beam shows more influence from the inertia nonlinearity, and indeed the resonant peak is shifted downward by about 3.3% from the linear natural frequency. As previously noted with the cantilevered beam, the frequency resolution is increased near the resonance peaks for each case.

Figure 3.7 plots the 3rd resonant RMS deflection data for the forward and backward frequency sweeps, respectively. The 3rd resonant frequency was chosen for study instead of the 2nd because exciting the 2nd would induce rigid body rotation of the beam, which is not developed in this model. Here, 4 w modes and 14 u and λ modes are computed. Note that more modes in u and λ are necessary to reach modal convergence for the third mode excitation than for the first mode excitation. Like the 1st resonant mode response, the fully nonlinear beam is strongly softened, with the resonant frequency shifting by about 8.2% of the linear natural frequency.

Figure 3.8a plots the linear and nonlinear responses for different loads with a

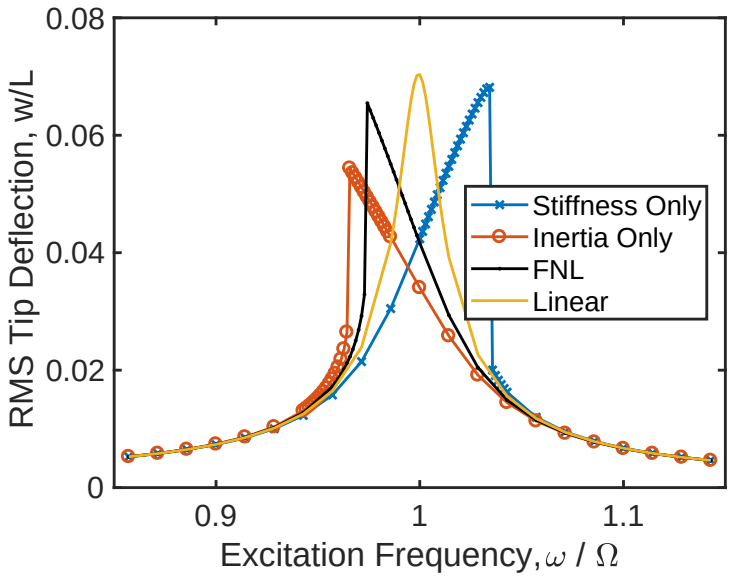

(a)

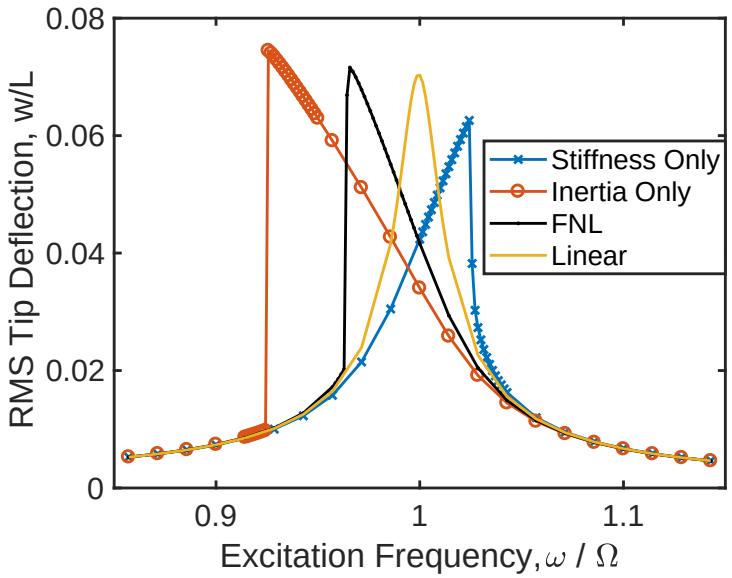

(b)

FIGURE 3.6: 1st mode RMS response diagrams of free-free beam to sinusoidal excitation force of $F = 1.47N$ at $X_F = L/2$ for (a) forward and (b) backward frequency sweep

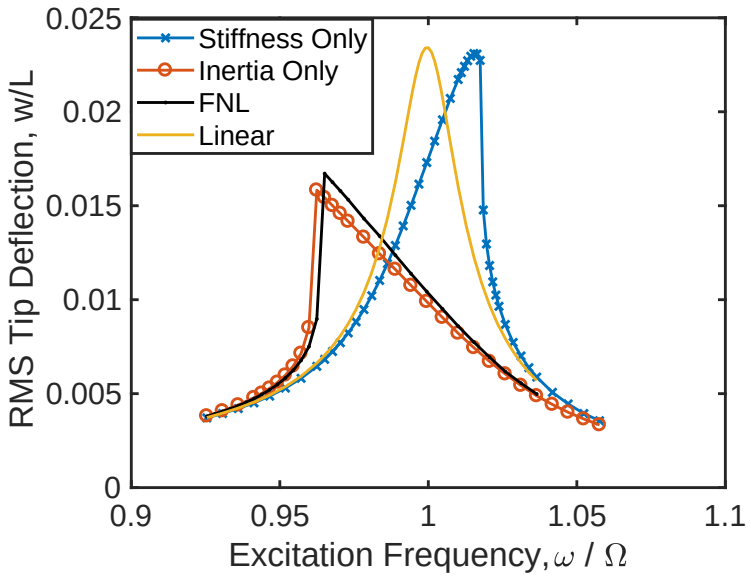

(a)

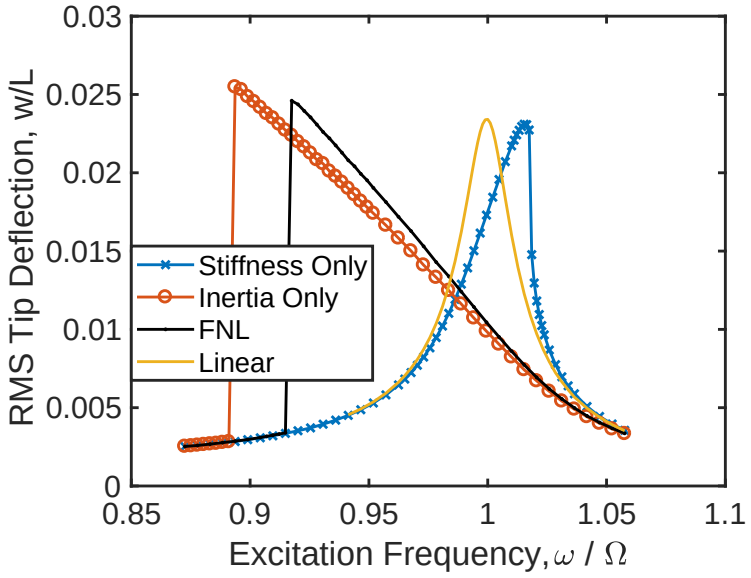

(b)

FIGURE 3.7: 3rd mode RMS response diagrams of free-free beam to sinusoidal excitation force of $F = 12.27N$ at $X_F = L/2$ for (a) forward and (b) backward frequency sweep

backward frequency sweep. As seen in the case of the cantilevered beam, the nonlinear inertia is prevalent in shifting the resonance frequency downwards at all loads.

3.4 Conclusions and Future Work

A new formulation and solution method of the equations of motion for inextensible beams has been developed and assessed. In the 1st resonant mode, it has been shown that the nonlinear cantilevered beam behaves more linearly than previously thought. Hysteresis is not shown, and the nonlinear resonant response is similar to the linear response for a representative case. In the 2nd resonant mode, the cantilevered beam response notably softens due to nonlinear effects at small deflections of 5 percent of the beam length.

In addition, the free-free beam configuration has been explored, and it has been determined that the nonlinear inertia in this configuration is very important. Hysteresis is clearly apparent in the 1st and 3rd resonant modes of free-free case, as the nonlinearity substantially decreases the resonance frequency at deflections of only 5 percent and 1.5 percent of the beam length, respectively.

The trend towards more dominant nonlinear inertia effects for higher resonant modes is perhaps due to the increased velocity and the decreased amplitude with which the beam vibrates at higher modes. Therefore, the inertial terms are dominant to the stiffness terms.

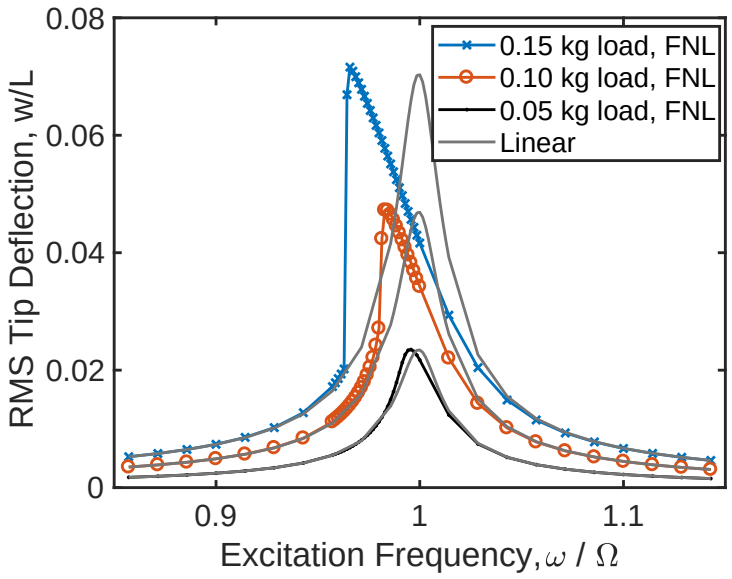

(a)

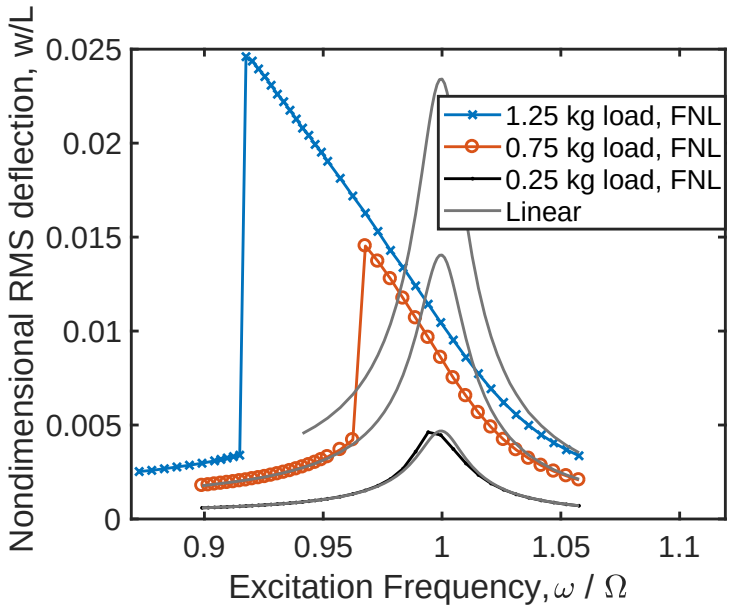

(b)

FIGURE 3.8: Linear vs nonlinear free-free beam RMS responses to varying loads acting at $X_F = L/2$, backward frequency sweep across (a) first and (b) third resonant frequencies

4

Nonlinear Response of an Inextensible, Cantilevered Beam Subjected to a Nonconservative Follower Force

4.1 Introduction

It may be noted that the next two chapters were originally intended to be simple introductions to nonconservative forces. Since aerodynamic loads are distributed nonconservative loads, the goal was to begin with simpler nonconservative point loads, such as the follower force. What we found was that there is a great deal of interest, subtlety and discovery to be made in this area, beginning with a classical mechanics problem of a cantilevered beam subjected to a follower load. This problem is the subject of this chapter, which includes work originally published in ASME's Journal of Computational and Nonlinear Dynamics [46].

A cantilevered beam with a compressive, nonconservative follower force is known as Beck's beam problem [21]. Figure 4.1 illustrates the schematic of this system, where $-F_T$ is said follower force. This structure has been studied both experimentally and computationally in the literature for its interesting Hopf bifurcation

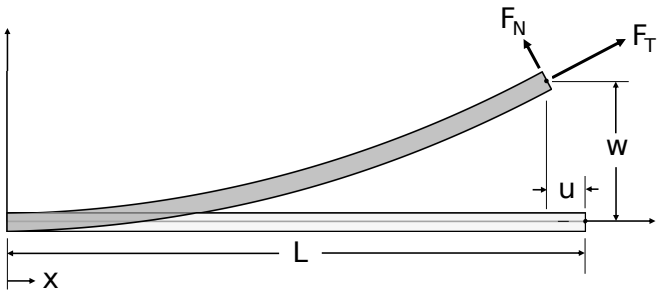

FIGURE 4.1: Schematic of cantilevered beam with follower force

behavior [22, 23, 25–29, 53], and a comprehensive survey of research studies was published in 2000 [30]. Using a linear model, Beck determined that a critical force of $-\overline{F_T} = 20.05\ EI/L^2$ causes the undamped beam to become unstable. Bolotin [22,53] demonstrated via an eigenvalue approach that small visco-elastic damping values can decrease the critical force significantly, a result known for various nonconservative systems and first shown by Ziegler in 1952 [54]. More recently, this system has been studied with the help of numerical methods [25–28] and the Finite Element Method [29] to illustrate the behavior of the bifurcation as well as the nonlinear post-critical behavior of the beam. Stanciulescu et al. [29] noted that their finite element mesh needed to be highly refined to handle the dynamic analysis required to analyze the post-critical behavior.

It is interesting to note that although the Hopf bifurcation is a *nonlinear* phenomenon, most of the literature to date has focused only on *linear* stability analyses [21, 22, 26, 29, 53]. Luongo and D'Annibale [28, 55] have performed pioneering studies into the nonlinear regime and provide a concise and insightful discussion of the state of the art. Of particular note they include work on discrete 2-bar systems such as that considered by Hagedorn to study nonlinear damping and its role on stability [56] and that of Thomsen to analyze chaos [57]. Continuous systems have been scrutinized with care as well. Crespo da Silva and Glynn [58, 59] provide excellent studies with their nonlinear model derived from Hamilton's Principle using a

Lagrange multiplier to enforce inextensibility, the method that is utilized in this document. They analyze stability and dynamical behavior by linearizing the equations of motion with the method of multiple time scales. Luongo et al. have contributed several notable works with their continuous beam model and multiple-scales and perturbation analyses to determine the role of damping in stability [25–28,55,60,61].

In the present chapter, the goal is to demonstrate the robustness of the same nonlinear model derived previously, expanded to explore Beck's problem. The effects of nonlinearity are again explored within this new framework for the equations of motion and their solution. The effects of linear damping are included as well. The principal focus is on the convergence of the modal series and a more in depth analysis of the transverse and longitudinal deformations of the beam and the in-plane force that provides the constraint between these two planar motions.

In Section 4.2 we derive the equations of motion, beginning with the unforced system and then including the follower force. Section 4.3 discusses the results. We show that our model yields the published critical force of 20.05 EI/L^2 for an undamped, linear system. Further, we illustrate agreement with published results which state that adding damping to the system reduces substantially the critical force, and we briefly explore the role that damping plays in the bifurcation. For the nonlinear model, an analysis is completed of the deflection and frequency of the limit cycle oscillations and the modal expansion of the constraint force is investigated. We then explore the importance of the number of modes in each equation of motion. It is determined that the behavior of the limit cycle oscillation requires only a small number of constraint force modes compared to longitudinal deflection modes, indicating quite interestingly that an underconstrained model is able to capture properly the dynamics of the system.

4.2 Methods

4.2.1 Unforced Governing Equations

The unforced, undamped normalized system of equations is as follows.

$$\boxed{\begin{aligned} 0 =& L^2 m \mathbf{M_u} \ddot{\mathbf{u}} - \mathbf{A}\boldsymbol{\lambda} \\ 0 =& L^2 m \mathbf{M_w} \ddot{\mathbf{w}} + L^2 m \boldsymbol{\omega}^{\mathbf{2}} \mathbf{M_w} \mathbf{w} \\ & + L^{-2} EI \ \left\{ \mathbf{P w^3} \right\} - \left\{ \mathbf{B w \lambda} \right\} \\ 0 =& \mathbf{A^T u} + \frac{1}{2} \left\{ \mathbf{B w w} \right\} \end{aligned}} \tag{4.1}$$

$$\tag{4.2}$$

$$\tag{4.3}$$

A full derivation is provided in Chapter 3. However, it may be important to note here that Eqn. 4.1 is the equation for longitudinal deflection u, where λ is the internal constraint force to enforce inextensibility. Equation 4.2 is the equation for transverse deflection w, and the final two terms are the nonlinear stiffness and inertia terms, respectively. Equation 4.3 is the constraint equation.

4.2.2 Modeling the Follower Force

The nonconservative work due to the follower force has contributions in both the u and w directions.

$$\delta W^{NC} = F_x \delta u|_{(x=x_F)} + F_y \delta w|_{(x=x_F)} \tag{4.4}$$

The follower force may have one component tangent to the axis of the beam and one component normal to the beam, respectively F_T and F_N. So, to translate the follower force back to the x and y coordinate axes, define an angle β to be the angle of the beam at any point relative to the original undeformed horizontal axis and consider the following transformation.

$$F_x = F_T(x_F)\cos\beta(x_F) - F_N(x_F)\sin\beta(x_F) \tag{4.5}$$

$$F_y = F_T(x_F)\sin\beta(x_F) + F_N(x_F)\cos\beta(x_F) \tag{4.6}$$

Thus, the nonconservative work, δW^{NC}, can be written using the modal expansions of u and w (Eqns. 3.6, 3.7 from the previous chapter), and 4.5, 4.6 as

$$\delta W^{NC} = \big(F_T(x_F)\cos\beta(x_F) - F_N(x_F)\sin\beta(x_F)\big)\sum_i \Psi_i^u(x_F)\delta u_i + \big(F_T(x_F)\sin\beta(x_F) + F_N(x_F)\cos\beta(x_F)\big)\sum_j \Psi_j^w(x_F)\delta w_j \quad (4.7)$$

To determine $\cos\beta$ and $\sin\beta$, we note that.

$$\tan\beta = \frac{\partial w}{\partial x + \partial u} = \frac{w'}{1+u'} = \frac{w\prime}{1-\frac{1}{2}(w')^2} \equiv f \quad (4.8)$$

Using trigonometry, we may compute

$$\cos\beta = \left(1+f^2\right)^{-1/2} \quad (4.9)$$

$$\sin\beta = f\left(1+f^2\right)^{-1/2} \quad (4.10)$$

The generalized forces to be added to Eqns. 4.1 and 4.2 are identified as the coefficients of δu_i and δw_j in Eqn. 4.7. A damping term $2L^2 m\boldsymbol{\zeta\omega}\mathbf{M_w}\dot{\mathbf{w}}$ is added to the system in the transverse coordinate. Note that the damping coefficient $\boldsymbol{\zeta}$ is a diagonal matrix of size J^2. Two linear damping models are explored: one in which the diagonals of $\boldsymbol{\zeta}$ are held constant and one in which the diagonals of $\boldsymbol{\zeta}$ are varied such that $\boldsymbol{\zeta\omega}$ is constant.

Finally the system of equations including the follower forces and damping is as follows.

$$
\begin{aligned}
0 =& L^2 m \mathbf{M_u} \ddot{\mathbf{u}} - \mathbf{A}\boldsymbol{\lambda} \\
& - \big(F_T(x_F)\cos\beta(x_F) - F_N(x_F)\sin\beta(x_F)\big)\boldsymbol{\Psi^u}(x_F) && (4.11) \\
0 =& L^2 m \mathbf{M_w} \ddot{\mathbf{w}} + L^2 m \boldsymbol{\omega^2} \mathbf{M_w} \mathbf{w} + 2L^2 m \boldsymbol{\zeta\omega} \mathbf{M_w} \dot{\mathbf{w}} \\
& + L^{-2} EI \left\{ \mathbf{P w^3} \right\} - \left\{ \mathbf{B w \lambda} \right\} \\
& - \big(F_T(x_F)\sin\beta(x_F) + F_N(x_F)\cos\beta(x_F)\big)\boldsymbol{\Psi^w}(x_F) && (4.12) \\
0 =& \mathbf{A^T u} + \frac{1}{2}\left\{ \mathbf{B w w} \right\} && (4.13)
\end{aligned}
$$

The system of equations is solved as follows. From Eqn. 4.11, $\ddot{\mathbf{u}}$ can be written as

$$
\ddot{\mathbf{u}} = \frac{1}{L^2 m} \mathbf{M_u^{-1}} \Big(\mathbf{A}\boldsymbol{\lambda} + \big(F_T(x_F)\cos\beta(x_F) - F_N(x_F)\sin\beta(x_F)\big)\boldsymbol{\Psi^u}(x_F) \Big) \tag{4.14}
$$

Inserting this into the second time derivative of Eqn. 4.13, we find λ in terms of w.

$$
\begin{aligned}
\boldsymbol{\lambda} = & \mathbf{A^{-1}} \boldsymbol{\Psi^u}(x_F) F_N(x_F) \sin\beta(x_F) - \mathbf{A^{-1}} \boldsymbol{\Psi^u}(x_F) F_T(x_F) \cos\beta(x_F) \\
& - L^2 m \Big([\mathbf{A M_u^{-1} A}]^{-1} \left\{ \mathbf{B \dot{w} \dot{w}} \right\} \Big) - L^2 m \Big([\mathbf{A M_u^{-1} A}]^{-1} \left\{ \mathbf{B w \ddot{w}} \right\} \Big) \qquad (4.15)
\end{aligned}
$$

Here, the vectors $\left\{ \mathbf{B \dot{w} \dot{w}} \right\}$ and $\left\{ \mathbf{B w \ddot{w}} \right\}$ are defined as

$$
\left\{ \mathbf{B \dot{w} \dot{w}} \right\} \equiv \sum_{j_1} \sum_{j_2} B_{k j_1 j_2} \dot{\overline{w}}_{j_1} \dot{\overline{w}}_{j_2}, \quad \left\{ \mathbf{B w \ddot{w}} \right\} \equiv \sum_{j_1} \sum_{j_2} B_{k j_1 j_2} \overline{w}_{j_1} \ddot{\overline{w}}_{j_2}
$$

As expected, each term in Eqn. 4.15 is a vector of length K and has units of force. Finally, we substitute this expression for $\boldsymbol{\lambda}$ into Eqn. 4.12 to solve for $\ddot{\mathbf{w}}$, which provides the equation of motion for the transverse deflection. This equation is solved via a 4th order Runge-Kutta time-marching scheme. From the solution for $\mathbf{w}$, we solve for $\mathbf{u}$ and $\boldsymbol{\lambda}$ from Eqns. 4.13 and 4.11.

$$\ddot{\mathbf{w}} = \Big(mL^2[\mathbf{BAM_uABww}] + mL^2\mathbf{M_w} \Big)^{-1} \Big(- mL^2\boldsymbol{\omega}^{\mathbf{2}}\mathbf{M_w}\mathbf{w} - 2L^2 m\boldsymbol{\zeta}\boldsymbol{\omega}\mathbf{M_w}\dot{\mathbf{w}} - L^{-2}EI\left\{\mathbf{Pw}^{\mathbf{3}}\right\} - mL^2\left\{\mathbf{BAM_uAB}\dot{\mathbf{w}}\dot{\mathbf{w}}\mathbf{w}\right\} + \left\{\mathbf{BA}\boldsymbol{\Psi}^{\boldsymbol{u}}\mathbf{w}\right\}\left(F_N(x_F)\sin\beta(x_F) - F_T(x_F)\cos\beta(x_F)\right) + F_T(x_F)\boldsymbol{\Psi}^{\boldsymbol{w}}(x_F)\sin\beta(x_F) + F_N(x_F)\boldsymbol{\Psi}^{\boldsymbol{w}}(x_F)\cos\beta(x_F)\Big) \quad (4.16)$$

The matrix $[\mathbf{BAM_uABww}]$ and vector $\left\{\mathbf{BAM_uAB}\dot{\mathbf{w}}\dot{\mathbf{w}}\mathbf{w}\right\}$ were defined in the last chapter, and the new vector $\left\{\mathbf{BA}\boldsymbol{\Psi}^{\boldsymbol{u}}\mathbf{w}\right\}$ is defined as follows.

$$\left\{\mathbf{BA}\boldsymbol{\Psi}^{\boldsymbol{u}}\mathbf{w}\right\} = \sum_{j1}\sum_{k} B_{kj1j} \sum_{i} A^{-1}_{ik}\Psi^{u}_{i}(x_F)\overline{w}_{j1}$$

To consider the model as a linear solver, the nonlinear terms in Eqns. 4.11–4.13 were set to zero. Therefore, $\mathbf{u} = 0$ by Eqn. 4.13. In addition, the expressions for $\cos\beta$ and $\sin\beta$ were redefined using small angle approximations of $\cos\beta = 1$ and $\sin\beta = \partial w/\partial x$. Therefore, from Eqn. 4.15, we can see that $\boldsymbol{\lambda} = -\mathbf{A}^{-1}\boldsymbol{\Psi}^{\boldsymbol{u}}(x_F)F_T(x_F)$ for a linear Beck's Beam problem. Note that in the linear model, λ is a constant and does not depend on x or t, as it does not depend on the deflection w. This is in agreement with and can be further verified through the rigorous mathematical derivations in published literature [43, 60].

4.2.3 Computational Methodology

For each time simulation, the beam was forced in compression with a purely tangential follower force of constant amplitude. The beam was given some small initial deflection in the first mode to displace the beam from the stable or unstable equilibrium point at zero deflection, thus biasing the system and inducing the instability

when above the critical follower force. The response was calculated for a range of time, until a steady state limit cycle was reached or until the beam deflection was sufficiently smaller than the initial displacement and showed a monotonic decrement in amplitude, indicating the response was stable and below the critical follower force.

The beam was defined to have certain material and geometric properties which were held constant for all time simulations. The beam was set to be aluminum with a modulus of elasticity of 69 GPa and a density of 2840 kg/m^3, a length of 0.508 m, a base of 0.0254 m, and a thickness of 0.0015 m.

4.3 Results and Discussion

4.3.1 Linear Model

To verify the model in the linear regime, a range of follower forces were applied to the linear, undamped model to demonstrate agreement with the known critical force of $20.05EI/L^2$. Figure 4.2 illustrates the tip response due to a force amplitude of $20.045EI/L^2$ versus $20.055EI/L^2$ for differing numbers of w modes.

Figure 4.2a shows that for a follower force below the critical force, the solution oscillates but does not decay since there is no damping in the system. (Adding damping will force the system to decay if the forcea applied is below the critical force, but adding damping also rather interestingly changes the critical force substantially. For a damping coefficient $\zeta = 0.01$, the critical force is reduced to $\overline{F} = 16.9EI/L^2$ and the flutter frequency to 10 Hz, as will be discussed in the following section. Note that Bolotin [22, 53] has a particularly nice discussion of the effect of damping.)

For the linear model, the post-critical response is an unbounded oscillation or flutter with a flutter frequency of 14.5 Hz, as seen in Figure 4.2b. Note that while the deflection becomes unphysical beyond an oscillation amplitude of $w/L = 1$, the monotonic increase in amplitudes depicts post-critical behavior. Figure 4.2c illustrates the same unbounded oscillation, but depicts a smaller range of time to

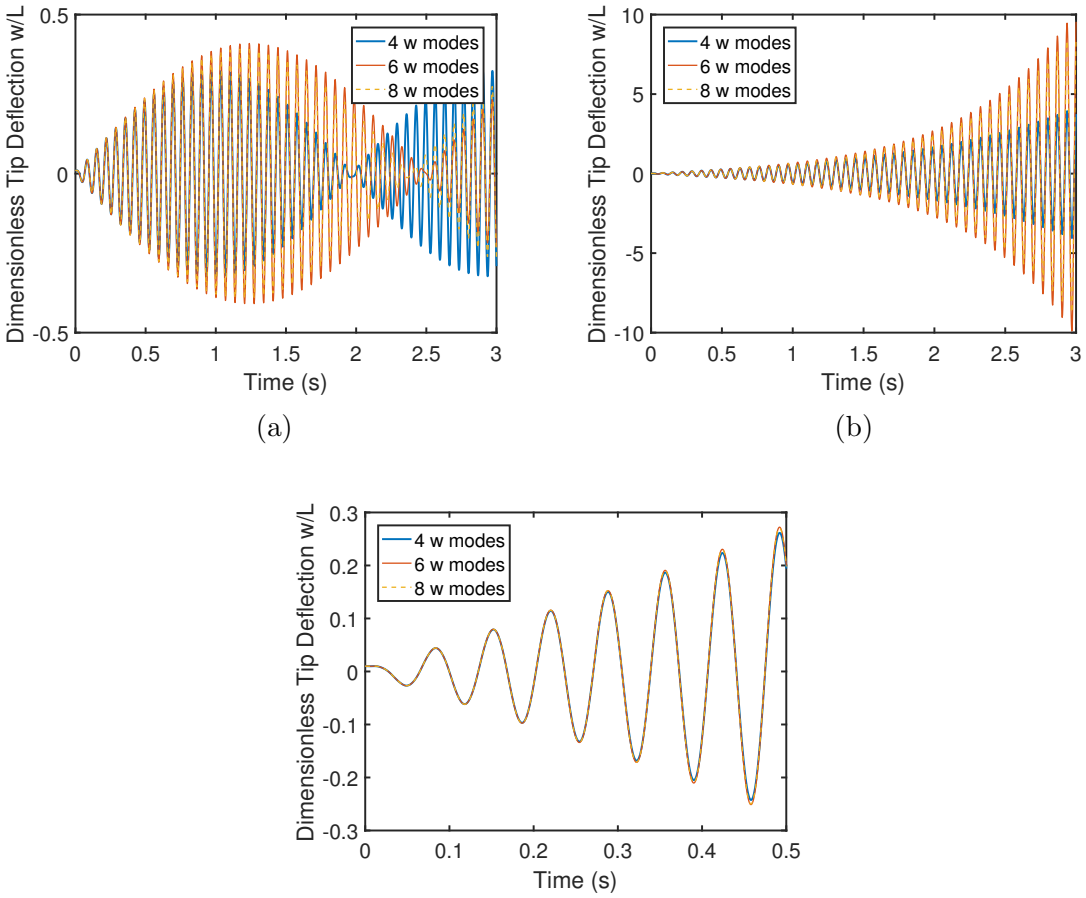

FIGURE 4.2: Time histories for follower force of (a) 20.045 and (b-c) 20.055 EI/L^2. Here (c) is a zoomed in plot of (b)

demonstrate that for reasonable tip amplitudes where the linear approximations are still valid, either 4, 6, or 8 modes yield equivalent results. Modal convergence is further studied in the following section.

4.3.2 Nonlinear Model

The post-critical behavior of the nonlinear model is a bounded limit cycle oscillation, as shown in Figure 4.3. This figure illustrates the response of a typical case. The follower force is $\overline{F} = 20EI/L^2$, damping matrix is a constant diagonal $\boldsymbol{\zeta}_{jj} = 0.01$, and there are 14 λ modes, 14 u modes, and 4 w modes. A time step of $2x10^{-4}$

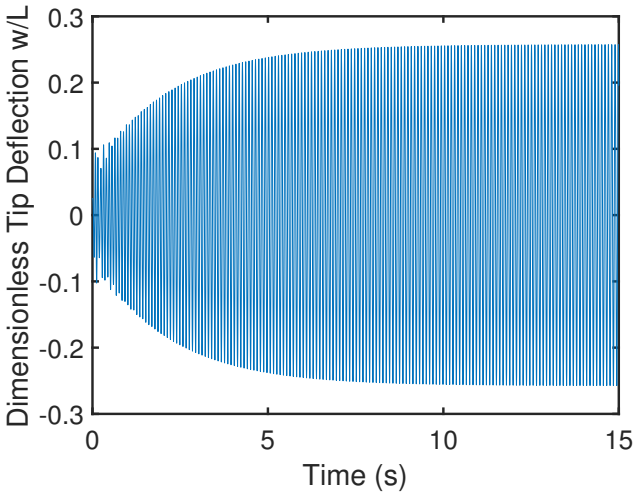

FIGURE 4.3: Limit cycle oscillation: transverse tip deflection versus time

seconds was chosen after initial testing demonstrated that this would capture the behavior of the system appropriately.

Post-critical beam behavior is also investigated by performing an FFT of the limit cycle oscillation. Figure 4.4 illustrates that the oscillation is a coupling of the first and second bending modes as the dominant flutter frequency of 10 Hz falls between the first and second natural frequencies, and was confirmed to be equal to the flutter frequency for the linear damped case at the flutter point. The frequency of the limit cycle oscillation increases modestly as the follower force increases beyond the instability boundary. This indicates that the instability is caused by the first two natural frequencies merging and therefore this behavior can be characterized as merging or coalescing frequency flutter.

The role of damping is briefly explored and the present results agree with published data stating that the critical force decreases with small constant damping $\boldsymbol{\zeta}_{jj}$ [22]. Figure 4.5 illustrates that the critical force $\overline{F}$ is reduced from its undamped value of $\overline{F} = 20.05$ to values closer to $\overline{F} \approx 17$ when the diagonals of the damping matrix are held constant at $\boldsymbol{\zeta}_{jj} = 0.01$. It may be noted that these values are dependent

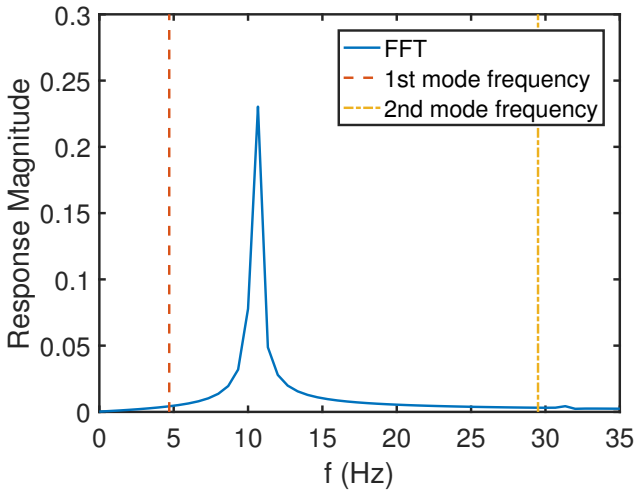

FIGURE 4.4: FFT of post-critical-force limit cycle (w/L) at steady state ($13.5 < t <$ 15 seconds)

on the chosen damping model, and are not universal. In fact, Bolotin [53] showed that with constant $[\boldsymbol{\zeta\omega}]_{jj}$ rather than constant $\boldsymbol{\zeta}_{jj}$, the critical force is equal to the undamped critical force. As a comparison, a case was computed with $[\boldsymbol{\zeta\omega}]_{jj}$ held constant for all modes. The first modal damping coefficient was set to $\zeta_1 = 0.01$. It was determined that for this case the critical force is indeed equal to the undamped case of $\overline{F} = 20.05$, and that the flutter frequency is 14.5 Hz, again equal to the linear undamped flutter frequency. This slight increase in flutter frequency from the constant $\boldsymbol{\zeta}_{jj}$ model is expected as the higher modes are more lightly damped. Further effects of chosen damping models have been presented by Luongo, D'Annibale, and Kirillov [28,61,62]. Additionally, Raviv [19] suggests a nonlinear aerodynamic damping model for this system may be necessary based on experimental results. Although the study of damping is interesting, it is not the primary focus of this dissertation and the constant $\boldsymbol{\zeta}_{jj}$ model is used as representative and typical.

A novelty of the current model is the modal expansion of each component of the deflections u and w as well as the constraint force λ. In this regard, the nonlinear model has more subtleties than the linear model. For the linear case, one may ignore

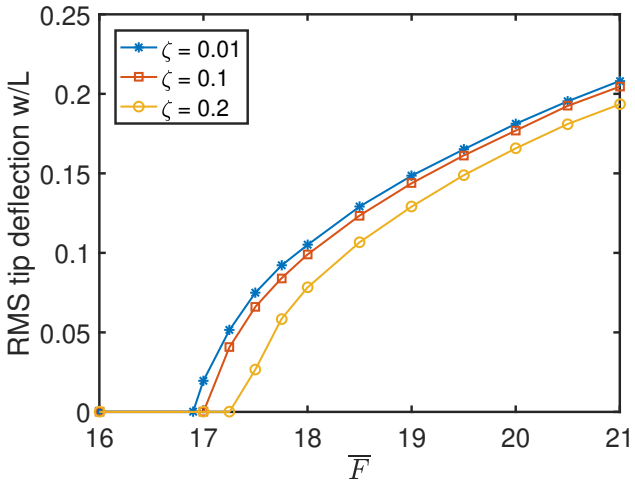

FIGURE 4.5: RMS of transverse tip deflection versus follower force for multiple damping coefficients

the u motion and consider only a single λ mode, because λ does not vary with x (or t). However for the nonlinear model, the values of λ and u are no longer constants, but vary with x and t. Therefore, all three components must demonstrate modal convergence. Figure 4.6 illustrates the modal contributions of each component, all normalized to the maximum modal coefficient. These contributions are generated from the rms of each mode's response for the case illustrated in Figure 4.3.

To further demonstrate modal convergence, Figures 4.7-4.9 illustrate the tip deflection behavior with respect to the number of modes in each generalized coordinate. Figure 4.7 shows the variation of tip deflection with respect to the number of u and λ coordinates. Note the number of u modes must be greater or equal to the number of λ coordinates to avoid an over constrained system. It can be seen that the solution is well converged with 5 modes in u and λ. Note that in Figure 4.6a the last modal coefficient is slightly larger than the previous coefficient. Thus even though the solution is well-converged overall, the highest modal coefficients may not be accurately determined whatever the total number of modes employed in the computation.

Figure 4.8 shows a similar plot but for the number of w modes. Only even numbers

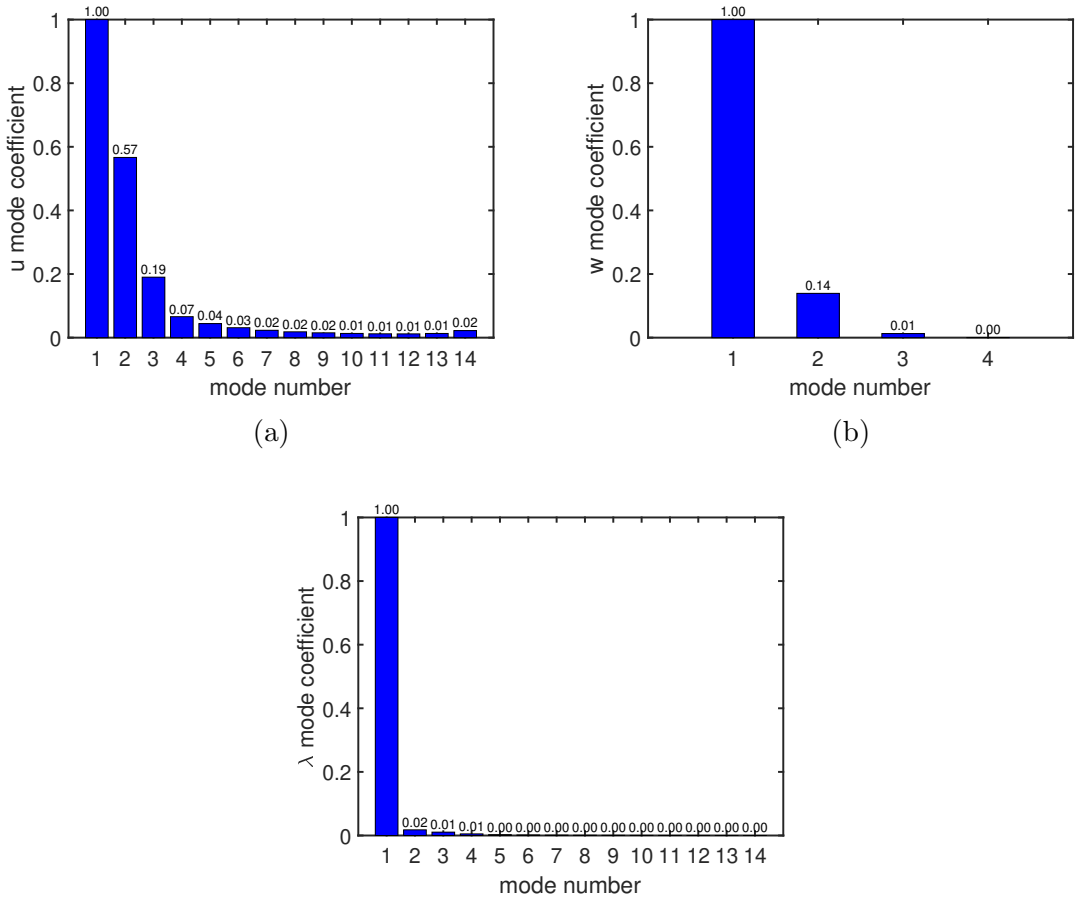

FIGURE 4.6: Modal convergence of (a) u modes, (b) w modes, and (c) λ modes

of modes are considered because the even and odd modes couple and therefore they are best considered in tandem. It is clearly seen that the solution is converged at 4 modes in w.

Figure 4.6c illustrates that λ reaches modal convergence quickly, but it is important to note that the first mode in λ is the rigid body mode. Interestingly, Figure 4.9 shows that if the system is solved with fewer λ modes than u modes—an under-constrained system—the results are acceptable for the response in each component.

To further understand this phenomenon, Figure 4.10 illustrates the manner in which λ relates to the beam deflection as the beam responds to the follower force

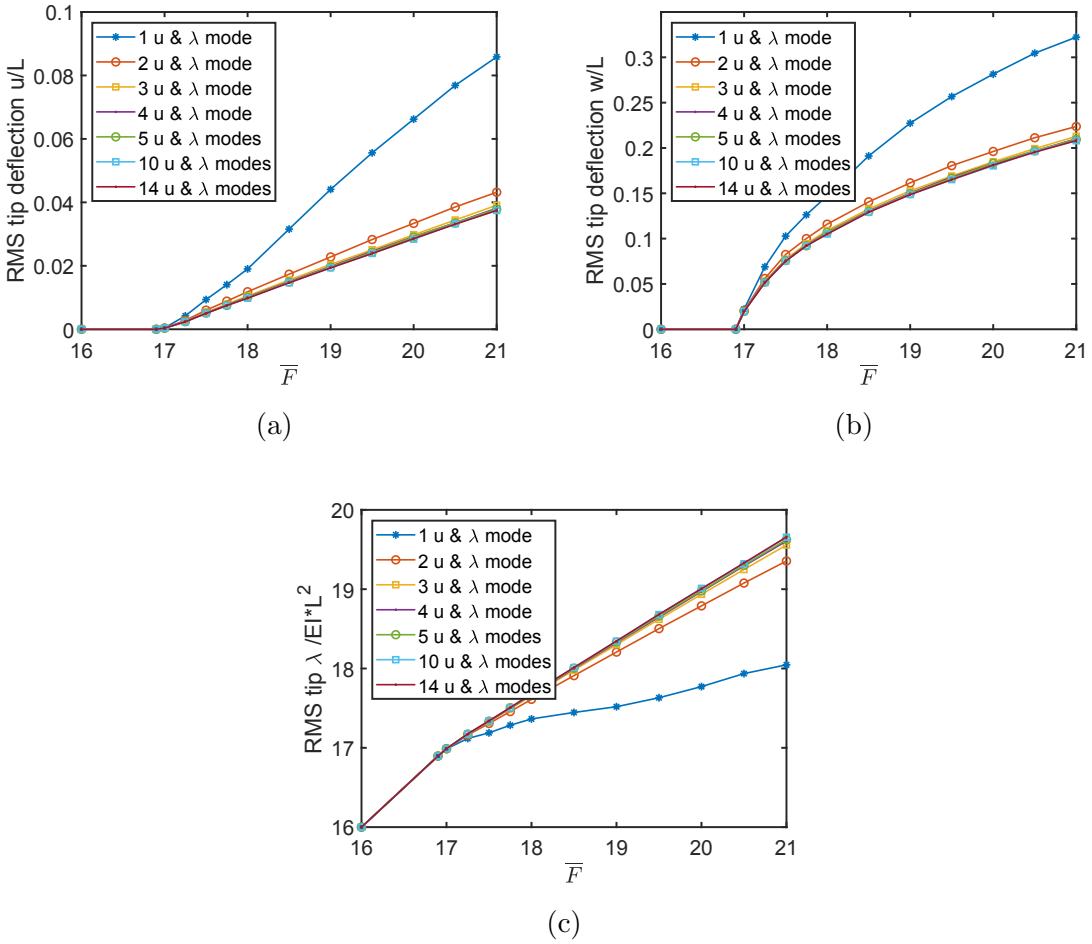

FIGURE 4.7: RMS tip deflection in (a) u and (b) w and (c) λ at tip versus follower force with varying numbers of u and λ modes

case of Figure 4.3. The bold orange curves show the beam deflection (marked on the right axis) and thin blue lines represent λ distribution (marked on the left axis). Three points in time are shown to illustrate how the internal force is related to the beam deflection. Interestingly, when the beam deflection is zero (marked by dotted lines), the distribution of λ is not constant, but at the tip is equivalent to the follower force amplitude. The lines marked by x's show when the internal force is constant. Finally, the solid lines show when the beam is at maximum deflection. Note that for these two deflected cases, the internal force at the tip is equal to the applied force

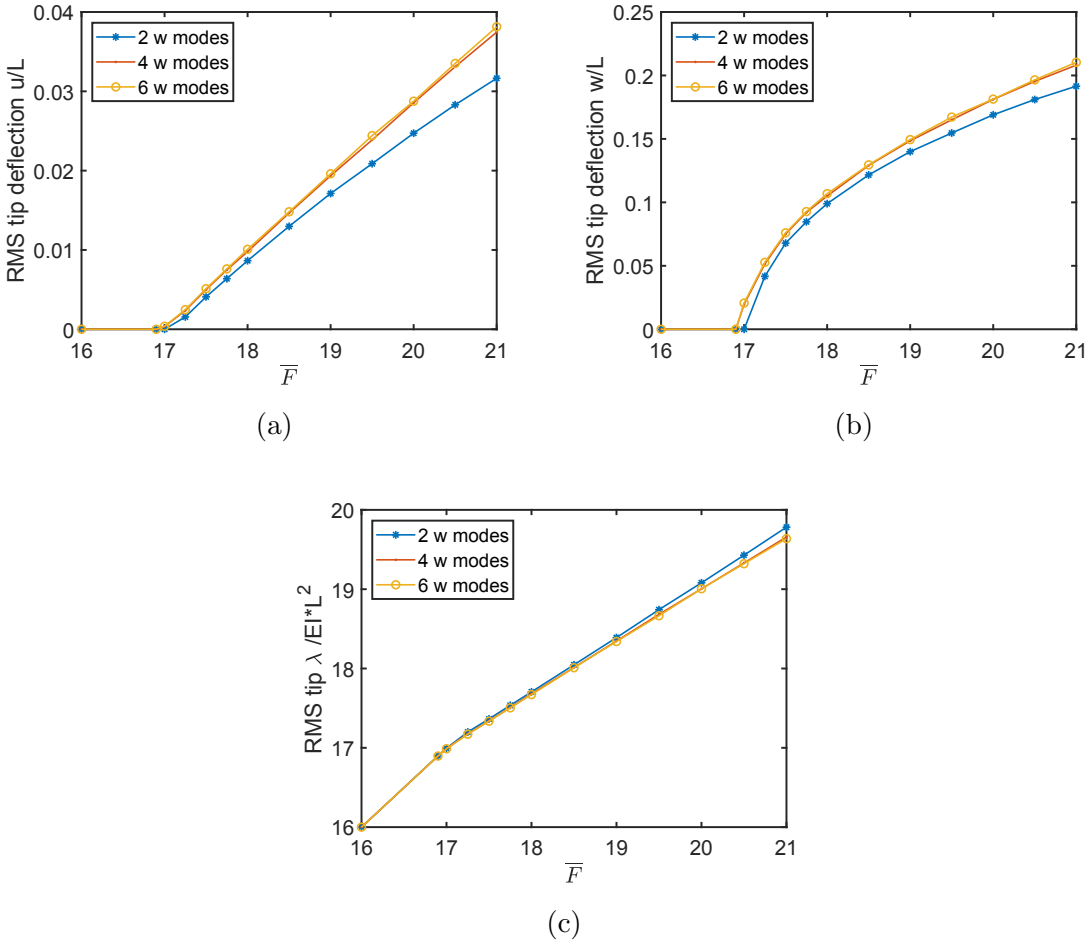

FIGURE 4.8: RMS tip deflection in (a) u and (b) w and (c) λ at tip versus follower force with varying numbers of w modes

scaled by $\cos\beta$ at the tip. Overall, λ is nearly constant and as shown in Fig. 4.9, not many λ modes are needed to capture the LCO behavior, since the first mode is dominant, especially at lower follower force amplitudes.

4.4 Conclusions

A nonconservative follower force has been applied to a contemporary, nonlinear, inextensible cantilever beam model. The governing equations were derived from the Lagrange Equations, and were expanded modally using the Raleigh-Ritz method.

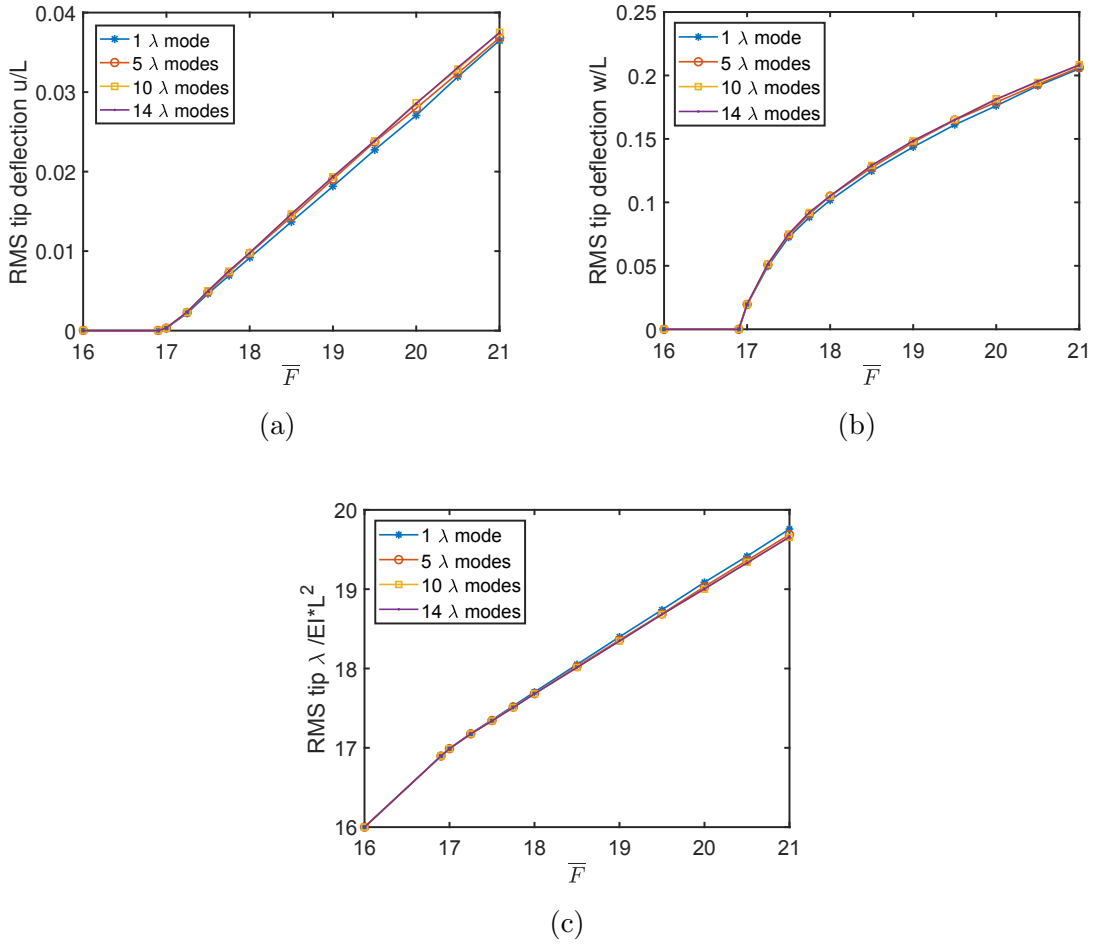

FIGURE 4.9: RMS tip deflection in (a) u and (b) w and (c) λ at tip versus follower force with varying numbers of λ modes

The results show new insight into the post-critical nonlinear characteristics of Beck's beam problem, including the behavior of the constraint force acting to relate transverse and longitudinal deflections.

The critical follower force was determined via a 4th order Runge-Kutta time-marching solver to be the same as that previously published. The results from two commonly used linear damping models were compared. It was found that one damping model decreased the critical follower force substantially, while the other did not.

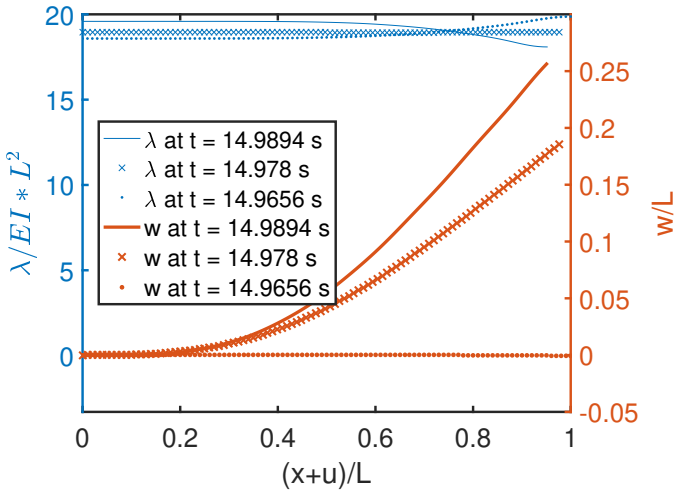

FIGURE 4.10: Distribution of λ values across beam at corresponding beam deflections

Post-critical nonlinear behavior was analyzed and it was shown to be a limit cycle oscillation due to a merging frequency flutter mechanism as indicated by the coupling of the first and second bending modes.

The constraint force that enforces inextensibility was analyzed and shown to be correlated to the applied follower force scaled by the angle of the tip during the limit cycle oscillations. It was shown that the modal series of λ converged rather quickly and the number of λ modes can be few to compute accurately the limit cycle amplitude in either u or w.

5

Nonlinear Response of an Inextensible, Free-Free Beam Subjected to a Nonconservative Follower Force

5.1 Introduction

Following the work of the previous chapter, we offer the same treatment of the follower force to the free-free beam. This chapter was originally published in ASME's Journal of Computational and Nonlinear Dynamics [47].

As we extend the inextensible beam model to free-free boundary conditions, there are fewer validating comparisons to be made. However, one comparison we may make is to a series of classic studies [31, 63] which investigate the stability of missiles and rockets subjected to a thrust force at one end. Beal [31] concluded via a linear eigenvalue analysis that a normalized follower force amplitude of $FL^2/EI = 109.9$ would force the rocket to become unstable. Here we show that our model produces equivalent results for this critical force, and we show the dynamics of the limit cycle oscillations (LCO) beyond the critical force.

In this chapter, a full derivation of the equations of motion of a free-free beam

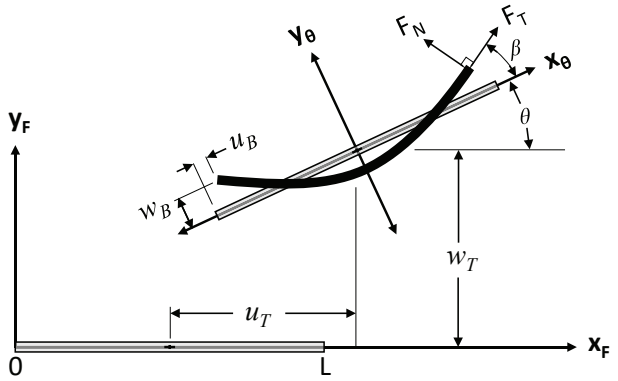

FIGURE 5.1: Schematic illustrating the coordinate transform from fixed Cartesian coordinate axes to translated beam axis

is derived including two rigid body translational modes and a rigid body rotational mode. The schematic for the system is shown in Fig. 5.1. The equations of motion include external forces such as vertical, horizontal, or follower forces which remain tangent or normal to the beam at a specified point. The transverse and longitudinal bending deformations are coupled via a Lagrange multiplier and a constraint function which enforces inextensibility.

Results agree with classical stability bounds and show that the system exhibits LCO behavior above a critical force. Modal convergence in all three coordinates is explored. A range of forcing values is applied and, at high forcing, a second bifurcation is discovered.

5.2 Equations of Motion

The equations of motion are derived from the Euler-Lagrange equations, where the kinetic and potential energies as well as the work done by the constraint are written in terms of longitudinal deflection u, transverse deflection w, rotational angle θ and Lagrange multiplier λ. Each component u, w, and λ is modally expanded into the respective linear eigenmodes in accordance with the boundary conditions. A full derivation is given in the Appendix, but presented here are the final equations

of motion. The equations are as follows: (5.1) rigid body rotation, (5.2) longitudinal bending, (5.3) transverse bending, (5.4) transverse rigid body translation, (5.5) longitudinal rigid body translation, and (5.6) the constraint equation. It should be noted that the rigid body translations in both u and w are fully decoupled from the other equations, and therefore they do not impact the bifurcation point or the LCO amplitude, and so for this study they are not included in the analysis. Note also that the equations are fully dimensional, where m is the mass per unit length of the beam, L is the length of the beam, and the single and double overdot notation represents first and second time derivatives, respectfully.

$$
\begin{aligned}
0 =& mL^3\Big(\frac{1}{12}\ddot{\theta} + \ddot{\theta}\{\mathbf{M_u u}\}^T\mathbf{u} + 2\dot{\theta}\{\mathbf{M_u}\dot{\mathbf{u}}\}^T\mathbf{u} + \ddot{\theta}\{\mathbf{M_w w}\}^T\mathbf{w} \\
&+ 2\dot{\theta}\{\mathbf{M_w}\dot{\mathbf{w}}\}^T\mathbf{w} + 2\ddot{\theta}\mathbf{H}^T\mathbf{u} + 2\dot{\theta}\mathbf{H}^T\dot{\mathbf{u}} + \{\mathbf{G}\ddot{\mathbf{w}}\}^T\mathbf{u} - \{\mathbf{Gw}\}^T\ddot{\mathbf{u}}\Big) \\
&- LF_y\big((\tilde{x}(x_F) + \mathbf{\Psi}_{\boldsymbol{u}}^T(x_F)\mathbf{u})\cos\theta - \mathbf{\Psi}_{\boldsymbol{w}}^T(x_F)\mathbf{w}\sin\theta\big) \\
&+ LF_x\big((\tilde{x}(x_F) + \mathbf{\Psi}_{\boldsymbol{u}}^T(x_F)\mathbf{u})\sin\theta + \mathbf{\Psi}_{\boldsymbol{w}}^T(x_F)\mathbf{w}\cos\theta\big) \\
&- L\Big(F_T(x_F)\big((\tilde{x}(x_F) + \mathbf{\Psi}_{\boldsymbol{u}}(x_F)\boldsymbol{u})\sin\beta(x_F) - \mathbf{\Psi}_{\boldsymbol{w}}(x_F)\boldsymbol{w}\cos\beta(x_F)\big) \\
&+ F_N(x_F)\big((\tilde{x}(x_F) + \mathbf{\Psi}_{\boldsymbol{u}}(x_F)\boldsymbol{u})\cos\beta(x_F) + \mathbf{\Psi}_{\boldsymbol{w}}(x_F)\boldsymbol{w}\sin\beta(x_F)\big)\Big) \qquad (5.1) \\
0 =& mL^2\mathbf{M_u}\ddot{\mathbf{u}} - mL^2\ddot{\theta}\mathbf{Gw} - 2mL^2\dot{\theta}\mathbf{G}\dot{\mathbf{w}} - mL^2\dot{\theta}^2\mathbf{M_u u} - mL^2\dot{\theta}^2\mathbf{H} - \mathbf{A}\lambda \\
&- \big(F_y(x_F)\sin\theta + F_x(x_F)\cos\theta \\
&+ F_T(x_F)\cos\beta(x_F) - F_N(x_F)\sin\beta(x_F)\big)\mathbf{\Psi}_{\boldsymbol{u}}(x_F) \qquad (5.2) \\
0 =& mL^2\mathbf{M_w}\ddot{\mathbf{w}} + 2mL^2\boldsymbol{\xi\omega}\mathbf{M_w}\dot{\mathbf{w}} + mL^2\boldsymbol{\omega^2}\mathbf{M_w w} \\
&+ L^{-2}EI\{\mathbf{Pwww}\} - [\mathbf{B}\boldsymbol{\lambda}]\mathbf{w} \\
&+ mL^2\ddot{\theta}\mathbf{G^T u} + 2mL^2\dot{\theta}\mathbf{G^T}\dot{\mathbf{u}} - mL^2\dot{\theta}^2\mathbf{M_w w} \\
&- \big(F_y(x_F)\cos\theta - F_x(x_F)\sin\theta \\
&+ F_T(x_F)\sin\beta(x_F) + F_N(x_F)\cos\beta(x_F)\big)\mathbf{\Psi}_{\boldsymbol{w}}(x_F) \qquad (5.3) \\
0 =& mL^2\ddot{\mathbf{w}}_{\mathbf{T}} - F_y(x_F) - F_T(x_F)(\cos\beta(x_F)\sin\theta + \sin\beta(x_F)\cos\theta) \\
&- F_N(x_F)(\cos\beta(x_F)\cos\theta - \sin\beta(x_F)\sin\theta) \qquad (5.4) \\
0 =& mL^2\ddot{\mathbf{u}}_{\mathbf{T}} - F_x(x_F) - F_T(x_F)(\cos\beta(x_F)\cos\theta - \sin\beta(x_F)\sin\theta) \\
&+ F_N(x_F)(\sin\beta(x_F)\cos\theta + \cos\beta(x_F)\sin\theta) \qquad (5.5) \\
0 =& \mathbf{Au} + \frac{1}{2}[\mathbf{Bw}]\mathbf{w} \qquad (5.6)
\end{aligned}
$$

Equations 5.1-5.6 are solved by isolating an equation for $\ddot{\theta}$ and an equation for $\ddot{\mathbf{w}}$ and solving each of these simultaneously with a Runge-Kutta solver.

5.3 Results and Discussion

5.3.1 Replicating Classical Results

For the purpose of comparing the current nonlinear model to the linear analysis, it is useful to show Beal's [31] eigenvalue results. The analysis completed by Beal was repeated to find the normalized natural frequencies $\overline{\omega}$ as a function of the follower

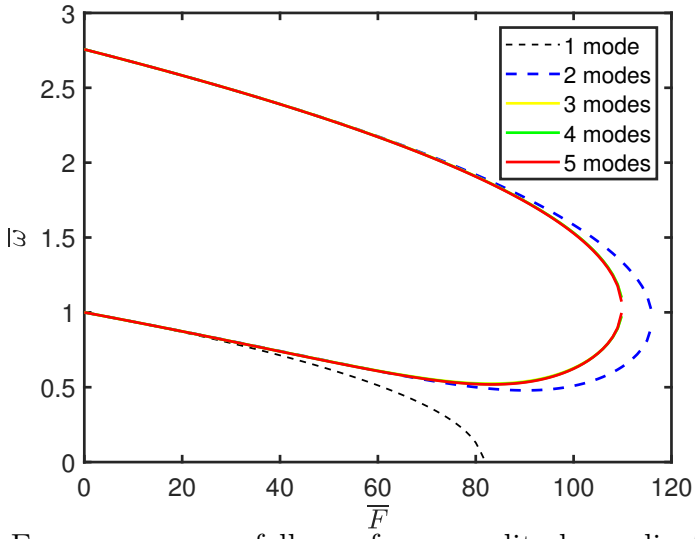

FIGURE 5.2: Frequency versus follower force amplitude, replicated from Beal

force $\overline{F}$ for various numbers of modes included. These stability envelopes are replicated in Fig. 5.2. As Beal showed, a 1 mode analysis results in an instability at $\overline{F} = 81.4$, and a 2 mode analysis becomes unstable at $\overline{F} = 116$. Indeed, there is no visible distinction between 3, 4, or 5 modes which all become unstable at $\overline{F} = 109.9$. In this document, we show nearly equivalent bifurcation points with our nonlinear model, and also show limit cycle oscillation (LCO) behavior beyond what this linear method can predict. We will investigate the modal convergence of each coordinate u, w, and λ.

5.3.2 Bifurcation Diagrams and Modal Convergence

Initial test cases were run by solving the equations of motion with 15 u modes, 15 λ modes, and a range of w modes. The damping model is that $\zeta\omega$ is constant throughout all w modes. The physical parameters of the beam are $L = 0.508$m, $b = 0.0254$m, $h = 0.0015$m, $E = 69$GPa (aluminum), and $m = 2840\text{kg/m}^3$.

A plot of follower force amplitude versus root mean square (RMS) of the beam's tip displacement for 1 through 9 w modes is shown in Fig. 5.3. This illustrates agreement with Beal [31] and Fig. 5.2.

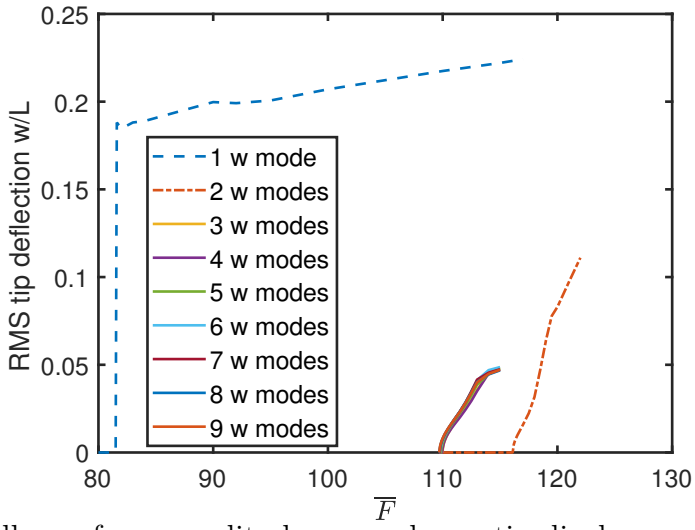

FIGURE 5.3: Follower force amplitude versus beam tip displacement for range of w modes

To better understand the role of the number of w modes, a zoomed in plot is shown in Fig. 5.4. Here, up to 9 modes are shown and it is seen that all cases are near the expected bifurcation value of $\overline{F} = 109.9$, with actual bifurcation points ranging from $\overline{F} = 109.7$ to 109.95. Beal concluded modal convergence based on percent difference of critical force between N number of modes versus N-1. A difference of less than 0.1% was considered converged. At 7 modes, $\overline{F}$ is 0.04% different than at 6 modes, hence we can say that 7 w modes are needed for convergence. However, Fig. 5.5 shows the convergence plots for various numbers of w modes calculated, all of which show that there is very little influence from modes higher than 3. This difference is interesting and it is worth noting that we have made a conclusion on convergence as Beal defined it, rather than basing convergence on Fig. 5.5. It is also interesting to note that with increasing modes, the bifurcation forcing level is reduced slightly.

The influence of the number of λ modes is shown in Fig. 5.6, which plots follower force versus beam tip displacement for a range of λ modes used in the calculation. Note that for this plot, all cases were run with 15 modes in the u deflection. The need for a significant number of λ modes compared to w modes is interesting, since

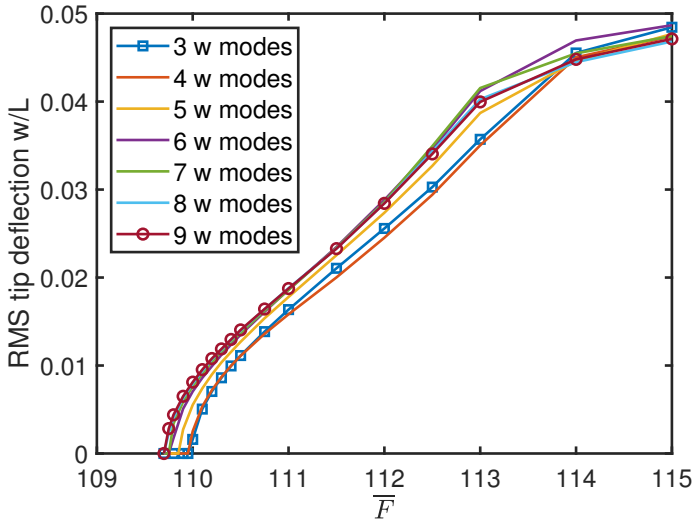

FIGURE 5.4: Follower force amplitude versus beam tip displacement for range of w modes

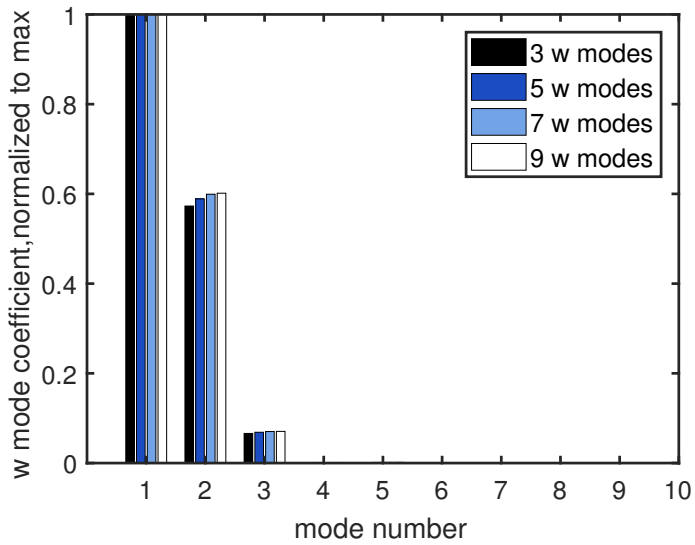

FIGURE 5.5: Modal convergence comparison for range of w modes at $\overline{F} = 111$, 20 u and 20 λ modes

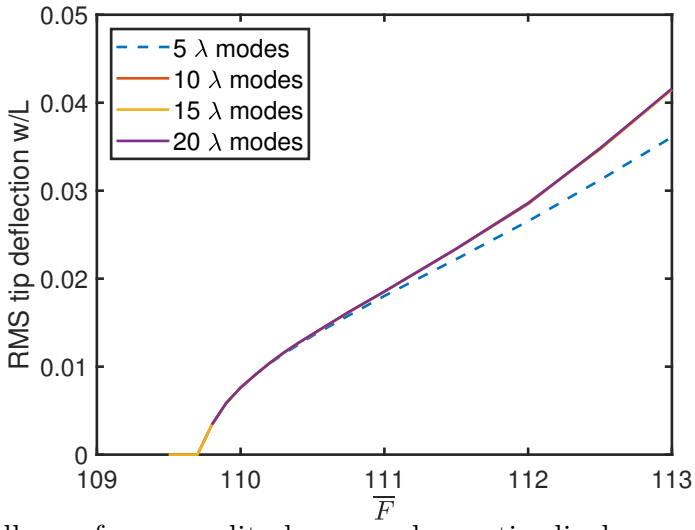

FIGURE 5.6: Follower force amplitude versus beam tip displacement for range of λ modes

λ itself is nearly linear and heavily weighted by its first mode. This is likely due to its coupling with u, which will be discussed next. Note also that it has been reported for a cantilever with a follower force that the number of λ modes had relatively little influence on the solution [46].

To demonstrate the influence of the number of u modes, Fig. 5.7 shows the tip deflection versus force for a range of u modes used. Note that the number of λ modes must be equal or less than the number of u modes, so the number of λ modes is set to be equal to the number of u modes for this plot. Also, this was generated for 7 w modes. There are a few interesting conclusions from Fig. 5.7. First, the need for a large number of u modes may be explained by a local failure in the modal summation at the endpoints of the beam. The mode shapes for the u deflection are the classical linear mode shapes which have zero slope at the endpoints, reflecting zero strain. However, the modes for w have nonzero slopes at the endpoints, and since the constraint equation states the slopes of u are related to the slopes of w, this is a contradiction. Therefore, the modal solution for u converges very slowly. By increasing the mode count, the region of the beam for which the solution is converging

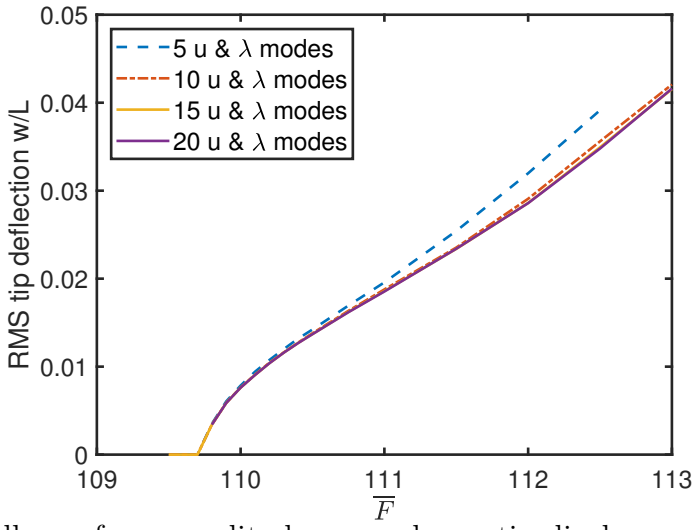

FIGURE 5.7: Follower force amplitude versus beam tip displacement for range of u and λ modes

increases while the region of the local failures near the endpoints decreases.

It is interesting that Fig. 5.7 and Fig. 5.6 show that neither the number of u modes nor λ modes affects the bifurcation point. Both plots show that 10 modes in each coordinate are probably sufficient, but 15 are used herein, since the computational efficiency is more dependent on the number of w modes than the number of u or λ modes.

Figure 5.8 illustrates the bifurcation of both u and w components and the percent difference between the constraint force at the tip of the beam and the follower force amplitude applied there. For this case, 7 w modes and 15 u and λ modes are calculated. This figure demonstrates a potential limitation of the model at high forcing values, as it can be seen that there is a growing deficit of $\overline{\lambda}$ as the forcing value increases. Ideally, at the forced tip, $\overline{\lambda}$ would be equal to $\overline{F}$. We have demonstrated irregularities at high forcing values, and this effect may be influencing this behavior.

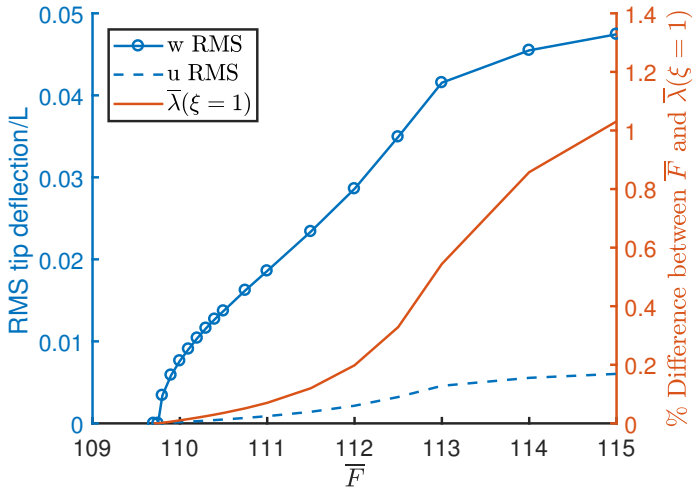

FIGURE 5.8: Bifurcation of u and w on left axis, percent difference between $\overline{F}$ and $\overline{\lambda}$ on right axis

5.3.3 Specific Case Study: $\overline{F} = 111$

To evaluate the limit cycle oscillation and the components of the model in a more detailed manner, this section presents results from the typical post-flutter case of $\overline{F} = 111$, using 7 w modes and 15 u and λ modes. Figures 5.9 and 5.10 show the time history of the forced beam tip and the FFT of the steady state solution. These plots illustrate the LCO behavior, and demonstrate that the LCO is occurring at a frequency between the first and second natural frequencies, albeit very close to the first. Thus, the first mode is prominent here. This result is in agreement with Beal's eigenvalue result, as it can be seen from Fig. 5.2 that the frequency at which the two modes coalesce is slightly larger than the first linear unforced natural frequency.

To illustrate how the constraint force λ acts throughout the beam, Fig. 5.11 shows λ versus beam position at ten points in time throughout one period of oscillation. Note that this is a nearly linear function from zero to $\overline{F}$ just as Beal [31] approximated, and that over time λ remains essentially constant. However, there is a very slight divergence from linear behavior at the beam tip, indicating that higher modes are present.

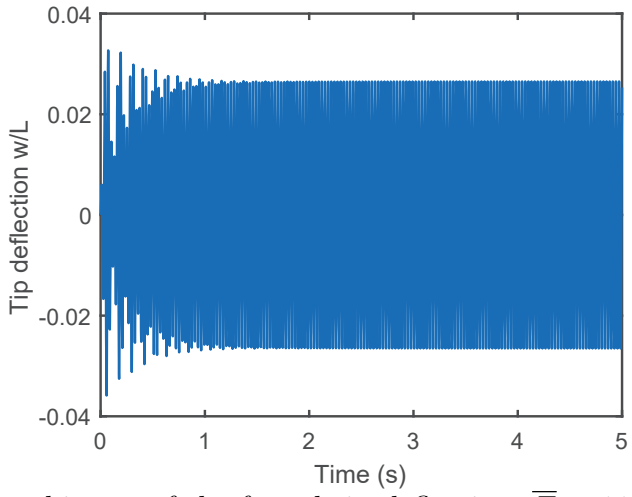

FIGURE 5.9: Time history of the forced tip deflection, $\overline{F} = 111$, 7 w modes and 20 u and λ modes

Figure 5.12 illustrates the behavior of all three components at one instant in time, when the deflection is at a maximum. This plot illustrates how the beam deflects in w especially. Upon careful inspection, it can be seen that the deflection in u has higher modal content, which can be attributed to the local failure at the endpoints in u as discussed above.

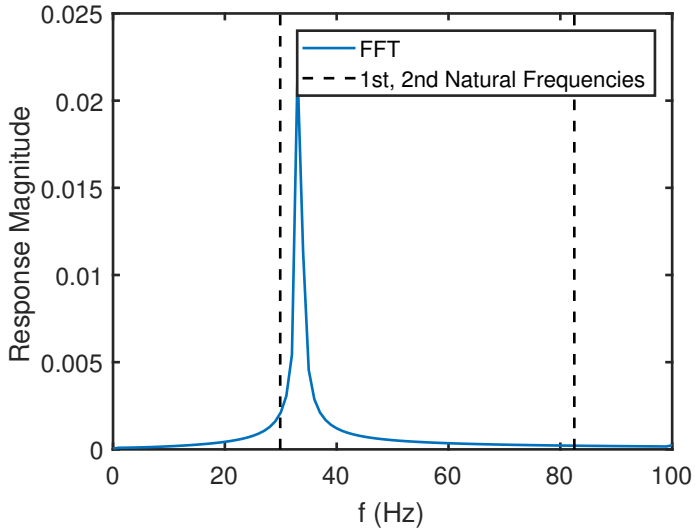

FIGURE 5.10: Fast Fourier Transform of the steady state results from Fig. 5.9

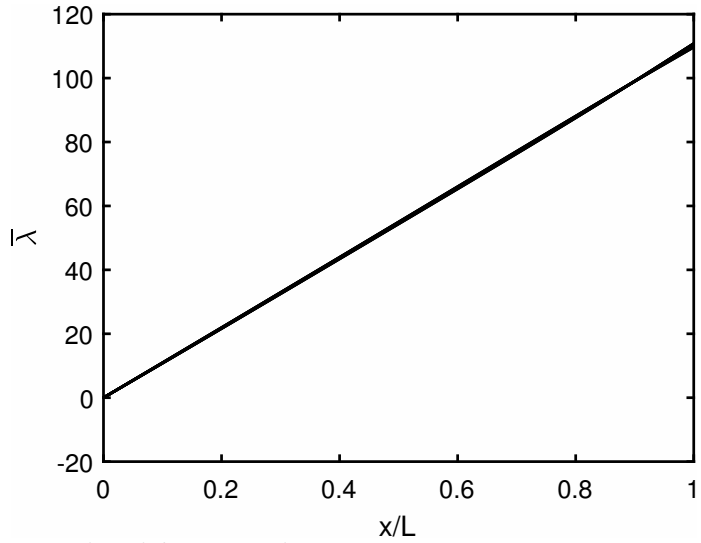

FIGURE 5.11: Normalized λ versus beam position at various times over one period

5.3.4 High Forcing Level Numerical Instability

For all computations with multiple modes included, there exists an instability beyond the initial bifurcation, initially indicated by a rapid increase in RMS values beyond $\overline{F} = 116$ seen in Fig. 5.13. To understand this phenomenon and to determine if it is a physical behavior or a numerical artifact, two trial cases of 7 w modes at $\overline{F} = 117$

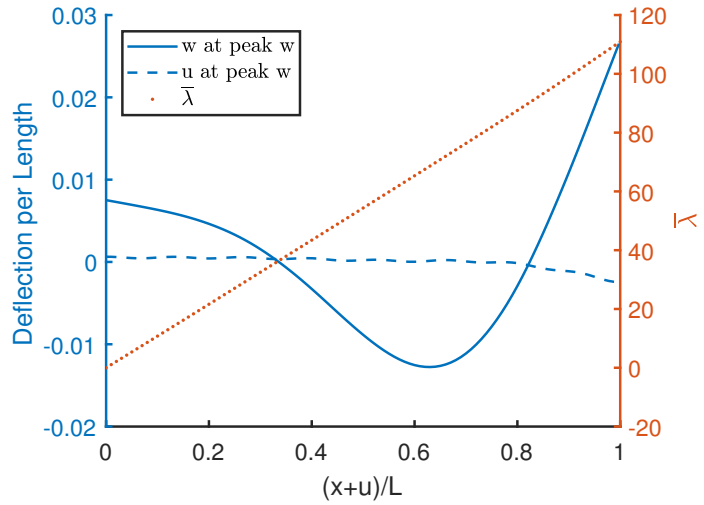

FIGURE 5.12: All three components, u, w, λ, plotted versus beam position for one instant in time. Left axis is deflection normalized to beam length and right axis is normalized λ

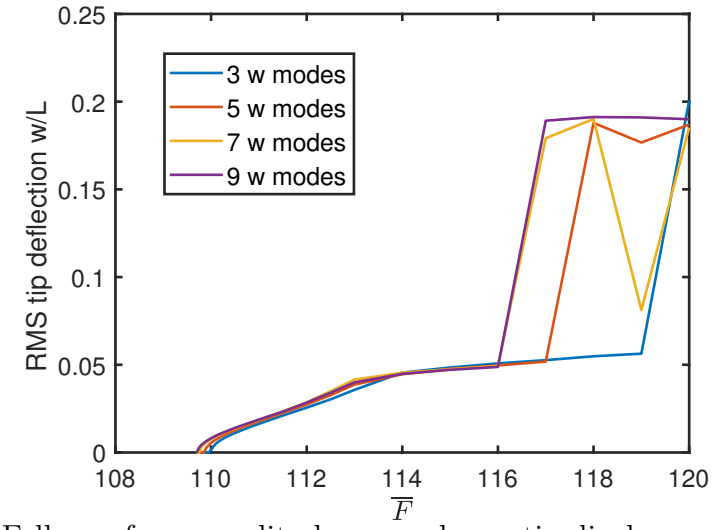

FIGURE 5.13: Follower force amplitude versus beam tip displacement for a range of w modes, illustrating numerical instability at high forcing levels

and 119 were inspected over long times. The time histories are shown in Fig. 5.14, and reveal that the system experiences a transition to chaos via intermittency [64]. Note that each time history shows two quasisteady limit cycle amplitudes. In Fig. 5.14a, the small LCO amplitude exists at the beginning of the simulation and again just after 60 seconds before returning to the larger amplitude. In Fig. 5.14b, the transition between amplitudes is clearly seen between 4 and 10 seconds.

To further understand this chaotic behavior, several FFTs were calculated at various time intervals for the $\overline{F} = 119$ case: $0 \leq t \leq 0.15$s during the small startup transient, $2 \leq t \leq 3$s when the LCO is large, $4 \leq t \leq 4.3$s when the behavior is transient and the amplitude is rising, and $5 \leq t \leq 6$s when the LCO is back to its lower level. This process is documented in Fig. 5.15. It is especially interesting to note the difference between Figs. 5.15 b and c versus a and d. That is, when the amplitude is small, the frequencies are more spread out, and when the amplitudes are large, the frequencies are heavily localised just below the first natural frequency.

Again by carefully selecting time intervals which bound these two response levels, we calculate the RMS of the response at each limit cycle amplitude. Repeating for

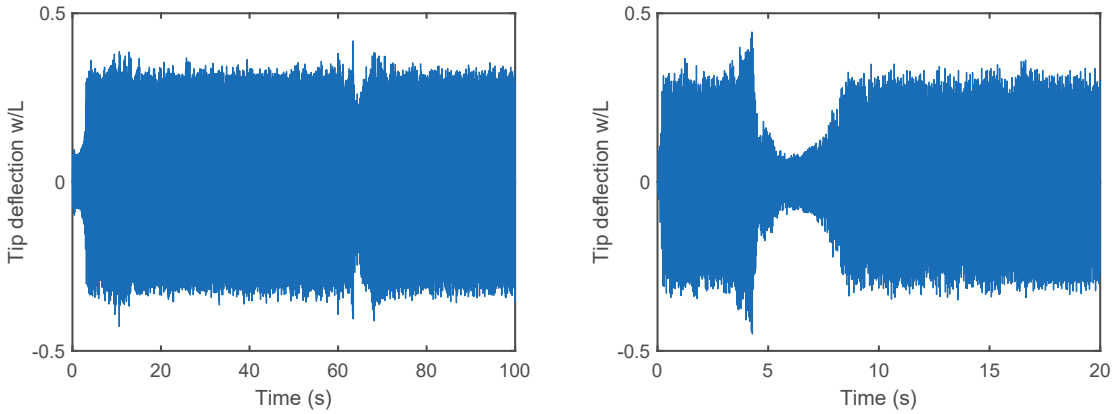

(a) $\overline{F} = 117$ (b) $\overline{F} = 119$

FIGURE 5.14: Time history of forced beam tip deflection with 7 w and 15 u and λ modes

each forcing level computation, we can generate an amended bifurcation plot, Fig. 5.16. Here the previously plotted calculations with 1 w mode and 7 w modes are shown for comparison, and the black stars indicate the intermittent limit cycle amplitudes. It can be seen that the lower limit cycle amplitude continues the expected trend of the 7 mode computations. However, there is a definitive upper limit cycle oscillation near the 1 mode RMS curve. In addition, there is also a more elusive third response value between these two limits which exists for some forcing levels but not others. We can use these points to generate an approximate bifurcation curve, Fig. 5.17.

5.4 Conclusions

Here we have shown the derivation of the equations of motion and the planar responses of the inextensible, nonlinear, free-free beam to a nonconservative follower force. Beginning with the Lagrange Equations including a Lagrange multiplier to enforce the inextensibility constraint, the equations of motion including rigid body rotation and translation were derived. A nonconservative follower force was added

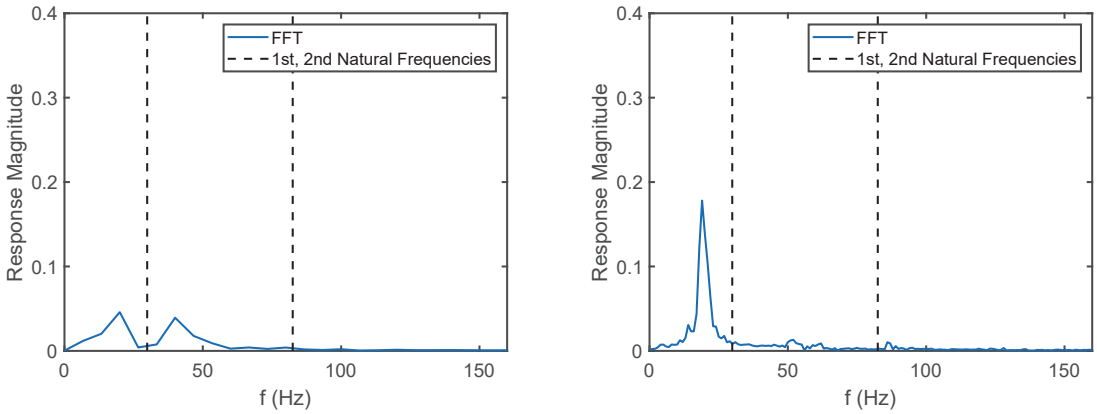

(a) $0 \leq t \leq 0.15s$

(b) $2 \leq t \leq 3s$

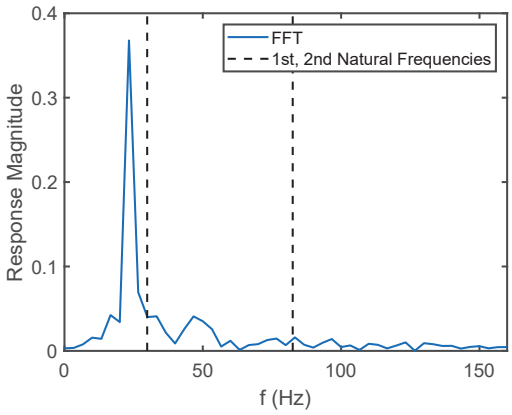

(c) $4 \leq t \leq 4.3s$

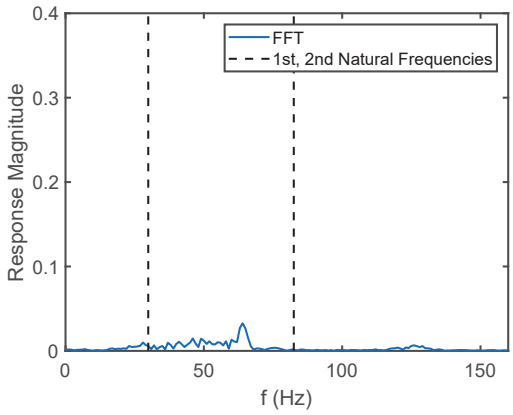

(d) $5 \leq t \leq 6s$

FIGURE 5.15: FFTs of response shown in Figure 5.14b at varying time intervals

to the equations of motion, and it was shown that the rigid body translation is fully decoupled from the forced response problem. The current numerical model produced nearly equivalent results to the classical eigenvalue approach. The results indicated a limit cycle oscillation: a supercritical pitchfork bifurcation to a steady state nonlinear oscillation as represented by a RMS response as a function of follower force amplitude. All three components of the response—axial, transverse deflection and Lagrange multiplier force (u, w, and λ)—were analyzed for modal convergence and it was determined that the model was highly dependent on u and λ modes; 15

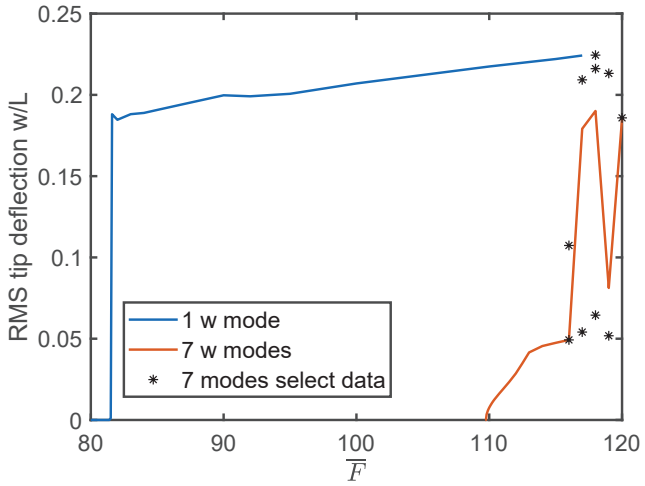

FIGURE 5.16: Bifurcation diagram including RMS responses calculated at select data intervals

were used in the calculations presented here while only 7 w modes were necessary for modal convergence. A second instability was discovered and analyzed for high forcing amplitudes.

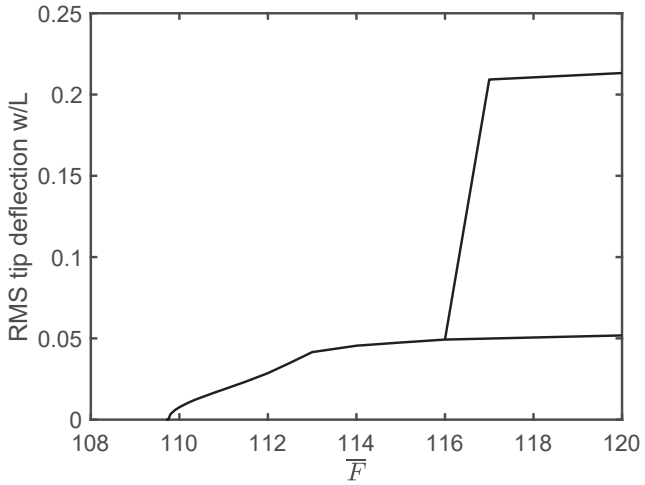

FIGURE 5.17: Bifurcation diagram illustrating the initial loss of stability at $\overline{F} = 109.8$ and the transition to chaos at $\overline{F} = 116$

5.5 Appendix: Derivation of Equations of Motion

5.5.1 Introduction to Energy Methods

The equations of motion are derived from the Euler-Lagrange equations,

$$\frac{\partial}{\partial t}\Big(\frac{\partial \mathcal{L}}{\partial \dot{q}_i}\Big) - \frac{\partial \mathcal{L}}{\partial q_i} = Q_i \tag{5.7}$$

where the generalized coordinates q_i are for the spatial coordinates u and w and also for the Lagrange multiplier λ. The Lagrangian including the work done by the constraint force is as follows.

$$\mathcal{L} = T - V + \int_0^L \lambda f \; dx \tag{5.8}$$

The kinetic and potential energy as well as the constraint f, respectively, are [8, 43, 44, 65]:

$$T = \frac{1}{2}\int_0^L m[\dot{u}^2 + \dot{w}^2] \; dx \tag{5.9}$$

$$V = \frac{1}{2}\int_0^L EI\Big(\frac{\partial^2 w_B}{\partial x^2}\Big)^2\left[1 + \Big(\frac{\partial w_B}{\partial x}\Big)^2\right] dx \tag{5.10}$$

$$f = \frac{\partial u_B}{\partial x} + \frac{1}{2}\Big(\frac{\partial w_B}{\partial x}\Big)^2 = 0 \tag{5.11}$$

where u and w are now comprised of the bending, rotating, and translating modes as shown in Fig. 5.1.

$$u = u_T + \tilde{x}(\cos\theta - 1) + u_B\cos\theta - w_B\sin\theta \tag{5.12}$$

$$w = w_T + (\tilde{x} + u_B)\sin\theta + w_B\cos\theta \tag{5.13}$$

Here $\tilde{x}$ is used to simplify the algebra while shifting the center of the beam to the axis origin.

$$\tilde{x} = x - L/2 \tag{5.14}$$

The expression for kinetic energy is as follows.

$$\begin{aligned} T = \frac{1}{2}\int_0^L m\Big(&\tilde{x}^2\dot{\theta}^2 + u_B^2\dot{\theta}^2 + w_B^2\dot{\theta}^2 + \dot{u}_B^2 + \dot{w}_B^2 + \dot{w}_T^2 + \dot{u}_T^2 \\ &+ 2\tilde{x}u_B\dot{\theta}^2 + 2\tilde{x}\dot{\theta}\dot{w}_B + 2u_B\dot{\theta}\dot{w}_B - 2w_B\dot{\theta}\dot{u}_B + 2\tilde{x}\cos\theta\dot{w}_T\dot{\theta} \\ &- 2w_B\cos\theta\dot{u}_T\dot{\theta} - 2\tilde{x}\sin\theta\dot{u}_T\dot{\theta} - 2u_B\sin\theta\dot{u}_T\dot{\theta} - 2\dot{w}_B\sin\theta\dot{u}_T + 2\dot{u}_B\cos\theta\dot{u}_T \\ &+ 2\dot{u}_B\dot{w}_T\sin\theta + 2u_B\dot{w}_T\dot{\theta}\cos\theta + 2\dot{w}_B\dot{w}_T\cos\theta - 2w_B\dot{w}_T\dot{\theta}\sin\theta\Big)\,dx \end{aligned} \tag{5.15}$$

5.5.2 Modally Expanded Expressions

The expressions for u_B, w_B, and λ are modally expanded and the Rayleigh-Ritz approach is used to derive the equations of motion.

$$u_B = \sum_i \Psi_i^u(x)u_i(t) \tag{5.16}$$

$$w_B = \sum_j \Psi_j^w(x)w_j(t) \tag{5.17}$$

$$\lambda = \sum_k \Psi_k^\lambda(x)\lambda_k(t) \tag{5.18}$$

Where Ψ_i^u, Ψ_j^w, and Ψ_k^λ are mode shapes of u_B, w_B, and λ respectively, defined below. Note that λ is defined with the pinned-free modes and has a rigid body mode.

$$\Psi_i^u = \cos(i\pi x/L) \quad \text{for i = 1,2,...,N} \tag{5.19}$$

$$\Psi_j^w = \cosh(\beta_w(j)x) + \cos(\beta_w(j)x) - R_w(j)\sin(\beta_w(j)x) - R_w(j)\sinh(\beta_w(j)x)$$
$$\text{for j = 1,2,...,N} \tag{5.20}$$

$$\Psi_k^\lambda = \begin{cases} x & \text{for k = 0} \\ \cosh(\beta_\lambda(k)(1-x)) + \cos(\beta_\lambda(k)(1-x)) & \\ -R_\lambda(k)\sin(\beta_\lambda(k)(1-x)) & \\ -R_\lambda(k)\sinh(\beta_\lambda(k)(1-x)) & \text{for k = 1,2,...,N} \end{cases} \tag{5.21}$$

Where

$$1 = \cosh(\beta_w(j))\cos(\beta_w(j)) \tag{5.22}$$

$$R_w(j) = \frac{\cosh(\beta_w(j)) - \cos(\beta_w(j))}{\sinh(\beta_w(j)) - \sin(\beta_w(j))} \tag{5.23}$$

$$\sin(\beta_\lambda(k))\cosh(\beta_\lambda(k)) = \sinh(\beta_\lambda(k))\cos(\beta_w(j)) \tag{5.24}$$

$$R_\lambda(k) = \frac{\cosh(\beta_\lambda(k)) + \cos(\beta_\lambda(k))}{\sinh(\beta_\lambda(j)) + \sin(\beta_\lambda(j))} \tag{5.25}$$

We can write kinetic and potential energies in their modal forms.

$$T = \frac{1}{2}\int_0^L m\Big(\tilde{x}^2\dot{\theta}^2 + \dot{\theta}^2\sum_{i1}\sum_{i2}\Psi^u_{i1}\Psi^u_{i2}u_{i1}u_{i2} + \dot{\theta}^2\sum_{j1}\sum_{j2}\Psi^w_{j1}\Psi^w_{j2}w_{j1}w_{j2}$$
$$+\sum_{i1}\sum_{i2}\Psi^u_{i1}\Psi^u_{i2}\dot{u}_{i1}\dot{u}_{i2} + \sum_{j1}\sum_{j2}\Psi^w_{j1}\Psi^w_{j2}\dot{w}_{j1}\dot{w}_{j2} + \dot{w}_T^2 + \dot{u}_T^2 + 2\tilde{x}\dot{\theta}^2\sum_i\Psi^u_i u_i$$
$$+2\tilde{x}\dot{\theta}\sum_j\Psi^w_j\dot{w}_j + 2\tilde{x}\dot{w}_T\dot{\theta}\cos\theta - 2\dot{u}_T\dot{\theta}\sum_j\Psi^w_j w_j\cos\theta - 2\tilde{x}\dot{u}_T\dot{\theta}\sin\theta$$
$$-2\dot{u}_T\dot{\theta}\sum_i\Psi^u_i u_i\sin\theta - 2\dot{u}_T\sum_j\Psi^w_j\dot{w}_j\sin\theta + 2\dot{u}_T\sum_i\Psi^u_i\dot{u}_i\cos\theta$$
$$+2\dot{\theta}\sum_i\Psi^u_i u_i\sum_j\Psi^w_j\dot{w}_j - 2\dot{\theta}\sum_j\Psi^w_j w_j\sum_i\Psi^u_i\dot{u}_i + 2\dot{w}_T\sum_i\Psi^u_i\dot{u}_i\sin\theta$$
$$+2\sum_i\Psi^u_i u_i\dot{w}_T\dot{\theta}\cos\theta + 2\dot{w}_T\sum_j\Psi^w_j\dot{w}_j\cos\theta - 2\dot{w}_T\dot{\theta}\sum_j\Psi^w_j w_j\sin\theta\Big)\,dx \quad (5.26)$$

Writing the potential energy in its modal form,

$$V = \frac{1}{2}\int_0^L EI\Big(\sum_{j1}\sum_{j2}\Psi^{w\prime\prime}_{j1}\Psi^{w\prime\prime}_{j2}w_{j1}w_{j2}$$
$$+\sum_{j1}\sum_{j2}\sum_{j3}\sum_{j4}\Psi^{w\prime\prime}_{j1}\Psi^{w\prime\prime}_{j2}\Psi^{w\prime}_{j3}\Psi^{w\prime}_{j4}w_{j1}w_{j2}w_{j3}w_{j4}\Big)\,dx \quad (5.27)$$

Next consider the Lagrange multiplier term. The modal expansion of the constraint f is

$$f = \sum_i\Psi^{u\prime}_i u_i + \frac{1}{2}\sum_{j1}\sum_{j2}\Psi^{w\prime}_{j1}\Psi^{w\prime}_{j2}w_{j1}w_{j2} \quad (5.28)$$

Then,

$$\int_0^L \lambda f\,dx = \int_0^L\Big(\sum_k\sum_i\Psi^\lambda_k\Psi^{u\prime}_i\lambda_k u_i + \frac{1}{2}\sum_k\sum_{j1}\sum_{j2}\Psi^\lambda_k\Psi^{w\prime}_{j1}\Psi^{w\prime}_{j2}\lambda_k w_{j1}w_{j2}\Big)\,dx \quad (5.29)$$

We use previously derived expressions for the relevant derivatives of potential energy V and the Lagrange multiplier [44] as they do not change with the new rotational formulation.

5.5.3 Equation for θ

$$\frac{\partial T}{\partial \theta} = \int_0^L m\dot{w}_T \Bigg(\Big(\sum_i \Psi_i^u \dot{u}_i - \dot{\theta} \sum_j \Psi_j^w w_j \Big) \cos\theta - \Big(\dot{\theta}\tilde{x} + \dot{\theta} \sum_i \Psi_i^u u_i + \sum_j \Psi_j^w \dot{w}_j \Big) \sin\theta \Bigg) + m\dot{u}_T \Bigg(\Big(\dot{\theta} \sum_j \Psi_j^w w_j - \sum_i \Psi_i^u \dot{u}_i \Big) \sin\theta - \Big(\dot{\theta}\tilde{x} + \dot{\theta} \sum_i \Psi_i^u u_i + \sum_j \Psi_j^w \dot{w}_j \Big) \cos\theta \Bigg) \, dx \quad (5.30)$$

$$\frac{\partial}{\partial t}\left(\frac{\partial T}{\partial \dot{\theta}}\right) = \int_0^L m\big(\tilde{x}^2\ddot{\theta} + \ddot{\theta}\sum_{i1}\sum_{i2}\Psi^u_{i1}\Psi^u_{i2}u_{i1}u_{i2} + 2\dot{\theta}\sum_{i1}\sum_{i2}\Psi^u_{i1}\Psi^u_{i2}\dot{u}_{i1}u_{i2}$$

$$+ \ddot{\theta}\sum_{j1}\sum_{j2}\Psi^w_{j1}\Psi^w_{j2}w_{j1}w_{j2} + 2\dot{\theta}\sum_{j1}\sum_{j2}\Psi^w_{j1}\Psi^w_{j2}\dot{w}_{j1}w_{j2} + 2\tilde{x}\ddot{\theta}\sum_i\Psi^u_i u_i$$

$$+ 2\tilde{x}\dot{\theta}\sum_i\Psi^u_i\dot{u}_i + \tilde{x}\sum_j\Psi^w_j\ddot{w}_j + \sum_i\sum_j\Psi^u_i u_i\Psi^w_j\ddot{w}_j - \sum_i\sum_j\Psi^u_i\ddot{u}_i\Psi^w_j w_j$$

$$+ \ddot{w}_T\cos\theta\sum_i\Psi^u_i u_i - \ddot{w}_T\sin\theta\sum_j\Psi^w_j w_j + \dot{w}_T\cos\theta\sum_i\Psi^u_i\dot{u}_i$$

$$- \dot{w}_T\dot{\theta}\sin\theta\sum_i\Psi^u_i u_i - \dot{w}_T\sin\theta\sum_j\Psi^w_j\dot{w}_j - \dot{w}_T\dot{\theta}\cos\theta\sum_j\Psi^w_j w_j$$

$$- \ddot{u}_T\cos\theta\sum_j\Psi^w_j w_j - \dot{u}_T\cos\theta\sum_j\Psi^w_j\dot{w}_j + \dot{u}_T\dot{\theta}\sin\theta\sum_j\Psi^w_j w_j - \tilde{x}\ddot{u}_T\sin\theta$$

$$- \tilde{x}\dot{u}_T\dot{\theta}\cos\theta - \ddot{u}_T\sin\theta\sum_i\Psi^u_i u_i - \dot{u}_T\sum_i\sin\theta\Psi^u_i\dot{u}_i - \dot{u}_T\dot{\theta}\cos\theta\sum_i\Psi^u_i u_i$$

$$- \tilde{x}\dot{\theta}\sin\theta\dot{w}_T + \tilde{x}\cos\theta\ddot{w}_T\big)\,dx \quad (5.31)$$

$$\frac{\partial}{\partial t}\left(\frac{\partial T}{\partial \dot{\theta}}\right) - \frac{\partial T}{\partial \theta} = 0 \quad (5.32)$$

So,

$$0 = \int_0^L m\big(\tilde{x}^2\ddot{\theta} + \ddot{\theta}\sum_{i1}\sum_{i2}\Psi^u_{i1}\Psi^u_{i2}u_{i1}u_{i2} + 2\dot{\theta}\sum_{i1}\sum_{i2}\Psi^u_{i1}\Psi^u_{i2}\dot{u}_{i1}u_{i2} + \tilde{x}\ddot{w}_T\cos\theta$$

$$- \tilde{x}\ddot{u}_T\sin\theta + \ddot{\theta}\sum_{j1}\sum_{j2}\Psi^w_{j1}\Psi^w_{j2}w_{j1}w_{j2} + 2\dot{\theta}\sum_{j1}\sum_{j2}\Psi^w_{j1}\Psi^w_{j2}\dot{w}_{j1}w_{j2}$$

$$+ 2\tilde{x}\ddot{\theta}\sum_i\Psi^u_i u_i + 2\tilde{x}\dot{\theta}\sum_i\Psi^u_i\dot{u}_i + \tilde{x}\sum_j\Psi^w_j\ddot{w}_j + \sum_i\sum_j\Psi^u_i u_i\Psi^w_j\ddot{w}_j$$

$$- \sum_i\sum_j\Psi^u_i\ddot{u}_i\Psi^w_j w_j + \ddot{w}_T\cos\theta\sum_i\Psi^u_i u_i - \ddot{w}_T\sin\theta\sum_j\Psi^w_j w_j$$

$$- \ddot{u}_T\cos\theta\sum_j\Psi^w_j w_j - \ddot{u}_T\sin\theta\sum_i\Psi^u_i u_i\big)\,dx \quad (5.33)$$

5.5.4 Equation for u_i

$$\frac{\partial T}{\partial u_i} = \int_0^L m\big(\dot{\theta}^2\Psi_i^u \sum_i \Psi_i^u u_i + \tilde{x}\dot{\theta}^2\Psi_i^u + \dot{\theta}\Psi_i^u \sum_j \Psi_j^w \dot{w}_j + \dot{\theta}\dot{w}_T \cos\theta\Psi_i^u - \dot{\theta}\dot{u}_T \sin\theta\Psi_i^u\big)\, dx \quad (5.34)$$

$$\frac{\partial}{\partial t}\left(\frac{\partial T}{\partial \dot{u}_i}\right) = \int_0^L m\Big(\Psi_i^u\Psi_i^u\ddot{u}_i - \ddot{\theta}\Psi_i^u \sum_j \Psi_j^w w_j - \dot{\theta}\Psi_i^u \sum_j \Psi_j^w \dot{w}_j + \dot{\theta}\dot{w}_T\Psi_i^u \cos\theta + \ddot{w}_T\Psi_i^u \sin\theta + \ddot{u}_T\Psi_i^u \cos\theta - \dot{u}_T\dot{\theta}\Psi_i^u \sin\theta\Big)\, dx \quad (5.35)$$

From λ expressions [44],

$$\frac{\partial}{\partial u_i}\Big(\int_0^L \lambda f\ dx\Big) = \sum_k \int_0^L \Psi_i^{w\prime}\Psi_k^\lambda\ dx\ \lambda_k \quad (5.36)$$

$$\frac{\partial}{\partial t}\left(\frac{\partial T}{\partial \dot{u}_i}\right) - \frac{\partial T}{\partial u_i} - \frac{\partial}{\partial u_i}\Big(\int_0^L \lambda f\ dx\Big) = 0 \quad (5.37)$$

$$0 = \int_0^L m\Big(-\ddot{\theta}\Psi_i^u \sum_j \Psi_j^w w_j - 2\dot{\theta}\Psi_i^u \sum_j \Psi_j^w \dot{w}_j + \ddot{w}_T\Psi_i^u \sin\theta - \dot{\theta}^2\Psi_i^u \sum_i \Psi_i^u u_i - \dot{\theta}^2\Psi_i^u\tilde{x} + \ddot{u}_T\Psi_i^u \cos\theta\Big)\, dx + mM_{ii}^u\ddot{u}_i - \sum_k \int_0^L \Psi_i^{w\prime}\Psi_k^\lambda\ dx\ \lambda_k \quad (5.38)$$

5.5.5 Equation for w_j

$$\frac{\partial T}{\partial w_j} = \int_0^L m\big(\dot{\theta}^2\Psi_j^w \sum_{j1} \Psi_{j1}^w w_{j1} - \dot{\theta}\Psi_j^w \sum_i \Psi_i^u \dot{u}_i - \dot{\theta}\dot{w}_T\Psi_j^w \sin\theta - \dot{\theta}\dot{u}_T\Psi_j^w \cos\theta\big)\, dx \quad (5.39)$$

$$\frac{\partial}{\partial t}\left(\frac{\partial T}{\partial \dot{w}_j}\right) = \int_0^L m\Big(\Psi_j^w \sum_{j1} \Psi_{j1}^w \ddot{w}_{j1} + \tilde{x}\ddot{\theta}\Psi_{j1}^w + \ddot{\theta}\Psi_j^w \sum_i \Psi_i^u u_i + \dot{\theta}\Psi_j^w \sum_i \Psi_i^u \dot{u}_i$$

$$+ \ddot{w}_T \Psi_j^w \cos\theta - \dot{\theta}\dot{w}_T \Psi_j^w \sin\theta - \ddot{u}_T \Psi_j^w \sin\theta - \dot{\theta}\dot{u}_T \Psi_j^w \cos\theta\Big)\, dx \quad (5.40)$$

As is done before [44], we can use orthogonality to write

$$\int_0^L m\Psi_j^w \sum_{j1} \Psi_{j1}^w \ddot{w}_{j1}\, dx = m\int_0^L \Psi_j^w \Psi_j^w\, dx \ddot{w}_j = mM_{jj}^w \ddot{w}_j \quad (5.41)$$

From the V expression from [44],

$$\frac{\partial V}{\partial w_j} = m\omega_j^2 M_{j,j}^w w_j + \sum_{j1}\sum_{j2}\sum_{j3} EIP_{j1,j2,j3,j} w_{j1} w_{j2} w_{j3} \quad (5.42)$$

From the λ expression [44],

$$\frac{\partial}{\partial w_j}\Big(\int_0^L \lambda f\, dx\Big) = \sum_k \sum_{j1} \int_0^L \Psi_k^\lambda \Psi_{j1}^{w\prime} \Psi_j^{w\prime}\, dx\ \lambda_k w_{j1} \quad (5.43)$$

So,

$$\frac{\partial}{\partial t}\left(\frac{\partial T}{\partial \dot{w}_j}\right) - \frac{\partial T}{\partial w_j} + \frac{\partial V}{\partial w_j} - \frac{\partial}{\partial w_j}\Big(\int_0^L \lambda f\, dx\Big) = 0 \quad (5.44)$$

$$0 = mM_{jj}^w \ddot{w}_j + m\omega_j^2 M_{jj}^w w_j + \sum_{j1}\sum_{j2}\sum_{j3} EIP_{j1,j2,j3,j} w_{j1} w_{j2} w_{j3}$$

$$+ \int_0^L m\Big(\tilde{x}\ddot{\theta}\Psi_j^w + \ddot{\theta}\Psi_j^w \sum_i \Psi_i^u u_i + 2\dot{\theta}\Psi_j^w \sum_i \Psi_i^u \dot{u}_i + \ddot{w}_T \Psi_j^w \cos\theta - \ddot{u}_T \Psi_j^w \sin\theta$$

$$- \dot{\theta}^2 \Psi_j^w \sum_j \Psi_j^w w_j\Big)\, dx - \sum_k \sum_{j1} \int_0^L \Psi_k^\lambda \Psi_{j1}^{w\prime} \Psi_j^{w\prime}\, dx\ \lambda_k w_{j1} + \left(2\xi_j \omega_j m M_{jj}^w \dot{w}_j\right) \quad (5.45)$$

5.5.6 Equation for u_T

$$\frac{\partial T}{\partial u_T} = 0 \tag{5.46}$$

$$\begin{aligned}\frac{\partial}{\partial t}\left(\frac{\partial T}{\partial \dot{u}_T}\right) = m\int_0^L \ddot{u}_T + \big(\sum_i \Psi_i^u \ddot{u}_i - 2\dot{\theta}\sum_i \Psi_j^w \dot{w}_j - \ddot{\theta}\sum_j \Psi_j^w w_j \\ - \dot{\theta}^2\sum_i \Psi_i^u u_i - \tilde{x}\dot{\theta}^2\big)\cos\theta + \big(\dot{\theta}^2\sum_j \Psi_j^w w_j - \sum_j \Psi_j^w \ddot{w}_j \\ - 2\dot{\theta}\sum_i \Psi_i^u \dot{u}_i - \ddot{\theta}\sum_i \Psi_i^u u_i - \tilde{x}\ddot{\theta}\big)\sin\theta\ dx\end{aligned} \tag{5.47}$$

Since all other derivatives are zero, the equation of motion is simply Eq. 5.47 set to zero.

5.5.7 Equation for w_T

$$\frac{\partial T}{\partial w_T} = 0 \tag{5.48}$$

$$\begin{aligned}\frac{\partial}{\partial t}\left(\frac{\partial T}{\partial \dot{w}_T}\right) = m\int_0^L \ddot{w}_T + \big(2\dot{\theta}\sum_i \Psi_i^u \dot{u}_i + \ddot{\theta}\sum_i \Psi_i^u u_i + \sum_j \Psi_j^w \ddot{w}_j \\ - \dot{\theta}^2\sum_j \Psi_j^w w_j + \tilde{x}\ddot{\theta}\big)\cos\theta + \big(\sum_i \Psi_i^u \ddot{u}_i - \dot{\theta}^2\sum_i \Psi_i^u u_i \\ - 2\dot{\theta}\sum_j \Psi_j^w \dot{w}_j - \ddot{\theta}\sum_j \Psi_j^w w_j - \tilde{x}\dot{\theta}^2\big)\sin\theta\ dx\end{aligned} \tag{5.49}$$

Since all other derivatives are zero, the equation of motion is simply Eq. 5.49 set to zero.

5.5.8 *Equation for λ_k*

The equations for λ_k are the same as reported before [44] since they do not depend on rigid body translation or rotation.

$$0 = \sum_i \int_0^L \Psi_k^{\lambda} \Psi_i^{w\prime} \, dx \; u_i + \frac{1}{2} \sum_{j1} \sum_{j2} \int_0^L \Psi_k^{\lambda} \Psi_{j1}^{w\prime} \Psi_{j2}^{w\prime} \, dx \; w_{j1} w_{j2} \tag{5.50}$$

Note that Eq. 5.50 arises from the requirement that the coefficient of the virtual change in λ_k must be zero.

5.5.9 *Unforced System of Equations of Motion*

The final system of equations is made up of Eqs. 5.33, 5.38, 5.45, 5.49, 5.47, and 5.50.

$$0 = \int_0^L m\big(\tilde{x}^2\ddot{\theta} + \ddot{\theta}\sum_{i1}\sum_{i2}\Psi^u_{i1}\Psi^u_{i2}u_{i1}u_{i2} + 2\dot{\theta}\sum_{i1}\sum_{i2}\Psi^u_{i1}\Psi^u_{i2}\dot{u}_{i1}u_{i2} + \tilde{x}\ddot{w}_T\cos\theta$$

$$- \tilde{x}\ddot{u}_T\sin\theta + \ddot{\theta}\sum_{j1}\sum_{j2}\Psi^w_{j1}\Psi^w_{j2}w_{j1}w_{j2} + 2\dot{\theta}\sum_{j1}\sum_{j2}\Psi^w_{j1}\Psi^w_{j2}\dot{w}_{j1}w_{j2}$$

$$+ 2\tilde{x}\ddot{\theta}\sum_i\Psi^u_i u_i + 2\tilde{x}\dot{\theta}\sum_i\Psi^u_i\dot{u}_i + \tilde{x}\sum_j\Psi^w_j\ddot{w}_j + \sum_i\sum_j\Psi^u_i u_i\Psi^w_j\ddot{w}_j$$

$$- \sum_i\sum_j\Psi^u_i\ddot{u}_i\Psi^w_j w_j + \ddot{w}_T\cos\theta\sum_i\Psi^u_i u_i - \ddot{w}_T\sin\theta\sum_j\Psi^w_j w_j$$

$$- \ddot{u}_T\cos\theta\sum_j\Psi^w_j w_j - \ddot{u}_T\sin\theta\sum_i\Psi^u_i u_i\big)\ dx \tag{5.51}$$

$$0 = \int_0^L m\Big(-\ddot{\theta}\Psi^u_i\sum_j\Psi^w_j w_j - 2\dot{\theta}\Psi^u_i\sum_j\Psi^w_j\dot{w}_j + \ddot{w}_T\Psi^u_i\sin\theta - \dot{\theta}^2\Psi^u_i\sum_i\Psi^u_i u_i$$

$$- \dot{\theta}^2\Psi^u_i\tilde{x} + \ddot{u}_T\Psi^u_i\cos\theta\Big)\ dx + mM^u_{ii}\ddot{u}_i - \sum_k\int_0^L\Psi^{u\prime}_i\Psi^\lambda_k\ dx\ \lambda_k \tag{5.52}$$

$$0 = mM^w_{jj}\ddot{w}_j + m\omega_j^2M^w_{jj}w_j + \sum_{j1}\sum_{j2}\sum_{j3}EIP_{j1j2j3j}w_{j1}w_{j2}w_{j3}$$

$$+ \int_0^L m\Big(\tilde{x}\ddot{\theta}\Psi^w_j + \ddot{\theta}\Psi^w_j\sum_i\Psi^u_i u_i + 2\dot{\theta}\Psi^w_j\sum_i\Psi^u_i\dot{u}_i + \ddot{w}_T\Psi^w_j\cos\theta$$

$$- \ddot{u}_T\Psi^w_j\sin\theta - \dot{\theta}^2\Psi^w_j\sum_j\Psi^w_j w_j\Big)\ dx$$

$$- \sum_k\sum_{j1}\int_0^L\Psi^\lambda_k\Psi^{w\prime}_{j1}\Psi^{w\prime}_j\ dx\ \lambda_k w_{j1} + \left(2\xi_j\omega_j mM^w_{jj}\dot{w}_j\right) \tag{5.53}$$

$$0 = m\int_0^L\ddot{w}_T + \big(2\dot{\theta}\sum_i\Psi^u_i\dot{u}_i + \ddot{\theta}\sum_i\Psi^u_i u_i + \sum_j\Psi^w_j\ddot{w}_j - \dot{\theta}^2\sum_j\Psi^w_j w_j + \tilde{x}\ddot{\theta}\big)\cos\theta$$

$$+ \big(\sum_i\Psi^u_i\ddot{u}_i - \dot{\theta}^2\sum_i\Psi^u_i u_i - 2\dot{\theta}\sum_j\Psi^w_j\dot{w}_j - \ddot{\theta}\sum_j\Psi^w_j w_j - \tilde{x}\dot{\theta}^2\big)\sin\theta\ dx \tag{5.54}$$

$$0 = m \int_0^L \ddot{u}_T + \big(\sum_i \Psi_i^u \ddot{u}_i - 2\dot{\theta} \sum_i \Psi_j^w \dot{w}_j - \ddot{\theta} \sum_j \Psi_j^w w_j - \dot{\theta}^2 \sum_i \Psi_i^u u_i - \tilde{x}\dot{\theta}^2 \big) \cos\theta$$

$$+ \big(\dot{\theta}^2 \sum_j \Psi_j^w w_j - \sum_j \Psi_j^w \ddot{w}_j - 2\dot{\theta} \sum_i \Psi_i^u \dot{u}_i - \ddot{\theta} \sum_i \Psi_i^u u_i - \tilde{x}\ddot{\theta} \big) \sin\theta \; dx \tag{5.55}$$

$$0 = \sum_i \int_0^L \Psi_k^\lambda \Psi_i^{u\prime} \; dx \; u_i + \frac{1}{2} \sum_{j1} \sum_{j2} \int_0^L \Psi_k^\lambda \Psi_{j1}^{w\prime} \Psi_{j2}^{w\prime} \; dx \; w_{j1} w_{j2} \tag{5.56}$$

By performing the integration before the summations, any variables not dependent on $\tilde{x}$ may be brought outside the integral and the remaining $\tilde{x}$ integrals performed. Using the following notations we may simplify the appearance of these equations and show similarities between terms. After skipping ahead to the typical nondimensionalization in which the integrals are evaluated from 0 to 1 over $x/L = \xi$, boldface matrix/vector notation is introduced after the right arrows.

$$\int_0^L \Psi_{i1}^u \Psi_{i2}^u \; dx = \int_0^L \Psi_i^u \Psi_i^u \; dx = M_{i,i}^u = L \int_0^1 \Psi_i^u \Psi_i^u \; d\xi \Rightarrow L\mathbf{M_u} \tag{5.57}$$

$$\int_0^L \Psi_{j1}^w \Psi_{j2}^w \; dx = \int_0^L \Psi_j^w \Psi_j^w \; dx = M_{j,j}^w = L \int_0^1 \Psi_j^w \Psi_j^w \; d\xi \Rightarrow L\mathbf{M_w} \tag{5.58}$$

$$\int_0^L \tilde{x} \Psi_i^u \; dx = H_i = L^2 \int_0^1 \frac{\tilde{x}}{L} \Psi_i^u \; d\xi \Rightarrow L^2\mathbf{H} \tag{5.59}$$

$$\int_0^L \tilde{x} \Psi_j^w \; dx \equiv 0 \tag{5.60}$$

$$\int_0^L \Psi_i^u \Psi_j^w \; dx = G_{i,j} = L \int_0^1 \Psi_i^u \Psi_j^w \; d\xi \Rightarrow L\mathbf{G} \tag{5.61}$$

$$\int_0^L \Psi_i^u \; dx \equiv 0 \tag{5.62}$$

$$\int_0^L \Psi_j^w \; dx \equiv 0 \tag{5.63}$$

$$\int_0^L \tilde{x}\ dx \equiv 0 \tag{5.64}$$

From before, [44], we have

$$\int_0^L \Psi_k^{\lambda}\Psi_i^{w\prime}\ dx = A_{k,i} = \int_0^1 \Psi_k^{\lambda}\Psi_i^{w\prime}\ d\xi \Rightarrow \mathbf{A} \tag{5.65}$$

$$\int_0^L \Psi_k^{\lambda}\Psi_{j1}^{w\prime}\Psi_{j2}^{w\prime}\ dx = L^{-1}\int_0^1 \Psi_k^{\lambda}\Psi_{j1}^{w\prime}\Psi_{j2}^{w\prime}\ d\xi = L^{-1}B_{k,j1,j2} \tag{5.66}$$

Also, nondimensionalizing the u and w deflections by L and rewriting in boldface vector form,

$$\{u\} = L\{\overline{u}\} \Rightarrow L\mathbf{u} \quad \text{and} \quad \{w\} = L\{\overline{w}\} \Rightarrow L\mathbf{w} \tag{5.67}$$

The final normalized system of equations then can be rewritten.

$$\begin{aligned}
0 =& mL^3\Big(\frac{1}{12}\ddot{\theta} + \ddot{\theta}\{\mathbf{M_u u}\}^T\mathbf{u} + 2\dot{\theta}\{\mathbf{M_u}\dot{\mathbf{u}}\}^T\mathbf{u} + \ddot{\theta}\{\mathbf{M_w w}\}^T\mathbf{w} + 2\dot{\theta}\{\mathbf{M_w}\dot{\mathbf{w}}\}^T\mathbf{w} \\
&+ 2\ddot{\theta}\mathbf{H}^T\mathbf{u} + 2\dot{\theta}\mathbf{H}^T\dot{\mathbf{u}} + \{\mathbf{G}\ddot{\mathbf{w}}\}^T\mathbf{u} - \{\mathbf{Gw}\}^T\ddot{\mathbf{u}}\Big)
\end{aligned} \tag{5.68}$$

$$0 = mL^2\mathbf{M_u}\ddot{\mathbf{u}} - mL^2\ddot{\theta}\mathbf{Gw} - 2mL^2\dot{\theta}\mathbf{G}\dot{\mathbf{w}} - mL^2\dot{\theta}^2\mathbf{M_u u} - mL^2\dot{\theta}^2\mathbf{H} - \mathbf{A}\lambda \tag{5.69}$$

$$\begin{aligned}
0 =& mL^2\mathbf{M_w}\ddot{\mathbf{w}} + 2mL^2\boldsymbol{\xi\omega}\mathbf{M_w}\dot{\mathbf{w}} + mL^2\boldsymbol{\omega^2}\mathbf{M_w w} \\
&+ L^{-2}\sum_{j1}\sum_{j2}\sum_{j3} EIP_{j1j2j3j}\overline{w}_{j1}\overline{w}_{j2}\overline{w}_{j3} - \Big[\sum_k B_{kj1j}\ \lambda_k\Big]\mathbf{w} \\
&+ mL^2\ddot{\theta}\mathbf{G^T u} + 2mL^2\dot{\theta}\mathbf{G^T}\dot{\mathbf{u}} - mL^2\dot{\theta}^2\mathbf{M_w w}
\end{aligned} \tag{5.70}$$

$$0 = mL\ddot{\mathbf{w}}_\mathbf{T} \tag{5.71}$$

$$0 = mL\ddot{\mathbf{u}}_\mathbf{T} \tag{5.72}$$

$$0 = \mathbf{Au} + \frac{1}{2}\Big[\sum_{j1} B_{kj1j}\overline{w}_{j1}\Big]\mathbf{w} \tag{5.73}$$

Note that Eq. 5.68 has units of torque (N-m), Eqs. 5.69-5.72 have units of force, and Eq. 5.73 has no units. Also note that after the integration, the translational

rigid body modes of u_T and w_T are fully decoupled from Eqs. 5.68-5.70 and 5.73 and therefore are not solved in these simulations.

5.5.10 External Forces

The effects of external forcing may be included through the term Q_i on the right hand side of Lagrange's Equations, Eq. 5.7, where Q_i represents the generalized forces acting on the system. These forces can be determined from the virtual work.

$$\delta W = \sum_n Q_n \delta q_n \tag{5.74}$$

Now we express δW as in the previous chapter (Eqn. 4.4).

$$\delta W = F_x \delta u|_{(x=x_F)} + F_y \delta w|_{(x=x_F)} \tag{5.75}$$

Here δw and δu can be expanded as follows using Eqs. 5.12 and 5.13.

$$\begin{aligned}
\delta w &= \delta(w_T + w_B \cos\theta + (\tilde{x} + u_B)\sin\theta) \\
&= \delta w_T + \cos\theta \delta w_B + w_B \delta(\cos\theta) + \delta(\tilde{x} + u_B)\sin\theta + (\tilde{x} + u_B)\delta(\sin\theta) \\
&= \delta w_T + \cos\theta \delta w_B - w_B \sin\theta \delta\theta + \sin\theta \delta u_B + (\tilde{x} + u_B)\cos\theta \delta\theta \\
&= \delta w_T + \cos\theta \delta w_B + \sin\theta \delta u_B + \big((\tilde{x} + u_B)\cos\theta - w_B \sin\theta\big)\delta\theta
\end{aligned} \tag{5.76}$$

Similarly,

$$\delta u = \cos\theta \delta u_B - \sin\theta \delta w_B - \big((\tilde{x} + u_B)\sin\theta + w_B \cos\theta\big)\delta\theta \tag{5.77}$$

So δW may be written in terms of the modal expansions of u_B and w_B as

$$\begin{aligned}
\delta W = (F_y \sin\theta + F_x \cos\theta) \sum_i \Psi_i^u(x_F)\delta u_i + (F_y \cos\theta - F_x \sin\theta) \sum_j \Psi_j^w(x_F)\delta w_j \\
F_y \delta w_T + L\big[F_y(\tilde{x} + \sum_i \Psi_i^u(x_F)u_i)\cos\theta - F_y \sum_j \Psi_j^w(x_F) w_j \sin\theta \\
- F_x(\tilde{x} + \sum_i \Psi_i^u(x_F)u_i)\sin\theta - F_x \sum_j \Psi_j^w(x_F) w_j \cos\theta\big]\delta\theta
\end{aligned} \tag{5.78}$$

By comparing Eq. 5.78 with 5.74 the generalized forces may be readily determined.

Follower Forces

Figure 5.1 illustrates the follower force configuration for a free-free beam as it is free to rotate. Here we add a nonconservative work term to the Lagrangian.

Now, we know from geometry of the system that the following relationships between the static coordinate system and the follower force coordinates F_T (tangent to beam) and F_N (normal to beam) are true.

$$F_x = F_T(\cos\beta\cos\theta - \sin\beta\sin\theta) - F_N(\sin\beta\cos\theta + \cos\beta\sin\theta) \tag{5.79}$$

$$F_y = F_T(\cos\beta\sin\theta + \sin\beta\cos\theta) + F_N(\cos\beta\cos\theta - \sin\beta\sin\theta) \tag{5.80}$$

With these relationships, we can simplify the expression for nonconservative work δW^{NC} to the following.

$$\begin{aligned}
\delta W^{NC} = &\Big(F_T(x_F)\cos\beta(x_F) - F_N(x_F)\sin\beta(x_F)\Big)\sum_i \Psi_i^u(x_F)\delta u_i \\
&+ \Big(F_T(x_F)\sin\beta(x_F) + F_N(x_F)\cos\beta(x_F)\Big)\sum_j \Psi_j^w(x_F)\delta w_j \\
&+ L\Big(F_T(x_F)\big((\tilde{x}(x_F) + \sum_i \Psi_i^u(x_F)u_i)\sin\beta(x_F) - \sum_j \Psi_j^w(x_F)w_j\cos\beta(x_F)\big) \\
&+ F_N(x_F)\big((\tilde{x}(x_F) + \sum_i \Psi_i^u(x_F)u_i)\cos\beta(x_F) + \sum_j \Psi_j^w(x_F)w_j\sin\beta(x_F)\big)\Big)\delta\theta \\
&+ \Big(F_T(\cos\beta\sin\theta + \sin\beta\cos\theta) + F_N(\cos\beta\cos\theta - \sin\beta\sin\theta)\Big)\delta w_T \\
&+ \Big(F_T(\cos\beta\cos\theta - \sin\beta\sin\theta) - F_N(\sin\beta\cos\theta + \cos\beta\sin\theta)\Big)\delta u_T
\end{aligned} \tag{5.81}$$

5.5.11 System of Forced Equations of Motion

For general loading with vertical, horizontal, or normal or tangential follower forces, we include the variation in work in Eqs. 5.78 and 5.81 to the system, and the full system of equations may be written as follows.

$$
\begin{aligned}
0 =& mL^3\Big(\frac{1}{12}\ddot{\theta} + \ddot{\theta}\{\mathbf{M_u u}\}^T\mathbf{u} + 2\dot{\theta}\{\mathbf{M_u}\dot{\mathbf{u}}\}^T\mathbf{u} + \ddot{\theta}\{\mathbf{M_w w}\}^T\mathbf{w} \\
&+ 2\dot{\theta}\{\mathbf{M_w}\dot{\mathbf{w}}\}^T\mathbf{w} + 2\ddot{\theta}\mathbf{H}^T\mathbf{u} + 2\dot{\theta}\mathbf{H}^T\dot{\mathbf{u}} + \{\mathbf{G}\ddot{\mathbf{w}}\}^T\mathbf{u} - \{\mathbf{Gw}\}^T\ddot{\mathbf{u}}\Big) \\
&- LF_y\big((\tilde{x}(x_F) + \boldsymbol{\Psi}_{\boldsymbol{u}}^T(x_F)\mathbf{u})\cos\theta - \boldsymbol{\Psi}_{\boldsymbol{w}}^T(x_F)\mathbf{w}\sin\theta\big) \\
&+ LF_x\big((\tilde{x}(x_F) + \boldsymbol{\Psi}_{\boldsymbol{u}}^T(x_F)\mathbf{u})\sin\theta + \boldsymbol{\Psi}_{\boldsymbol{w}}^T(x_F)\mathbf{w}\cos\theta\big) \\
&- L\Big(F_T(x_F)\big((\tilde{x}(x_F) + \boldsymbol{\Psi}_{\boldsymbol{u}}(x_F)\boldsymbol{u})\sin\beta(x_F) - \boldsymbol{\Psi}_{\boldsymbol{w}}(x_F)\boldsymbol{w}\cos\beta(x_F)\big) \\
&+ F_N(x_F)\big((\tilde{x}(x_F) + \boldsymbol{\Psi}_{\boldsymbol{u}}(x_F)\boldsymbol{u})\cos\beta(x_F) + \boldsymbol{\Psi}_{\boldsymbol{w}}(x_F)\boldsymbol{w}\sin\beta(x_F)\big)\Big)
\end{aligned} \tag{5.82}
$$

$$
\begin{aligned}
0 =& mL^2\mathbf{M_u}\ddot{\mathbf{u}} - mL^2\ddot{\theta}\mathbf{Gw} - 2mL^2\dot{\theta}\mathbf{G}\dot{\mathbf{w}} - mL^2\dot{\theta}^2\mathbf{M_u u} - mL^2\dot{\theta}^2\mathbf{H} - \mathbf{A}\lambda \\
&- \big(F_y(x_F)\sin\theta + F_x(x_F)\cos\theta \\
&+ F_T(x_F)\cos\beta(x_F) - F_N(x_F)\sin\beta(x_F)\big)\boldsymbol{\Psi}_{\boldsymbol{u}}(x_F)
\end{aligned} \tag{5.83}
$$

$$
\begin{aligned}
0 =& mL^2\mathbf{M_w}\ddot{\mathbf{w}} + 2mL^2\boldsymbol{\xi\omega}\mathbf{M_w}\dot{\mathbf{w}} + mL^2\boldsymbol{\omega^2}\mathbf{M_w w} \\
&+ L^{-2}EI\{\mathbf{Pwww}\} - [\mathbf{B}\boldsymbol{\lambda}]\mathbf{w} \\
&+ mL^2\ddot{\theta}\mathbf{G^T u} + 2mL^2\dot{\theta}\mathbf{G^T}\dot{\mathbf{u}} - mL^2\dot{\theta}^2\mathbf{M_w w} \\
&- \big(F_y(x_F)\cos\theta - F_x(x_F)\sin\theta \\
&+ F_T(x_F)\sin\beta(x_F) + F_N(x_F)\cos\beta(x_F)\big)\boldsymbol{\Psi}_{\boldsymbol{w}}(x_F)
\end{aligned} \tag{5.84}
$$

$$
\begin{aligned}
0 =& mL^2\ddot{\mathbf{w}}_\mathbf{T} - F_y(x_F) - F_T(x_F)(\cos\beta(x_F)\sin\theta + \sin\beta(x_F)\cos\theta) \\
&- F_N(x_F)(\cos\beta(x_F)\cos\theta - \sin\beta(x_F)\sin\theta)
\end{aligned} \tag{5.85}
$$

$$
\begin{aligned}
0 =& mL^2\ddot{\mathbf{u}}_\mathbf{T} - F_x(x_F) - F_T(x_F)(\cos\beta(x_F)\cos\theta - \sin\beta(x_F)\sin\theta) \\
&+ F_N(x_F)(\sin\beta(x_F)\cos\theta + \cos\beta(x_F)\sin\theta)
\end{aligned} \tag{5.86}
$$

$$
0 = \mathbf{Au} + \frac{1}{2}[\mathbf{Bw}]\mathbf{w} \tag{5.87}
$$

Here, the tensor summations all reduce to matrices and vectors, and are expressed compactly as follows.

$$
\{\mathbf{Pwww}\} \equiv \sum_{j1}\sum_{j2}\sum_{j3} P_{j1,j2,j3,j}\overline{w}_{j1}\overline{w}_{j2}\overline{w}_{j3} \tag{5.88}
$$

$$
[\mathbf{B}\boldsymbol{\lambda}] \equiv \sum_{k} B_{kj1j}\ \lambda_k \tag{5.89}
$$

$$
[\mathbf{Bw}] \equiv \sum_{j1} B_{kj1j}\ \overline{w}_{j1} \tag{5.90}
$$

Solving the Equations of Motion for θ and w_B

The equations of motion may be solved by isolating an equation for $\ddot{\theta}$ and an equation for $\ddot{\mathbf{w}}$ and solving each of these simultaneously with a Runge-Kutta solver. The steps are detailed below.

Eliminating Eq. 5.87 by Solving for u, $\dot{u}$, and $\ddot{u}$

From Eq. 5.87, $\mathbf{u}$ may be solved in terms of $\mathbf{w}$.

$$\mathbf{u} = -\frac{1}{2}\mathbf{A}^{-1}\mathbf{B}\mathbf{w}\mathbf{w} \tag{5.91}$$

Now $\dot{\mathbf{u}}$ may be solved to be inserted into Eqs. 5.82 and 5.84.

$$\dot{\mathbf{u}} = -\mathbf{A}^{-1}\mathbf{B}\mathbf{w}\dot{\mathbf{w}} = -\mathbf{A}^{-1}\mathbf{B}\dot{\mathbf{w}}\mathbf{w} \tag{5.92}$$

Note that the addition works out elegantly due to the symmetry of tensor B, and that the order of $\dot{\mathbf{w}}\mathbf{w}$ vs $\mathbf{w}\dot{\mathbf{w}}$ does not matter. Lastly from Eq. 5.87, $\ddot{\mathbf{u}}$ may be solved to be inserted into Eqs. 5.82 and 5.83.

$$\ddot{\mathbf{u}} = -\mathbf{A}^{-1}\mathbf{B}\mathbf{w}\ddot{\mathbf{w}} - \mathbf{A}^{-1}\mathbf{B}\dot{\mathbf{w}}\dot{\mathbf{w}} \tag{5.93}$$

Eliminating Eq. 5.83 by Solving for λ

From Eq. 5.83 and the substitution of $\ddot{\mathbf{u}}$, we can solve for $\boldsymbol{\lambda}$ to be inserted into Eq. 5.84.

$$\begin{aligned}\boldsymbol{\lambda} = &-mL^2\mathbf{A}^{-1}\mathbf{M_u}\mathbf{A}^{-1}\mathbf{B}\dot{\mathbf{w}}\dot{\mathbf{w}} - mL^2\mathbf{A}^{-1}\mathbf{M_u}\mathbf{A}^{-1}\mathbf{B}\mathbf{w}\ddot{\mathbf{w}} - mL^2\ddot{\theta}\mathbf{A}^{-1}\mathbf{G}\mathbf{w} \\ &- 2mL^2\dot{\theta}\mathbf{A}^{-1}\mathbf{G}\dot{\mathbf{w}} + \frac{1}{2}mL^2\dot{\theta}^2\mathbf{A}^{-1}\mathbf{M_u}\mathbf{A}^{-1}\mathbf{B}\mathbf{w}\mathbf{w} - mL^2\dot{\theta}^2\mathbf{A}^{-1}\mathbf{H} \\ &- \big(F_y(x_F)\sin\theta + F_x(x_F)\cos\theta + F_T(x_F)\cos\beta(x_F) - F_N(x_F)\sin\beta(x_F)\big)\mathbf{A}^{-1}\boldsymbol{\Psi}_{\boldsymbol{u}}(x_F)\end{aligned} \tag{5.94}$$

Now Eqs. 5.82 and 5.84 can be written in terms of only $\mathbf{w}$, θ, and their first and second time derivatives.

Solving Eqs. 5.82 and 5.84

Substituting the expressions for $\mathbf{u}$, $\dot{\mathbf{u}}$, and $\ddot{\mathbf{u}}$ into Eq. 5.82, simplifying, and isolating $\ddot{\theta}$ and $\ddot{\mathbf{w}}$,

$$\begin{aligned}
&\Big[\frac{1}{12}mL^3 + \frac{1}{4}mL^3\{\mathbf{M_u}(\mathbf{A}^{-1}\mathbf{Bww})\}^T(\mathbf{A}^{-1}\mathbf{Bww}) \\
&\qquad + mL^3\{\mathbf{M_w w}\}^T\mathbf{w} - mL^3\mathbf{H}^T(\mathbf{A}^{-1}\mathbf{Bww})\Big]\ddot{\theta} \\
&\qquad + \Big[mL^3\{\mathbf{Gw}\}^T(\mathbf{A}^{-1}\mathbf{Bw}) - \frac{1}{2}mL^3(\mathbf{G}^T\mathbf{A}^{-1}\mathbf{Bww})^T\Big]\ddot{\mathbf{w}} = \\
&\quad - mL^3\dot{\theta}\{\mathbf{M_u}(\mathbf{A}^{-1}\mathbf{Bw}\dot{\mathbf{w}})\}^T(\mathbf{A}^{-1}\mathbf{Bww}) - 2mL^3\dot{\theta}\{\mathbf{M_w}\dot{\mathbf{w}}\}^T\mathbf{w} \\
&\quad + 2mL^3\dot{\theta}\mathbf{H}^T(\mathbf{A}^{-1}\mathbf{Bw}\dot{\mathbf{w}}) - mL^3\{\mathbf{Gw}\}^T(\mathbf{A}^{-1}\mathbf{B}\dot{\mathbf{w}}\dot{\mathbf{w}}) \\
&\quad + LF_y\big((\tilde{x}(x_F) + \boldsymbol{\Psi}_{\boldsymbol{u}}^T(x_F)(-\frac{1}{2}\mathbf{A}^{-1}\mathbf{Bww}))\cos\theta - \boldsymbol{\Psi}_{\boldsymbol{w}}^T(x_F)\mathbf{w}\sin\theta\big) \\
&\quad - LF_x\big((\tilde{x}(x_F) + \boldsymbol{\Psi}_{\boldsymbol{u}}^T(x_F)\mathbf{u})\sin\theta + \boldsymbol{\Psi}_{\boldsymbol{w}}^T(x_F)\mathbf{w}\cos\theta\big) \\
&+ L\Big(F_T(x_F)\big((\tilde{x}(x_F) + \boldsymbol{\Psi}_{\boldsymbol{u}}(-\frac{1}{2}\mathbf{A}^{-1}\mathbf{Bww})(x_F))\sin\beta(x_F) - \boldsymbol{\Psi}_{\boldsymbol{w}}\boldsymbol{w}(x_F)\cos\beta(x_F)\big) \\
&+ F_N(x_F)\big((\tilde{x}(x_F) + \boldsymbol{\Psi}_{\boldsymbol{u}}(-\frac{1}{2}\mathbf{A}^{-1}\mathbf{Bww})(x_F))\cos\beta(x_F) + \boldsymbol{\Psi}_{\boldsymbol{w}}\boldsymbol{w}(x_F)\sin\beta(x_F)\big)\Big)
\end{aligned} \tag{5.95}$$

Now, follow the same process for Eq. 5.84 to solve for $\mathbf{w}$. First, substitute the expressions for $\mathbf{u}$, $\dot{\mathbf{u}}$, $\ddot{\mathbf{u}}$ and λ into Eq. 5.84, simplify, and isolate $\ddot{\theta}$ and $\ddot{\mathbf{w}}$.

$$
\begin{aligned}
&\Big[mL^2\mathbf{M_w} + mL^2(\mathbf{BA^{-1}M_uA^{-1}Bww})\Big]\ddot{\mathbf{w}} \\
&\qquad + \Big[mL^2(\mathbf{BA^{-1}Gw})\mathbf{w} - \frac{1}{2}mL^2\mathbf{G^TA^{-1}Bww}\Big]\ddot{\theta} \\
&= -2mL^2\boldsymbol{\xi\omega}\mathbf{M_w}\dot{\mathbf{w}} - mL^2\boldsymbol{\omega^2}\mathbf{M_w w} - L^{-2}EI\{\mathbf{Pwww}\} \\
&\qquad + 2mL^2\dot{\theta}\mathbf{G^TA^{-1}Bw}\dot{\mathbf{w}} + mL^2\dot{\theta}^2\mathbf{M_w w} \\
&\qquad - mL^2(\mathbf{BA^{-1}M_uA^{-1}B}\dot{\mathbf{w}}\dot{\mathbf{w}})\mathbf{w} - 2mL^2\dot{\theta}(\mathbf{BA^{-1}G}\dot{\mathbf{w}})\mathbf{w} \\
&\qquad + \frac{1}{2}mL^2\dot{\theta}^2(\mathbf{BA^{-1}M_uA^{-1}Bww})\mathbf{w} - mL^2\dot{\theta}^2\mathbf{BA^{-1}Hw} \\
&-\big(F_y(x_F)\sin\theta + F_x(x_F)\cos\theta + F_T(x_F)\cos\beta(x_F) - F_N(x_F)\sin\beta(x_F)\big)\mathbf{BA^{-1}}\boldsymbol{\Psi_u}(x_F)\mathbf{w} \\
&\quad + \big(F_T(x_F)\sin\beta(x_F) + F_N(x_F)\cos\beta(x_F) + F_y(x_F)\cos\theta - F_x(x_F)\sin\theta\big)\boldsymbol{\Psi_w}(x_F)
\end{aligned}
\tag{5.96}
$$

To solve for $\ddot{\theta}$ and $\ddot{w}_j$ simultaneously, express Eqs. 5.95 and 5.96 compactly as follows.

$$
\alpha\ddot{\theta} + \Big[\beta_{1,j}\Big]\ddot{w}_j = RHS_\theta \tag{5.97}
$$

$$
\Big[\Gamma_{j,j}\Big]\ddot{w}_j + \Big\{\Omega_{j,1}\Big\}\ddot{\theta} = \Big\{RHS_w\Big\}_j \tag{5.98}
$$

This can be rewritten as a matrix system.

$$
\begin{bmatrix} [\Gamma] & [\Omega] \\ [\beta] & \alpha \end{bmatrix}
\begin{Bmatrix} \ddot{w}_j \\ \ddot{\theta} \end{Bmatrix}
= \begin{Bmatrix} \{RHS_w\} \\ RHS_\theta \end{Bmatrix} \tag{5.99}
$$

Equation 5.99 is marched through time via a Runge-Kutta solver.

6

Flutter and Limit Cycle Oscillations of a Cantilevered Plate in Supersonic/Hypersonic Flow

6.1 Introduction

When coupled with aerodynamic models, the presented nonlinear structural models for beams and plates offer an opportunity to study efficiently the dynamics of aircraft wings and other structures. In this chapter, the structural model discussed thus far is excited by Classical Piston Theory for supersonic and hypersonic flow. Some of this work was published in the proceedings of the 2019 IFASD conference [48].

The inextensible beam is a good approximation for large deflections of wings and other components such as control surfaces which have fixed-free boundary conditions. To study flutter due to supersonic flow, piston theory is a usual choice for high Mach number flows and has been shown to effectively capture the dynamics of a cantilevered beam in hypersonic flow *below* the onset of flutter [5] and also the post-flutter Limit Cycle Oscillations of a pinned-pinned plate in hypersonic flow [34]. Presented here is a new aerodynamic and structural model which demonstrates flutter and limit cycle behavior of a nonlinear, inextensible, cantilevered plate subjected to

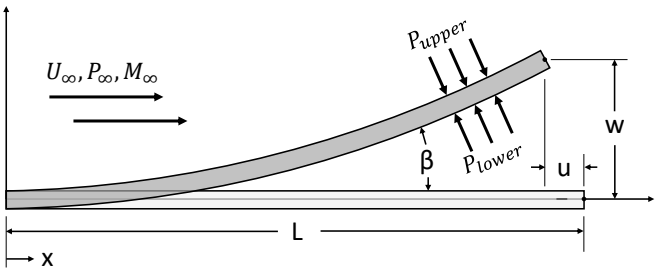

FIGURE 6.1: Schematic of cantilevered beam with uniform flow over top and bottom surfaces.

supersonic flow.

Here we extend the model presented thus far by adding aerodynamic forces modeled by Piston Theory. A schematic of the cantilevered beam model in flow is shown in Figure 6.1. This configuration is of interest for modeling engineering structures such as trailing edge control surfaces on supersonic and hypersonic aircraft.

Classical Piston Theory, developed by Lighthill [32] and later exploited by Ashley and Zartarian [33], is developed from Lighthill's assertion that finding the pressure acting on an oscillatory airfoil at high Mach number is analogous to finding the pressure on an oscillatory 1-D piston. Because the shock and expansion waves on a surface in high Mach number flows are set at small angles to the undisturbed flow, the velocity components perpendicular to the undisturbed flow are much greater than those parallel to it. Therefore, any transverse plane of fluid perpendicular to the flow acts on the airfoil independently of its neighboring planes, and the pressure acting on the plate is dependent only on the instantaneous velocity of the airfoil at each location.

Piston Theory is utilized throughout the literature for high speed potential flow [34–36] and is relevant to contemporary studies in supersonic configurations [5]. Notably, Nydick et al. [34] performed an admirable study in which 1st and 3rd order Piston Theory were used to compute the aeroelastic LCO response of a pinned-pinned

panel in hypersonic flow. Although their results indicate that 3rd order Piston Theory matches well with Euler results, they also suggest that viscous effects have a large damping effect on the results "because the surface motion occurs mainly within the boundary layer." The cantilevered boundary conditions in the present study allow for the surface motion to be much greater than a typical boundary layer thickness, so it is assumed that an inviscid flow treatment will be adequate.

To the extent of the author's knowledge of the literature, the pressure defined by Classical Piston Theory is always applied perpendicular to the airfoil's chord regardless of the angle the airfoil takes to the undisturbed flow. Because of the large deflections of the structure, a new geometric modification to piston theory is introduced. With use of the parameter $\beta(x)$—the angle of the beam with respect to its undeformed horizontal datum—the pressure is always normal to the instantaneous shape of the beam, i.e. the pressure is a follower force and we use the same principles from Chapters 4 and 5 for the pressure application.

The present model includes four nonlinearities: two structural and two aerodynamic. While the effects of the structural nonlinearities alone have been reported by the authors [44, 46], the aerodynamic nonlinearities are novel and certainly the interplay between the four nonlinearities is interesting. It is found that the geometric modification to piston theory introduces a further aerodynamic nonlinearity, and increases the stability of the model. It is also found that third order nonlinear Piston Theory predicts a higher limit cycle amplitude than the first order linear theory. This distinction is important as we look to experimental validation, since the prediction for the amplitude of deflection will impact the design and safety of the experiment.

To demonstrate that Piston Theory is valid in this novel, large-amplitude deflection setting, colleagues Kai Bastos and Maxim Freydin employed an Euler solver to calculate pressures on the beam. The domain is modeled in ANSYS Fluent, the solver is given freestream conditions, and the beam motion is prescribed as the struc-

tural response from the fully nonlinear aeroelastic case. The pressures from Euler were found to match closely with those of third order Piston Theory, but not first order Piston Theory. Therefore, it is concluded that third order piston theory is valid across the range of testing parameters.

Also note that when modeling any physical system and certainly a fluid-structural (aeroelastic) system, it is important to study the sensitivity of the results to (1) the mathematical model of the physical system, (2) the parameters that appear in the mathematical model or which are considered in the design of an experimental model and (3) the accuracy of the numerical methods employed to extract solutions from the mathematical model. Each of these is considered in the present chapter.

Finally, a word about the nomenclature of beam or plate may be useful. Because the structure is assumed to be clamped along its entire leading edge, the structure bends principally in the streamwise direction and thus the bending in the spanwise direction is negligible. Within the framework of linear theory, this is exact for clamping all along the leading edge. It is expected this carries over to a good approximation to the nonlinear case. Were the leading edge only partially clamped, then bending in the spanwise direction would occur and a structural plate theory would be needed.

With regard to piston theory, whether first order or higher order, the effective aerodynamic aspect ratio is the product of $\sqrt{M^2-1} * (b/L)$ where b is the plate span and L is the plate chord. Thus even for a square plate with $b/L = 1$, the aerodynamic aspect ratio will be large for the Mach number range of interest to the present chapter. On the other hand, were b/L sufficiently small for a given M, then three-dimensional aerodynamic effects might be included. Yet one might still invoke the essential piston theory assumption of the transverse plane of fluid at each chordwise position being independent of each other. But now the "piston" would have finite width.

Thus the structure considered here has a finite width, b, but because the factor

b appears in both the structural model and aerodynamic model in proportion, it cancels and does not appear in the final results. If in future work spanwise bending is included in the structural model or finite aspect ratio effects are included in the aerodynamic model, then b and its non-dimensional counterpart, b/L, will appear as another parameter to be considered.

6.2 Development of Governing Equations

6.2.1 Unforced Equations of Motion

Previous chapters show the derivation of the modal system of governing equations which describes the unforced cantilevered beam motion, and these equations are reproduced here in dimensionless form.

$$\boxed{\begin{aligned} \ddot{\mathbf{u}} - \mathbf{A}\boldsymbol{\lambda} &= 0 \qquad (6.1)\\ \ddot{\mathbf{w}} + 2\boldsymbol{\zeta}\boldsymbol{\omega}\ \dot{\mathbf{w}} + \boldsymbol{\omega}^2\ \mathbf{w} - \mathbf{B}\mathbf{w}\boldsymbol{\lambda} + \mathbf{P}\ \mathbf{w}^{\mathbf{3}} &= 0 \qquad (6.2)\\ \mathbf{u} + \frac{1}{2}\mathbf{A}^{-1}\mathbf{B}\mathbf{w}\mathbf{w} &= 0 \qquad (6.3) \end{aligned}}$$

A short nondimensionalization from the equations given in previous chapters is given in the Appendix, while a brief explanation of the equations terms is given here. Eq. 6.1 is the equation for longitudinal deflection u, where λ is the internal constraint force to enforce inextensibility. Equation 6.2 is the equation for transverse deflection w, where ζ is the damping parameter and the final two terms are the nonlinear inertia and stiffness terms, respectively. Equation 6.3 is the constraint equation which couples the slope of the longitudinal deflection u to that of the transverse deflection w to enforce inextensibility. u, w, and λ are all expressed in a modal series.

Each of the variables appear as boldface Roman text, indicating that they are written in matrix form. The definition of each term and the transcriptions from

index notation to matrix notation are shown below.

$$\overline{u}_i \equiv \frac{u_i}{L} \;\Rightarrow\; \mathbf{u}, \quad \overline{w}_j \equiv \frac{w_j}{L} \;\Rightarrow\; \mathbf{w}$$

$$\overline{\lambda_k} \equiv \frac{L^2}{EI}\lambda_k \;\Rightarrow\; \boldsymbol{\lambda}, \quad \overline{\omega_j} \;\equiv\; \Big(\frac{mL^4}{EI}\Big)^{1/2}\omega_j \Rightarrow \boldsymbol{\omega}$$

$$\overline{M}^u_{ii} \equiv \frac{M^u_{ii}}{L} \equiv \int_0^1 \Psi^u_i \Psi^u_i \; d\xi \;\Rightarrow\; \mathbf{M_u}, \quad \overline{M}^w_{jj} \equiv \frac{M^w_{jj}}{L} \equiv \int_0^1 \Psi^w_j \Psi^w_j \; d\xi \;\Rightarrow\; \mathbf{M_w}$$

$$\overline{A}_{ik} \equiv \int_0^1 \Psi^{u\prime}_i \Psi^\lambda_k \; d\xi \;\Rightarrow\; \mathbf{A}, \qquad \overline{B}_{kj_1j} \equiv LB_{kj_1j} \equiv \int_0^1 \Psi^\lambda_k \Psi^{w\prime}_{j_1} \Psi^{w\prime}_j \; d\xi \;\Rightarrow\; \mathbf{B}$$

$$\overline{P}_{j_1j_2j_3j} \equiv L^5 P_{j_1j_2j_3j} \equiv \int_0^1 (\Psi^{w\prime\prime}_{j_1}\Psi^{w\prime\prime}_{j_2}\Psi^{w\prime}_{j_3}\Psi^{w\prime}_j + \Psi^{w\prime\prime}_{j_1}\Psi^{w\prime}_{j_2}\Psi^{w\prime}_{j_3}\Psi^{w\prime\prime}_j) \; d\xi \;\Rightarrow\; \mathbf{P}$$

Note that the prime ($\prime$) symbol represents $\dfrac{\partial}{\partial x}$. Therefore, when nondimensionalizing length, the following relationships are important.

$$x = L\xi \qquad \frac{\partial}{\partial x} = \frac{1}{L}\frac{\partial}{\partial \xi} \qquad \frac{\partial^2}{\partial x^2} = \frac{1}{L^2}\frac{\partial^2}{\partial \xi^2} \tag{6.4}$$

We also nondimensionalize time and its derivatives as follows, where the overlined terms are dimensionless.

$$t = \big(\frac{mL^4}{EI}\big)^{1/2}\,\bar{t} \qquad \frac{\partial}{\partial t} = \Big(\frac{EI}{mL^4}\Big)^{1/2}\frac{\partial}{\partial \bar{t}} \qquad \frac{\partial^2}{\partial t^2} = \frac{EI}{mL^4}\frac{\partial^2}{\partial \bar{t}^2} \tag{6.5}$$

6.2.2 Piston Theory Aerodynamic Forcing

Piston theory [32,33,35,36] provides a simple relation between pressure perturbation and motion of a structure, one side of which is under a free stream flow with properties $\rho_\infty, U_\infty, M_\infty$. Because our plate model has fluid acting on both sides, we calculate a change in pressure across the upper and lower surfaces.

$$p_{upper} = \frac{\rho_\infty U_\infty}{M_\infty}\left[(\dot{w} + U_\infty\frac{\partial w}{\partial x}) + \frac{\gamma+1}{4a_\infty}(\dot{w} + U_\infty\frac{\partial w}{\partial x})^2 + \frac{\gamma+1}{12a_\infty^2}(\dot{w} + U_\infty\frac{\partial w}{\partial x})^3\right]$$

$$p_{lower} = \frac{\rho_\infty U_\infty}{M_\infty}\left[(-\dot{w} - U_\infty \frac{\partial w}{\partial x}) + \frac{\gamma+1}{4a_\infty}(-\dot{w} - U_\infty \frac{\partial w}{\partial x})^2 + \frac{\gamma+1}{12a_\infty^2}(-\dot{w} - U_\infty \frac{\partial w}{\partial x})^3\right]$$

Note that x is positive in the flow direction. Now we subtract the upper surface from the lower [35], and note the second order terms cancel one another due to symmetry. However, this would not be the case for a plate with a non-zero initial angle of attack or initial curvature.

$$\Delta p = p_{lower} - p_{upper} = -2\frac{\rho_\infty U_\infty}{M_\infty}\left[\left(\dot{w} + U_\infty \frac{\partial w}{\partial x}\right) + \frac{\gamma+1}{12a_\infty^2}(\dot{w} + U_\infty \frac{\partial w}{\partial x})^3\right] \tag{6.6}$$

Large Deflection Correction

Classical uses of Piston Theory apply the pressure only in the vertical direction, which corresponds to δw in our notation. The virtual work would be expressed as Eqn 6.7. However, due to the large displacement of the beam, we understand that pressure must be everywhere normal to the deflected beam. Therefore, the pressure contributes to both the δu and δw components of the virtual work, just as the follower force of previous chapters acted. Now, we propose that the expression for virtual work is given as Eqn. 6.8.

$$\delta W^{NC_{aero}} = \int_0^L b\Delta p \;\; \delta w \; dx \tag{6.7}$$

$$\delta W^{NC_{aero}} = \int_0^L -b\Delta p \; \sin(\beta) \; \delta u + b\Delta p \; \cos(\beta) \; \delta w \; dx \tag{6.8}$$

Where $\sin\beta$ and $\cos\beta$ are defined from geometric relationships as follows.

$$\tan\beta = \frac{\dfrac{\partial w}{\partial x}}{1 + \dfrac{\partial u}{\partial x}} = \frac{w'}{1+u'} = \frac{w'}{1 - 1/2w'^2} \equiv f \tag{6.9}$$

$$\tan\beta = \frac{\sin\beta}{\cos\beta} = f \tag{6.10}$$

$$\sin^2\beta + \cos^2\beta = 1 \tag{6.11}$$

$$f^2 = \frac{\sin^2\beta}{\cos^2\beta} \tag{6.12}$$

So then,

$$\left(f^2+1\right)\cos^2\beta = 1 \tag{6.13}$$

$$\cos\beta = \frac{1}{\left(f^2+1\right)^{1/2}} \tag{6.14}$$

From this, we can find $\sin\beta$ as well.

$$\sin\beta = \frac{f}{\left(f^2+1\right)^{1/2}} \tag{6.15}$$

Now, substituting 6.9 into 6.14 and 6.15, we can write the definitions of $\sin\beta$ and $\cos\beta$ in terms of w.

$$\cos\beta = (1-w'^2)^{1/2} \approx (1-1/2w'^2) \tag{6.16}$$

$$\sin\beta = w' \tag{6.17}$$

So, Eqn. 6.8 can be written as follows.

$$\delta W^{NC_{aero}} = \int_0^L b\Delta p\Big(-w'\ \delta u + (1-1/2w'^2)\ \delta w\Big)\ dx \tag{6.18}$$

First Order Piston Theory

For first order piston theory, we neglect the third order term in Eqn. 6.6, so the change in pressure across the beam is the classical result.

$$\Delta p = -2\frac{\rho_\infty U_\infty}{M_\infty}\left(\dot{w} + U_\infty\frac{\partial w}{\partial x}\right) \tag{6.19}$$

Substituting 6.19 into 6.18, scaling length and time with Eqns. 6.4 and 6.5 and multiplying both sides by L/EI to nondimensionalize, the expression for nondimensional virtual work is as follows.

$$\frac{L}{EI}\delta W^{NC_{aero}} = -\int_0^1 2b\frac{\rho_\infty L}{M_\infty m}\Big(U_\infty\Big(\frac{mL^2}{EI}\Big)^{1/2}\frac{\partial \overline{w}}{\partial \bar{t}} + \frac{mL^2U_\infty^2}{EI}\frac{\partial \overline{w}}{\partial \xi}\Big)$$

$$\times\Big(-\frac{\partial \overline{w}}{\partial \xi}\,\delta\overline{u} + \left(1 - 1/2\left(\frac{\partial \overline{w}}{\partial \xi}\right)^2\right)\,\delta\overline{w}\Big)\,d\xi \quad (6.20)$$

Now we can use the following nondimensional parameters to simplify the equation. Note that μ is the aerodynamic to structural mass ratio and λ is the aerodynamic to structural compliance ratio and both incorporate the Mach number in their definition.

$$\mu \equiv \frac{\rho_\infty bL}{mM_\infty} \quad (6.21)$$

$$\Lambda \equiv \frac{\rho_\infty U_\infty^2 bL^3}{EIM_\infty} \quad (6.22)$$

$$(\Lambda\mu)^{1/2} = \frac{\rho_\infty U_\infty bL^2}{M_\infty\,(EIm)^{1/2}} \quad (6.23)$$

$$\frac{L}{EI}\delta W^{NC_{aero}} = 2\int_0^1 \Bigg[\left((\Lambda\mu)^{1/2}\,\frac{\partial \overline{w}}{\partial \bar{t}}\frac{\partial \overline{w}}{\partial \xi} + \Lambda\left(\frac{\partial \overline{w}}{\partial \xi}\right)^2\right)\,\delta\overline{u}$$

$$+\left(-(\Lambda\mu)^{1/2}\,\frac{\partial \overline{w}}{\partial \bar{t}} - \Lambda\frac{\partial \overline{w}}{\partial \xi} + \frac{1}{2}\,(\Lambda\mu)^{1/2}\,\frac{\partial \overline{w}}{\partial \bar{t}}\left(\frac{\partial \overline{w}}{\partial \xi}\right)^2 + \frac{1}{2}\Lambda\left(\frac{\partial \overline{w}}{\partial \xi}\right)^3\right)\,\delta\overline{w}\Bigg]\,d\xi \quad (6.24)$$

Now, we can show that several of these terms are orders of magnitude smaller than others, and therefore negligible. To show this, we can scale $\frac{\partial \overline{w}}{\partial \overline{t}}$ by $\omega \overline{w}$.

$$\frac{L}{EI}\delta W^{NC_{aero}} = 2\int_0^1 \Bigg[\left((\Lambda\mu)^{1/2}\,\omega\overline{w}\frac{\partial \overline{w}}{\partial \xi} + \Lambda\left(\frac{\partial \overline{w}}{\partial \xi}\right)^2 \right)\ \delta\overline{u}$$

$$+ \left(-(\Lambda\mu)^{1/2}\,\omega\overline{w} - \Lambda\frac{\partial \overline{w}}{\partial \xi} + \frac{1}{2}(\Lambda\mu)^{1/2}\,\omega\overline{w}\left(\frac{\partial \overline{w}}{\partial \xi}\right)^2 + \frac{1}{2}\Lambda\left(\frac{\partial \overline{w}}{\partial \xi}\right)^3 \right)\ \delta\overline{w} \Bigg]\, d\xi \quad (6.25)$$

Lastly, we note the order of each term, using the physical geometries and properties given in the Appendix.

$$\mu = O[10^{-4}]$$

$$\Lambda = O[10^{2}]$$

$$\overline{\omega} = O[10^{1}]$$

$$\overline{w} = O[10^{-1}]$$

$$\frac{\partial \overline{w}}{\partial \xi} = O[10^{-1}]$$

This approximation then leads to the following orders of magnitude.

$$\frac{L}{EI}\delta W^{NC_{aero}} = 2\int_0^1 \Bigg[\left(O[10^{-2}] + O[10^{0}] \right)\ \delta\overline{u}$$

$$+ \left(-O[10^{-1}] - O[10^{1}] + O[10^{-3}] + O[10^{-1}] \right)\ \delta\overline{w} \Bigg]\, d\xi \quad (6.26)$$

It should be no surprise that the largest term comes from the classical linear piston theory which corresponds to having no β effect, i.e. when $\beta = 0$. However, it is notable that the second term in the u coordinate is so large. For now, we will neglect the terms of order $O[10^{-2}]$ or higher. Therefore, the final form of the nonlinear

follower-style 1st order piston theory virtual work becomes the following.

$$\frac{L}{EI}\delta W^{NC_{aero}} = 2\int_0^1 \left[\Lambda\left(\frac{\partial \overline{w}}{\partial \xi}\right)^2 \ \delta\overline{u} \right. \\ \left. + \left(-(\Lambda\mu)^{1/2}\frac{\partial \overline{w}}{\partial \overline{t}} - \Lambda\frac{\partial \overline{w}}{\partial \xi} + \frac{\Lambda}{2}\left(\frac{\partial \overline{w}}{\partial \xi}\right)^3\right) \ \delta\overline{w}\right] d\xi \quad (6.27)$$

Now substitute the following modal expansions of w and u into Eqn. 6.27.

$$\frac{L}{EI}\delta W^{NC_{aero}} = 2\int_0^1 \left[\Lambda\sum_{j1}\sum_{j2}\Psi_{j1}^{w\prime}\Psi_{j2}^{w\prime}w_{j1}w_{j2}\ \delta\left(\sum_i \Psi_i^u u_i\right)\right. \\ + \left(-(\Lambda\mu)^{1/2}\sum_{j1}\Psi_{j1}^{w}\dot{w}_{j1} - \Lambda\sum_{j1}\Psi_{j1}^{w\prime}w_{j1}\right. \\ \left.\left. + \frac{\Lambda}{2}\sum_{j1}\sum_{j2}\sum_{j3}\Psi_{j1}^{w\prime}\Psi_{j2}^{w\prime}\Psi_{j3}^{w\prime}w_{j1}w_{j2}w_{j3}\right)\ \delta\left(\sum_j \Psi_j^w w_j\right)\right] d\xi \quad (6.28)$$

$$\frac{L}{EI}\delta W^{NC_{aero}} = 2\sum_i\left(\Lambda\sum_{j1}\sum_{j2}\int_0^1 \Psi_i^u\Psi_{j1}^{w\prime}\Psi_{j2}^{w\prime}\ d\xi\ w_{j1}w_{j2}\right)\delta u_i \\ + 2\sum_j\left(-(\Lambda\mu)^{1/2}\sum_{j1}\int_0^1 \Psi_j^w\Psi_{j1}^{w}\ d\xi\ \dot{w}_{j1} - \Lambda\sum_{j1}\int_0^1 \Psi_j^w\Psi_{j1}^{w\prime}\ d\xi\ w_{j1}\right. \\ \left. + \frac{\Lambda}{2}\sum_{j1}\sum_{j2}\sum_{j3}\int_0^1 \Psi_j^w\Psi_{j1}^{w\prime}\Psi_{j2}^{w\prime}\Psi_{j3}^{w\prime}\ d\xi\ w_{j1}w_{j2}w_{j3}\right)\delta w_j \quad (6.29)$$

Now, we can concisely write the integrals in our matrix form.

$$D_{ijj1} = \int_0^1 \Psi_i^u\Psi_j^{w\prime}\Psi_{j1}^{w\prime}\ d\xi \Rightarrow \mathbf{D} \quad (6.30)$$

$$G_{j1j2j3j} = \frac{1}{2}\int_0^1 \Psi_j^w \Psi_{j1}^{w\prime}\Psi_{j2}^{w\prime}\Psi_{j3}^{w\prime}\, d\xi \Rightarrow \mathbf{G} \tag{6.31}$$

$$H_{jj1} = \int_0^1 \Psi_j^w \Psi_{j1}^{w\prime}\, d\xi \Rightarrow \mathbf{H} \tag{6.32}$$

And finally the virtual work can be concisely written as follows.

$$\frac{L}{EI}\delta W^{NC_{aero}} = 2\sum_i \left(\Lambda \mathbf{Dww}\right)\delta u_i + 2\sum_j \left(-(\Lambda\mu)^{1/2}\mathbf{M}\dot{\mathbf{w}} - \Lambda\mathbf{Hw} + \Lambda\mathbf{Gwww}\right)\delta w_j \tag{6.33}$$

Now using the principle of virtual work and Lagrange's equations to apply these forces to Eqns. 6.1 and 6.2, we yield the following set of equations including the aerodynamic forces. Note that the terms which originated from our new β modification are noted by multiplying by a scalar δ_β, which can be set to one for calculations which include the β effect or zero for calculations which omit the β effect.

$$\ddot{\mathbf{u}} - \mathbf{A}\boldsymbol{\lambda} = 2\delta_\beta \Lambda \mathbf{D}\mathbf{w}^{\mathbf{2}} \tag{6.34}$$

$$\ddot{\mathbf{w}} + 2\boldsymbol{\zeta}\boldsymbol{\omega}\ \dot{\mathbf{w}} + \boldsymbol{\omega}^2\ \mathbf{w} - \mathbf{B}\mathbf{w}\boldsymbol{\lambda} + \mathbf{P}\ \mathbf{w}^{\mathbf{3}} = -2\left(\Lambda\mu\right)^{1/2}\dot{\mathbf{w}} - 2\Lambda\mathbf{Hw} + 2\delta_\beta\Lambda\mathbf{G}\mathbf{w}^{\mathbf{3}} \tag{6.35}$$

$$\mathbf{u} + \frac{1}{2}\mathbf{A}^{-1}\mathbf{Bww} = 0 \tag{6.36}$$

Third Order Piston Theory

The next step is to continue the expansion of piston theory to the third order form [5, 36]. We can rearrange Equation 6.6 as follows.

$$\Delta p = -2\frac{\rho_\infty U_\infty}{M_\infty}(\dot{w} + U_\infty\frac{\partial w}{\partial x})\left[1 + \frac{\gamma+1}{12}(\frac{\dot{w}}{a_\infty} + M_\infty\frac{\partial w}{\partial x})^2\right] \tag{6.37}$$

By assuming that $(\frac{\dot{w}}{a_\infty} + M_\infty \frac{\partial w}{\partial x})^2$ is small compared to 1, we arrive at Eqn. 6.19. However, if this term is not sufficiently small, it should be included in our formulations.

To demonstrate the scale of this term, we first simlify and rearrange the terms in brackets.

$$\Delta p = -2\frac{\rho_\infty U_\infty}{M_\infty}(\dot{w} + U_\infty \frac{\partial w}{\partial x}) \left[1 + \frac{M_\infty^2(\gamma+1)}{12}(\frac{\dot{w}}{U_\infty} + \frac{\partial w}{\partial x})^2\right] \tag{6.38}$$

Nondimensionalizing the terms in brackets allows their comparison with respect to 1.

$$\left[1 + \frac{M_\infty^2(\gamma+1)}{12}\left(\left(\frac{\mu}{\Lambda}\right)^{1/2}\dot{\overline{w}} + \frac{\partial \overline{w}}{\partial \xi}\right)^2\right]$$

Finally, if $\dot{\overline{w}}$ scales with characteristic frequency we are left with the following.

$$\left[1 + \frac{M_\infty^2(\gamma+1)}{12}\left(\left(\frac{\mu}{\Lambda}\right)\overline{\omega}^2\overline{w}^2 + 2\left(\frac{\mu}{\Lambda}\right)^{1/2}\overline{\omega w}\frac{\partial \overline{w}}{\partial x} + \left(\frac{\partial \overline{w}}{\partial x}\right)^2\right)\right]$$

Again, we note the order of each term.

$$M_\infty = O[1]$$
$$\mu = O[10^{-4}]$$
$$\Lambda = O[100]$$
$$\overline{\omega} = O[10]$$
$$\overline{w} = O[10^{-1}]$$
$$\frac{\partial \overline{w}}{\partial \xi} = O[10^{-1}]$$

This approximation then leads to the following orders of magnitude.

$$\left[1 + O[10^{-6}] + O[10^{-4}] + O[10^{-2}]\right]$$

Note that in our original derivation, we keep the $\left(\frac{\partial w}{\partial x}\right)^2$ term, so we will keep it here, but disregard the higher order terms. So, the third order piston theory may be appropriately simplified as follows.

$$\Delta p = -2\frac{\rho_\infty U_\infty}{M_\infty}(\dot{w} + U_\infty \frac{\partial w}{\partial x}) \left[1 + \frac{M_\infty^2(\gamma+1)}{12}\left(\frac{\partial w}{\partial x}\right)^2\right] \tag{6.39}$$

Note that the third order piston theory pressure is always larger than that given by first order theory. We can include the third order piston theory terms in the equation of motion by beginning again with Eq. 6.8 and substitute Eqn. 6.39 into Δp.

$$\begin{aligned}\delta W^{NC_{aero}} &= \int_0^L -b\Delta p\ \sin(\beta)\ \delta u + b\Delta p\ \cos(\beta)\ \delta w\ dx \\ &= -\int_0^L 2b\frac{\rho_\infty U_\infty}{M_\infty}\Big(\frac{\partial w}{\partial t} + U_\infty\frac{\partial w}{\partial x}\Big)\left[1 + \frac{M_\infty^2(\gamma+1)}{12}\left(\frac{\partial w}{\partial x}\right)^2\right] \\ &\qquad \times\Big(-\sin(\beta)\ \delta u + \cos(\beta)\ \delta w\Big)\ dx \end{aligned} \tag{6.40}$$

To reduce the complexity of the full equations, we can utilize the steps already taken in the First Order Piston Theory scaling analysis to truncate any higher order terms. By similar analysis, the following can be shown.

$$\begin{aligned}\frac{L}{EI}\delta W^{NC_{aero}} &= -\int_0^1 2\mu\left(\left(\frac{\Lambda}{\mu}\right)^{1/2}\frac{\partial \overline{w}}{\partial \overline{t}} + \frac{\Lambda}{\mu}\frac{\partial \overline{w}}{\partial \xi}\right)\left[1 + \frac{M_\infty^2(\gamma+1)}{12}\left(\frac{\partial \overline{w}}{\partial \xi}\right)^2\right] \\ &\qquad \times\Big(-\frac{\partial \overline{w}}{\partial \xi}\ \delta\overline{u} + \left(1 - 1/2\left(\frac{\partial \overline{w}}{\partial \xi}\right)^2\right)\ \delta\overline{w}\Big)\ d\xi \end{aligned} \tag{6.41}$$

$$\frac{L}{EI}\delta W^{NC_{aero}} = 2\int_0^1 \Bigg[\Bigg(\left(\Lambda\mu\right)^{1/2}\frac{\partial\overline{w}}{\partial\overline{t}}\frac{\partial\overline{w}}{\partial\xi} + \Lambda\left(\frac{\partial\overline{w}}{\partial\xi}\right)^2$$

$$+ \left(\Lambda\mu\right)^{1/2}\frac{M_\infty^2(\gamma+1)}{12}\frac{\partial\overline{w}}{\partial\overline{t}}\left(\frac{\partial\overline{w}}{\partial\xi}\right)^3 + \Lambda\frac{M_\infty^2(\gamma+1)}{12}\left(\frac{\partial\overline{w}}{\partial\xi}\right)^4\Bigg)\ \delta\overline{u}$$

$$+\Bigg(-\left(\Lambda\mu\right)^{1/2}\frac{\partial\overline{w}}{\partial\overline{t}} - \Lambda\frac{\partial\overline{w}}{\partial\xi} + \frac{1}{2}\left(\Lambda\mu\right)^{1/2}\frac{\partial\overline{w}}{\partial\overline{t}}\left(\frac{\partial\overline{w}}{\partial\xi}\right)^2 + \frac{1}{2}\Lambda\left(\frac{\partial\overline{w}}{\partial\xi}\right)^3$$

$$-\left(\Lambda\mu\right)^{1/2}\frac{M_\infty^2(\gamma+1)}{12}\frac{\partial\overline{w}}{\partial\overline{t}}\left(\frac{\partial\overline{w}}{\partial\xi}\right)^2 + \left(\Lambda\mu\right)^{1/2}\frac{M_\infty^2(\gamma+1)}{24}\frac{\partial\overline{w}}{\partial\overline{t}}\left(\frac{\partial\overline{w}}{\partial\xi}\right)^4$$

$$-\Lambda\frac{M_\infty^2(\gamma+1)}{12}\left(\frac{\partial\overline{w}}{\partial\xi}\right)^3 + \Lambda\frac{M_\infty^2(\gamma+1)}{24}\left(\frac{\partial\overline{w}}{\partial\xi}\right)^5\Bigg)\ \delta\overline{w}\Bigg]\ d\xi \quad (6.42)$$

This approximation then leads to the following orders of magnitude.

$$\frac{L}{EI}\delta W^{NC_{aero}} = 2\int_0^1 \Bigg[\left(O[10^{-2}] + O[10^{0}] + O[10^{-4}] + O[10^{-2}]\right)\ \delta\overline{u}$$

$$+\left(-O[10^{-1}] - O[10^{1}] + O[10^{-3}] + O[10^{-1}]\right.$$

$$\left.-O[10^{-3}] + O[10^{-5}] - O[10^{-1}] + O[10^{-3}]\right)\ \delta\overline{w}\Bigg]\ d\xi \quad (6.43)$$

We can neglect any terms of order $O[10^{-2}]$ or higher. So the nonconservative work becomes the following.

$$\frac{L}{EI}\delta W^{NC_{aero}} = 2\int_0^1 \Bigg[\Lambda\left(\frac{\partial\overline{w}}{\partial\xi}\right)^2\ \delta\overline{u}$$

$$+\Bigg(-\left(\Lambda\mu\right)^{1/2}\frac{\partial\overline{w}}{\partial\overline{t}} - \Lambda\frac{\partial\overline{w}}{\partial\xi} + \frac{1}{2}\Lambda\left(\frac{\partial\overline{w}}{\partial\xi}\right)^3 - \Lambda\frac{M_\infty^2(\gamma+1)}{12}\left(\frac{\partial\overline{w}}{\partial\xi}\right)^3\Bigg)\ \delta\overline{w}\Bigg]\ d\xi \quad (6.44)$$

Again substituting the modal expansions for u and w yields the following.

$$\frac{L}{EI}\delta W^{NC_{aero}} = 2\sum_i \left(\Lambda \sum_{j1}\sum_{j2} \int_0^1 \Psi_i^u \Psi_{j1}^{w\prime} \Psi_{j2}^{w\prime}\, d\xi\; w_{j1} w_{j2} \right) \delta u_i$$

$$+ 2\sum_j \left(-(\Lambda\mu)^{1/2} \sum_{j1} \int_0^1 \Psi_j^w \Psi_{j1}^w\, d\xi\; \dot{w}_{j1} - \Lambda \sum_{j1} \int_0^1 \Psi_j^w \Psi_{j1}^{w\prime}\, d\xi\; w_{j1} \right.$$

$$\left. + \Lambda \left(1 - \frac{M_\infty^2(\gamma+1)}{6}\right) \frac{1}{2} \sum_{j1}\sum_{j2}\sum_{j3} \int_0^1 \Psi_j^w \Psi_{j1}^{w\prime} \Psi_{j2}^{w\prime} \Psi_{j3}^{w\prime}\, d\xi\; w_{j1} w_{j2} w_{j3} \right) \delta w_j \quad (6.45)$$

Now, after transcribing the summation notation to our matrix notation, we have the following system of equations. Note that third order piston theory only adds one term, a function of M_∞ which was not already accounted for by first order piston theory. We will show that this term *increases* the pressure on the plate for a given Λ and M_∞.

$$\ddot{\mathbf{u}} - \mathbf{A}\boldsymbol{\lambda} = 2\delta_\beta \Lambda \mathbf{D}\mathbf{w}^{\mathbf{2}} \quad (6.46)$$

$$\ddot{\mathbf{w}} + 2\boldsymbol{\zeta}\boldsymbol{\omega}\, \dot{\mathbf{w}} + \boldsymbol{\omega}^2\, \mathbf{w} - \mathbf{B}\mathbf{w}\boldsymbol{\lambda} + \mathbf{P}\, \mathbf{w}^{\mathbf{3}} = -2\left(\Lambda\mu\right)^{1/2} \dot{\mathbf{w}} - 2\Lambda \mathbf{H}\mathbf{w} + 2\Lambda \left(\delta_\beta - \frac{M_\infty^2(\gamma+1)}{6}\right) \mathbf{G}\mathbf{w}^{\mathbf{3}} \quad (6.47)$$

$$\mathbf{u} + \frac{1}{2}\mathbf{A}^{-1}\mathbf{B}\mathbf{w}\mathbf{w} = 0 \quad (6.48)$$

6.3 Computational Methods

6.3.1 Modal Solution Method

Equations 6.46-6.48 are manipulated to form one equation for w, and this equation is solved with a 4th order Runge-Kutta time-marching integration scheme. The three independent parameters Λ, μ, and M_∞ are set by physical properties of a proposed experimental setup, as discussed in the Appendix.

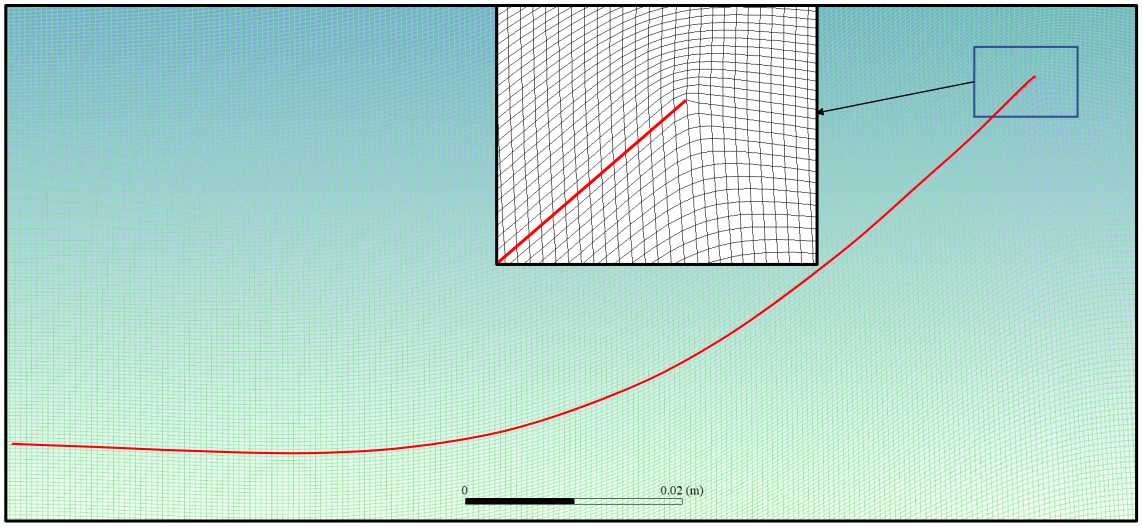

FIGURE 6.2: Deformed computational mesh at maximum beam deflection, $\Lambda = 71.75$

6.3.2 Euler Equation Validation Method

The Piston Theory aerodynamic model is validated for this configuration by comparison to the Euler equations computed with commercial CFD software ANSYS FLUENT 19.2[1]. The Fully Nonlinear model coupled with 3rd order Piston Theory was used to generate unsteady beam response during limit cycle oscillation, i.e. past flutter onset condition. The results were then utilized to prescribe wall motion in the computational domain. Five cases of freestream flow conditions are considered with static pressure parameter in the range of $67.75 \leq \Lambda \leq 71.75$, $M = 4$ and $\mu = 2\text{e}{-4}$.

6.4 Sensitivity of the Results

The results are presented in several sections to address several forms of sensitivites. First, we demonstrate the sensitivities to the number of modes and the time step for integration. Next, we present results which show sensitivities to the four key

[1] These computations, including mesh generation and deformation, are credited to coworkers Maxim Freydin and Kai Bastos. A sincere thanks for their efforts is due here.

nonlinear modeling components: structural nonlinearities stiffness and inertia; and aerodynamic nonlinearites due to higher (3rd) order Piston Theory and the nonlinear geometric modification, β. Finally, we present a sensitivity study of the key nondimensional parameters M_∞, Λ, and μ. We show that the model is highly sensitive to Λ, moderately sensitive to M_∞, but relatively insensitive to μ. However recall that M_∞ also appears implicitly in the definitions of Λ and μ.

6.4.1 Sensitivity to Number of Modes and Time Step of Integration

Before presenting LCO results, it should be reported that the sensitivity to parameters such as total numbers of modes as well as time steps of the integration scheme was determined to be negligible. After investigating several cases, it was determined that modal convergence was reached with 4 w, 6 u, and 6 λ modes. Using any more than these modes, the results are not significantly changed (RMS values differ less than 0.5%). It may be noted, however, that the time to complete a simulation grows with the number of w modes to the third power.

In addition, the time step was chosen as a constant in order to be more consistent across different cases when defining RMS values. To determine the necessary time step, MATLAB's ode45 solver was employed to use its adaptive time stepping ability, and then an appropriately small time step was chosen based upon these results. Again, a smaller time step was shown not to improve accuracy of the scheme. For each computation, the time step was $\bar{t} = 0.0018$ (dimensionless time units).

6.4.2 Nonlinear Modeling Sensitivities

A fully linear fluid-structural model harmonically decays when perturbed from rest in a subcritical flow where flow parameters are below a stability boundary, and exponentially oscillates to (±)infinity in a supercritical flow. However, from our nonlinear theory insights are gained from analyzing *bounded* limit cycle oscillations.

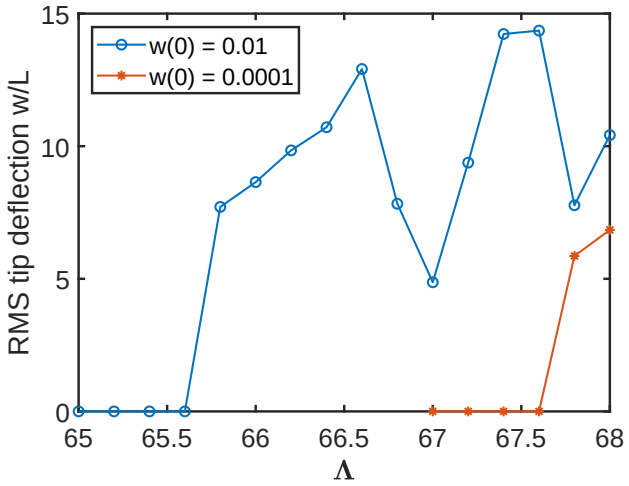

FIGURE 6.3: LCO amplitudes versus aerodynamic forcing levels for 1st order piston theory, $\delta_\beta = 0$, and fully nonlinear structure (FNS).

Originally, it was expected that the nonlinearities in the structural model would be strong enough to overcome flutter due to First Order Piston Theory, thereby leading to a bounded limit cycle oscillation (LCO). However, it can be seen in Fig. 6.3 that the LCO deflection response when normalized to beam length is much larger than 1, indicating that the model predicts behavior well beyond the physical system's realistic behavior. The results do, however, show an interesting phenomenon: that the initial conditions directly impact the flutter point. That is, for a small initial displacement of the beam ($w(0) = 0.0001$), the flutter point is larger than for a higher initial condition ($w(0) = 0.01$). This indicates a subcritical nonlinear bifurcation would occur at the flutter point of $\Lambda = 67.6$ and curve backwards towards the first nonzero point on the open-circled curve at $\Lambda = 65.8$.

Introducing the geometric modification to Piston Theory (the β effect) ensures that the pressure acts always normal to the plate surface. By including the nonlinear aerodynamic terms which are functions of β for First Order Piston Theory, the Limit Cycle Oscillation is much smaller and physically credible. Indeed even the

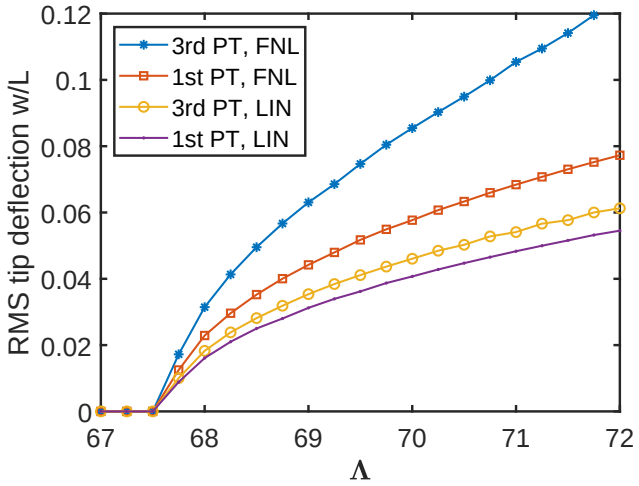

FIGURE 6.4: LCO amplitudes versus aerodynamic forcing levels for 3rd order versus 1st order nonlinear piston theory and linear (LIN) or fully nonlinear (FNL) structural models.

linear structural model response is bounded when coupled with this new aerodynamic model. These results can be seen in Figure 6.4, which plots the bifurcation diagram for several conditions and nonlinearities. Figure 6.4 includes the responses for the plate excited by First Order Piston Theory (1st PT) and Third Order Piston Theory (3rd PT) with this new β effect included, each aerodynamic model is considered with a fully nonlinear structural model (FNL) and a linear structural model (LIN). Because of the large deflection of the plate, it can be seen that the Third Order Piston Theory term is significant and increases the limit cycle amplitude. Also note that the nonlinear structural model increases the amplitude as well. This is due to the nonlinear inertia term dominating the nonlinear stiffness term. Finally, note the absence of any subcritical bifurcation.

To gain understanding of the sensitivities of the model to each of these different nonlinearities (aerodynamic and structural), cases were run with the several aerodynamic and structural terms either included or omitted. Table 6.1 concisely describes the limit cycle response of each case. The classification of "nonphysical" means

Table 6.1: Limit cycle classifications for different Piston Theory nonlinearities versus structural nonlinearities.

		Aerodynamics			
		$\mathcal{O}1$, $\delta_\beta = 0$	$\mathcal{O}1$, $\delta_\beta = 1$	$\mathcal{O}3$, $\delta_\beta = 0$	$\mathcal{O}3$, $\delta_\beta = 1$
Structure	Full nonlinear	non-physical	supercritical	unbounded	supercritical*
	NL inertia	non-physical	supercritical	unbounded	supercritical*
	NL stiffness	supercritical	supercritical	subcritical	supercritical
	Linear	—	supercritical	subcritical	supercritical

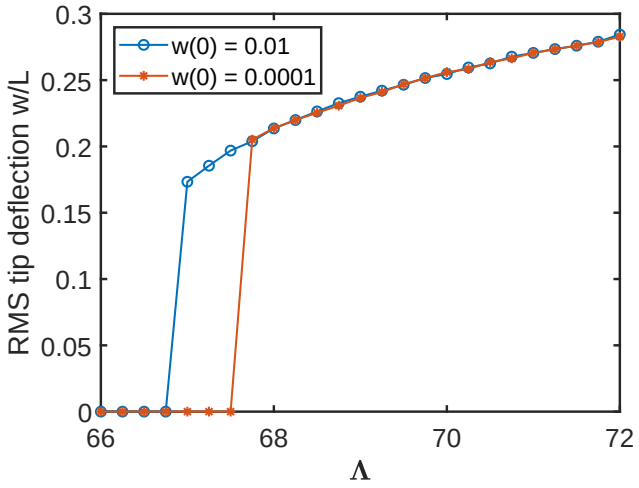

FIGURE 6.5: LCO amplitudes versus aerodynamic forcing levels for 3rd order piston theory, $\delta_\beta = 0$, and nonlinear stiffness as the only structural nonlinearity.

that the response is not physically plausible because of excessive displacement, e.g. $w/L > 1$. "Unbounded" signifies that the model's solution grows to infinity. "Supercritical" indicates that the LCO is stable for all Λ considered and the bifurcation is supercritical in nature, while "subcritical" indicates a stable LCO after a subcritical bifurcation, as seen in Figs. 6.3, 6.5, and 6.6. "Supercritical*" designates that the limit cycle is bounded for a limited range of Λ, and then grows to infinity for larger Λ.

The effects of the various structural nonlinearities are demonstrated in Fig. 6.7, which depicts the bifurcation diagram for Third Order Nonlinear Piston Theory

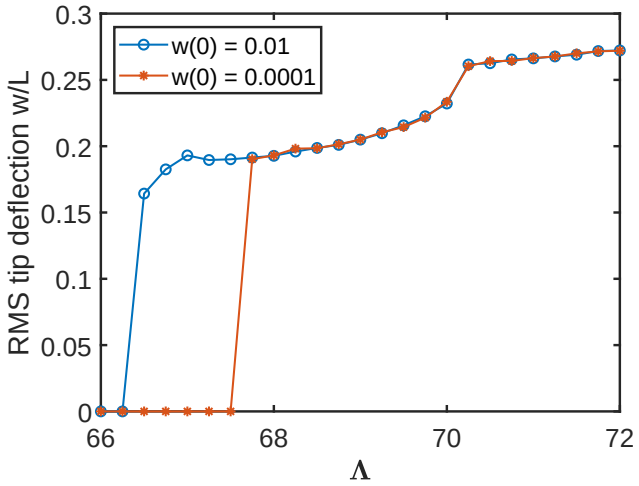

FIGURE 6.6: LCO amplitudes versus aerodynamic forcing levels for 3rd order piston theory, $\delta_\beta = 0$, and a linear structural model.

and $\delta_\beta = 1$. It can be seen that for the model with the inertia nonlinearity only (labeled "Inertia"), the amplitude is greatest. Opposing the inertia is the stiffness nonlinearity only case (labeled "Stiffness"), which when combined with the inertia only case becomes the Fully Nonlinear ("Full NL") case. Note that the nonlinear stiffness only case is similar to the linear structural case, and the stiffness nonlinearity only seems to influence the system when the amplitudes become large. Also note that the fully nonlinear and inertia nonlinearity plots do not continue across the entire range of Λ values. The plots are stopped when the RMS value is no longer bounded, but instead extends to infinity. The point at which this occurs can be related to the point at which Piston Theory is no longer applicable more broadly, which will be discussed later.

6.4.3 Nondimensional Physical Parameter Sensitivity

We now consider how the physical system behaves with respect to key nondimensional parameters, μ, Λ, and M_∞. Each of these cases are run with Third Order nonlinear piston theory with the β effect included ($\delta_\beta = 1$) and the fully nonlinear structural

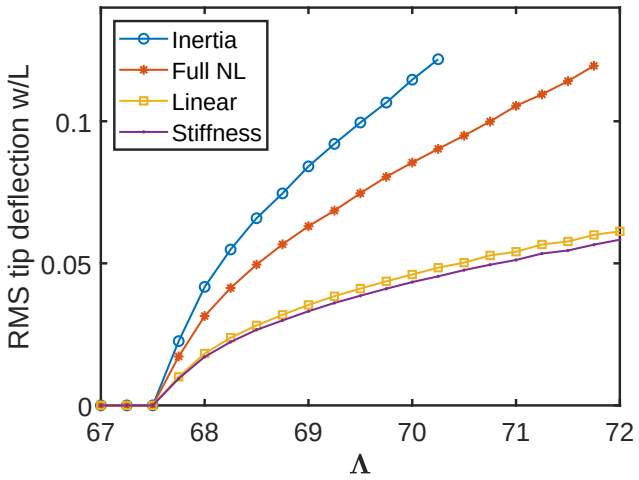

FIGURE 6.7: LCO amplitudes versus aerodynamic forcing levels for 3rd order piston theory, $\delta_\beta = 1$.

model. This is the most complete and physically realistic model considered in the present work.

The non-dimensionalization of the equations results in the most compact and efficient way of determining sensitivity of the results to the various physical parameters. Note that a "good choice" of non-dimensional parameters will reveal the order of importance of the non-dimensional parameters. In our present study the order is Λ (a ratio of aerodynamic to structural stiffness or compliance); M_∞ (Mach number) and μ (a ratio of fluid to structural mass).

Figure 6.8 illustrates the model's sensitivity to Λ and M_∞. Each curve pictures the limit cycle oscillation amplitude of a different Mach number flow as the fluid forcing (Λ) is increased. Note here the termination points of the plots for all flows. (Figure 6.8a is a zoomed in plot of Fig. 6.8b to show the termination of responses for Mach 4, 5, and 6 flow.) Beyond the values of Λ for which no solution is plotted, the solutions diverge towards infinity. This is at a different value for each Mach number; however, it is calculated that each curve's termination point occurs at $M_\infty *$

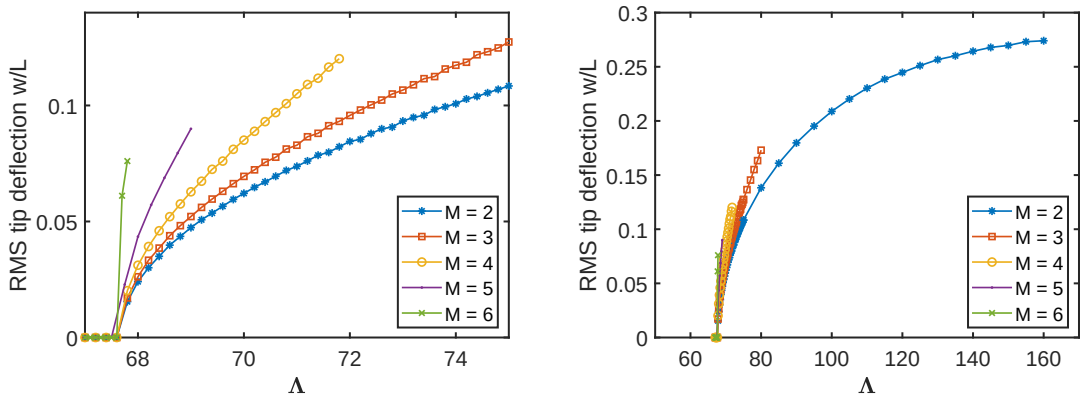

FIGURE 6.8: LCO amplitudes versus aerodynamic forcing levels across several Mach numbers, all for 3rd order Piston Theory, $\delta_\beta = 1$, and Fully Nonlinear Structure. Here, (a) is a zoomed in plot of (b).

(RMS of tip deflection) ≈ 0.5. This is significant since classical Piston Theory is said to be valid for $M_\infty \delta < 0.5$, where δ is a measure of structural slope or angle of attack. See the discussion in Lighthill [32]. In addition, it is of practical significance to note that our model is limited in its predictions for high Mach number post-critical behavior.

Note also that although Fig. 6.8 shows a strong dependence on Mach number, this is not the case for a model with only first order piston theory included. For first order piston theory, all of the effect of M_∞ is included in the definitions of μ and Λ and there is no separate dependence on Mach number per se. Indeed the bifurcation plots lay on top of one another for a first order piston theory model.

Figure 6.9 shows that there is modest dependence on the mass ratio μ. The range of $1 * 10^{-4} < \mu < 8 * 10^{-4}$ was chosen based on appropriate physical values given in Section 6.8. For all other computations, a value of $\mu = 2 * 10^{-4}$ is chosen.

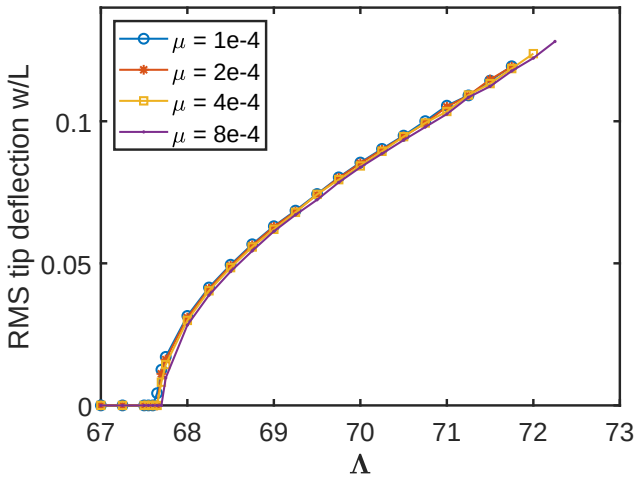

FIGURE 6.9: LCO amplitudes versus aerodynamic forcing levels across several values of μ, all for 3rd order Piston Theory, $\delta_\beta = 1$, and Fully Nonlinear Structure.

6.5 Aerodynamic Model Validation

Due to the significant differences between first order and third order Piston Theory results in Figure 6.4, one may rightfully ask the question of how valid is third order Piston Theory. To answer this question, the pressures on the beam as calculated by Piston Theory in the fully nonlinear aeroelastic computation are compared to those calculated from the Euler equations using a prescribed motion on the beam from the same aeroelastic case. A representative solution from the Euler calculations is shown in Fig. 6.10, where $\Lambda = 71.75$ and the deflection is at a maximum. Note that a shock forms on the surface turned towards the flow. At large deflections, the beam becomes analogous to a ramp, and a strong shock forms on the deflected surface. This is characteristic of each of these simulations, but the following results show that this does not result in greatly different pressures from third order Piston Theory, which interestingly is derived from the assumption that there are no shocks on the surface.

To compare Euler to Piston Theory, Fig. 6.11 illustrates the change in pressure

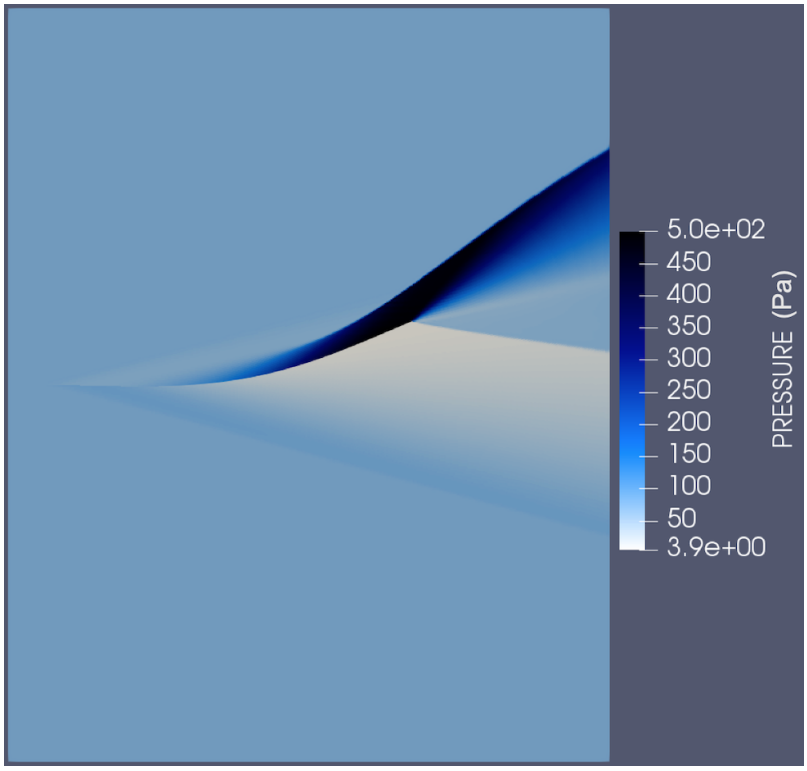

FIGURE 6.10: Pressures calculated from Euler solution at maximum deflection, $\Lambda = 71.75$

calculated from the three theories across the beam's length at a given instance in time for various values of Λ. The time step chosen is when the deflection is largest in the cycle. Note that the quantity of interest is the pressure as calculated in the aeroelastic case. Since the pressure was calculated without the effect of the beam moving in u direction, this effect is not included in these plots for the Piston Theory case. However, to compare to a higher fidelity model, the u deflection is considered for the Euler computation. Therefore these plots evaluate the Piston Theory method and its means of application.

To condense this information into one plot, Figure 6.12 shows the maximum aerodynamic work (Q_F) done on the beam's surface as the forcing function (and therefore the deflection) increases. Aerodynamic work is defined as $Q_F \equiv \int_0^L \Delta p(x) w_F(x)\, dx$

for the Piston Theory cases, where $w_F(x)$ is the vertical deflection of the beam at its peak deflection during a limit cycle oscillation. For the Euler case, aerodynamic work is defined as

$Q_F \equiv \int_0^{L+u(L)} \Delta p(x+u)\hat{w}_F(x+u)\ dx$, where $\hat{w}_F(x+u) \equiv w(x)$. Physically this accounts for the deflection of the beam including the u deflections in the Euler case. Note that because $u(L)$ is negative, the limits of integration are smaller for the Euler case than for the Piston Theory cases, which results in slightly more work done by 3rd order Piston Theory than that of Euler at large deflections, despite the pressures being similar.

Finally, Fig. 6.13 illustrates a representative plot of the change in pressure across the beam at a point at 80% of the beam length. Figure 6.13a shows one full deflection period in time and Fig. 6.13b shows the Fourier Transform of pressure, which illuminates the higher frequency behavior.

It can be seen from these figures that pressures from all three theories align at small deflections but differ at larger forcing functions and deflections. Indeed, in Fig. 6.12, at a value of $\Lambda = 67.75$ (where the rms tip deflection is small), the aerodynamic work values all differ by only about 2.5%. As the forcing function and thus the deflections increase, first order Piston Theory begins to differ from Euler and at finally all three differ at the highest forcing levels. Additionally, Fig. 6.13b shows that 1st order Piston Theory does not capture higher modal content, but 3rd order Piston Theory and Euler do.

It is interesting to note a subtle difference between Fig. 6.4 and Fig. 6.12. That is, the fully coupled aeroelastic results show that 1st order and 3rd order piston theory aerodynamics result in a relatively large difference in deflections, while the aerodynamic results of Fig. 6.12 show that the aerodynamic work is relatively close between the two theories, especially at small deflections. This indicates that the fully

aeroelastic solver is sensitive to changes in the aerodynamic model.

6.6 Conclusion

When modeling any physical system and certainly a fluid-structural (aeroelastic) system, it is important to study the sensitivity of the results to (1) the mathematical model of the physical system, (2) the parameters that appear in the mathematical model or which are considered in the design of an experimental model and (3) the accuracy of the numerical methods employed to extract solutions from the mathematical model. Each of these is considered in the present chapter.

The (3) accuracy of the numerical solution method is considered by doing a convergence study to insure that a sufficient number of structural modes are using in the computation and that the time step in the time marching scheme is sufficiently small.

The (2) sensitivity to the parameters of the mathematical/physical system is addressed by first identifying the essential non-dimensional parameters of the model. For the model considered here there are three such non-dimensional parameters. They are Λ, a ratio of aerodynamic forces to structural stiffness; μ, a ratio of fluid to structural mass; and M_∞, the Mach number. Indeed if the first order piston theory aerodynamic model is used, then only two parameters appear, namely Λ and μ, i.e. the Mach number does not appear explicitly as an independent parameter but is included implicitly in the definitions of Λ and μ. On the other hand if the third order piston theory is used then M_∞ appears as an independent parameter. The current example also illustrates a more general point, namely that the number of essential non-dimensional parameters depends on the mathematical/physical model adopted and the choice of these parameters (based upon a thorough analysis of the model and model results) can be such as to reduce the sensitivity of the model to the parameters. For example, it is found that the results are much less sensitive

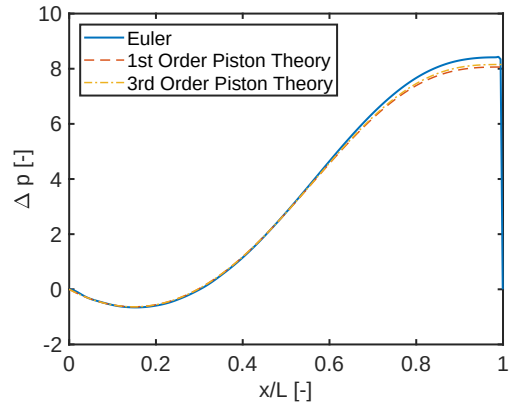

(a) $\Lambda = 67.75$

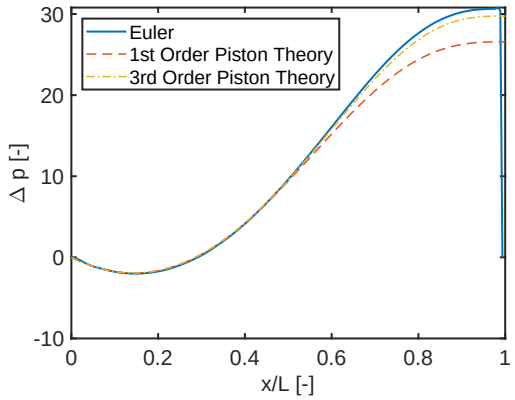

(b) $\Lambda = 68.75$

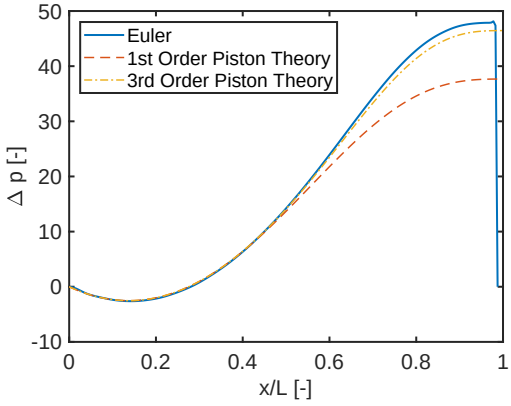

(c) $\Lambda = 69.75$

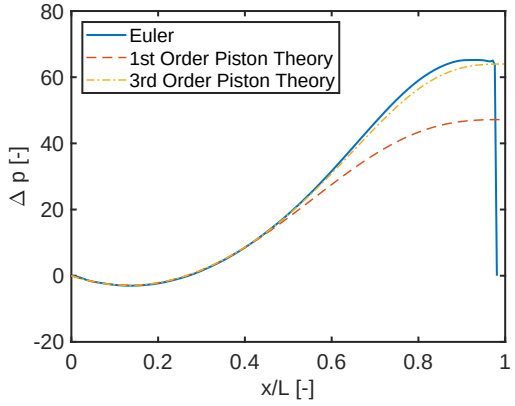

(d) $\Lambda = 70.75$

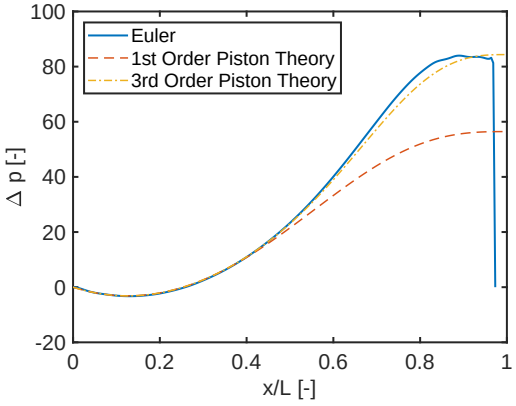

(e) $\Lambda = 71.75$

FIGURE 6.11: Change in pressure across the beam length calculated by Euler, 1st order and 3rd order Piston Theory for various levels of Λ.

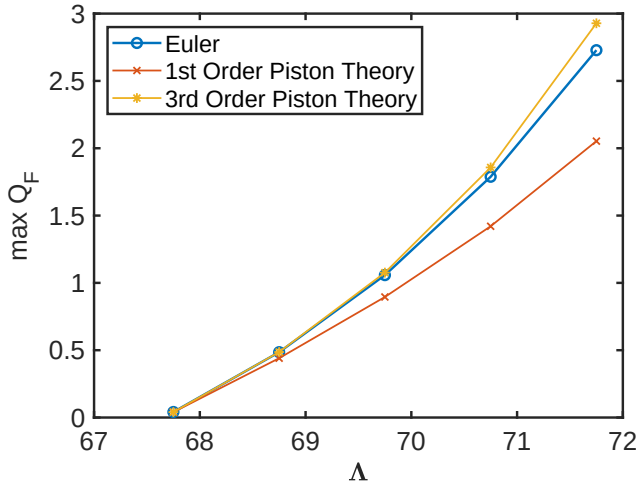

FIGURE 6.12: Aerodynamic work done on the beam for various fluid forcing levels.

to μ than to Λ and also by incorporating M_∞ into Λ and μ the sensitivity to M_∞ can also be reduced. On the other hand it is well to remember that the basic mathematical/physical model is only valid for a certain range of parameters. For example, in the present model, the Mach number must be sufficiently large compared to 1 for piston theory to be valid. How large is to some degree in the judgement of

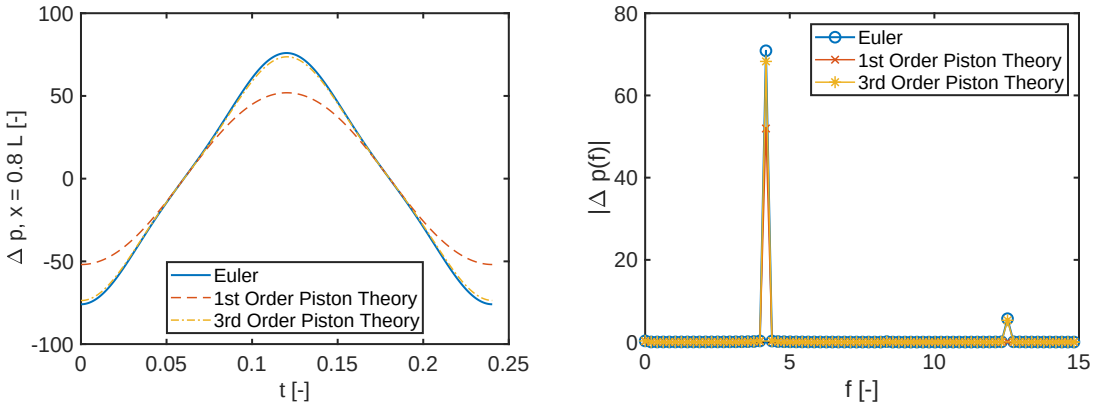

(a) (b)

FIGURE 6.13: Change in pressure at 80% beam length in (a) time space and (b) frequency space.

the analyst, but most investigators would say $M_\infty > 2$ should suffice. But then if M_∞ is too large other physical effects such as chemical reactions of the flow might be important or the effects of fluid viscosity might be important even at lower M_∞ and these are neglected in the present aerodynamic model. Also it is shown that even without these additional physical effects, the (third order) piston theory fails when the LCO response becomes too large, i.e. $M_\infty w/L > 1$.

Finally, even within the framework of the present mathematical/physical model, there are various physical effects that have greater or lesser impact on the model. That is, there is (1) sensitivity in the model to whether a completely linear theory is used or whether the effects of structural stiffness or inertial nonlinearity is included in the model. Also whether the effect of aerodynamic pressure acting normal to the instantaneous position of the mode is included (the β effect) or whether first or third order piston theory is included. All of these effects have been considered and discussed here. Indeed, our discussion of the Piston Theoretic pressures compared to Euler pressures show that the aeroelastic solution is highly dependent on the aerodynamic model, and therefore that third order Piston Theory is more appropriate for this configuration than first order.

Looking ahead, we note several future topics which may be explored. Firstly, due to symmetry of the flow over the structure, the second order aerodynamic terms from Piston Theory are omitted here, but could be important for other related configurations, e.g. flow over only one side of the structure or a structure with initial curvature or angle of attack. In addition, a study of the viscous and thermal effects may be of interest. Finally, a study using nonlinear plate theory for the structural model and this newly developed piston theory with follower effects for the aerodynamic model would also be valuable.

6.7 Appendix A: Nondimensionalizing the Structural Equations of Motion

Written dimensionally in previous chapters, the equations of motion are as follows.

$$0 = m \int_0^L \Psi_i^u \Psi_i^u \, dx \, \ddot{u}_i - \sum_k \lambda_k \int_0^L \Psi_i^{w\prime} \Psi_k^\lambda \, dx \tag{6.49}$$

$$\begin{aligned} 0 =& m \int_0^L \Psi_j^w \Psi_j^w \, dx \, \ddot{w}_j + 2m\zeta_j\omega_j \int_0^L \Psi_j^w \Psi_j^w \, dx \, \dot{w}_j + \omega_j^2 m \int_0^L \Psi_j^w \Psi_j^w \, dx \, w_j \\ & - \sum_k \sum_{j1} \int_0^L \Psi_k^\lambda \Psi_{j1}^{w\prime} \Psi_j^{w\prime} \, dx \, \lambda_k \, w_{j1} \\ & + EI \sum_{j1} \sum_{j2} \sum_{j3} \int_0^L (\Psi_{j1}^{w\prime\prime} \Psi_{j2}^{w\prime\prime} \Psi_{j3}^{w\prime} \Psi_j^{w\prime} + \Psi_{j1}^{w\prime\prime} \Psi_{j2}^{w\prime} \Psi_{j3}^{w\prime} \Psi_j^{w\prime\prime}) \, dx \, w_{j1} w_{j2} w_{j3} \end{aligned} \tag{6.50}$$

$$0 = \sum_i u_i \int_0^L \Psi_k^\lambda \Psi_i^{w\prime} \, dx + \frac{1}{2} \sum_{j1} \sum_{j2} w_{j1} w_{j2} \int_0^L \Psi_k^\lambda \Psi_{j1}^{w\prime} \Psi_{j2}^{w\prime} \, dx \tag{6.51}$$

The system of equations now can be nondimensionalized as follows, using definitions of the matrices and the nondimensional parameters given in Section 6.2.1. First, consider Eqn. 6.49.

$$\begin{aligned} 0 &= mL\mathbf{M_u} \frac{EI}{mL^3} \ddot{\mathbf{u}} - \mathbf{A} \frac{EI}{L^2} \boldsymbol{\lambda} \\ 0 &= \mathbf{M_u} \ddot{\mathbf{u}} - \mathbf{A}\boldsymbol{\lambda} \\ 0 &= \ddot{\mathbf{u}} - \mathbf{A}\boldsymbol{\lambda} \end{aligned} \tag{6.52}$$

Here, the final simplification is true if we normalize the modes such that $\mathbf{M_u} = I$.

Next, consider Eqn. 6.50.

$$
\begin{aligned}
0 =& mL\mathbf{M_w}\frac{EI}{mL^3}\ \ddot{\mathbf{w}} + 2m\boldsymbol{\zeta}\Big(\frac{EI}{mL^4}\Big)^{1/2}\boldsymbol{\omega}L\mathbf{M_w}\Big(\frac{EI}{mL^4}\Big)^{1/2}L\ \dot{\mathbf{w}} \\
&+ \Big(\frac{EI}{mL^4}\Big)\boldsymbol{\omega}^2 mL\mathbf{M_w}L\ \mathbf{w} - \Big(\frac{EI}{L^2}\Big)L^{-1}\mathbf{B}L\mathbf{w}\boldsymbol{\lambda} + \Big(\frac{EI}{L^5}\Big)\mathbf{P}L^3\ \mathbf{www} \\
0 =& \mathbf{M_w}\frac{EI}{L^2}\ \ddot{\mathbf{w}} + 2\boldsymbol{\zeta}\Big(\frac{EI}{L^2}\Big)\boldsymbol{\omega}\mathbf{M_w}\ \dot{\mathbf{w}} + \Big(\frac{EI}{L^2}\Big)\boldsymbol{\omega}^2\mathbf{M_w}\ \mathbf{w} \\
&- \Big(\frac{EI}{L^2}\Big)\mathbf{B}\mathbf{w}\boldsymbol{\lambda} + \Big(\frac{EI}{L^2}\Big)\mathbf{P}\ \mathbf{www} \\
0 =& \mathbf{M_w}\ \ddot{\mathbf{w}} + 2\boldsymbol{\zeta}\boldsymbol{\omega}\mathbf{M_w}\ \dot{\mathbf{w}} + \boldsymbol{\omega}^2\mathbf{M_w}\ \mathbf{w} - \mathbf{B}\mathbf{w}\boldsymbol{\lambda} + \mathbf{P}\ \mathbf{www} \\
0 =& \ddot{\mathbf{w}} + 2\boldsymbol{\zeta}\boldsymbol{\omega}\ \dot{\mathbf{w}} + \boldsymbol{\omega}^2\ \mathbf{w} - \mathbf{B}\mathbf{w}\boldsymbol{\lambda} + \mathbf{P}\ \mathbf{w^3}
\end{aligned}
\tag{6.53}
$$

Where again the final step is true if $\mathbf{M_w} = I$.

Lastly, consider Eqn. 6.51.

$$
\begin{aligned}
0 &= \mathbf{A}L\mathbf{u} + \frac{1}{2L}\mathbf{B}L^2\mathbf{ww} \\
0 &= \mathbf{Au} + \frac{1}{2}\mathbf{Bww} \\
0 &= \mathbf{u} + \frac{1}{2}\mathbf{A}^{-1}\mathbf{Bww}
\end{aligned}
\tag{6.54}
$$

Summarizing, we can succinctly write the unforced equations of motion, rearranging the zeros on the right hand side to signify the absence of forcing.

$$
\boxed{\begin{aligned}
\ddot{\mathbf{u}} - \mathbf{A}\boldsymbol{\lambda} &= 0 \qquad (6.55)\\
\ddot{\mathbf{w}} + 2\boldsymbol{\zeta}\boldsymbol{\omega}\ \dot{\mathbf{w}} + \boldsymbol{\omega}^2\ \mathbf{w} - \mathbf{B}\mathbf{w}\boldsymbol{\lambda} + \mathbf{P}\ \mathbf{w^3} &= 0 \qquad (6.56)\\
\mathbf{u} + \frac{1}{2}\mathbf{A}^{-1}\mathbf{Bww} &= 0 \qquad (6.57)
\end{aligned}}
$$

6.8 Appendix B: Typical Model Physical Properties

Structural Properties:

$$b = 0.04m$$

$$h = 0.0001m;$$

$$L = 0.1m;$$

$$\rho = 2770kg/m^3;$$

$$E = 71\text{x}10^9 Pa;$$

$$I = bh^3/(12(1 - 0.33^2));$$

$$EI = E * I;$$

$$m = \rho bh;$$

Air Properties:

$$112 \leq T_0 \leq 120K$$

$$R = 287.058J/(kg - K)$$

$$\gamma = 1.4$$

$$2 \leq M_\infty \leq 6$$

$$74 \leq p_\infty \leq 81$$

$$p_0 = p_\infty(1 + 0.2M_\infty^2)^{(\gamma/(\gamma-1))}$$

$$\frac{\rho U_\infty}{M_\infty} = \frac{p_0\sqrt{\gamma}}{\sqrt{RT_0}}(1 + 0.2M_\infty^2)^{(-1/(\gamma-1))}(1 + 0.2M_\infty^2)^{(-1/2)}$$

$$\frac{\rho U_\infty^2}{M_\infty} = \gamma p_\infty M_\infty$$

7

A Note on Euler vs Piston Theory Pressure Calculations for an Oscillating Cantilevered Plate in Supersonic/Hypersonic Axial Flow

7.1 Introduction

In the classic text by Hayes and Probstein on Hypersonic Flow Theory [37], it is established that at sufficiently high Mach number, the flow over a streamlined body may be considered to occur in transverse slabs and the flow in each slab can indeed be considered as the flow in a piston. Note that for an axisymmetric body the piston may be in the form of a ring that is moving transverse to the body in a ring like deformation. For a wing like planar body the effects of three dimensional flow may be neglected provided that $\beta * AR$ is sufficiently greater than 1 where $\beta = (M^2 - 1)^{1/2}$ and AR is the wing aspect ratio. For even moderate AR this product will be large in the hypersonic range. Thus each "piston" acts locally at a point on a wing. The question is in what range of flight parameters does this transverse slab approximation hold?

Motivated by the results of the previous chapter, a thorough investigation into

Piston Theory and its envelope of utility is of interest. It was shown that third order Piston Theory predicts pressures that are in agreement with an Euler solver[1] in a small range of Mach numbers and surface slopes. In this chapter, we expand this range and compare pressures from Euler simulations and two ways of calculating Classical Third Order Piston Theory. From these results, a new theory is presented.

Piston Theory, introduced by Lighthill [32] and formalized as an aeroelasticity tool by Ashley and Zartarian [33], is widely used to calculate pressures on airfoils in supersonic flow [35, 36, 66].

As explained by Lighthill, simple wave theory (Eqn. 7.1) predicts pressures in the following form if no shock wave is present.

$$\frac{p_2}{p_1} = \left(1 + \frac{\gamma - 1}{2}\frac{w}{a_1}\right)^{2\gamma/(\gamma-1)} \tag{7.1}$$

Lighthill's 3rd order Classical Piston Theory, Eqn. 7.2, is an expansion of simple wave theory, Eqn. 7.1, and it is widely used because it is capable of *explicitly* predicting pressures from given values of the piston or transverse airfoil motion.

$$\frac{p_2}{p_1} = 1 + \gamma\frac{w}{a_1} + \frac{\gamma(\gamma+1)}{4}\left(\frac{w}{a_1}\right)^2 + \frac{\gamma(\gamma+1)}{12}\left(\frac{w}{a_1}\right)^3 \tag{7.2}$$

If a shock wave is present, however, the shock expansion theory accounts for changes across the shock and relates pressure on the piston face to speed of the moving body more accurately. As per Liepmann and Roshko [38], the speed of the piston is related to the pressure difference across the shock and on the face of the piston as in Eqn. 7.3. Note that now the pressure is written *implicitly* with respect

[1] The Euler CFD computations, including mesh generation and deformation, are credited to coworkers Maxim Freydin and Kai Bastos. A sincere thanks for their efforts is due here.

to the transverse velocity (downwash) of the airfoil, w.

$$\frac{w}{a_1} = \frac{1}{\gamma}\left(\frac{p_2}{p_1} - 1\right)\left(\frac{\frac{2\gamma}{\gamma+1}}{\frac{p_2}{p_1} + \frac{\gamma-1}{\gamma+1}}\right)^{1/2} \tag{7.3}$$

Lighthill showed good agreement between the third order approximation and both the simple wave theory and the shock expansion theory when $-1 < w/a_1 < 1$. However for some applications the magnitude of w/a_1 may be greater than this limit, and defining the true range of Piston Theory and proposing changes to the theory has been the subject of several researchers.

Ashley [33] noted this limitation, stating that "the surface can nowhere be inclined too sharply to the direction of U [freestream velocity] and that normal velocities produced by the unsteady motion must be limited in comparison with the speed of sound." Zhang, et al. [67] developed "Local Piston Theory," a method in which the mean flow parameters are determined by a steady Euler solution and unsteady effects are considered by applying Piston Theory locally along the airfoil. Dowell and Bliss [68] expanded unsteady potential flow theory in terms of inverse Mach number to expand the usable range of Piston Theory.

The nature of this work, however, is slightly different than these predecessors. Rather than being used as a tool to predict flutter margins, Piston Theory is employed here to drive a limit cycle oscillation of a nonlinear plate undergoing large deflection. Therefore, Local Piston Theory may not be viable if the motion is too large, as the amplitude of deflection may cause the mean flow parameters to change throughout one period of oscillation. Therefore, this work aims to characterize the range of Classical Piston Theory when applied to an elastic structure undergoing large deflections.

To do this, we investigate the pressures on an inextensible cantilevered plate in

axial flow due to a prescribed large elastic motion. The pressures calculated by third order piston theory are compared to pressures calculated by an Euler CFD solver. The prescribed constant amplitude, simple harmonic structural motion, is shown in Fig. 7.1. This motion is determined by first running the fully-coupled, nonlinear modal aeroelastic solver described in Chapter 6. Note that the axes are to scale, and that the deflection is on the order of the plate length, and therefore the plate deflection in the horizontal component is non-negligible. It is interesting and pertinent to note that in the modal aeroelastic solver, only deflection in the vertical component is considered when evaluating the aerodynamic pressure—rather than deflection in the horizontal and vertical components—which results in a diminished value of the slope of the plate. To understand this difference, the pressure calculated by third order piston theory in the modal solver is also compared to the pressures calculated by third order piston theory and Euler on the true deflection.

Figure 7.2 shows the downwash ratio, w/a_1, along the plate length when the plate is at its maximum deflection, considering deflection in the horizontal component. Mach numbers for the cases described here are $M = 4, 4.5,$ and 5, and the maximum downwash ratio examined here is $w/a_1 = 2.13$, more than double Lighthill's recommended range for piston theory.

7.2 Euler vs 3rd Order Piston Theory Results

Figure 7.3 shows the pressure difference across the plate, normalized to the freestream static pressure, along the length of the plate. Here the plate is at its maximum deflection amplitude in the oscillation. The legend label "PT3" is third order piston theory computed *with* the horizontal displacement, and "PT3 AE" is that calculated *without* the horizontal displacement, as the aeroelastic solver normally would. For all three Mach numbers considered, third order piston theory computes higher pressure differentials than the Euler solver does near the plate's free edge where the downwash

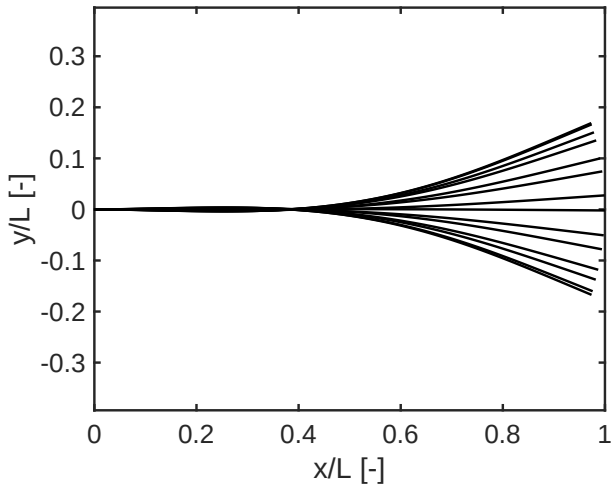

FIGURE 7.1: Plate deflection over one period

ratio is greatest. Interestingly, when calculated without the horizontal displacement, piston theory agrees better with the Euler pressures, even at these large deflections. This appears to be due to a cancellation of effects.

Figure 7.4 shows the pressure differential at the plate's free edge throughout one period of oscillation. Again, third order piston theory results in higher pressures than the Euler solver, but the aeroelastic solver would compute pressures closer to

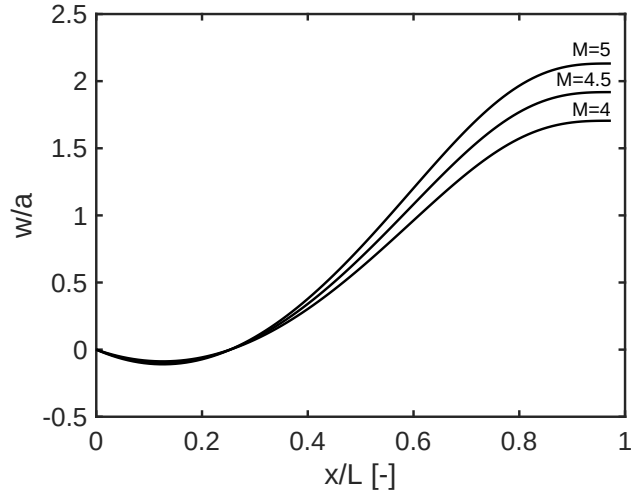

FIGURE 7.2: Downwash ratio across length of deflected plate for Mach numbers 4, 4.5, and 5

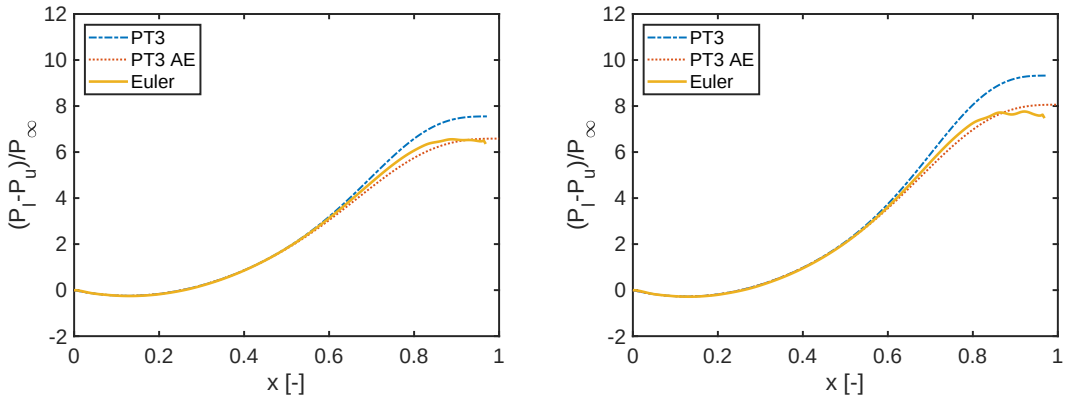

(a) Mach 4

(b) Mach 4.5

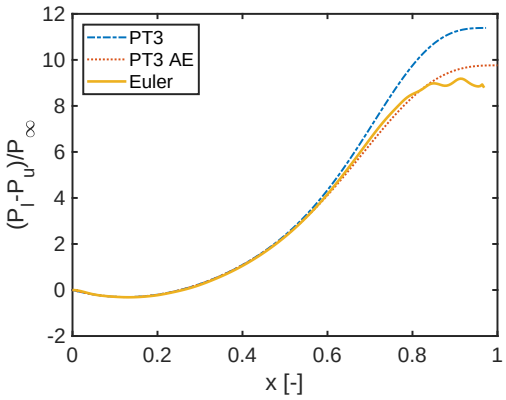

(c) Mach 5

FIGURE 7.3: Pressure values across the plate at maximum deflection

those computed by the Euler solution.

Figures 7.3 and 7.4 are interesting because they show agreement to a large degree between third order piston theory and an Euler solution, but this result is even more intriguing when noting that the corresponding Euler solution has a complex flow field. Figure 7.5 shows the pressure field around the plate at its maximum deflection for the Mach 4 case. A shock can be seen forming from a coalescence of the pressure gradient on the top of the plate. Piston theory, stemming from Eqn. 7.1, does not account for shocks on the surface and makes the assumption that each differential element along the surface is independent of the surrounding flow field, corresponding

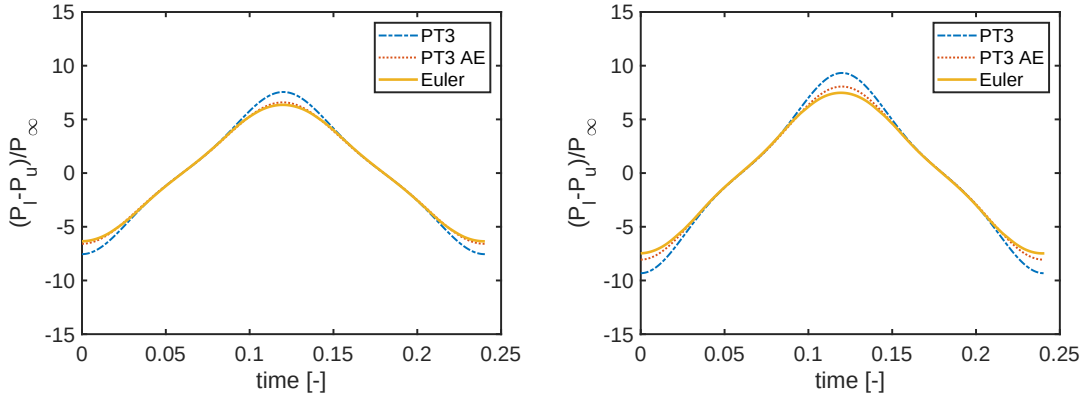

(a) Mach 4

(b) Mach 4.5

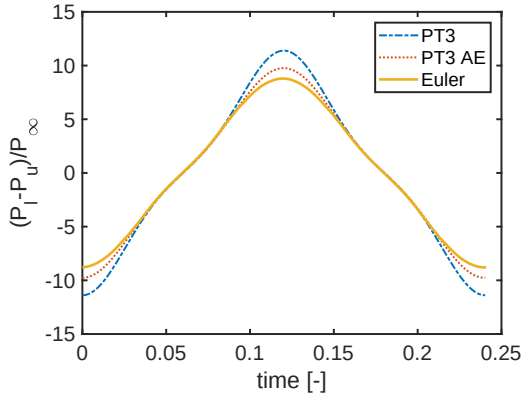

(c) Mach 5

FIGURE 7.4: Pressure across the plate at the free end across one period of oscillation

to a flow that behaves as if in a one-dimensional piston.

Finally, it may be noted that Lighthill's recommendation for piston theory's valid range of use is supported by this work. Lighthill suggested that the downwash ratios should be within $-1 < w/a_1 < 1$ and that the Mach number times a characteristic slope should be less than 1. Both of these conditions may be checked with the present results. The pressure calculations begin to diverge from one another around 60% beam length, and Fig. 7.2 shows that at this point, $w/a_1 \approx 1$. Similarly, at this point, the slopes are such that the Mach number times the slope is approximately 1. This also supports the idea that further development of piston theory is needed to

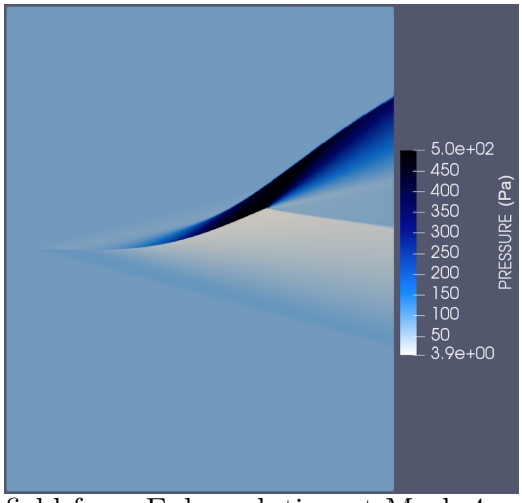

FIGURE 7.5: Pressure field from Euler solution at Mach 4 and maximum deflection

predict pressures on very large deflection cases such as a cantilevered plate in axial flow at high Mach numbers.

7.3 A Generalization of Piston Theory to Very Large Motions

To generalize Piston Theory to very large motion, several ideas are presented. First, a method is presented for expanding Eqn. 7.3 to third order in a form similar to Eqn. 7.2. The final form is referenced throughout literature as the Busemann expansion, but the primary source has not been identified, so we share our method herein. Define $p_2/p_1 = \Delta p/p_1 + 1$ where $\Delta p = p_2 - p_1$. Therefore, 7.3 becomes

$$\left(\frac{2\gamma}{\gamma+1}\right)^{-1/2} \gamma \frac{w}{a_1} = \frac{\Delta p}{p_1}\left(\frac{\Delta p}{p_1} + 1 + \frac{\gamma-1}{\gamma+1}\right)^{-1/2} \tag{7.4}$$

Dividing the right side through by $\left(1+\frac{\gamma-1}{\gamma+1}\right)^{-1/2}$ yields

$$\left(\frac{2\gamma}{\gamma+1}\right)^{-1/2} \gamma \frac{w}{a_1} = \left(1+\frac{\gamma-1}{\gamma+1}\right)^{-1/2} \frac{\Delta p}{p_1}\left(\frac{\Delta p}{p_1}\left(1+\frac{\gamma-1}{\gamma+1}\right)^{-1} + 1\right)^{-1/2}$$

Note the following definition.

$$\left(\frac{2\gamma}{\gamma+1}\right) = \frac{\gamma+1+\gamma-1}{\gamma+1} = 1+\frac{\gamma-1}{\gamma+1} \equiv \eta \tag{7.5}$$

Now 7.3 is written

$$\eta^{-1/2}\gamma\frac{w}{a_1} = \eta^{-1/2}\frac{\Delta p}{p_1}\left(\frac{\Delta p}{p_1}\eta^{-1}+1\right)^{-1/2}$$

$$\gamma\frac{w}{a_1} = \frac{\Delta p}{p_1}\left(\frac{\Delta p}{p_1}\eta^{-1}+1\right)^{-1/2} \tag{7.6}$$

This expression can be expanded in a Taylor Series of $\frac{\Delta p}{p_1}\eta^{-1}$.

$$\gamma\frac{w}{a_1} = \frac{\Delta p}{p_1}\left(1-\frac{1}{2}\frac{\Delta p}{p_1}\eta^{-1}-\frac{\frac{1}{2}\left(-\frac{3}{2}\right)}{2}\left(\frac{\Delta p}{p_1}\eta^{-1}\right)^2-\frac{\frac{1}{2}\left(-\frac{3}{2}\right)\left(-\frac{5}{2}\right)}{6}\left(\frac{\Delta p}{p_1}\eta^{-1}\right)^3+HOT\right)$$

So, this can be expressed as linear, quadratic, and cubic expansions.

Linear:

$$\gamma\frac{w}{a_1} = \frac{\Delta p}{p_1}$$

Quadratic:

$$\gamma\frac{w}{a_1} = \frac{\Delta p}{p_1}-\frac{1}{2}\left(\frac{\Delta p}{p_1}\right)^2\eta^{-1}$$

Cubic:

$$\gamma\frac{w}{a_1} = \frac{\Delta p}{p_1}-\frac{1}{2}\left(\frac{\Delta p}{p_1}\right)^2\eta^{-1}+\frac{3}{8}\left(\frac{\Delta p}{p_1}\right)^3\eta^{-2}$$

Because pressure is desired as a function of position w, the ansatz is made that

$$\frac{\Delta p}{p_1} = C_1\frac{w}{a_1}+C_2\left(\frac{w}{a_1}\right)^2+C_3\left(\frac{w}{a_1}\right)^3 \tag{7.7}$$

From the linear case, it is clear that $C_1 = \gamma$. Equating the quadratic expansion to the ansatz, it can be shown that $C_2 = \frac{1}{2}\frac{\gamma^2}{\eta}$. From the cubic equality, $C_3 = \frac{\gamma^3}{8\eta^2}$. Now, the expression for the pressure change reads.

$$\frac{\Delta p}{p_1} = \gamma\frac{w}{a_1} + \frac{1}{2}\frac{\gamma^2}{\eta}\left(\frac{w}{a_1}\right)^2 + \frac{\gamma^3}{8\eta^2}\left(\frac{w}{a_1}\right)^3$$

Substituting the expressions for η and Δp, the explicit form of shock expansion theory becomes the following.

$$\frac{p_2}{p_1} = 1 + \gamma\frac{w}{a_1} + \frac{\gamma(\gamma+1)}{4}\left(\frac{w}{a_1}\right)^2 + \frac{\gamma(\gamma+1)^2}{32}\left(\frac{w}{a_1}\right)^3 \tag{7.8}$$

This is expressed as Eqn. 7.3.2 in Hayes and Probstein [37] as the Busemann Expansion. Note that Equations 7.2 and 7.8 are identical to second order and only modestly different even to third order Classical Piston Theory as Lighthill [32] has noted.

At very large positive downwash ($w/a_1 > 1$), however, even this formulation for shock expansion is insufficient. Therefore, another modification to 7.3 may be made assuming that $p_2/p_1 \gg 1$. First, define $\epsilon = 1/(p_2/p_1)$ and then rearrange Eqn. (2) to perform a binomial expansion where $\epsilon \ll 1$.

$$\begin{aligned}\frac{w}{a_1} &= \frac{1}{\gamma}\left(\frac{1}{\epsilon} - 1\right)\left(\frac{\frac{2\gamma}{\gamma+1}}{\frac{1}{\epsilon} + \frac{\gamma-1}{\gamma+1}}\right)^{1/2} \\ &= \frac{1}{\gamma}\left(\frac{2\gamma}{\gamma+1}\right)^{1/2}\left(\frac{1-\epsilon}{\epsilon^{1/2}}\right)\left(1 + \epsilon\frac{\gamma-1}{\gamma+1}\right)^{-1/2}\end{aligned} \tag{7.9}$$

Now, the radius of convergence for a Taylor series expansion of $(1+x)^{-1/2}$ is $-1 < x \leq 1$. Ignoring that ϵ has no physical relevance when negative, this means that the expansion for Eqn. 7.9 converges while $0 < \epsilon \leq (\gamma+1)/(\gamma-1)$. Or, when $(\gamma-1)/(\gamma+1) \leq p_2/p_1$. For air, this expansion therefore converges when $p_2/p_1 \geq 1/6$, which is true for all positive w/a_1.

To order ϵ, this expansion is written as follows.

$$\begin{aligned}\frac{w}{a_1} &= \frac{1}{\gamma}\left(\frac{2\gamma}{\gamma+1}\right)^{1/2}\left(\frac{1-\epsilon}{\epsilon^{1/2}}\right)\left(1-\frac{1}{2}\epsilon\frac{\gamma-1}{\gamma+1}+\mathcal{O}(\epsilon^2)\right)\\ &= \frac{1}{\gamma}\left(\frac{2\gamma}{\gamma+1}\right)^{1/2}\left(1-\left(1+\frac{1}{2}\frac{\gamma-1}{\gamma+1}\right)\epsilon+\mathcal{O}(\epsilon^2)\right)\epsilon^{-1/2}\end{aligned} \tag{7.10}$$

Now, square both sides and neglect any terms of order ϵ^2 or greater since $\epsilon \ll 1$.

$$\left(\frac{w}{a_1}\right)^2 = \left(\frac{2}{\gamma(\gamma+1)}\right)\frac{1}{\epsilon} - \left(\frac{2}{\gamma(\gamma+1)}\right)\left(2+\frac{\gamma-1}{\gamma+1}\right)$$

From the definition of ϵ, we are left with an expression for the pressure ratio which we will call Large Pressure Shock Expansion Theory.

$$\frac{p_2}{p_1} = \frac{\gamma(\gamma+1)}{2}\left(\frac{w}{a_1}\right)^2 + 2 + \frac{\gamma-1}{\gamma+1} \tag{7.11}$$

It can be shown that this is equivalent to Eqn. 7.3.4 in Hayes and Probstein [37] for the pressures given by the Tangent Wedge Approximation. This is interesting because to derive the Tangent Wedge Approximation, oblique shock relations are used. Here, simpler 1-dimensional wave equations are used to derive the same result.

However, it will be shown that at high ϵ, or rather low p_2/p_1 values, this expansion does not converge and therefore more terms are needed.

To order ϵ^2, the expansion is as follows.

$$\begin{aligned}\frac{w}{a_1} &= \frac{1}{\gamma}\left(\frac{2\gamma}{\gamma+1}\right)^{1/2}\left(\frac{1-\epsilon}{\epsilon^{1/2}}\right)\left(1-\frac{1}{2}\epsilon\frac{\gamma-1}{\gamma+1}+\frac{3}{8}\epsilon^2\left(\frac{\gamma-1}{\gamma+1}\right)^2+\mathcal{O}(\epsilon^3)\right)\\ &= \frac{1}{\gamma}\left(\frac{2\gamma}{\gamma+1}\right)^{1/2}\left(1-\left(1+\frac{1}{2}\frac{\gamma-1}{\gamma+1}\right)\epsilon\right.\\ &\quad\left.+\left(\frac{1}{2}\left(\frac{\gamma-1}{\gamma+1}\right)+\frac{3}{8}\left(\frac{\gamma-1}{\gamma+1}\right)^2\right)\epsilon^2+\mathcal{O}(\epsilon^3)\right)\epsilon^{-1/2}\end{aligned} \tag{7.12}$$

Now, neglect any terms of order ϵ^3 and square both sides.

$$\left(\frac{w}{a_1}\right)^2 = \left(\frac{2}{\gamma(\gamma+1)}\right)\left(\frac{1}{\epsilon} - \left(2+\frac{\gamma-1}{\gamma+1}\right) + \left(1+2\frac{\gamma-1}{\gamma+1}+\left(\frac{\gamma-1}{\gamma+1}\right)^2\right)\epsilon\right)$$

Substitute p_1/p_2 back in for ϵ.

$$\left(\frac{w}{a_1}\right)^2 = \left(\frac{2}{\gamma(\gamma+1)}\right)\left(\frac{p_2}{p_1} - \left(2+\frac{\gamma-1}{\gamma+1}\right) + \left(1+2\frac{\gamma-1}{\gamma+1}+\left(\frac{\gamma-1}{\gamma+1}\right)^2\right)\frac{p_1}{p_2}\right)$$

Multiply both sides by p_2/p_1.

$$\left(\frac{w}{a_1}\right)^2 \frac{p_2}{p_1} = \left(\frac{2}{\gamma(\gamma+1)}\right)\left(\left(\frac{p_2}{p_1}\right)^2 - \left(2+\frac{\gamma-1}{\gamma+1}\right)\frac{p_2}{p_1} + \left(1+2\frac{\gamma-1}{\gamma+1}+\left(\frac{\gamma-1}{\gamma+1}\right)^2\right)\right)$$

Collecting terms in powers of p_2/p_1 and dividing by $2/(\gamma(\gamma+1))$, this becomes

$$0 = \left(\frac{p_2}{p_1}\right)^2 - \left(\frac{\gamma(\gamma+1)}{2}\left(\frac{w}{a_1}\right)^2 + 2 + \frac{\gamma-1}{\gamma+1}\right)\frac{p_2}{p_1} + \left(1+2\frac{\gamma-1}{\gamma+1}+\left(\frac{\gamma-1}{\gamma+1}\right)^2\right)$$

By the quadratic theory, the next order expansion of the Large Pressure Shock Expansion Theory can finally be written as follows.

$$\frac{p_2}{p_1} = \frac{1}{2}\left(\frac{w}{a_1}\right)^2\frac{\gamma(\gamma+1)}{2} + \frac{1}{2}\left(2+\frac{\gamma-1}{\gamma+1}\right)$$
$$\pm\frac{1}{2}\sqrt{\left(\frac{\gamma(\gamma+1)}{2}\right)^2\left(\frac{w}{a_1}\right)^4 + \left(2+\frac{\gamma-1}{\gamma+1}\right)\gamma(\gamma+1)\left(\frac{w}{a_1}\right)^2 - \frac{\gamma-1}{\gamma+1}\left(4+3\frac{\gamma-1}{\gamma+1}\right)} \tag{7.13}$$

Note that the first two terms are one half of those of the first order expansion, Eqn. 7.11. This scaling is corrected by the terms within the square root. Also note that the terms in the square root become negative at sufficiently small values of w/a_1. For air, Eqn. 7.13 is valid for $w/a_1 > 0.33$.

7.4 Comparison of Theories

Lighthill's table showing values of pressure for a larger range of w/a_1 can be expanded to include these new formulations of shock expansion theory. See Table 1. Note that Eqns. 7.2 and 7.8 are closely similar as Lighthill anticipated. Also note that results for Eqns. 7.11 and 7.13 are only given where this formulation is valid, i.e. large positive downwash.

It is for larger magnitudes of the w/a_1 (positive or negative) that the differences among the several models are more pronounced. First consider Fig. 7.6, which plots 7.1 along with expansions up to 7.2. (Note that the minimum downwash ratio occurs when $p_2 = 0$, i.e. when $w/a_1 = -2/(\gamma - 1)$, which occurs at $w/a_1 = -5$ for air.) It can be seen that for magnitudes of w/a_1 greater than say 2, Third Order Classical Piston Theory (Eqn. 7.2) is inaccurate.

Now if a shock is expected on the airfoil surface, Shock Expansion Theory (Eqn. 7.3) may be used to predict the pressure, but the question is can 3rd Order Shock Expansion Theory (Eqn. 7.8) be used to model these pressures as an explicit function of the downwash or piston speed. The differences between these two theories, as well as Simple Wave Theory (Eqn. 7.1) and Classical Third Order Piston Theory (Eqn. 7.2) are shown in Fig. 7.7. The values of the various theories differ less than a percent for $-1 < w/a_1 < 1$. For $w/a_1 = 2$, the explicit shock expansion is only 5% off the implicit shock expansion value, as compared with a 10% difference between Simple Wave and Classical Piston Theories. However note that for $w/a_1 = 5$, the explicit shock expansion is 37% off the implicit shock expansion value, and the cubic expansion of the simple wave theory is 45% off of the implicit value.

These discrepancies at high positive downwash can be resolved by using the proposed Large Pressure Shock Expansions, Eqn. 7.11 or 7.13. Figure 7.8 shows that for $2 < w/a_1 < 5$ (and assuredly beyond), these formulations are more accurate in

Table 7.1: Pressure to downwash relations for several theories

w/a_1	SWT	1st Ord. CPT	2nd Ord. CPT	3rd Ord. CPT	SET	3rd Ord. SET	Large SET	2nd Ord. Large SET
5	128.0	8.000	29.00	64.00	44.14	60.50	44.17	44.14
2	10.54	3.800	7.160	9.400	8.734	9.176	8.887	8.731
1	3.583	2.400	3.240	3.520	3.473	3.492	3.847	3.452
0.5	1.949	1.700	1.910	1.945	1.941[1]	1.942	–	1.8515
0	1.000	1.000	1.000	1.000	1.000	1.000	–	–
-0.5	0.478	0.300	0.510	0.475	0.479[1]	0.479	–	–
-1	0.210	-0.400	0.440	0.160	0.207[1]	0.188	–	–
-2	0.028	-1.800	1.560	-0.680	-0.014	-0.456	–	–
-5	0	-6.000	15.00	-20.00	-0.136	-16.5	–	–

[1] Lighthill's original table contains modestly different numbers than those calculated here. The original table reads 1.916, 0.488, 0.220 for w/a_1 values of 0.5, -0.5, and -1, respectively.
SWT = Simple Wave Theory, Eqn. 7.1, CPT = Classical Piston Theory, Eqn. 7.2, SET = Shock Expansion Theory, Eqn. 7.3, 3 O SET = Eqn. 7.8, Large SET = Eqn. 7.11, 2nd Ord. Large SET = Eqn. 7.13.

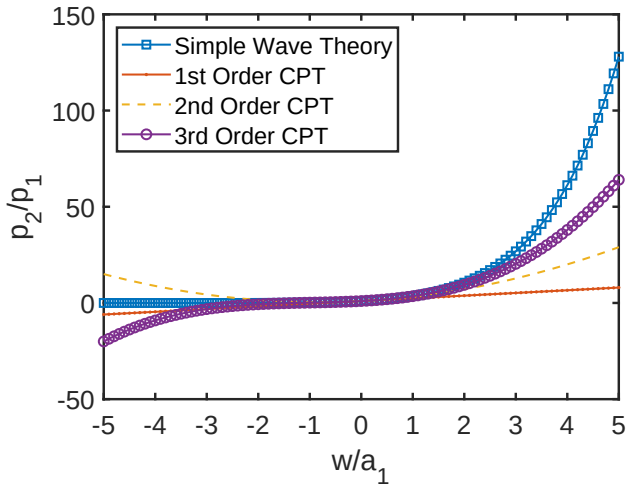

FIGURE 7.6: Pressure change versus piston speed for 7.1 and its expansions up to 7.2.

comparison to the implicit Shock Expansion (Eqn. 7.3) than the third order Shock Expansion (Eqn. 7.8). Figure 7.8b is a zoomed in plot of Fig. 7.8a, and shows the difference between the 1st and 2nd order expansions of Large Pressure Shock Expansion Theory, Eqns. 7.11 versus 7.13. Note that 1st order Large Shock Expansion does not converge to the Implicit Shock Expansion function until about $w/a_1 > 2$, whereas the 2nd order Large Shock Expansion is suitable from $0.5 \leq w/a_1$.

Note also that for negative values of w/a_1, the piston is being withdrawn from the fluid and creating an expansion front into the fluid on the top piston face and a shock expansion on the bottom piston face. On the top face, the simple wave theory is most appropriate as explained in Liepmann and Roshko [38] and Lighthill [32]. And on the bottom the shock expansion theory is more appropriate. The converse is true for positive w/a of course. The implication of this is that for an airfoil with flow over both top and bottom sides, the pressure on top side and the pressure on the bottom side should be computed by two distinct piston models for large w/a_1.

From Figure 7.7, it can be seen that neither the explicit shock expansion theory nor 3rd Order CPT closely models the simple wave expansion or implicit shock

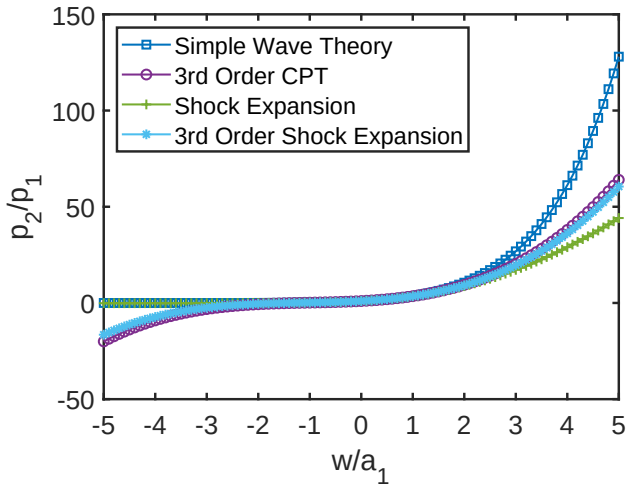

FIGURE 7.7: Pressure change versus piston speed for 7.1, 7.2, 7.3, and 7.8.

expansion for $-5 < w/a_1 \lessapprox -1.4$. In this range, both series expansions result in negative pressure ratios, which is physically impossible. It may be noted here that for the best pressure calculation of a face with an expansion front, simple wave theory with negative w/a_1 should be used. However, in practice, for $w/a_1 \lessapprox -1.4$, p_2/p_1 could be simply set to zero on this face.

7.5 Predicting Pressures from Prescribed Body Motion

Returning to the prescribed motion cases of Section 7.2, we now compare these three formulations (Eqns. 7.8, 7.11, 7.13) to Classical Piston Theory and Euler.

It should be noted that while the Large Pressure Shock Expansion Theory still provides a local spatial relationship between the downwash, w, and the pressure, one must keep track of whether, for a given (top or bottom) surface, w/a_1 is greater or less than zero. This is a complication beyond Classical Piston Theory for aeroelastic applications, but not an insurmountable one. By coupling several of these theories together, using separate theories on discrete areas of the plate based on the downwash, we can create a new Enhanced Piston Theory.

To summarize then, for the face of the piston moving into the fluid, one uses Eqn.

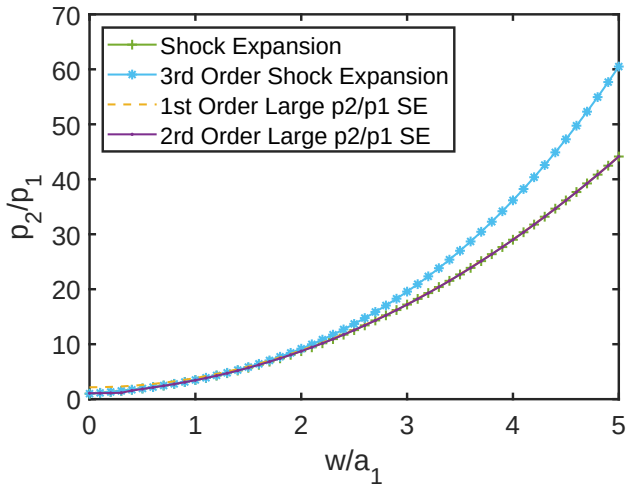

(a)

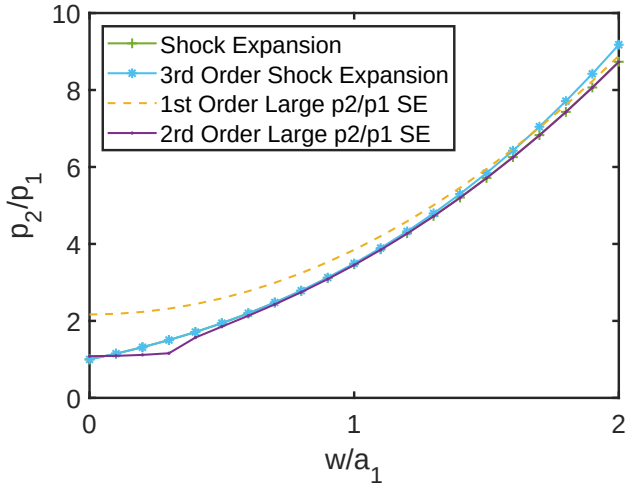

(b)

FIGURE 7.8: Pressure change versus piston speed for 7.3, 7.8, and 7.11.

7.3 or its approximations 7.8, 7.11 or 7.13, and for the face moving away from the fluid one uses Eqn. 7.1 or its approximation 7.2 (noting that w/a_1 is negative by the fluid sign convention). However in the wing application there is always a top and bottom surface. So if the wing is moving up, Eqn. 7.3,7.8, 7.11 or 7.13 is used for the top surface with w/a_1 taken as positive and Eqn. 7.1 or 7.2 is taken for the bottom surface with w/a_1 negative. Conversely if the wing is moving down, then Eqn. 7.1

or 7.2 is used for the top surface with w/a_1 taken as negative and Eqn. 7.3, 7.8, 7.11 or 7.13 is used for for the bottom surface with w/a_1 taken as positive.

To know whether any one point on the wing is moving up or down relative to the fluid, one must compute the downwash $w = \frac{\partial f}{\partial t} + U_\infty \left(\frac{\partial f}{\partial x}\right)$ to determine its sign. Up to third order in the various expansions (Eqns. 7.2 and 7.8), the signs are taken care of automatically, but for very large motions the above protocol must be followed.

In Figs. 7.9 and 7.10, pressure predictions are shown on the surface from Fig. 7.3c, the flapping cantilevered plate at Mach 5. Figure 7.9 shows the Euler result in yellow and the 3rd order Classic Piston Theory result greatly varying from it at the free end of the plate. This is corrected by the Enhanced Piston Theory, but there is not much difference between the use of 1st and 2nd order Large Pressure Shock Expansion for this case. Figure 7.10 removes the 1st order Enhanced Piston Theory model and instead shows the 3rd order Explicit Shock Expansion and the 3rd order Piston Theory from the aeroelastic model, where the horizontal component of deflection is neglected. It can be seen that the 3rd order Shock Expansion does not approximate the pressure well at the free end, but that the aeroelastic case of Piston Theory does a very good job, and is nearly indistinguishable from the Enhanced Piston Theory. However, for a general case of prescribed motion or geometry, this is not a feasible modeling technique, and therefore the Enhanced Piston Theory is argued to be the best theory when compared to Euler.

Enhanced Piston Theory, when compared to Classical Piston Theory, is more accurate at large deflections but also has one disadvantage. That is that the theory on the surface of the body must be made piece wise. In Figs. 7.9 and 7.10, the Enhanced Piston Theory was only applied when the downwash ratio was at or above a threshold of where Classical Piston Theory matched with Enhanced Piston Theory. Therefore, to use this theory for prescribed geometry is easy. However in an aeroelastic setting, this becomes more computationally taxing but not impossi-

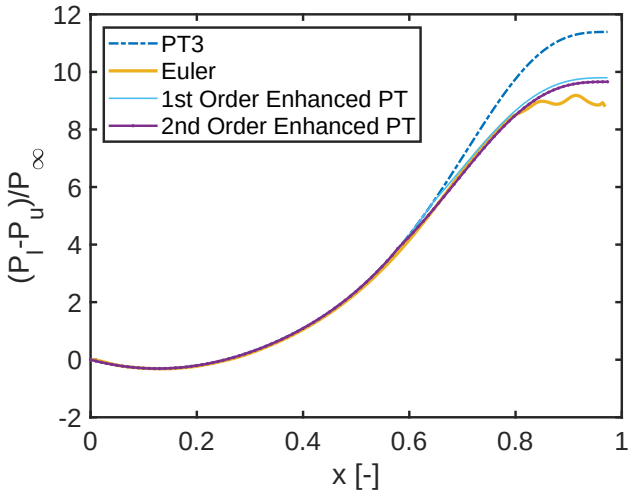

FIGURE 7.9: Comparison of Pressure predictions from 3rd order Classical Piston Theory, Euler CFD, and 1st and 2nd order Enhanced Piston Theory

ble. The deflections of the body would need to be calculated at each time step to determine which theory to use where, and then the generalized forces would need to be integrated appropriately. Indeed it is quite remarkable that for the case explored here, the "extensible" aeroelastic Piston Theory matches with this new theory so well without this shortcoming.

7.6 Conclusions

Classical Piston Theory has been analyzed as a tool for pressure predictions on largely deflected surfaces. Using the prescribed motion of a cantilevered plate experiencing a limit cycle oscillation in axial flow, pressures from Piston Theory were compared to those computed by an Euler CFD code and found that at large deflections, Piston Theory fails to adequately model the pressures. To remedy this, three other solutions are proposed. One is known as the Busemann approximation, another is called Enhanced Piston Theory, and a third is a higher order approximation of the Enhanced Piston Theory. It was found that the Busemann approximation was insufficient, but both orders of the Enhanced Piston Theory matched the Euler solutions up to the

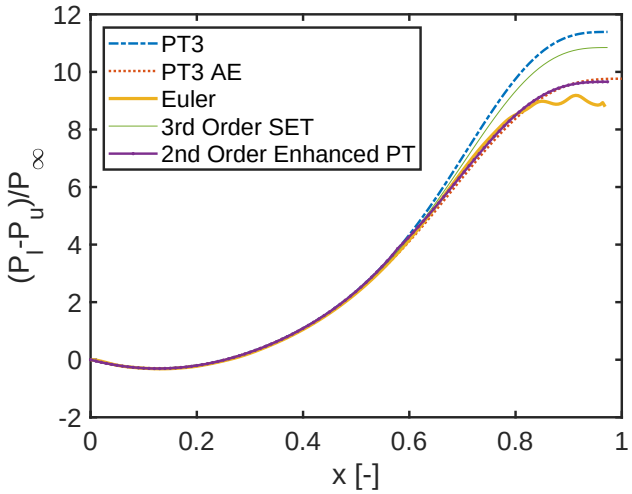

FIGURE 7.10: Comparison of Pressure predictions from 3rd order Classical Piston Theory, aeroelastic 3rd order Classical Piston Theory, Euler CFD, 3rd order Explicit Shock Expansion Theory, and 2nd order Enhanced Piston Theory

downwash ratio limit studied.

This new Enhanced Piston Theory is useful especially in cases of prescribed motion, but may also be useful in a modal aeroelastic code with some increase in computational effort. Interestingly, the pressures derived by the aeroelastic code (which did not consider longitudinal deflection and therefore had smaller slopes than the true geometry) used for generating the prescribed motion were almost equivalent to this new theory. However, this may be coincidental and limited only to the case explored here.

8

Nonlinear Responses of the Inextensible Cantilevered Plate Undergoing Large Deflections

8.1 Introduction

Following the work of the inextensible beam, the present chapter explores the natural extension of the inextensible plate. There is ample classical literature on plate theory, including the notable book by Leissa [69] as the standard reference for linear modes and frequencies and the work of Dowell [70] which describes the equations of motion of plates in the context of aeroelasticity. More recently, there are substantial works by Lacarbonara [42] and Pai [39] which describe various plate theories and their approximations. Even among these exhaustive texts, however, there is a notable lack of material on the use of the inextensibility assumptions to simplify plate theory for plates with cantilevered or free boundary conditions.

Early work on the inextensible plate by Mansfield [71] inspired the work of Simmonds and Libai [9, 10], both of which use one-dimensional generator curves—a line of zero curvature—to derive equations of motion. While Mansfield's early work results in one equation of motion, Simmonds and Libai show a series of 13 differential

equations.

A different method to treat the inextensible plate is introduced by Tang et al. [8], in which Hamilton's principle is used to derive the equations of motion from the energy associated with the displacement of the plate. The potential energy used is from the fundamental strain energies derived by Novozhilov [15]. The Rayleigh-Ritz method is used to write the expressions in a modal form. This method is used in the current work beginning from the potential energy expressions given in Tang et al. [8]. The difference in the current work may be found in the treatment of kinetic energy. Whereas Tang et al. simplify the kinetic energy using the inextensibility constraint to write longitudinal displacements u and v in terms of transverse displacement w, here two Lagrange multipliers are used to enforce inextensibility within the kinetic energy. This method offers the benefit that the kinetic energy is now integrated across the entire domain rather than at a certain location in the plane, and therefore the integration of the mode shapes may be computed prior to the computer simulation.

To validate the current model, we compare static nonlinear results with a nonlinear ANSYS Finite Element model. Inspired by the work of Pai et al. [41], who derived a geometrically exact finite element model for a thin plate, we analyze a plate with the same parameters and some of the same forcing conditions. It is found that the current model matches well with the finite element method for loading cases in which bending is the dominant mode, and that the agreement is less accurate for a torsion loading and response. Indeed Pai et al. [41] demonstrate buckling of a plate for a certain torsion loading, and the current model does not predict such behavior under the same loads.

It is therefore proposed that the assumptions from which potential energy is derived by Tang et al. [8] are not compatible with one another and therefore the potential energy should be reconsidered. For the inextensibility conditions to be enforced, the model must allow for in-plane shear, whereas the expressions given in

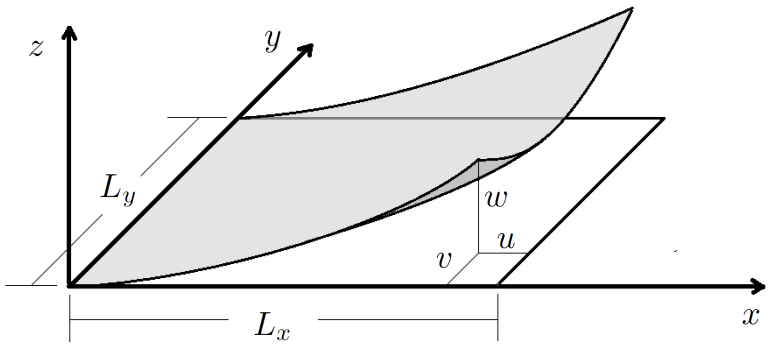

FIGURE 8.1: Plate Schematic

Tang et al. [8] include a no-shear assumption. Therefore, the potential energy for the inextensible plate is derived again with no restriction on in-plane shear.

8.2 Methods

Figure 8.1 shows the schematic of the cantilevered plate. Note that the three deflections u, v, and w correspond to plate motion in the x, y, and z directions, respectively, and the clamped edge is along the y axis, with the other three edges remaining free.

8.2.1 Lagrange's Equations

To derive the equations of motion, we use the Lagrange equations for the transverse (w) and longitudinal (u and v) coordinates, as well as the Lagrange multipliers λ_u and λ_v which enforce the inextensibility constraints. Note that there are two constraints, corresponding to the inextensibility in both x and y coordinates.

$$\frac{\partial}{\partial t}\left(\frac{\partial \mathcal{L}}{\partial \dot{q}_n}\right) - \frac{\partial \mathcal{L}}{\partial q_n} = Q_n \tag{8.1}$$

$$\mathcal{L} = T - V + \int_0^{L_y}\int_0^{L_x} \lambda_u f_u \, dx \, dy + \int_0^{L_y}\int_0^{L_x} \lambda_v f_v \, dx \, dy \tag{8.2}$$

$$T = \frac{1}{2}\int_0^{L_y}\int_0^{L_x} m[\dot{u}^2 + \dot{v}^2 + \dot{w}^2]\, dx\, dy \tag{8.3}$$

$$V = \frac{1}{2}\int_0^{L_y}\int_0^{L_x} \frac{Eh^3}{12(1-\nu^2)}\left[1 + \left(\frac{\partial w}{\partial x}\right)^2 + \left(\frac{\partial w}{\partial y}\right)^2\right]$$
$$\times\left[\left(\frac{\partial^2 w}{\partial x^2}\right)^2 + \left(\frac{\partial^2 w}{\partial y^2}\right)^2 + 2\nu\frac{\partial^2 w}{\partial x^2}\frac{\partial^2 w}{\partial y^2} + 2(1-\nu)\left(\frac{\partial^2 w}{\partial x \partial y}\right)^2\right] dx\, dy \tag{8.4}$$

$$f_u = \frac{\partial u}{\partial x} + \frac{1}{2}\left(\frac{\partial w}{\partial x}\right)^2 = 0 \tag{8.5}$$

$$f_v = \frac{\partial v}{\partial y} + \frac{1}{2}\left(\frac{\partial w}{\partial y}\right)^2 = 0 \tag{8.6}$$

Note that Eqn. 8.4 is the expression for potential energy proposed by Tang et al. [8].

8.2.2 Nondimensionalization

Before deriving the equations of motion from Lagrange's equations, we nondimensionalize the parameters in the following way. Note that the overlined terms are dimensionless and that f_u and f_v are already dimensionless parameters.

$$x = \overline{x}L_x \quad y = \overline{y}L_y \quad u = \overline{u}L_x \quad v = \overline{v}L_x \quad f_u = \overline{f_u} \quad f_v = \overline{f_v}$$

$$\lambda_u = \frac{D}{L_x^2}\overline{\lambda_u} \quad \lambda_v = \frac{D}{L_x^2}\overline{\lambda_v} \quad t = \left(\frac{mL_x^4}{D}\right)^{1/2}\overline{t}$$

The final two terms in Eqn. 8.2 can be written as follows.

$$\int_0^{L_y}\int_0^{L_x} \lambda_u f_u \; dx \; dy = L_x L_y \int_0^1 \int_0^1 \frac{D}{L_x^2} \overline{\lambda_u f_u} \; d\overline{x} \; d\overline{y} = \frac{D L_y}{L_x} \int_0^1 \int_0^1 \overline{\lambda_u f_u} \; d\overline{x} \; d\overline{y} \tag{8.7}$$

$$\int_0^{L_y}\int_0^{L_x} \lambda_v f_v \; dx \; dy = L_x L_y \int_0^1 \int_0^1 \frac{D}{L_x^2} \overline{\lambda_v f_v} \; d\overline{x} \; d\overline{y} = \frac{D L_y}{L_x} \int_0^1 \int_0^1 \overline{\lambda_v f_v} \; d\overline{x} \; d\overline{y} \tag{8.8}$$

The kinetic energy term can be written in the following manner after nondimensionalizing the spatial components as well as the time derivatives.

$$T = \frac{D L_y}{L_x} \frac{1}{2} \int_0^1 \int_0^1 [\dot{\overline{u}}^2 + \dot{\overline{v}}^2 + \dot{\overline{w}}^2] \; d\overline{x} \; d\overline{y} = \frac{D L_y}{L_x} \overline{T} \tag{8.9}$$

So it can be seen that the dimensionless kinetic energy is

$$\overline{T} = \frac{1}{2} \int_0^1 \int_0^1 [\dot{\overline{u}}^2 + \dot{\overline{v}}^2 + \dot{\overline{w}}^2] \; d\overline{x} \; d\overline{y} \tag{8.10}$$

The potential energy can be written as follows.

$$\begin{aligned} V = {} & \frac{1}{2} D L_x L_y \int_0^1 \int_0^1 \left[1 + \left(\frac{\partial \overline{w}}{\partial \overline{x}} \right)^2 + \left(\frac{\partial \overline{w}}{\partial \overline{y}} \right)^2 \right] \\ & \times \left[\frac{1}{L_x^2} \left(\frac{\partial^2 \overline{w}}{\partial \overline{x}^2} \right)^2 + \frac{L_x^2}{L_y^4} \left(\frac{\partial^2 \overline{w}}{\partial \overline{y}^2} \right)^2 + 2 \frac{1}{L_y^2} \nu \frac{\partial^2 \overline{w}}{\partial \overline{x}^2} \frac{\partial^2 \overline{w}}{\partial \overline{y}^2} + 2 \frac{1}{L_y^2} (1 - \nu) \left(\frac{\partial^2 \overline{w}}{\partial \overline{x} \partial \overline{y}} \right)^2 \right] d\overline{x} \; d\overline{y} \\ = {} & \frac{1}{2} D \int_0^1 \int_0^1 \left[1 + \left(\frac{\partial \overline{w}}{\partial \overline{x}} \right)^2 + \left(\frac{\partial \overline{w}}{\partial \overline{y}} \right)^2 \right] \\ & \times \left[\frac{L_y}{L_x} \left(\frac{\partial^2 \overline{w}}{\partial \overline{x}^2} \right)^2 + \frac{L_x^3}{L_y^3} \left(\frac{\partial^2 \overline{w}}{\partial \overline{y}^2} \right)^2 + 2 \frac{L_x}{L_y} \nu \frac{\partial^2 \overline{w}}{\partial \overline{x}^2} \frac{\partial^2 \overline{w}}{\partial \overline{y}^2} + 2 \frac{L_x}{L_y} (1 - \nu) \left(\frac{\partial^2 \overline{w}}{\partial \overline{x} \partial \overline{y}} \right)^2 \right] d\overline{x} \; d\overline{y} \end{aligned}$$

Moving one factor of L_y/L_x in front of the integral to match the other terms in the Lagrangian, the potential energy appears as the following.

$$V = \frac{DL_y}{L_x}\frac{1}{2}\int_0^1\int_0^1 \left[1+\left(\frac{\partial \overline{w}}{\partial \overline{x}}\right)^2+\left(\frac{\partial \overline{w}}{\partial \overline{y}}\right)^2\right]$$
$$\times\left[\left(\frac{\partial^2 \overline{w}}{\partial \overline{x}^2}\right)^2+\frac{L_x^4}{L_y^4}\left(\frac{\partial^2 \overline{w}}{\partial \overline{y}^2}\right)^2+2\frac{L_x^2}{L_y^2}\nu\frac{\partial^2 \overline{w}}{\partial \overline{x}^2}\frac{\partial^2 \overline{w}}{\partial \overline{y}^2}+2\frac{L_x^2}{L_y^2}(1-\nu)\left(\frac{\partial^2 \overline{w}}{\partial \overline{x}\partial \overline{y}}\right)^2\right] d\overline{x}\ d\overline{y}$$

Noting that L_x/L_y is the Aspect Ratio AR of the plate, this can be written as follows.

$$V = \frac{DL_y}{L_x}\frac{1}{2}\int_0^1\int_0^1 \left[1+\left(\frac{\partial \overline{w}}{\partial \overline{x}}\right)^2+\left(\frac{\partial \overline{w}}{\partial \overline{y}}\right)^2\right]$$
$$\times\left[\left(\frac{\partial^2 \overline{w}}{\partial \overline{x}^2}\right)^2+AR^4\left(\frac{\partial^2 \overline{w}}{\partial \overline{y}^2}\right)^2+2AR^2\nu\frac{\partial^2 \overline{w}}{\partial \overline{x}^2}\frac{\partial^2 \overline{w}}{\partial \overline{y}^2}+2AR^2(1-\nu)\left(\frac{\partial^2 \overline{w}}{\partial \overline{x}\partial \overline{y}}\right)^2\right] d\overline{x}\ d\overline{y}$$
$$= \frac{DL_y}{L_x}\overline{V} \tag{8.11}$$

Or fully expanded,

$$\overline{V} = \frac{1}{2}\int_0^1\int_0^1 \left[\left(\frac{\partial^2 \overline{w}}{\partial \overline{x}^2}\right)^2+AR^4\left(\frac{\partial^2 \overline{w}}{\partial \overline{y}^2}\right)^2+2AR^2\nu\frac{\partial^2 \overline{w}}{\partial \overline{x}^2}\frac{\partial^2 \overline{w}}{\partial \overline{y}^2}\right.$$
$$+2AR^2(1-\nu)\left(\frac{\partial^2 \overline{w}}{\partial \overline{x}\partial \overline{y}}\right)^2+\left(\frac{\partial \overline{w}}{\partial \overline{x}}\right)^2\left(\frac{\partial^2 \overline{w}}{\partial \overline{x}^2}\right)^2+AR^4\left(\frac{\partial \overline{w}}{\partial \overline{x}}\right)^2\left(\frac{\partial^2 \overline{w}}{\partial \overline{y}^2}\right)^2$$
$$+2AR^2\nu\left(\frac{\partial \overline{w}}{\partial \overline{x}}\right)^2\frac{\partial^2 \overline{w}}{\partial \overline{x}^2}\frac{\partial^2 \overline{w}}{\partial \overline{y}^2}+2AR^2(1-\nu)\left(\frac{\partial \overline{w}}{\partial \overline{x}}\right)^2\left(\frac{\partial^2 \overline{w}}{\partial \overline{x}\partial \overline{y}}\right)^2$$
$$+\left(\frac{\partial \overline{w}}{\partial \overline{y}}\right)^2\left(\frac{\partial^2 \overline{w}}{\partial \overline{x}^2}\right)^2+AR^4\left(\frac{\partial \overline{w}}{\partial \overline{y}}\right)^2\left(\frac{\partial^2 \overline{w}}{\partial \overline{y}^2}\right)^2+2AR^2\nu\left(\frac{\partial \overline{w}}{\partial \overline{y}}\right)^2\frac{\partial^2 \overline{w}}{\partial \overline{x}^2}\frac{\partial^2 \overline{w}}{\partial \overline{y}^2}$$
$$\left.+2AR^2(1-\nu)\left(\frac{\partial \overline{w}}{\partial \overline{y}}\right)^2\left(\frac{\partial^2 \overline{w}}{\partial \overline{x}\partial \overline{y}}\right)^2\right] d\overline{x}\ d\overline{y} \tag{8.12}$$

Now Eqn. 8.2 can be written with the dimensional parameters out front which yields the nondimensional Lagrangian.

$$\mathcal{L} = \frac{DL_y}{L_x}\overline{T} - \frac{DL_y}{L_x}\overline{V} + \frac{DL_y}{L_x}\int_0^1\int_0^1 \overline{\lambda_u f_u}\; d\overline{x}\; d\overline{y} + \frac{DL_y}{L_x}\int_0^1\int_0^1 \overline{\lambda_v f_v}\; d\overline{x}\; d\overline{y}$$

$$= \frac{DL_y}{L_x}\overline{\mathcal{L}} \tag{8.13}$$

To nondimensionalize the right hand side of Eqn. 8.1, note that the generalized forces Q_n are known from the virtual work.

$$\delta W = \sum_n Q_n \delta q_n \tag{8.14}$$

The generalized coordinate q_n can be made dimensionless by defining $q_n = L_x\overline{q_n}$. Therefore,

$$\delta W = \sum_n Q_n L_x \delta\overline{q_n}$$

Nondimensionalizing the virtual work by the same factor DL_y/L_x as the other terms in the Lagrangian, the dimensionless generalized forces are therefore

$$\overline{Q_n} = \frac{L_x^2}{DL_y} Q_n \tag{8.15}$$

Alternatively simply nondimensionalize from Eqn. 8.1. From Eqn. 8.13 and noting again that $q_n = L_x\overline{q_n}$,

$$\frac{DL_y}{L_x^2}\frac{\partial}{\partial\overline{t}}\Big(\frac{\partial\overline{\mathcal{L}}}{\partial\dot{\overline{q}}_n}\Big) - \frac{DL_y}{L_x^2}\frac{\partial\overline{\mathcal{L}}}{\partial\overline{q_n}} = Q_n$$

Dividing both sides by the dimensional factor yields the dimensionless Lagrange's Equations.

$$\frac{\partial}{\partial\overline{t}}\Big(\frac{\partial\overline{\mathcal{L}}}{\partial\dot{\overline{q}}_n}\Big) - \frac{\partial\overline{\mathcal{L}}}{\partial\overline{q_n}} = \frac{L_x^2}{DL_y}Q_n = \overline{Q_n} \tag{8.16}$$

Note that Eqn. 8.16 has the same form as Eqn. 8.1; the Lagrange Equations are self-similar. Therefore, for brevity the overlines are dropped and all quantities are assumed dimensionless herein.

8.2.3 Modal Expansion

The deflections and the Lagrange multiplier, u, w, and λ, are expressed in terms of modal expansions as follows.

$$u(x,y,t) = \sum_i \Psi_i^u(x,y)u_i(t) \tag{8.17}$$

$$v(x,y,t) = \sum_j \Psi_j^v(x,y)v_j(t) \tag{8.18}$$

$$w(x,y,t) = \sum_k \Psi_k^w(x,y)w_k(t) \tag{8.19}$$

$$\lambda_u(x,y,t) = \sum_m \Psi_m^{\lambda_u}(x,y)\lambda_m^u(t) \tag{8.20}$$

$$\lambda_v(x,y,t) = \sum_n \Psi_n^{\lambda_v}(x,y)\lambda_n^v(t) \tag{8.21}$$

The mode shapes Ψ are chosen to satisfy the geometric constraints, i.e. $u = \dfrac{\partial u}{\partial x} = 0$ for a clamped end. Because the mode shapes are functions of two spatial variables, we will define them by multiplying the beam mode shapes in the x direction with the beam mode shapes in the y direction. For a cantilevered plate, then, the x mode shapes are cantilevered beam modes while the y mode shapes are the free-free modes. Note that since the inextensibility constraint requires that the slopes of u and v are directly related to the slopes of w, we again use the same modes for u, v, and w.

$$\Psi_i^u(x,y) = \Psi_{cf}(x)\Psi_{ff}(y) \tag{8.22}$$

$$\Psi_j^v(x,y) = \Psi_{cf}(x)\Psi_{ff}(y) \tag{8.23}$$

$$\Psi_k^w(x,y) = \Psi_{cf}(x)\Psi_{ff}(y) \tag{8.24}$$

$$\Psi_{ff}(y) = \cosh(\beta_v y) + \cos(\beta_v y) - R_v \sin(\beta_v x) - R_v \sinh(\beta_v x)^1 \tag{8.25}$$

$$\Psi_{cf}(x) = \cosh(\beta_u x) - \cos(\beta_u x) + R_u \sin(\beta_u x) - R_u \sinh(\beta_u x) \tag{8.26}$$

Where β_v, R_v, β_u, and R_u are given by

$$\tag{8.27}$$

$$1 = \cosh(\beta_v)\cos(\beta_v) \tag{8.28}$$

$$R_v = \frac{\cosh(\beta_v) - \cos(\beta_v)}{\sinh(\beta_v) - \sin(\beta_v)} \tag{8.29}$$

$$0 = \cos(\beta_x)\cosh(\beta_x) + 1 \tag{8.30}$$

$$R_u = (\cosh(\beta_u) + \cos(\beta_u))/(\sinh(\beta_u) + \sin(\beta_u)) \tag{8.31}$$

Similarly, the mode shapes for λ_u and λ_v will be composed of λ modes from the beam cases.

$$\Psi_m^{\lambda_u}(x,y) = \Psi_{cf}^{\lambda}(x)\Psi_{ff}^{\lambda}(y) \tag{8.32}$$

$$\Psi_n^{\lambda_v}(x,y) = \Psi_{cf}^{\lambda}(x)\Psi_{ff}^{\lambda}(y) \tag{8.33}$$

[1] Note that a rigid body translation is naturally included since $\beta_v = 0$ is a solution of 8.25, but a rigid body rotation $\Psi_{ff}(y) = 2y - 1$ is also manually added as the second mode.

$$\Psi^{\lambda}_{cf} = \sin((2m-1)/2\pi(1-x)) \tag{8.34}$$

$$\Psi^{\lambda}_{ff} = \sin(n\pi x) \tag{8.35}$$

Kinetic Energy

Let us begin with the derivation of the Kinetic Energy in dimensionless modal form. From Eqns. 8.10 and 8.17-8.19, we can write kinetic energy in terms of it's modal expansion.

$$T = \frac{1}{2}\int_0^1\int_0^1 \Big[\sum_{i1}\sum_{i2}\Psi^u_{i1}\Psi^u_{i2}\dot{u}_{i1}\dot{u}_{i2} + \sum_{j1}\sum_{j2}\Psi^v_{j1}\Psi^v_{j2}\dot{v}_{j1}\dot{v}_{j2} + \sum_{k1}\sum_{k2}\Psi^w_{k1}\Psi^w_{k2}\dot{w}_{k1}\dot{w}_{k2}\Big]\, dx\, dy \tag{8.36}$$

So the derivatives from Lagrange's Equations (8.1 or 8.16) are the following.

$$\frac{\partial}{\partial t}\left(\frac{\partial T}{\partial \dot{u}_i}\right) = \sum_{i1}\int_0^1\int_0^1 \Psi^u_i\Psi^u_{i1}\, dx\, dy\, \ddot{u}_{i1} \tag{8.37}$$

$$\frac{\partial T}{\partial u_i} = 0 \tag{8.38}$$

Similarly for the other coordinates, the relevant non-zero kinetic energy derivatives from Lagrange's Equations are the following.

$$\frac{\partial}{\partial t}\left(\frac{\partial T}{\partial \dot{v}_j}\right) = \sum_{j1}\int_0^1\int_0^1 \Psi^v_j\Psi^v_{j1}\, dx\, dy\, \ddot{v}_{j1} \tag{8.39}$$

$$\frac{\partial}{\partial t}\left(\frac{\partial T}{\partial \dot{w}_k}\right) = \sum_{k1}\int_0^1\int_0^1 \Psi^w_k\Psi^w_{k1}\, dx\, dy\, \ddot{w}_{k1} \tag{8.40}$$

Potential Energy

From Eqns. 8.12 and 8.17-8.19, we can write potential energy in terms of it's modal expansion.

$$
\begin{aligned}
V = \frac{1}{2}\int_0^1\int_0^1 \Bigg[& \sum_{k1}\sum_{k2} \Psi^w_{xx,k1}\Psi^w_{xx,k2}\ w_{k1}w_{k2} \\
& + AR^4 \sum_{k1}\sum_{k2} \Psi^w_{yy,k1}\Psi^w_{yy,k2}\ w_{k1}w_{k2} \\
& + 2\nu AR^2 \sum_{k1}\sum_{k2} \Psi^w_{xx,k1}\Psi^w_{yy,k2}\ w_{k1}w_{k2} \\
& + 2(1-\nu)AR^2 \sum_{k1}\sum_{k2} \Psi^w_{xy,k1}\Psi^w_{xy,k2}\ w_{k1}w_{k2} \\
& + \sum_{k1}\sum_{k2}\sum_{k3}\sum_{k4} \Psi^w_{x,k1}\Psi^w_{x,k2}\Psi^w_{xx,k3}\Psi^w_{xx,k4}\ w_{k1}w_{k2}w_{k3}w_{k4} \\
& + AR^4 \sum_{k1}\sum_{k2}\sum_{k3}\sum_{k4} \Psi^w_{x,k1}\Psi^w_{x,k2}\Psi^w_{yy,k3}\Psi^w_{yy,k4}\ w_{k1}w_{k2}w_{k3}w_{k4} \\
& + 2\nu AR^2 \sum_{k1}\sum_{k2}\sum_{k3}\sum_{k4} \Psi^w_{x,k1}\Psi^w_{x,k2}\Psi^w_{xx,k3}\Psi^w_{yy,k4}\ w_{k1}w_{k2}w_{k3}w_{k4} \\
& + 2(1-\nu)AR^2 \sum_{k1}\sum_{k2}\sum_{k3}\sum_{k4} \Psi^w_{x,k1}\Psi^w_{x,k2}\Psi^w_{xy,k3}\Psi^w_{xy,k4}\ w_{k1}w_{k2}w_{k3}w_{k4} \\
& + \sum_{k1}\sum_{k2}\sum_{k3}\sum_{k4} \Psi^w_{y,k1}\Psi^w_{y,k2}\Psi^w_{xx,k3}\Psi^w_{xx,k4}\ w_{k1}w_{k2}w_{k3}w_{k4} \\
& + AR^4 \sum_{k1}\sum_{k2}\sum_{k3}\sum_{k4} \Psi^w_{y,k1}\Psi^w_{y,k2}\Psi^w_{yy,k3}\Psi^w_{yy,k4}\ w_{k1}w_{k2}w_{k3}w_{k4} \\
& + 2\nu AR^2 \sum_{k1}\sum_{k2}\sum_{k3}\sum_{k4} \Psi^w_{y,k1}\Psi^w_{y,k2}\Psi^w_{xx,k3}\Psi^w_{yy,k4}\ w_{k1}w_{k2}w_{k3}w_{k4} \\
& + 2(1-\nu)AR^2 \sum_{k1}\sum_{k2}\sum_{k3}\sum_{k4} \Psi^w_{y,k1}\Psi^w_{y,k2}\Psi^w_{xy,k3}\Psi^w_{xy,k4}\ w_{k1}w_{k2}w_{k3}w_{k4} \Bigg]\ dx\ dy
\end{aligned}
\tag{8.41}
$$

So the only non-zero derivative from Lagrange's Equations (8.1) is the following.

$$\frac{\partial V}{\partial w_k} = \sum_{k1} K_{kk1} w_{k1} + \sum_{k1}\sum_{k2}\sum_{k3} P_{kk1k2k3} w_{k1} w_{k2} w_{k3} \tag{8.42}$$

Where

$$K_{kk1} = \int_0^1 \int_0^1 \Big[\Psi^w_{xx,k}\Psi^w_{xx,k1} + AR^4 \Psi^w_{yy,k}\Psi^w_{yy,k1} + \nu AR^2 \Psi^w_{xx,k}\Psi^w_{yy,k2} + \nu AR^2 \Psi^w_{yy,k}\Psi^w_{xx,k2} + 2(1-\nu)AR^2 \Psi^w_{xy,k}\Psi^w_{xy,k1} \Big]\, dx\, dy \tag{8.43}$$

$$\begin{aligned} P_{kk1k2k3} = \int_0^1 \int_0^1 \Big[& \Psi^w_{x,k}\Psi^w_{x,k1}\Psi^w_{xx,k2}\Psi^w_{xx,k3} + \Psi^w_{xx,k}\Psi^w_{x,k1}\Psi^w_{x,k2}\Psi^w_{xx,k3} \\ & + AR^4 \Psi^w_{x,k2}\Psi^w_{x,k1}\Psi^w_{yy,k2}\Psi^w_{yy,k3} + AR^4 \Psi^w_{yy,k2}\Psi^w_{x,k1}\Psi^w_{x,k2}\Psi^w_{yy,k3} \\ & + 2\nu AR^2 \Psi^w_{x,k}\Psi^w_{x,k1}\Psi^w_{xx,k2}\Psi^w_{yy,k3} + \nu AR^2 \Psi^w_{yy,k}\Psi^w_{x,k1}\Psi^w_{x,k2}\Psi^w_{xx,k3} \\ & + \nu AR^2 \Psi^w_{xx,k}\Psi^w_{x,k1}\Psi^w_{x,k2}\Psi^w_{yy,k3} + 2(1-\nu)AR^2 \Psi^w_{x,k}\Psi^w_{x,k1}\Psi^w_{xy,k2}\Psi^w_{xy,k3} \\ & + 2(1-\nu)AR^2 \Psi^w_{xy,k}\Psi^w_{x,k1}\Psi^w_{x,k2}\Psi^w_{xy,k3} + \Psi^w_{y,k}\Psi^w_{y,k1}\Psi^w_{xx,k2}\Psi^w_{xx,k3} \\ & + \Psi^w_{xx,k}\Psi^w_{y,k1}\Psi^w_{y,k2}\Psi^w_{xx,k3} + AR^4 \Psi^w_{y,k}\Psi^w_{y,k1}\Psi^w_{yy,k2}\Psi^w_{yy,k3} \\ & + AR^4 \Psi^w_{yy,k}\Psi^w_{y,k1}\Psi^w_{y,k2}\Psi^w_{yy,k3} + 2\nu AR^2 \Psi^w_{y,k}\Psi^w_{y,k1}\Psi^w_{xx,k2}\Psi^w_{yy,k3} \\ & + \nu AR^2 \Psi^w_{xx,k}\Psi^w_{y,k1}\Psi^w_{y,k2}\Psi^w_{yy,k3} + \nu AR^2 \Psi^w_{yy,k}\Psi^w_{y,k1}\Psi^w_{y,k2}\Psi^w_{xx,k3} \\ & + 2(1-\nu)AR^2 \Psi^w_{y,k}\Psi^w_{y,k1}\Psi^w_{xy,k2}\Psi^w_{xy,k3} + 2(1-\nu)AR^2 \Psi^w_{xy,k}\Psi^w_{y,k1}\Psi^w_{y,k2}\Psi^w_{xy,k3} \Big]\, dx\, dy \end{aligned} \tag{8.44}$$

Lagrange Multlipliers

From Eqns. 8.20, 8.21 and 8.17-8.19, we can write Lagrange Multiplier terms in terms of their modal expansions.

$$\int_0^1\int_0^1 \lambda_u f_u \; dx \; dy = \int_0^1\int_0^1 \sum_m \Psi_m^{\lambda_u}\lambda_m^u \Bigg(\sum_i \Psi_{x,i}^u u_i + \frac{1}{2}\sum_{k1}\sum_{k2} \Psi_{x,k1}^w \Psi_{x,k2}^w w_{k1} w_{k2} \Bigg) \; dx \; dy$$

$$= \int_0^1\int_0^1 \Bigg(\sum_m \sum_i \Psi_m^{\lambda_u}\Psi_{x,i}^u \lambda_m^u u_i + \frac{1}{2}\sum_m\sum_{k1}\sum_{k2} \Psi_m^{\lambda_u}\Psi_{x,k1}^w \Psi_{x,k2}^w \lambda_m^u w_{k1} w_{k2} \Bigg) \; dx \; dy \tag{8.45}$$

The relevant non-zero derivatives are the following.

$$\frac{\partial}{\partial u_i}\left(\int_0^1\int_0^1 \lambda_u f_u \; dx \; dy \right) = \sum_m \int_0^1\int_0^1 \Psi_m^{\lambda_u}\Psi_{x,i}^u \; dx \; dy \; \lambda_m^u \tag{8.46}$$

$$\frac{\partial}{\partial w_k}\left(\int_0^1\int_0^1 \lambda_u f_u \; dx \; dy \right) = \sum_m\sum_{k1} \int_0^1\int_0^1 \Psi_m^{\lambda_u}\Psi_{x,k1}^w \Psi_{x,k}^w \; dx \; dy \; \lambda_m^u w_{k1} \tag{8.47}$$

$$\frac{\partial}{\partial \lambda_{u,m}}\left(\int_0^1\int_0^1 \lambda_u f_u \; dx \; dy \right) = \sum_i \int_0^1 \Psi_m^{\lambda_u}\Psi_{x,i}^u \; dx \; dy \; u_i + \frac{1}{2}\sum_{k1}\sum_{k2} \int_0^1\int_0^1 \Psi_m^{\lambda_u}\Psi_{x,k1}^w \Psi_{x,k2}^w \; dx \; dy \; w_{k1} w_{k2} \tag{8.48}$$

Similarly, for the constraint in the y direction, the relevant derivatives are the following.

$$\frac{\partial}{\partial v_j}\left(\int_0^1\int_0^1 \lambda_v f_v \; dx \; dy\right) = \sum_n \int_0^1\int_0^1 \Psi_n^{\lambda_v}\Psi_{y,j}^{v} \; dx \; dy \; \lambda_n^v \tag{8.49}$$

$$\frac{\partial}{\partial w_k}\left(\int_0^1\int_0^1 \lambda_v f_v \; dx \; dy\right) = \sum_n \sum_{k1} \int_0^1\int_0^1 \Psi_n^{\lambda_v}\Psi_{y,k1}^{w}\Psi_{y,k}^{w} \; dx \; dy \; \lambda_n^v w_{k1} \tag{8.50}$$

$$\begin{aligned}\frac{\partial}{\partial \lambda_{v,n}}\left(\int_0^1\int_0^1 \lambda_v f_v \; dx \; dy\right) &= \sum_j \int_0^1\int_0^1 \Psi_n^{\lambda_v}\Psi_{y,j}^{v} \; dx \; dy \; v_j \\ &\quad + \frac{1}{2}\sum_{k1}\sum_{k2} \int_0^1\int_0^1 \Psi_n^{\lambda_v}\Psi_{y,k1}^{w}\Psi_{y,k2}^{w} \; dx \; dy \; w_{k1}w_{k2}\end{aligned} \tag{8.51}$$

8.2.4 System of Unforced Governing Equations

From Lagrange's Equations (8.16), a system of equations is obtained.

$$\sum_{i1} \int_0^1\int_0^1 \Psi_i^u\Psi_{i1}^u \; dx \; dy \; \ddot{u}_{i1} - \sum_m \int_0^1\int_0^1 \Psi_m^{\lambda_u}\Psi_{x,i}^{u} \; dx \; dy \; \lambda_m^u = 0 \tag{8.52}$$

$$\sum_{j1} \int_0^1\int_0^1 \Psi_j^v\Psi_{j1}^v \; dx \; dy \; \ddot{v}_{j1} - \sum_n \int_0^1\int_0^1 \Psi_n^{\lambda_v}\Psi_{y,j}^{v} \; dx \; dy \; \lambda_n^v = 0 \tag{8.53}$$

$$\begin{aligned}&\sum_{k1} \int_0^1\int_0^1 \Psi_k^w\Psi_{k1}^w \; dx \; dy \; \ddot{w}_{k1} + \sum_{k1} K_{kk1}w_{k1} + \sum_{k1}\sum_{k2}\sum_{k3} P_{kk1k2k3}w_{k1}w_{k2}w_{k3} \\ &\quad - \sum_m\sum_{k1} \int_0^1\int_0^1 \Psi_m^{\lambda_u}\Psi_{x,k1}^{w}\Psi_{x,k}^{w} \; dx \; dy \; \lambda_m^u w_{k1} \\ &\quad - \sum_n\sum_{k1} \int_0^1\int_0^1 \Psi_n^{\lambda_v}\Psi_{y,k1}^{w}\Psi_{y,k}^{w} \; dx \; dy \; \lambda_n^v w_{k1} = 0\end{aligned} \tag{8.54}$$

$$\sum_i \int_0^1 \int_0^1 \Psi_m^{\lambda_u} \Psi_{x,i}^u \, dx \, dy \, u_i + \frac{1}{2} \sum_{k1} \sum_{k2} \int_0^1 \int_0^1 \Psi_m^{\lambda_u} \Psi_{x,k1}^w \Psi_{x,k2}^w \, dx \, dy \, w_{k1} w_{k2} = 0 \quad (8.55)$$

$$\sum_i \int_0^1 \int_0^1 \Psi_n^{\lambda_v} \Psi_{y,j}^v \, dx \, dy \, v_j + \frac{1}{2} \sum_{k1} \sum_{k2} \int_0^1 \int_0^1 \Psi_n^{\lambda_v} \Psi_{y,k1}^w \Psi_{y,k2}^w \, dx \, dy \, w_{k1} w_{k2} = 0 \quad (8.56)$$

We can simplify the appearance of these equations by introducing matrix notation for the integrals. The index notation is replaced by matrix notation on the right hand side of the arrows.

$$u_i \;\Rightarrow\; \mathbf{u}, \quad v_j \;\Rightarrow\; \mathbf{v}, \quad w_k \;\Rightarrow\; \mathbf{w} \lambda_m^u \;\Rightarrow\; \boldsymbol{\lambda_u}, \quad \lambda_n^v \;\Rightarrow\; \boldsymbol{\lambda_v}$$

$$M_{ii1}^u \equiv \int_0^1 \int_0^1 \Psi_i^u \Psi_{i1}^u \, d\xi_x \, d\xi_y \;\Rightarrow\; \mathbf{M_u} \quad M_{jj1}^v \equiv \int_0^1 \int_0^1 \Psi_j^v \Psi_{j1}^v \, d\xi_x \, d\xi_y \;\Rightarrow\; \mathbf{M_v}$$

$$M_{kk1}^w \equiv \int_0^1 \int_0^1 \Psi_k^w \Psi_{k1}^w \, d\xi_x \, d\xi_y \;\Rightarrow\; \mathbf{M_w} \quad A_{mi} \equiv \int_0^1 \int_0^1 \Psi_m^{\lambda_u} \Psi_{x,i}^u \, dx \, dy \;\Rightarrow\; \mathbf{A_u},$$

$$A_{nj} \equiv \int_0^1 \int_0^1 \Psi_n^{\lambda_v} \Psi_{y,j}^v \, dx \, dy \;\Rightarrow\; \mathbf{A_v} \quad B_{mk1k2} \equiv \int_0^1 \int_0^1 \Psi_m^{\lambda_u} \Psi_{x,k1}^w \Psi_{x,k2}^w \, dx \, dy \;\Rightarrow\; \mathbf{B_u}$$

$$B_{nk1k2} \equiv \int_0^1 \int_0^1 \Psi_n^{\lambda_v} \Psi_{y,k1}^w \Psi_{y,k2}^w \, dx \, dy \;\Rightarrow\; \mathbf{B_v}$$

In matrix notation, this system is written as follows.

$$\mathbf{M_u} \, \ddot{\mathbf{u}} - \mathbf{A_u} \, \boldsymbol{\lambda_u} = 0 \quad (8.57)$$

$$\mathbf{M_v} \, \ddot{\mathbf{v}} - \mathbf{A_v} \, \boldsymbol{\lambda_v} = 0 \quad (8.58)$$

$$\mathbf{M_w}\ \ddot{\mathbf{w}} + \mathbf{K}\ \mathbf{w} + \mathbf{P}\ \mathbf{w}^3 - \mathbf{B_u}\boldsymbol{\lambda}_u\mathbf{w} - \mathbf{B_v}\boldsymbol{\lambda}_v\mathbf{w} = 0 \tag{8.59}$$

$$\mathbf{A_u u} + \frac{1}{2}\mathbf{B_u ww} = 0 \tag{8.60}$$

$$\mathbf{A_v v} + \frac{1}{2}\mathbf{B_v ww} = 0 \tag{8.61}$$

8.3 Plate Configuration

The plate analyzed here is the same aluminum plate explored by Pai [41] with properties as follows.

$$L_x = 0.25\text{m} \quad L_y = 0.2\text{m} \quad h = 0.0007\text{m}$$
$$E = 73\text{GPa} \quad \nu = 0.33 \quad \rho = 2800\text{kg/m}^3$$

An illustration of the plate as modeled in ANSYS is given in Fig. 8.2. The plate is clamped along one edge, marked "A: Fixed Support" and emphasized by the black line. Three forces at points B, C, and D are applied separately in several loading cases. In the Case 1 of simple plate bending, only the force at point D is applied. For Case 2, only force at point B is applied and the response is a combination of bending and torsion. For Case 3, a force is applied at B and an equal and opposite force is applied at C to form a coupled moment acting on the plate.

For each configuration, the results from the current model are compared to the results from ANSYS finite element model. Linear solutions are used as a baseline validation and nonlinear solutions are also evaluated. For each case, a mesh convergence study was done to ensure that the finite element mesh was sufficiently dense.

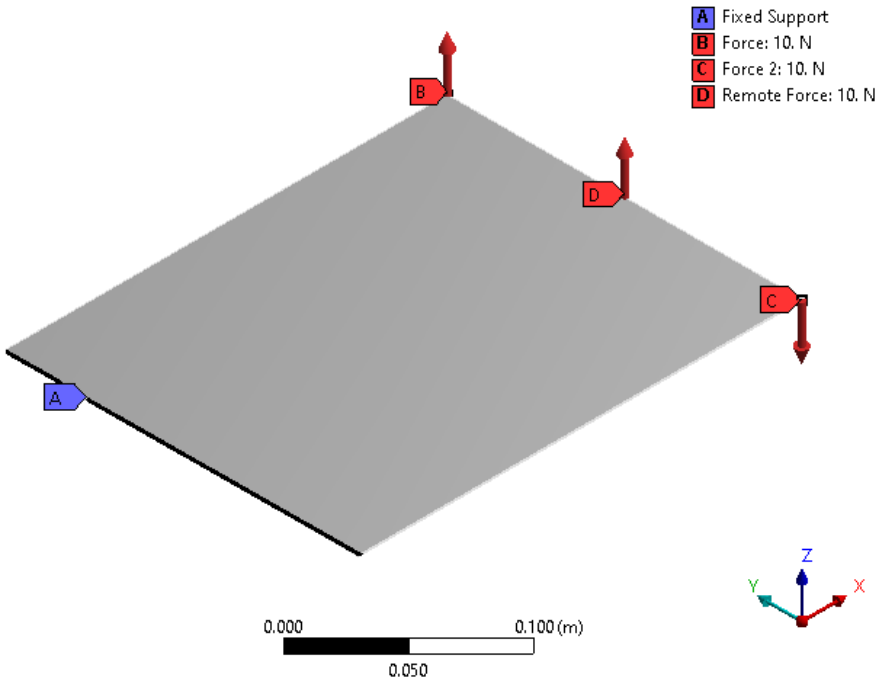

FIGURE 8.2: Plate loading schematic, generated in ANSYS

8.4 Results

To validate the model, we apply static loading to the plate in several interesting configurations and compare the results for the current linear and nonlinear model against ANSYS results with and without nonlinear effects. For these cases, all forces are applied in the z direction only, i.e. out of plane of the plate.

For each case, we show the plate in its deflected steady state and also plot the deflection of point B versus a range of forcing values. Finally, we show the contribution from each mode to demonstrate modal convergence at steady state. Note that for these cases, 16 modes were used, 4 modes each in x and y. However, from the modal convergence plots, we can see that the solutions are converged after 9 modes: 3 in x and 3 in y.

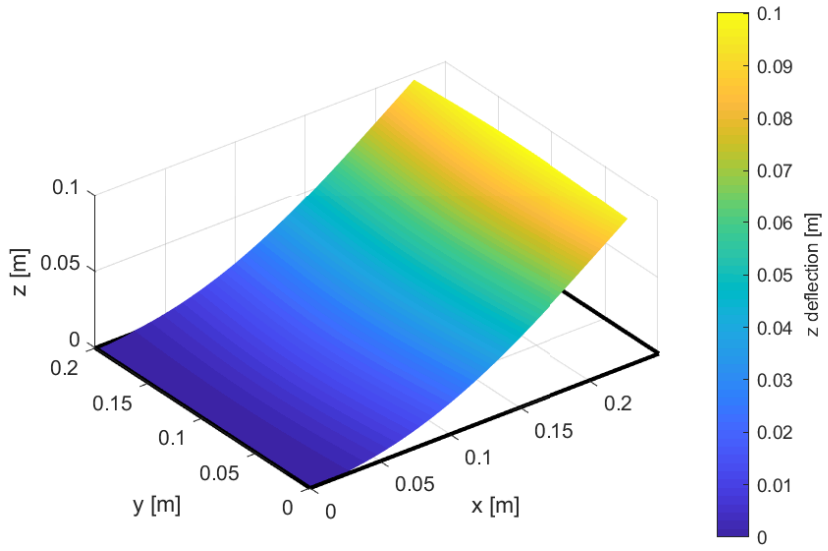

FIGURE 8.3: Case 1: Plate deflection due to 10 N force at midpoint of free edge

8.4.1 Case 1

First, a force is applied at point D, the midpoint of the free edge opposite the clamped edge. Figure 8.3 shows the deflected steady state from a force of 10 N, and 8.4 shows the deflection of point B versus the forcing level applied. Note that the agreement between the inextensible plate model and ANSYS for both linear and nonlinear cases is quite good here, and that the results are evaluated up to a deflection of nearly 40% plate length for the nonlinear case. Figure 8.5 shows the various modal amplitudes.

8.4.2 Case 2

Next, Fig. 8.6 shows the plate deflection from a 10 N force at one corner. Figure 8.7 shows the response of this corner versus a range of forcing values for each of the four models. Note here that the response is greater than that of the force applied at the midpoint, and that the difference between ANSYS and the current nonlinear model is greater than that for the force applied at the midpoint. The results show

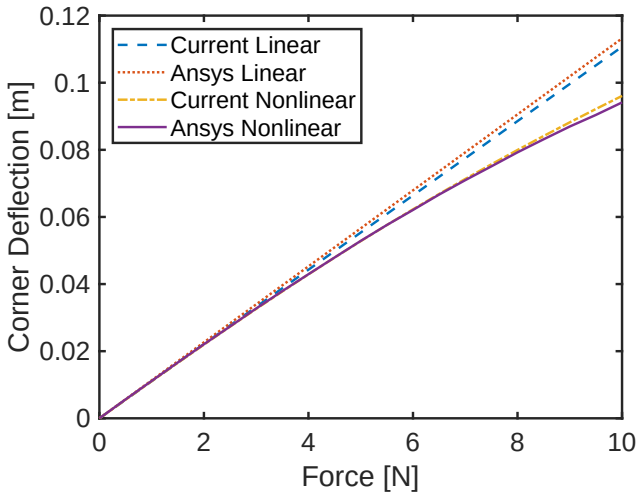

FIGURE 8.4: Case 1: Deflection of corner point B versus force level applied at midpoint of free edge

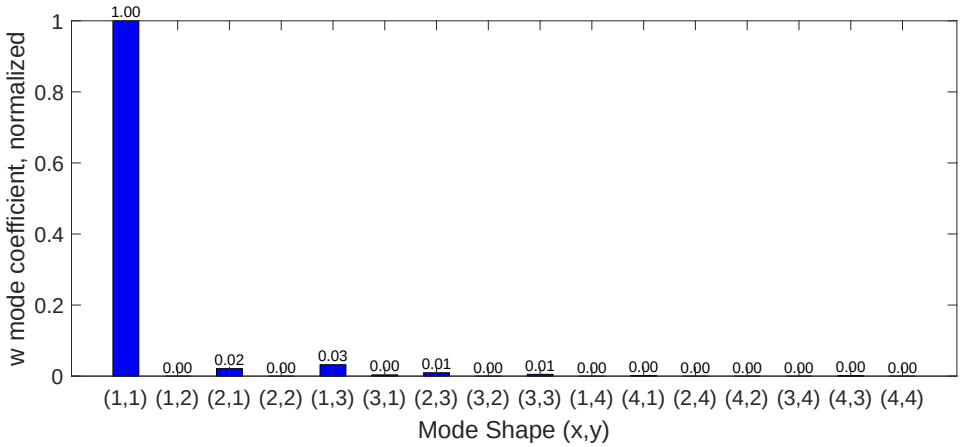

FIGURE 8.5: Case 1: Modal composition of steady state solution, 10 N applied

that the current model is qualitatively valid in the static nonlinear range for large deflections, i.e. for plate deflections up to around 40% plate length. Moreover, note that the current model is less stiff than the ANSYS model. Figure 8.8 shows that the discrepency is not due to a modal convergence problem, but rather that the model is simply not as stiff as ANSYS.

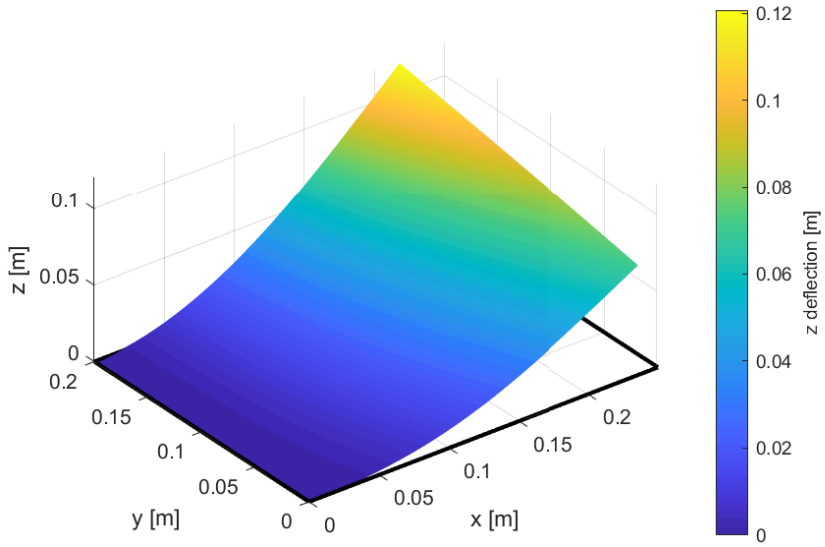

FIGURE 8.6: Case 2: Plate deflection due to 10 N force at free corner

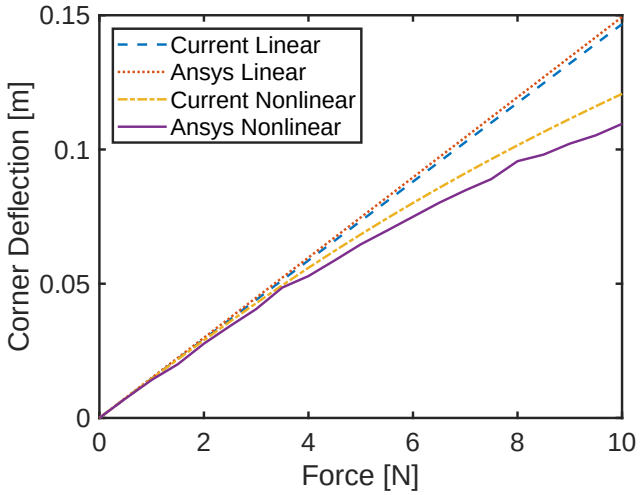

FIGURE 8.7: Case 2: Deflection of corner point B versus force level applied at corner point B

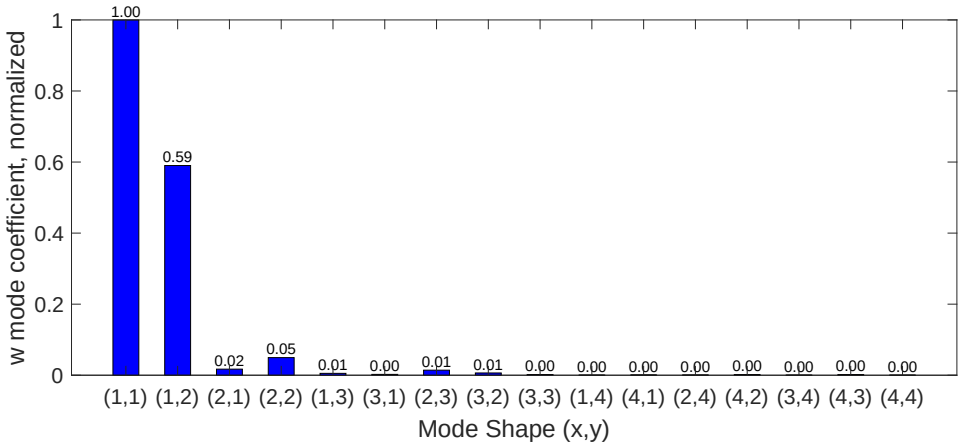

FIGURE 8.8: Case 2: Modal composition of steady state solution, 10 N applied

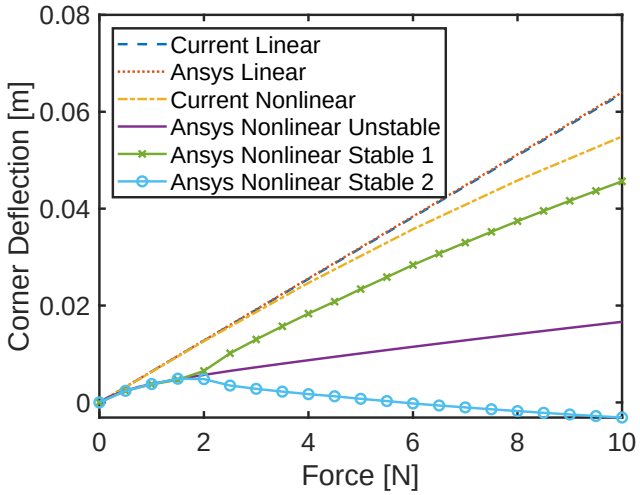

FIGURE 8.9: Case 3 Response Diagram: Deflection of corner point B versus force level applied at corner points B and C

8.4.3 Case 3

An interesting highly nonlinear behavior is observed for the case studied in Pai [41] of the plate with equal and opposite forces on each free corner B and C. In this case, the plate rotates as expected around its centerline for low forcing levels, but at moderate forcing a bifurcation occurs and the plate buckles. This bifurcation behavior is shown in Fig. 8.9.

Figure 8.9 shows that with a linear solution method, the current model is equiv-

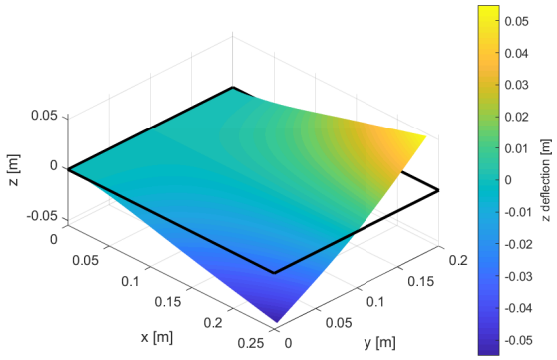

(a) Current Model, 10 N force at B, -10 N at C

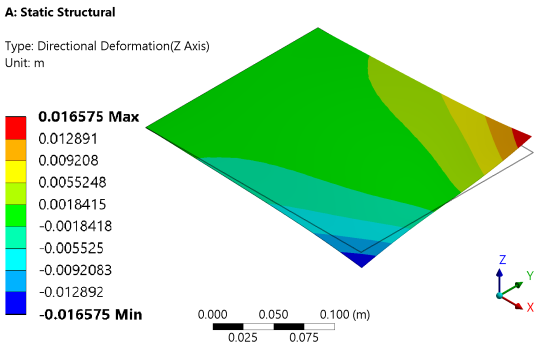

(b) ANSYS Model, 10 N force at B, -10 N at C

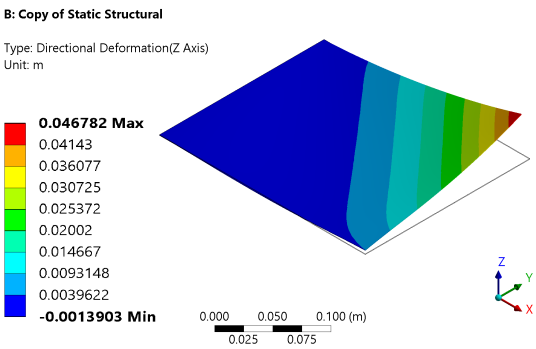

(c) ANSYS Model, 10 N force at B, -9.9 N at C

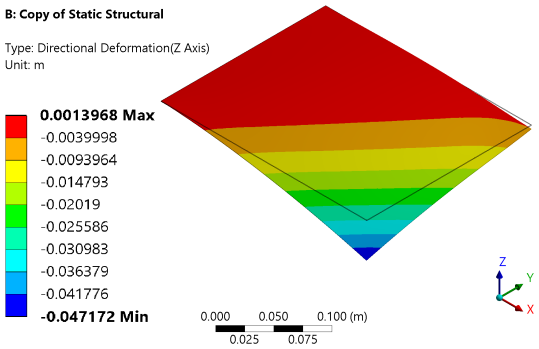

(d) ANSYS Model, 10 N force at B, -10.1 N at C

FIGURE 8.10: Case 3: Plate deflection due to a nominal 10 N force in opposing directions at each corner

alent to the ANSYS model. However, for the nonlinear model, the behavior is quite different. Firstly, by looking at the behavior at low forcing levels, it can be seen that the ANSYS model is much stiffer than the current model. With only a small forcing level, when the plate is deflected only on the order of its thickness, the plate buckles and a bifurcation occurs. After buckling, two stable solutions and one unstable solution are found. This situation is described by Pai [41] and is replicated here using an ANSYS solution.

Figure 8.10 shows the deflected structure for a force of 10 N on each corner

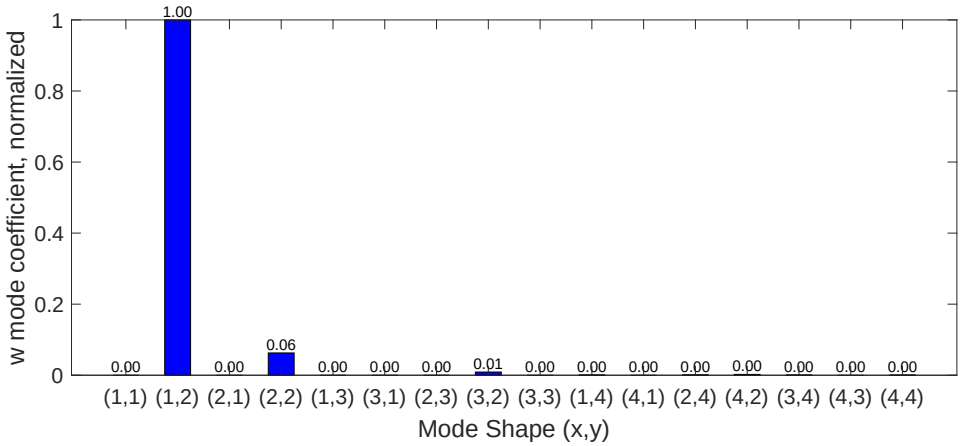

FIGURE 8.11: Case 3 modal convergence plot

in opposing directions. Figure 8.10a shows the result from the current model as compared to Fig. 8.10b from ANSYS. It is clear that ANSYS computes a much stiffer result, as the corner displacement of Fig. 8.10b is much less than that of Fig. 8.10a. Also note that the ANSYS solution has curvature along the free edge, whereas the current model has a straight diagonal edge. This straight diagonal twisting is indicative of rigid body rotation, but the ANSYS solution is indicative of higher modal contribution. To evaluate modal convergence in the inextensible plate model, Fig. 8.11 illustrates the contribution from each mode at the steady state. This shows that no higher modes are contributing and that the inextensible plate model solution is modally converged.

It is important to note that the deflection state shown in Fig. 8.10b is unstable, and also that the current model does not indicate any instability. By applying a slightly asymmetric loading to the plate, ANSYS returns two stable solutions, shown in Figs. 8.10c and 8.10d. Figure 8.10c shows the computed deflection if the force at point B is 10 N while the force at point C is 9.9 N, one percent less. This corresponds the "Stable 1" curve in Fig. 8.9. Figure 8.10c shows the computed deflection if the force at point B is 10 N while the force at point C is 10.1 N, one percent more. This

corresponds to the "Stable 2" curve in Fig. 8.9.

The bifurcation is due to buckling along the centerline at $y = 0.1$m as it experiences a compressive force. As the applied force moves the corners upwards, the stiffness along the plate acts to pull the corners towards the clamped edge, resulting in a compressive force along the centerline. Beyond a critical force, the centerline buckles and the plate finds a stable solution to either side of the undeformed plane.

The question we must ask then is why does the current model not capture this behavior? Indeed the model is much less stiff than the ANSYS model even before the intruiging bifurcation behavior should occur. Additionally, does this stiffness relate to the comparisons of Case 2, in which both the bending and torsion modes were excited?

To gain understanding into these questions, let us examine the potential energy (Eqn. 8.4) for the inextensible plate model and its underlying assumptions.

8.5 Modeling the Potential Energy

The expression for potential energy, Eqn. 8.4, is derived in Tang et al. [8] based on the expressions for strain energy by Novozhilov, [15].

From Tang et al. [8], the potential energy of a plate is

$$V = \frac{1}{2}\frac{E}{1-\nu^2}\int\int\int\left[\epsilon_{xx}^2 + \epsilon_{yy}^2 + 2\nu\epsilon_{xx}\epsilon_{yy} + \frac{1-\nu}{2}\epsilon_{xy}^2\right]\,dx\,dy\,dz \tag{8.62}$$

From Novozhilov [15], the strain expressions are given as

$$\epsilon_{xx} = \frac{\partial u}{\partial x} + \frac{1}{2}\left[\left(\frac{\partial u}{\partial x}\right)^2 + \left(\frac{\partial v}{\partial x}\right)^2 + \left(\frac{\partial w}{\partial x}\right)^2\right] \approx \frac{\partial u}{\partial x} + \frac{1}{2}\left(\frac{\partial w}{\partial x}\right)^2 \tag{8.63}$$

$$\epsilon_{yy} = \frac{\partial v}{\partial y} + \frac{1}{2}\left[\left(\frac{\partial u}{\partial y}\right)^2 + \left(\frac{\partial v}{\partial y}\right)^2 + \left(\frac{\partial w}{\partial y}\right)^2\right] \approx \frac{\partial v}{\partial y} + \frac{1}{2}\left(\frac{\partial w}{\partial y}\right)^2 \tag{8.64}$$

$$\epsilon_{xy} = \frac{\partial u}{\partial y} + \frac{\partial v}{\partial x} + \frac{\partial u}{\partial x}\frac{\partial u}{\partial y} + \frac{\partial v}{\partial x}\frac{\partial v}{\partial y} + \frac{\partial w}{\partial x}\frac{\partial w}{\partial y} \approx \frac{\partial u}{\partial y} + \frac{\partial v}{\partial x} + \frac{\partial w}{\partial x}\frac{\partial w}{\partial y} \tag{8.65}$$

Note that an approximation is made to simplify the strains. We can assume that the displacements u and v will be small compared to w, and therefore that their squares will be negligible compared to the square of w. This approximation results in the argument that u and v are on the order of w^2.

Novozhilov approximates the displacement at any point on the plate as

$$u(x, y, z) = \hat{u}(x, y) + z\Theta(x, y) \tag{8.66}$$

$$v(x, y, z) = \hat{v}(x, y) + z\Psi(x, y) \tag{8.67}$$

$$w(x, y, z) = \hat{w}(x, y) + z\chi(x, y) \tag{8.68}$$

Where the hatted terms are the displacement of the point along the midplane $z = 0$ plus the height z of the point times a respective angle.

After careful consideration and derivation, Novozhilov gives the expressions for the rotations in terms of $\hat{u}$, $\hat{v}$, and $\hat{w}$.

$$\Theta = -\frac{\partial \hat{w}}{\partial x} - \frac{\partial \hat{w}}{\partial x}\frac{\partial \hat{v}}{\partial y} + \frac{\partial \hat{v}}{\partial x}\frac{\partial \hat{w}}{\partial y} \tag{8.69}$$

$$\Psi = -\frac{\partial \hat{w}}{\partial y} - \frac{\partial \hat{w}}{\partial y}\frac{\partial \hat{u}}{\partial x} + \frac{\partial \hat{u}}{\partial y}\frac{\partial \hat{w}}{\partial x} \tag{8.70}$$

$$\chi = \frac{\partial \hat{u}}{\partial x} + \frac{\partial \hat{v}}{\partial y} + \frac{\partial \hat{u}}{\partial x}\frac{\partial \hat{v}}{\partial y} - \frac{\partial \hat{u}}{\partial y}\frac{\partial \hat{v}}{\partial x} \approx \frac{\partial \hat{u}}{\partial x} + \frac{\partial \hat{v}}{\partial y} \tag{8.71}$$

By substituting Eqns. 8.69–8.71 into 8.66–8.68 and substituting the resultant set of equations into 8.63–8.65, the strains are written in terms of the midplane displace-

ments and the height z above the midplane.

$$\epsilon_{xx} = \frac{\partial \hat{u}}{\partial x} + \frac{1}{2}\left[\left(\frac{\partial \hat{u}}{\partial x}\right)^2 + \left(\frac{\partial \hat{v}}{\partial x}\right)^2 + \left(\frac{\partial \hat{w}}{\partial x}\right)^2\right] + z\left[-\frac{\partial^2 \hat{w}}{\partial x^2}\left(1 + \frac{\partial \hat{u}}{\partial x} + \frac{\partial \hat{v}}{\partial y}\right) + \frac{\partial \hat{w}}{\partial x}\frac{\partial^2 \hat{u}}{\partial x^2} + \frac{\partial \hat{w}}{\partial y}\frac{\partial^2 \hat{v}}{\partial x^2}\right] + HOT \tag{8.72}$$

$$\epsilon_{yy} = \frac{\partial \hat{v}}{\partial y} + \frac{1}{2}\left[\left(\frac{\partial \hat{u}}{\partial y}\right)^2 + \left(\frac{\partial \hat{v}}{\partial y}\right)^2 + \left(\frac{\partial \hat{w}}{\partial y}\right)^2\right] + z\left[-\frac{\partial^2 \hat{w}}{\partial y^2}\left(1 + \frac{\partial \hat{u}}{\partial x} + \frac{\partial \hat{v}}{\partial y}\right) + \frac{\partial \hat{w}}{\partial x}\frac{\partial^2 \hat{u}}{\partial y^2} + \frac{\partial \hat{w}}{\partial y}\frac{\partial^2 \hat{v}}{\partial y^2}\right] + HOT \tag{8.73}$$

$$\epsilon_{xy} = \frac{\partial \hat{u}}{\partial y} + \frac{\partial \hat{v}}{\partial x} + \frac{\partial \hat{u}}{\partial x}\frac{\partial \hat{u}}{\partial y} + \frac{\partial \hat{v}}{\partial x}\frac{\partial \hat{v}}{\partial y} + \frac{\partial \hat{w}}{\partial x}\frac{\partial \hat{w}}{\partial y} + 2z\left[-\frac{\partial^2 \hat{w}}{\partial x \partial y}\left(1 + \frac{\partial \hat{u}}{\partial x} + \frac{\partial \hat{v}}{\partial y}\right) + \frac{\partial \hat{w}}{\partial x}\frac{\partial^2 \hat{u}}{\partial x \partial y} + \frac{\partial \hat{w}}{\partial y}\frac{\partial^2 \hat{v}}{\partial x \partial y}\right] + HOT \tag{8.74}$$

Note that the truncated higher order terms are z^2 terms; otherwise all terms are retained. By making the order of magnitude assumption, any terms higher than order w^3 may be truncated. The complete potential energy of the system in terms of midplane displacement is given by substituting these expressions 8.72–8.74 into the potential energy expression 8.62.

Noting the complexity of each strain term, we can expect that the potential energy expression—which requires the multiples of these terms—will be highly complicated. Therefore it is prudent to make several assumptions regarding strain to simplify the expression for potential energy.

8.5.1 Assume Inextensibility and No-Shear Strain

We begin with the assumptions made in Tang et al. [8] which are in turn used in this chapter as Eqn. 8.4. First, we assume inextensibility, which states that there is no elongation along the midplane of the plate. Novozhilov justifies this assumption given the expectation that the plane strain along the midplane will be much less

than the slopes that define it, i.e. the right hand side is a small difference of large terms so the left hand side can be set to zero. In the same vein, if we further state the assumption as Tang does that there is no shear along the midplane of the plate, we arrive at the following three assumptions.

$$\hat{\epsilon}_{xx} \equiv 0 = \frac{\partial \hat{u}}{\partial x} + \frac{1}{2}\left[\left(\frac{\partial \hat{u}}{\partial x}\right)^2 + \left(\frac{\partial \hat{v}}{\partial x}\right)^2 + \left(\frac{\partial \hat{w}}{\partial x}\right)^2\right] \tag{8.75}$$

$$\hat{\epsilon}_{yy} \equiv 0 = \frac{\partial \hat{v}}{\partial y} + \frac{1}{2}\left[\left(\frac{\partial \hat{u}}{\partial y}\right)^2 + \left(\frac{\partial \hat{v}}{\partial y}\right)^2 + \left(\frac{\partial \hat{w}}{\partial y}\right)^2\right] \tag{8.76}$$

$$\hat{\epsilon}_{xy} \equiv 0 = \frac{\partial \hat{u}}{\partial y} + \frac{\partial \hat{v}}{\partial x} + \frac{\partial \hat{u}}{\partial x}\frac{\partial \hat{u}}{\partial y} + \frac{\partial \hat{v}}{\partial x}\frac{\partial \hat{v}}{\partial y} + \frac{\partial \hat{w}}{\partial x}\frac{\partial \hat{w}}{\partial y} \tag{8.77}$$

From the intextensible assumptions, 8.75 and 8.76, the expressions $\partial u/\partial x$ and $\partial v/\partial y$ can be rewritten in terms of w. With the no-shear assumption, the mixed derivative terms can be rewritten in terms of w and therefore it can be shown that they may be rearranged to match terms with the other terms in brackets. By neglecting any terms greater than order w^3, we are left with the following equations for strain.

$$\epsilon_{xx} = z\left[-\frac{\partial^2 \hat{w}}{\partial x^2}\left(1 + \frac{1}{2}\left(\frac{\partial w}{\partial x}\right)^2 + \frac{1}{2}\left(\frac{\partial w}{\partial y}\right)^2\right)\right] + HOT \tag{8.78}$$

$$\epsilon_{yy} = z\left[-\frac{\partial^2 \hat{w}}{\partial y^2}\left(1 + \frac{1}{2}\left(\frac{\partial w}{\partial x}\right)^2 + \frac{1}{2}\left(\frac{\partial w}{\partial y}\right)^2\right)\right] + HOT \tag{8.79}$$

$$\epsilon_{xy} = 2z\left[-\frac{\partial^2 \hat{w}}{\partial x \partial y}\left(1 + \frac{1}{2}\left(\frac{\partial w}{\partial x}\right)^2 + \frac{1}{2}\left(\frac{\partial w}{\partial y}\right)^2\right)\right] + HOT \tag{8.80}$$

By substituting these expressions 8.78–8.80 into 8.62, the expression for potential energy used in this chapter as Eqn. 8.4 is the result.

Compatibility of Assumptions

To check for compatibility of these three assumptions, differentiate 8.75 twice with respect to y, 8.76 twice with respect to x, and 8.77 with respect to x and y.

From 8.77 $\hat{\epsilon}_{xy} = 0$,

$$-\frac{\partial^2}{\partial y^2}\left(\frac{\partial \hat{u}}{\partial x}\right) - \frac{\partial^2}{\partial x^2}\left(\frac{\partial \hat{v}}{\partial y}\right) = \hat{u}_y\hat{u}_{xxy} + \hat{u}_{xx}\hat{u}_{yy} + \hat{u}_{xy}^2 + \hat{u}_x\hat{u}_{xyy} + \hat{v}_x\hat{v}_{xyy} + \hat{v}_{xy}^2 + \hat{v}_y\hat{v}_{xxy} + \hat{v}_{xx}\hat{v}_{yy} + \hat{w}_x\hat{w}_{xyy} + \hat{w}_{xy}^2 + \hat{w}_y\hat{w}_{xxy} + \hat{w}_{xx}\hat{w}_{yy} \quad (8.81)$$

From 8.75 and 8.76, $\hat{\epsilon}_{xx} = \hat{\epsilon}_{yy} = 0$,

$$-\frac{\partial^2}{\partial y^2}\left(\frac{\partial \hat{u}}{\partial x}\right) = \hat{u}_x\hat{u}_{xyy} + \hat{u}_{xy}^2 + \hat{v}_x\hat{v}_{xyy} + \hat{v}_{xy}^2 + \hat{w}_x\hat{w}_{xyy} + \hat{w}_{xy}^2 \quad (8.82)$$

$$-\frac{\partial^2}{\partial x^2}\left(\frac{\partial \hat{v}}{\partial y}\right) = \hat{u}_y\hat{u}_{xxy} + \hat{u}_{xy}^2 + \hat{v}_y\hat{v}_{xxy} + \hat{v}_{xy}^2 + \hat{w}_y\hat{w}_{xxy} + \hat{w}_{xy}^2 \quad (8.83)$$

By substituting 8.82 and 8.83 into 8.81, we are left with

$$\hat{u}_{xy}^2 + \hat{v}_{xy}^2 + \hat{w}_{xy}^2 = \hat{u}_{xx}\hat{u}_{yy} + \hat{v}_{xx}\hat{v}_{yy} + \hat{w}_{xx}\hat{w}_{yy} \quad (8.84)$$

Since the above expression is not always true, the assumption of zero shear strain is not compatible with that of inextensibility. Following with the order of magnitude approximation, if u and v are on the order of w^2, and we neglect any terms of order w^4, we are left with $\hat{w}_{xy}^2 = \hat{w}_{xx}\hat{w}_{yy}$ which is also not guaranteed. Therefore, the no-shear strain approximation is not compatible with the inextensible assumptions.

8.5.2 Assume Inextensible but Allow for Midplane Shear Strain

Enforcing the inextensibility assumption but relaxing the assumption on shear, we can write the strain expressions as follows.

$$\epsilon_{xx} = z\left[-\frac{\partial^2\hat{w}}{\partial x^2}\left(1+\frac{\partial\hat{u}}{\partial x}+\frac{\partial\hat{v}}{\partial y}\right)+\frac{\partial\hat{w}}{\partial x}\frac{\partial^2\hat{u}}{\partial x^2}+\frac{\partial\hat{w}}{\partial y}\frac{\partial^2\hat{v}}{\partial x^2}\right]+HOT \tag{8.85}$$

$$\epsilon_{yy} = z\left[-\frac{\partial^2\hat{w}}{\partial y^2}\left(1+\frac{\partial\hat{u}}{\partial x}+\frac{\partial\hat{v}}{\partial y}\right)+\frac{\partial\hat{w}}{\partial x}\frac{\partial^2\hat{u}}{\partial y^2}+\frac{\partial\hat{w}}{\partial y}\frac{\partial^2\hat{v}}{\partial y^2}\right]+HOT \tag{8.86}$$

$$\begin{aligned}\epsilon_{xy} =& \frac{\partial\hat{u}}{\partial y}+\frac{\partial\hat{v}}{\partial x}+\frac{\partial\hat{u}}{\partial x}\frac{\partial\hat{u}}{\partial y}+\frac{\partial\hat{v}}{\partial x}\frac{\partial\hat{v}}{\partial y}+\frac{\partial\hat{w}}{\partial x}\frac{\partial\hat{w}}{\partial y}\\ &+2z\left[-\frac{\partial^2\hat{w}}{\partial x\partial y}\left(1+\frac{\partial\hat{u}}{\partial x}+\frac{\partial\hat{v}}{\partial y}\right)+\frac{\partial\hat{w}}{\partial x}\frac{\partial^2\hat{u}}{\partial x\partial y}+\frac{\partial\hat{w}}{\partial y}\frac{\partial^2\hat{v}}{\partial x\partial y}\right]+HOT\end{aligned} \tag{8.87}$$

Substituting these expressions into Eqn. 8.62, the expression for potential energy is much more complex than before.

$$V = \frac{1}{2}\int_0^{L_y}\int_0^{L_x}\int_{-h/2}^{h/2}\frac{E}{1-\nu^2}\left(z^2\alpha_2+z\alpha_1+\alpha_0\right)\,dx\,dy \tag{8.88}$$

Where

$$\begin{aligned}\alpha_2 =& \left(1+2\frac{\partial u}{\partial x}+2\frac{\partial u}{\partial y}\right)\left(\left(\frac{\partial^2 w}{\partial x^2}\right)^2+\left(\frac{\partial^2 w}{\partial y^2}\right)^2+2\nu\frac{\partial^2 w}{\partial x^2}\frac{\partial^2 w}{\partial y^2}+2(1-\nu)\left(\frac{\partial^2 w}{\partial x\partial y}\right)^2\right)\\ &-2\frac{\partial^2 u}{\partial x^2}\frac{\partial w}{\partial x}\frac{\partial^2 w}{\partial x^2}-2\frac{\partial^2 v}{\partial x^2}\frac{\partial w}{\partial y}\frac{\partial^2 w}{\partial x^2}-2\frac{\partial^2 u}{\partial y^2}\frac{\partial w}{\partial x}\frac{\partial^2 w}{\partial y^2}-2\frac{\partial^2 v}{\partial y^2}\frac{\partial w}{\partial y}\frac{\partial^2 w}{\partial y^2}\\ &-2\nu\frac{\partial^2 w}{\partial x^2}\left(\frac{\partial^2 u}{\partial y^2}\frac{\partial w}{\partial x}+\frac{\partial^2 v}{\partial y^2}\frac{\partial w}{\partial y}\right)-2\nu\frac{\partial^2 w}{\partial y^2}\left(\frac{\partial^2 u}{\partial x^2}\frac{\partial w}{\partial x}+\frac{\partial^2 v}{\partial x^2}\frac{\partial w}{\partial y}\right)\\ &-4(1-\nu)\frac{\partial^2 w}{\partial x\partial y}\left(\frac{\partial^2 u}{\partial x\partial y}\frac{\partial w}{\partial x}+\frac{\partial^2 v}{\partial x\partial y}\frac{\partial w}{\partial y}\right)\end{aligned} \tag{8.89}$$

$$\alpha_1 = 2(1-\nu)\frac{\partial^2 w}{\partial x\partial y}\left(\frac{\partial u}{\partial y}+\frac{\partial v}{\partial x}\right) \tag{8.90}$$

$$\alpha_0 = \frac{(1-\nu)}{2}\left[\frac{\partial^2 u}{\partial y^2}+2\frac{\partial u}{\partial y}\frac{\partial v}{\partial x}+\frac{\partial^2 v}{\partial x^2}+2\frac{\partial u}{\partial y}\frac{\partial w}{\partial x}\frac{\partial w}{\partial y}+2\frac{\partial v}{\partial x}\frac{\partial w}{\partial x}\frac{\partial w}{\partial y}+\frac{\partial^2 w}{\partial x^2}\frac{\partial^2 w}{\partial y^2}\right] \tag{8.91}$$

After integrating across z, the potential energy is the following.

$$V = \frac{1}{2}\int_0^{L_y}\int_0^{L_x} \frac{Eh^3}{12(1-\nu^2)}\alpha_2 + \frac{Eh}{(1-\nu^2)}\alpha_0 \; dx \; dy \tag{8.92}$$

The same methodology may be applied with this potential energy expression as what was done with the original expression, Eqn. 8.4. While we may use the inextensibility conditions to translate some u and v terms to terms in w, note that the final expression must be written in terms of u, v, and w when a non-zero mid-plane shear strain is retained. Nonetheless, nondimensionalizing this expression and using it in the nondimensional Lagrange's equations will result in the equations of motion. It is expected that the linear terms will be identical to the previous linear equations of motion, the nonlinear stiffness and inertia terms will appear, and there will be several novel nonlinear terms owing to the mid-plane shear strain effects. We expect that with the addition of these terms in the potential energy expression, the loading cases with significant torsion included in the response of the plate will be more comparable to the results of the finite element method and to future experiments. In other words, these terms are expected to stiffen the plate's nonlinear torsional response. It is not immediately clear, however, if the changes proposed here will result in the interesting bifurcation behavior of Case 3.

8.6 Conclusions

In this chapter the equations of motion have been derived from Lagrange's Equations for a thin rectangular plate which is clamped on one edge and free on the other three. To simplify the expressions, the inextensibility and no-mid-plane-shear strain assumptions have been employed. In addition, two Lagrange multipliers have been utilized to enforce the inextensibility assumptions and the Rayleigh-Ritz approach

has been used to discretize the deflections and Lagrange multipliers into modal coordinates.

The plate responses were compared to ANSYS Finite Element Analysis for three static cases which are fundamental. In all cases, static forces were applied to the plate at specific locations along its free edge opposite the clamped edge. In Case 1, a static force was applied at the midpoint of the plate's free edge to represent simple bending. In Case 2, a static force was applied to one free corner of the plate to induce a response in a combination of bending and torsion. In Case 3, a force was applied on one free corner, and on the other free corner a force equal in magnitude and opposite in direction was applied. This induced a substantial torsion response.

It has been found that the current model agrees with the ANSYS model well into the nonlinear range for Case 1 of simple bending. For Case 2 of bending and torsion, the current nonlinear model is slightly less stiff than the nonlinear ANSYS model. Finally Case 3 demonstrates a substantial loss of agreement both qualitatively and quantitatively between the current model and the ANSYS model. The current model is less stiff in the nonlinear range and does not predict the buckling behavior that the ANSYS model does.

An investigation to account for the differences in the two cases with significant torsion response has been made. The assumption of no-shear strain along the midplane of the plate has been shown to be incompatible with the inextensibility assumptions, and a new expression for potential energy has been derived without this assumption. It is hypothesized that this new expression will better predict the responses to load cases which induce substantial torsion in the plate.

9

Conclusions

Theory, modeling, and insight have been presented on beam and plate models subject to conservative and nonconservative forces, including supersonic and hypersonic aerodynamic pressures.

A new theory was derived for the inextensible beam and plate in Chapter 2, and insights into the use of a Lagrange multiplier for this work were gained. This theory was utilized in computational models in the subsequent chapters to gain insight into the basic physics of the structure's nonlinear responses to various forces.

From the harmonically-forced responses of the inextensible beam in Chapter 3, several interesting conclusions were drawn. First is that the first bending mode of a cantilevered beam responds as if the system is linear, whereas higher modes exhibit nonlinear softening. This is caused by a cancellation of the nonlinear stiffness and the nonlinear inertia effects opposing one another at the first mode, but the inertia dominating in higher mode dynamics. Second is that in the second mode, the nonlinearities affect the softening of the cantilevered beam at smaller deflections than previously thought, as low as 5% beam length. Third is that for free-free beams, all modes soften, including the first, and this effect is observed for deflections from

as low as 5% beam length.

Applying a nonconservative point force to the cantilevered beam gave rise to a limit cycle oscillation beyond the flutter point. It was verified that adding damping to a dynamic system can, paradoxically, decrease its stability. To apply a similar force on a free-free beam, our model was equipped with free body rotation and translation modes. Interestingly, the free body translation modes were fully decoupled from the system. The results matched classical theory for the flutter point and illustrated a rich post-flutter limit cycle, complete with a secondary bifurcation to chaotic motion.

Moving to the aeroelastic realm, piston theoretic pressures were applied to the current nonlinear beam model. In doing so, insight was gathered into how the pressure was to be applied to the beam, since the beam deflection was much greater than usual applications of piston theory. In the literature, the pressure from piston theory acts normal to the freestream flow, since assumptions are made about the small angle of the structure to freestream. However, we have demonstrated that for large deflections such as those common to cantilevered plates, piston theory pressure must act as follower force pressure, i.e. the pressure always must act normal to the deflected structure. The model contained four nonlinearities: two fluid and two structural. The sensitivity of the model to each nonlinearity was discussed and it was found that the model was very sensitive to the inclusion or exclusion of each nonlinearity. In addition, the pressures on the plate calculated in the current method were compared to pressures given by a commercial Euler CFD code with very good agreement for the range of parameters investigated.

Following the aeroelastic work, suggestions were made for new methods to increase the range of utility of piston theory. It was shown that 1-dimensional Shock Expansion Theory may be used to derive the pressure relations given by Tangent Wedge Theory, an interesting result given the latter theory's 2-dimensional basis. Indeed, this theory was shown to be a better predictor of pressures on a surface with

large slopes than classical piston theory.

Finally, after the bulk of the present work was completed using the beam theory, the full nonlinear plate theory was evaluated. It was found, using static analysis, that the plate model was accurate for predominantly bending responses, but less accurate in substantial torsion responses. It was hypothesized that the plate theory had one subtle nuance that was not present in the beam theory; the plate must be shearable along its otherwise inextensible midplane. It was shown that the no-shear strain assumption along the mid-plane is incompatible with the inextensibility assumption, and a new expression for potential energy was derived.

9.1 Future Work

9.1.1 Computational Investigation of Inextensible Plates to Harmonic, Follower, and Aerodynamic Loading

A clear path for future work begins at the end of Chapter 8, which describes the development of a new expression for potential energy of the plate model. By using the expression 8.92 in Lagrange's equations, a new system of equations for a plate which is inextensible yet shearable may be derived. It is expected that this plate model will predict torsion responses better than the original inextensible plate model discussed in Chapter 8.

Upon completion of this theory, the computation of the plate's responses to harmonic input is of interest. In Chapter 3, the beam's response to harmonic input is computed and insights are gained into the nature of the nonlinearity of each mode. This insight for the plate is crucial as well, as the nonlinear behavior for torsion modes is of interest to the flutter community.

The methods to apply nonconservative forces such as follower loads and aerodynamic loads to the inextenstible beam in Chapters 4–6 may be applied to the inextensible plate as well. It is of interest to determine flutter boundaries and post-flutter

Limit Cycle behaviors for the plate and explore how the responses to nonconservative forces of plate theory may differ from those of beam theory.

9.1.2 Computational Investigation of Enhanced Piston Theory for Aeroelastic Models

The large pressure ratio shock expansion aerodynamic theory proposed in Chapter 7 may be evaluated in an aeroelastic model. By incorporating the new theory into the equations of motion for the beam or plate, insights may be gained into the efficacy of the theory for aeroelasticity of largely deflected structures. The challenge will be the separating of the structure into small spatial areas which will be acted on by different aerodynamic theories. Then one may determine whether the computational cost is reasonable for the increased fidelity of highly deflected aeroelastic models.

These results may be supplemented and supported by further CFD comparisons using prescribed motion, or even using a CFD model coupled with a structural solver to evaluate fully aeroelastic responses. It is possible to use commercial tools such as ANSYS Fluent to compute fully aeroelastic cases of the plate in flow to be compared to the current model. Validation from these higher fidelity theories may demonstrate the capability of the current model in terms of computational efficiency and accuracy.

9.1.3 Piston Theory with Initial Angle of Attack

For use in cantilevered structures such as trailing edge control surfaces, angle of attack is a necessary consideration in modeling the fluid pressures. Consider a plate at an angle of attack, rotated about the leading edge, as in Fig. 9.1. Piston theory predicts pressures given by Eqn. 9.1, and an expression is needed for downwash $\overline{w}$ for the rotated plate.

$$\frac{P}{P_\infty} = 1 + \frac{\gamma}{a_\infty}\overline{w} \tag{9.1}$$

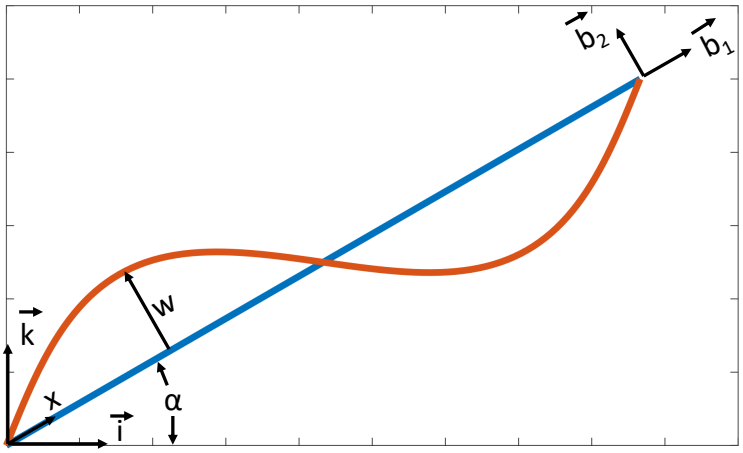

FIGURE 9.1: Schematic of plate with angle of attack

The expression for downwash $\overline{w}$ is given by Dowell [35] as

$$-\frac{\partial f}{\partial t}+\left[(U_\infty+u)\,\vec{i}+v\vec{j}+\overline{w}\vec{k}\right]\cdot\left[-\frac{\partial f}{\partial x}\vec{i}-\frac{\partial f}{\partial y}\vec{j}+\vec{k}\right]=0 \tag{9.2}$$

or, when $u << U_\infty$, $v=0$, $f=f(x,t)$,

$$\overline{w}=\frac{\partial f}{\partial t}+U_\infty\frac{\partial f}{\partial x} \tag{9.3}$$

Where f is the magnitude of the $\vec{k}$ component of position $\vec{w}$. The expression for position $\vec{w}$ is written in both coordinates as

$$\vec{w}=x\vec{b_1}+w\vec{b_2}=(x\cos\alpha-w\sin\alpha)\vec{i}+(x\sin\alpha+w\cos\alpha)\vec{k} \tag{9.4}$$

And thus we can write

$$f=x\sin\alpha+w\cos\alpha \tag{9.5}$$

$$\frac{\partial f}{\partial t}=\frac{\partial w}{\partial t}\cos\alpha \tag{9.6}$$

$$\frac{\partial f}{\partial x}=\sin\alpha+\frac{\partial w}{\partial x}\cos\alpha \tag{9.7}$$

Therefore, the downwash is written from Eqn. 9.3 as

$$\overline{w} = \frac{\partial w}{\partial t}\cos\alpha + U_\infty \frac{\partial w}{\partial x}\cos\alpha + U_\infty \sin\alpha \tag{9.8}$$

And pressures are derived from 9.1.

Note that the downwash could also be rewritten so that the classical expression for piston theory appears clearly.

$$\overline{w} = \left(\frac{\partial w}{\partial t} + U_\infty \frac{\partial w}{\partial x}\right)\cos\alpha + U_\infty \sin\alpha \tag{9.9}$$

Note, however, that in the nonlinear form, the angle between the uniform flow and the beam at any point, $\beta(x)$ is defined as

$$\beta(x) = \arctan\left(\frac{\frac{\partial w}{\partial x}}{1 + \frac{\partial u}{\partial x}}\right) + \alpha \tag{9.10}$$

Thus, the expression for aerodynamic work done on the plate considering the large angle of the plate relative to the freestream flow (Eqn. 6.8) becomes much more complex than for the case without an angle of attack α.

9.1.4 Sensitivity Analysis

Sensitivity analysis may be used to gain insight into the system's stability characteristics as a function of changing system parameters. Martins and his team have published extensively on this topic and its role in multidisciplinary optimization for aircraft design [72–74]. Thomas et al. [75] have shown the benefits of automatic differentiation for gradient based approaches to sensitivities. Stanford and Beran [76,77] have used gradient-based derivatives to demonstrate optimization schemes in nonlinear aeroelastic and aerothermoelastic settings.

By coupling adjoint sensitivity capability to the presented computational models, the sensitivities may be calculated to show flutter and limit cycle oscillation depen-

dencies on system parameters such as wing thickness, wing span, angle of attack, and the addition of lumped masses.

9.1.5 Extension to Non-Uniform Wing Geometry

An intriguing possibility for this model is to consider non-uniform, high-fidelity wing geometries to determine their responses at high deflections. The models developed in this thesis account for any mass and stiffness distribution. Then, solving the equations of motion with these mass and stiffness parameters, a wing of various spatial properties may be analyzed by the current model.

For the work described in this document, the mass and stiffness distributions were assumed constant. However, this was a convenient assumption rather than a necessity of the theory.

Using the mode shapes for a uniform beam, the recalculation of the modal mass and stiffness matrices allows the equations of motion to be solved for a non-uniform wing. Note that the mode shapes may also be derived from an FEM analysis. Also note that if the uniform beam modes are used then the orthogonality of linear modal characteristics is lost for the non-uniform structure, which may increase the computational cost.

Bibliography

[1] Thomas E Noll, John M Brown, Marla E Perez-Davis, Stephen D Ishmael, Geary C Tiffany, and Matthew Gaier. Investigation of the helios prototype aircraft mishap: Volume i mishap report. 2004.

[2] Jessica Jones and Carlos E. Cesnik. *Nonlinear Aeroelastic Analysis of the X-56 Multi-Utility Aeroelastic Demonstrator*. 2016.

[3] Julian Theis, Harald Pfifer, and Peter J. Seiler. *Robust Control Design for Active Flutter Suppression*. 2016.

[4] Eli Livne. Aircraft active flutter suppression: State of the art and technology maturation needs. *Journal of Aircraft*, 55(1):410–452, 2018.

[5] Gaetano MD Currao, Andrew J Neely, David R Buttsworth, and Sudhir L Gai. Hypersonic fluid-structure interaction on a cantilevered plate. EUCASS, 2017.

[6] Gaetano MD Currao, Andrew J Neely, Christopher M Kennell, Sudhir L Gai, and David R Buttsworth. Hypersonic fluid–structure interaction on a cantilevered plate with shock impingement. *AIAA Journal*, 57(11):4819–4834, 2019.

[7] D. Tang, S.C. Gibbs, and E.H. Dowell. Nonlinear aeroelastic analysis with inextensible plate theory including correlation with experiment. *AIAA Journal*, 53(5):1299–1308, 2015.

[8] D. Tang, M. Zhao, and E.H. Dowell. Inextensible beam and plate theory: Computational analysis and comparison with experiment. *Journal of Applied Mechanics*, 81(6), 2014.

[9] J.G. Simmonds and A. Libai. Exact equations for the inextensional deformation of cantilevered plates. *Journal of Applied Mechanics*, 46(3):631–636, 1979.

[10] J.G. Simmonds and A. Libai. Alternate exact equations for the deformation of arbitrary quadrilateral and triangular plates. *Journal of Applied Mechanics*, 46(4):895–900, 1979.

[11] J.G. Simmonds and A. Libai. Exact equations for the large inextensional motion of plates. *Journal of Applied Mechanics*, 48(1):109–112, 1981.

[12] P. Darmon and R.C. Benson. Numerical solution to an inextensible plate theory with experimental results. *Journal of Applied Mechanics*, 53(4):886–890, 1986.

[13] M.P. Paidoussis. *Fluid-Structure Interactions: Slender Structures and Axial Flow, Volume 2*. Academic Press, 2004.

[14] D.M. Tang, H. Yamamoto, and E.H. Dowell. Flutter and limit cycle oscillations of two-dimensional panels in three-dimensional flow. *Journal of Fluids and Structures*, 17(2):225–242, 2003.

[15] V.V. Novozhilov. *Foundations of the Nonlinear Theory of Elasticity*. Graylock Press, 1953.

[16] M.N. Hamdan and M.H.F. Dado. Large amplitude free vibrations of a uniform cantilever beam carrying an intermediate lumped mass and rotary inertia. *Journal of Sound and Vibration*, 206(2):151–168, 1997.

[17] L.G. Villanueva, R. B. Karabalin, M. H. Matheny, D. Chi, J.E. Sader, and M.L. Roukes. Nonlinearity in nanomechanical cantilevers. *Physical Review B*, 87(2):024304, 2013.

[18] W. Lacarbonara and H. Yabuno. Refined models of elastic beams undergoing large in-plane motions: Theory and experiment. *International Journal of Solids and Structures*, 43(17):5066–5084, 2006.

[19] M. Raviv Sayag and E.H. Dowell. Linear versus nonlinear response of a cantilevered beam under harmonic base excitation: Theory and experiment. *Journal of Applied Mechanics*, 83:101002, 2016.

[20] M.R.M. Crespo da Silva and C.C. Glynn. Non-linear flexural-flexural-torsional dynamics of inextensional beams. ii. forced motions. *Journal of Structural Mechanics*, 6(4):449–461, 1978.

[21] Max Beck. Die knicklast des einseitig eingespannten, tangential gedrückten stabes. *Zeitschrift für angewandte Mathematik und Physik ZAMP*, 3:225–228, May 1952.

[22] V.V. Bolotin and N.I. Zhinzher. Effects of damping on stability of elastic systems subjected to nonconservative forces. *International Journal of Solids and Structures*, 5:965–989, 1969.

[23] M. Chen. Hopf bifurcation in beck's problem. *Nonlinear Analysis, Theory, Methods and Applications*, 11(9):1061–1073, 1987.

[24] Y. Sugiyama, K. Katayama, and S. Kinoi. Flutter of a cantilevered column under rocket thrust. *Journal of Aerospace Engineering*, 8(1):9–15, 1995.

[25] A. Di Egidio, A. Luongo, and A. Paolone. Linear and non-linear interactions between static and dynamic bifurcations of damped planar beams. *International Journal of Non-Linear Mechanics*, 42:88–98, 2007.

[26] A. Luongo and A. Di Egidio. Bifurcation equations through multiple-scales analysis for a continuous model of a planar beam. *Nonlinear Dynamics*, 41:171–190, 2005.

[27] A. Luongo and A Di Egidio. Divergence, hopf and double-zero bifurcations of a nonlinear planar beam. *Computers and Structures*, 84:1596–1605, 2006.

[28] A. Luongo and F. D'Annibale. Nonlinear hysteretic damping effects on the post-critical behaviour of the visco-elastic becks beam. *Mathematics of Mechanics and Solids*, 22(6):1347–1365, 2017.

[29] I. Stanciulescu, L.N. Virgin, and T.A. Laursen. Slender solar sail booms: Finite element analysis. *Journal of Spacecraft and Rockets*, 44(3):528–537, 2007.

[30] M.A. Langthjem and Y. Sugiyama. Dynamic stability of columns subjected to follwer loads: A survey. *Journal of Sound and Vibration*, 238(5):809 – 851, 2000.

[31] T.R. Beal. Dynamic stability of a flexible missile under constant and pulsating thrusts. *AIAA Journal*, 3(3):486–494, 1965.

[32] M.J. Lighthill. Oscillating airfoils at high mach number. *Journal of the Aeronautical Sciences*, 20:402–406, 1953.

[33] Holt Ashley and Garabed Zartarian. Piston theory-a new aerodynamic tool for the aeroelastician. *Journal of the Aeronautical Sciences*, 23:1109–1118, 1956.

[34] Ira Nydick, Peretz P. Friedmann, and Xaolin Zhong. Hypersonic panel flutter studies on curved panels. AIAA 95-1485-CP, 1995.

[35] Earl H. Dowell. *A Modern Course in Aeroelasticity*. Springer, New York, 2015.

[36] Jack J. McNamara, Andrew R. Crowell, Peretz P. Friedmann, Bryan Glaz, and Abhijit Gogulapati. Approximate modeling of unsteady aerodynamics for hypersonic aeroelasticity. *Journal of Aircraft*, 47:1932–1945, 2010.

[37] W.D. Hayes and R.F. Probstein. *Hypersonic Flow Theory*. Academic Press, New York, 1959.

[38] H.W. Liepmann and A. Roshko. *Elements of Gas Dynamics*. Wiley, New York, 1957.

[39] P. Frank Pai. *Highly Flexible Structures: Modeling, Computation, and Experimentation*. American Institute of Aeronautics and Astronautics, Reston, VA, 2000.

[40] A.H. Nayfeh and P.F. Pai. *Linear and Nonlinear Structural Mechanics*. Wiley Series in Nonlinear Science. Wiley, 2004.

[41] P. Frank Pai, Robert D. Chapman, and Zaichun Feng. Geometrically exact displacement-based shell theory. *Thin-Walled Structures*, 70:1–18, 2013.

[42] Walter Lacarbonara. *Nonlinear Structural Mechanics: Theory, Dynamical Phenomena, and Modeling*. Springer, New York, 2013.

[43] E.H. Dowell and K.A. McHugh. Equations of motion for an inextensible beam undergoing large deflections. *Journal of Applied Mechanics*, 83:051007, 2016.

[44] K.A. McHugh and E.H. Dowell. Nonlinear responses of inextensible cantilever and free-free beams undergoing large deflections. *Journal of Applied Mechanics*, 85:051008, 2018.

[45] Kevin McHugh and Earl Dowell. Nonlinear response of an inextensible, cantilevered beam subjected to a nonconservative follower force. Manuscript submitted for publication, 2018.

[46] Kevin A McHugh and Earl H Dowell. Nonlinear response of an inextensible, cantilevered beam subjected to a nonconservative follower force. *Journal of Computational and Nonlinear Dynamics*, 14(3):031004, 2019.

[47] Kevin A McHugh and Earl H Dowell. Nonlinear response of an inextensible, free-free beam subjected to a nonconservative follower force. *Journal of Computational and Nonlinear Dynamics*, 15(2):021003, 2020.

[48] Kevin A McHugh, Philip Beran, Maxim Freydin, and Earl H Dowell. Flutter and limit cycle oscillations of a cantilevered plate in supersonic/hypersonic flow. *Proceedings of IFASD*, 2019.

[49] M.R.M. Crespo da Silva and C.C. Glynn. Non-linear flexural-flexural-torsional dynamics of inextensional beams. i. equations of motion. *Journal of Structural Mechanics*, 6(4):437–448, 1978.

[50] Herbert Goldstein, Charles Poole, and John Safko. *Classical Mechanics*. Addison Wesley, 1301 Sansome St., San Francisco, CA 94111, 3 edition, 2002.

[51] S. Nima Mahmoodi, Nader Jalili, and Siamak E. Khadem. An experimental investigation of nonlinear vibration and frequency response analysis of cantilever viscoelastic beams. *Journal of Sound and Vibration*, 311:1409–1419, 2008.

[52] Raymond L. Bisplinghoff, Holt Ashley, and Robert L. Halfman. *Aeroelasticity*. Dover Publications, Inc., Mineola, NY, 1996.

[53] V.V Bolotin. *Nonconservative Problems of the Theory of Elastic Stability*. Pergamon Press, Oxford, 1963.

[54] H. Ziegler. Die stabilitätskriterien der elastomechanik. *Ingenieur-Archiv*, 20(1):49–56, Jan 1952.

[55] A. Luongo and F. D'Annibale. On the destabilizing effect of damping on discrete and continuous circulatory systems. *Journal of Sound and Vibration*, 333:67236741, 2014.

[56] Peter Hagedorn. On the destabilizing effect of non-linear damping in non-conservative systems with follower forces. *International Journal of Non-Linear Mechanics*, 5(2):341 – 358, 1970.

[57] J.J. Thomson. Chaotic dynamics of the partially follower-loaded elastic double pendulum. *Journal of Sound and Vibration*, 188(3):385 – 405, 1995.

[58] M.R.M. Crespo da Silva. Harmonic non-linear response of beck's column to a lateral excitation. *International Journal of Solids and Structures*, 14(12):987 – 997, 1978.

[59] M.R.M. Crespo da Silva. Flexural-flexural oscillations of beck's column subjected to a planar harmonic excitation. *Journal of Sound and Vibration*, 60(1):133 – 144, 1978.

[60] A. Luongo and F. D'Annibale. Double zero bifurcation of non-linear viscoelastic beams under conservative and non-conservative loads. *International Journal of Non-Linear Mechanics*, 55(Supplement C):128 – 139, 2013.

[61] F. D'Annibale, M. Ferretti, and A. Luongo. Improving the linear stability of the beck's beam by added dashpots. *International Journal of Mechanical Sciences*, 110:151–159, 2016.

[62] O.N. Kirillov and A.O. Seyranian. The effect of small internal and external damping on the stability of distributed non-conservative systems. *Journal of Applied Mathematics and Mechanics*, 69:529–552, 2005.

[63] D.A. Peters and J.J. Wu. Dynamic stability of a flexible missile under constant and pulsating thrusts. *Journal of Sound and Vibration*, 59(4):591–610, 1978.

[64] J. M. T. Thompson and H. B. Stewart. *Nonlinear Dynamics and Chaos*. John Wiley & Sons, Ltd, West Sussex, England, 2 edition, 2002.

[65] Dean Culver, Kevin McHugh, and Earl Dowell. An assessment and extension of geometrically nonlinear beam theories. *Mechanical Systems and Signal Processing*, 134:106340, 2019.

[66] McNamara J.J. Thuruthimattam B.J. Friedmann, P.P. and I. Nydick. Aeroelastic analysis of hypersonic vehicles. *Journal of Fluids and Structures*, 19(5):681 – 712, 2004. Aeroelasticity.

[67] Wei-Wei Zhang, Zheng-Yin Ye, Chen-An Zhang, and Feng Liu. Supersonic flutter analysis based on a local piston theory. *AIAA Journal*, 47(10):2321–2328, 2009.

[68] Earl H. Dowell and Donald B. Bliss. New look at unsteady supersonic potential flow aerodynamics and piston theory. *AIAA Journal*, 51(9):2278–2281, 2013.

[69] Arthur W Leissa. *Vibration of plates*. National Aeronautics and Space Administration, 1969.

[70] Earl H. Dowell. *Aeroelasticity of Plates and Shells*. Noordhoff International Publishing, Leyden, The Netherlands, 1975.

[71] E. H. Mansfield. The inextensional theory for thin flat plates. *Quarterly Journal of Mechanics and Applied Math*, 8(3):338–352, 1955.

[72] Joaquim R. R. A. Martins, Juan J. Alonso, and James Reuther. Aero-structural wing design optimization using high-fidelity sensitivity analysis. Technical report, National Aeronautics and Space Administration,Ames Research Center,Moffett Field,CA,94035, 2001.

[73] Joaquim R.R.A. Martins, Juan J. Alonso, and James J. Reuther. A coupled-adjoint sensitivity analysis method for high-fidelity aero-structural design. *Optimization and Engineering*, 6:33–62, 2005.

[74] Joaquim R.R.A. Martins and J. T. Hwang. Review and unification of methods for computing derivatives of multidisciplinary computational models. *AIAA Journal*, 51:2582–2599, 2013.

[75] Jeffrey P. Thomas, Kenneth C. Hall, and Earl H. Dowell. Discrete adjoint approach for modeling unsteady aerodynamic design sensitivities. *AIAA Journal*, 43:1931–1936, 2005.

[76] Bret Stanford and Philip Beran. Formulation of analytical design derivatives for nonlinear unsteady aeroelasticity. *AIAA Journal*, 49:598–610, 2011.

[77] Bret Stanford and Philip Beran. Aerothermoelastic topology optimization with flutter and buckling metrics. *Structural and Multidisciplinary Optimization*, 48:149–171, 2013.

Biography

Kevin Andrew McHugh earned a Bachelor's of Science with Honors in Mechanical Engineering from Lafayette College in May 2015. He then studied aeroelasticity under the advisement of Dr. Earl H. Dowell at Duke University, where he was awarded the Department of Defense SMART Scholarship to fund his graduate studies. Kevin successfully defended this dissertation on February 28, 2020 to earn his PhD, and began his career at the Air Force Research Lab at Wright-Patterson Air Force Base in Dayton, OH.

Publications

Dowell, E. and McHugh, K., 2016. "Equations of Motion for an Inextensible Beam Undergoing Large Deflections." Journal of Applied Mechanics, 83, p. 051007.

McHugh, K. and Dowell, E., 2018. "Nonlinear Responses of Inextensible Cantilever and Free-Free Beams Undergoing Large Deflections." Journal of Applied Mechanics, 85, p. 051008.

McHugh, K. and Dowell, E., 2019. "Nonlinear Response of an Inextensible, Cantilevered Beam Subjected to a Nonconservative Follower Force." Journal of Computational and Nonlinear Dynamics, 14, p. 031004.

McHugh, K. and Dowell, E., 2020. "Nonlinear Response of an Inextensible, Free-Free Beam Subjected to a Nonconservative Follower Force." Journal of Computational and Nonlinear Dynamics, 15, p. 021003.

McHugh, K., Freydin, M., Kruger Bastos, K., Beran, P., and Dowell, E., 2019. "Flutter and Limit Cycle Oscillations of a Cantilevered Plate in Supersonic Flow." Submitted for publication.

Culver, D., McHugh, K., and Dowell, E., 2019. "An assessment and extension of geometrically nonlinear beam theories." Mechanical Systems and Signal Processing, 134, p. 106340.